



The
University
Of
Sheffield.

**Department of Civil & Structural
Engineering**

*A Practical Approach to Modelling Integrity Failure of
Composite Floors in Fire*

Mohammadali Javaheriafif

Supervisor(s):

Professor Buick Davison

Professor Ian Burgess

15/03/2017

Declaration of Authors Right

Unless otherwise stated, this thesis is the original work of author

Mohammadali Javaheriafif

Acknowledgement

I would like to express my sincere gratitude to my supervisors, Professor Buick Davison and Professor Ian Burgess for their valuable guidance, stimulating discussions and continued encouragement throughout.

Thanks are also extended to my fellow researchers and friends in the department and across the faculty for making my time enjoyable.

I have been extremely fortunate to receive endless love and support from my family throughout, which I am immensely grateful. Without them the completion of this work would have not been possible.

Table of Contents

1. Introduction.....	1
1.1 Structural Fire Engineering	1
1.1.1 Natural fire behaviour	1
1.1.2 Standard fires	2
1.2 Connection behaviour and Structural Integrity	5
1.3 Scope of the Research	7
1.4 Thesis Outline.....	8
2. Literature Review	10
2.1 Material Properties at Elevated Temperature	10
2.1.1 Properties of Steel at Elevated Temperature	10
2.1.2 Properties of Concrete at Elevated Temperature	14
2.1.3 Properties of Shear Studs at Elevated Temperature	17
2.1.4 Thermal Expansion	18
2.2 Connections in Steel Frames	19
2.3 Behaviour of Different Structural Elements in Fire	22
2.3.1 Steel beam behaviour at elevated temperature.....	22
2.3.2 Concrete Slab behaviour at elevated temperature.....	25
2.3.3 Connection behaviour at elevated temperature	31
2.4 Numerical modelling.....	33
2.4.1 Component-based method.....	34
2.4.2 <i>VULCAN</i> program.....	36
2.5 The Importance of Composite Slab Break Element	45
2.5.1 Behaviour of composite slab in hogging regions.....	45
2.5.2 Integrity and insulation criterion of composite slab in fire	47
2.5.3 Remarks.....	50
2.6 Factors Influencing Composite Slab Break Element	51
2.6.1 Minimum reinforcement area.....	51
2.6.2 Temperature	52
2.6.3 Bond Strength	59
2.7 Component- based composite joint model	68
2.8 Conclusion.....	71
3. Methodology	72

3.1	Bare steel connection with 3D slab shell element.....	72
3.2	Characterisation of Break Element.....	73
3.2.1	The effects of shear bond interaction.....	75
3.2.2	The effects of temperature.....	77
3.3	Development of 2D Break Element.....	77
3.3.1	<i>Vulcan</i> Programming.....	78
3.3.2	Force-Displacement Relationship.....	82
3.3.3	Stiffness Matrix.....	83
3.4	Conclusion.....	85
4.	Numerical Modelling and Validation.....	86
4.1	Convergence and Sensitivity Study.....	86
4.2	Evaluation of Break Element against Theoretical Model.....	90
4.3	Comparison of the FE model with experimental data.....	91
4.3.1	Seat Cleat Composite Joint Experiment.....	91
4.3.2	Flexible End Plate Composite Joint.....	102
4.4	Qualitative comparison.....	122
4.4.1	FRACOF test.....	122
4.5	Conclusion.....	126
5.	Parametric Studies.....	127
5.1	Case study I: Composite frame with rigid connections.....	127
5.1.1	Boundary conditions.....	129
5.1.2	Influence of reinforcement ratio on vertical deflection/ crack development of composite panel.....	130
5.1.3	Influence of reinforcement ratio on connection performance of composite panel.....	144
5.1.4	Influence of reinforcement material properties on vertical deflection/ crack development of composite panel.....	147
5.1.5	Influence of reinforcement material properties on connection performance of composite panel.....	155
5.1.6	Influence of slab thickness on vertical deflection/ crack development of composite panel.....	157
5.1.7	Influence of slab thickness on connection performance of composite panel.....	165
5.1.8	Influence of concrete compressive strength on vertical deflection/ crack development of composite panel.....	167

5.1.9	Influence of concrete compressive strength on connection performance of composite panel	174
5.1.10	Influence of aspect ratio on vertical deflection/ crack development of composite panel	176
5.1.11	Influence of aspect ratio on connection performance of composite panel	183
5.1.12	Remarks.....	185
5.2	Case study II: Composite frame with semi-rigid connections.....	186
5.2.1	Influence of connection ductility on vertical deflection/crack development of composite panel	187
5.3	Conclusion.....	192
6.	Conclusion and Recommendations for Further Work	193
6.1	Conclusions	193
6.1.1	Behaviour of structural members in fire	195
6.1.2	Numerical modelling and validation	196
6.1.3	Parametric studies	198
6.2	Recommendations for further work.....	203
7.	References.....	207
8.	APPENDIX I	215

List of Figures

Figure 1.1: Development of natural fire in a compartment.....	2
Figure 1.2: Parametric fire curve – ISO834.....	4
Figure 1.3: Nominal fire curves.....	5
Figure 2.1: Stress-strain relationship for carbon steel – ambient temperature.....	10
Figure 2.2: Stress-strain curve of steel material – elevated temperature.....	12
Figure 2.3: Degradation of strength and stiffness for steel at elevated temperature.....	13
Figure 2.4: Stress-strain curves for concrete at elevated temperature.....	15
Figure 2.5: Degradation of concrete strength at elevated temperature.....	16
Figure 2.6: Comparison of thermal expansion of steel and concrete at elevated temperature.....	19
Figure 2.7: Effects of connections characteristics on beam behaviour.....	20
Figure 2.8: a) Rotational deformation of beam-to-column connection, b) Connection types – Rotational characteristics.....	21
Figure 2.9: Thermal bowing in a simply supported beam.....	22
Figure 2.10: Illustrative behaviour of axially/rotationally restrained beam in fire.....	24
Figure 2.11: Compressive membrane action in fire.....	26
Figure 2.12: Different mechanism of tensile membrane action in slab.....	28
Figure 2.13: Load deflection of a slab.....	28
Figure 2.14: Failure mechanism of slab.....	29
Figure 2.15: Schematic of floor division, Baily-BRE method.....	30
Figure 2.16: Behaviour of steel beam in fire condition.....	32
Figure 2.17: Typical beam-to-column joint – component model.....	35
Figure 2.18: Tri-linear force-displacement representations of joint component.....	36
Figure 2.19: Three noded- beam element configuration.....	38
Figure 2.20: Concrete slab configuration in <i>Vulcan</i>	39
Figure 2.21: Concrete bi-axial failure envelopes at elevated temperature.....	40
Figure 2.22: Bi-linear smeared concrete crack model used in <i>Vulcan</i>	42
Figure 2.23: General procedure of static-dynamic solver in <i>Vulcan</i>	44
Figure 2.24: a) membrane forces of single slab, b) membrane forces of two adjacent slabs.....	46
Figure 2.25: Cracked floor slab around the connection.....	47
Figure 2.26: Cracked section of the first Munich test.....	48
Figure 2.27: Gaping crack, first Munich test.....	49
Figure 2.28: Plan view of the compartment arrangement, second Munich test.....	49
Figure 2.29: Crack location at the edge of composite slab – second Munich test.....	50
Figure 2.30: Geometrical notation of steel decking according to EC4.....	52
Figure 2.31: Coefficient $k_s(\theta)$ allowing for decrease of characteristic strength (f_{yk}) of tension and compression reinforcement (Class N).....	54
Figure 2.32: Stress-strain of rebar at different temperature.....	54
Figure 2.33: Tensile strength of steel rebar – temperature.....	55
Figure 2.34: Temperature distribution in slab-Munich.....	56
Figure 2.35: Temperature distribution in slab-FRACOF.....	57
Figure 2.36: Characteristic compressive strength (f_{ck}) against temperature.....	57

Figure 2.37: Shearing of concrete between the lugs in pull-out failure	59
Figure 2.38: Wedging action causing splitting failure	59
Figure 2.39: Bond-stress and slip relationship	61
Figure 2.40: Bar stress-slip model by	63
Figure 2.41: Bar slip model	64
Figure 2.42: Uniaxial stress-strain relationship	66
Figure 2.43: Degradation of bond strength between concrete and reinforcing steel bar at elevated temperatures.....	67
Figure 2.44: Behaviour of joint subjected to axial.....	69
Figure 2.45: Idealised representation of composite connection component model	69
Figure 3.1: Idealised representation of composite connection component model	74
Figure 3.2: Transfer of tensile forces through bond stresses	75
Figure 3.3: Bar slip model	76
Figure 3.4: Element arrangement in <i>Vulcan</i>	79
Figure 3.5: 3-D representation of floor compartments in <i>Vulcan</i>	80
Figure 3.6: Corresponding slab area for individual break element in <i>Vulcan</i>	81
Figure 3.7: Elemental arrangement- <i>Vulcan</i>	81
Figure 3.8: Multi-linear force-displacement relationship – break element.....	82
Figure 3.9: Possible crack location & bottom face contact.....	84
Figure 3.10: Nodal force vector – local co-ordinates.....	84
Figure 4.1: Slab panels with identical overall dimensions.....	87
Figure 4.2: Mesh sensitivity study - slab central deflection.....	87
Figure 4.3: Composite lab panels with break element - identical overall dimensions.....	88
Figure 4.4: Mesh sensitivity study - slab crack development	89
Figure 4.5: Comparison of theoretical and numerical model for lateral displacements – pull out test.....	90
Figure 4.6: Cantilever composite joint – C3 test arrangement.....	91
Figure 4.7: Dimensions of typical test specimen	92
Figure 4.8: Moment-rotation curve of S2 – comparison of numerical analysis with experimental data	95
Figure 4.9: Moment-Rotation Curves of S2/C3 – comparison of test data with numerical model	96
Figure 4.10: Formation of cracks around column.....	97
Figure 4.11: C3 composite joint – numerical model for <i>Vulcan</i>	98
Figure 4.12: C3 test - lateral displacement of composite slab from <i>Vulcan</i> 30kN.m	99
Figure 4.13: C3 test - lateral displacement of composite slab from <i>Vulcan</i> at 60kN.m.....	100
Figure 4.14: Comparison of crack development in the slab at different load levels.....	101
Figure 4.15: Cruciform arrangement –bare steel connection.....	103
Figure 4.16: Flexible end plate composite connection detail – Group 4.....	104
Figure 4.17: Flexible end plate composite connection detail – Group 4.....	104
Figure 4.18: Composite joint – Group 4 – Numerical model, <i>Vulcan</i>	106
Figure 4.19: Moment- rotation of composite joint – Group 4.....	108
Figure 4.20: Moment- rotation of composite joint – Enhanced - Group 4.....	110

Figure 4.21: Slab crack locations in Group4.....	111
Figure 4.22: Group4 test - lateral displacement of composite slab from <i>Vulcan</i>	112
Figure 4.23: Crack development in composite slab – Group 4 - <i>Vulcan</i>	113
Figure 4.24: Plan view of specimen arrangement, Group 4 - <i>Vulcan</i>	114
Figure 4.25: Force-displacement of break elements - <i>Vulcan</i>	114
Figure 4.26: Flexible end plate composite connection detail – Group 5.....	115
Figure 4.27: Moment- rotation of composite joint – Group 5.....	116
Figure 4.28: Moment- rotation of composite joint – Enhanced - Group 5.....	118
Figure 4.29: Slab crack locations in Group5.....	119
Figure 4.30: Lateral displacement of composite slab - Group 5 - <i>Vulcan</i>	120
Figure 4.31: Crack development in composite slab – Group 5 - <i>Vulcan</i>	121
Figure 4.32: Slab cross-section of FRACOF test.....	122
Figure 4.33: Plan view of FRACOF test.....	123
Figure 4.34: Numerical model of FRACOF test, <i>Vulcan</i>	124
Figure 4.35: Crack development of FRACOF test, <i>Vulcan</i>	125
Figure 5.1: Composite floor arrangement	127
Figure 5.2: 3D isometric view of full floor slab area with 864 elements.....	128
Figure 5.3: Boundary conditions for model-scale interior composite panel.....	129
Figure 5.4: 3D view of the deformed shape of the A142 interior composite panel	131
Figure 5.5: Plan view of slab horizontal movement, A142 interior composite panel.....	132
Figure 5.6: Comparison of the A142-slab central deflection from <i>Vulcan1</i> and <i>Vulcan2</i> ...	133
Figure 5.7: Horizontal crack development – exterior secondary edge beam, A142 panel...	134
Figure 5.8: Horizontal crack development – interior secondary edge beam, A142 panel ...	135
Figure 5.9: Horizontal crack development – interior primary edge beam, A142 panel.....	136
Figure 5.10: Distribution of membrane forces – A142 composite panel	137
Figure 5.11: 3D view of the deformed shape of the A252 interior composite panel	138
Figure 5.12: Plan view of slab horizontal movement, A252 interior composite panel.....	139
Figure 5.13: Comparison of the A252-slab central deflection from <i>Vulcan1</i> and <i>Vulcan2</i> .	139
Figure 5.14: Horizontal crack development – interior secondary edge beam, A252 panel .	141
Figure 5.15: Horizontal crack development – interior primary edge beam, A252 panel.....	142
Figure 5.16: Comparison of the A393-slab central deflection from <i>Vulcan1</i> and <i>Vulcan2</i> .	143
Figure 5.17: Comparison of rotational displacement at connection- A142	144
Figure 5.18: Comparison of rotational displacement at connection- A252	145
Figure 5.19: Comparison of rotational displacement at connection- A393	145
Figure 5.20: General comparison of slab central deflection from <i>Vulcan1</i> and <i>Vulcan2</i>	146
Figure 5.21: General comparison of connection rotational displacement from <i>Vulcan1</i> and <i>Vulcan2</i>	147
Figure 5.22: 3D view of the deformed shape of the A142 interior composite panel- $f_y=600\text{N/mm}^2$	148
Figure 5.23: Plan view of slab horizontal movement, A142 interior composite panel- $f_y=600\text{N/mm}^2$	148
Figure 5.24: Comparison of the A142-slab central deflection from <i>Vulcan1</i> and <i>Vulcan2</i> .	149
Figure 5.25: Comparison of the A142-slab central deflection from A1 and A2.....	150

Figure 5.26: Horizontal crack development – exterior secondary edge beam- $f_y=600\text{N/mm}^2$	152
Figure 5.27: Horizontal crack development – interior secondary edge beam- $f_y=600\text{N/mm}^2$	153
Figure 5.28: Horizontal crack development – interior primary edge beam- $f_y=600\text{N/mm}^2$.	154
Figure 5.29: Comparison of rotational displacement at connection- A142- $f_y=600\text{N/mm}^2$.	155
Figure 5.30: General comparison of connection rotational displacement from <i>Vulcan1</i> & <i>Vulcan2</i>	156
Figure 5.31: 3D view of the deformed shape of the A142 interior composite panel-90mm thickness (B1 model)	158
Figure 5.32: Plan view of slab horizontal movement, A142 interior composite panel- 90mm thickness (B1 model)	158
Figure 5.33: Comparison of the B1 model - slab central deflection from <i>Vulcan1</i> and <i>Vulcan2</i>	159
Figure 5.34: Comparison of the A142-slab central deflection from A1 and B1 models	160
Figure 5.35: Horizontal crack development – exterior secondary edge beam – B1 model	162
Figure 5.36: Horizontal crack development – interior secondary edge beam – B1 model	163
Figure 5.37: Horizontal crack development – interior primary edge beam – B1 model	164
Figure 5.38: Comparison of rotational displacement at connection- B1 model	165
Figure 5.39: General comparison of connection rotational displacement from <i>Vulcan1</i> and <i>Vulcan2</i>	166
Figure 5.40: 3D view of the deformed shape of the A142 interior composite panel - C1 model	167
Figure 5.41: Plan view of slab horizontal movement, A142 interior composite panel - C1 model	168
Figure 5.42: Comparison of the C1 model - slab central deflection from <i>Vulcan1</i> and <i>Vulcan2</i>	168
Figure 5.43: Comparison of the A142-slab central deflection from A1 and C1	169
Figure 5.44: Horizontal crack development – exterior secondary edge beam – C1 model	171
Figure 5.45: Horizontal crack development – interior secondary edge beam – C1 model	172
Figure 5.46: Horizontal crack development – interior primary edge beam – C1 model	173
Figure 5.47: Comparison of rotational displacement at connection- C1 model	174
Figure 5.48: General comparison of connection rotational displacement from <i>Vulcan1</i> and <i>Vulcan2</i>	175
Figure 5.49: 3D view of the deformed shape of the A142 interior composite panel - D1 model	176
Figure 5.50: Plan view of slab horizontal movement, A142 interior composite panel - D1 model	177
Figure 5.51: Comparison of the D1 model - slab central deflection from <i>Vulcan1</i> and <i>Vulcan2</i>	178
Figure 5.52: Comparison of the A142-slab central deflection from A1 and D1	178
Figure 5.53: Horizontal crack development – exterior secondary edge beam – D1 model	180
Figure 5.54: Horizontal crack development – exterior secondary edge beam – D1 model	181
Figure 5.55: Horizontal crack development – interior primary edge beam – D1 model	182

Figure 5.56: Plan view of ultimate slab horizontal movement, D1 model.....	183
Figure 5.57: Comparison of the D1 model - slab central deflection from <i>Vulcan1</i> and <i>Vulcan2</i>	183
Figure 5.58: Comparison of the A142-slab central deflection from A1 and D1	184
Figure 5.59: 3D isometric view of full floor slab area.....	186
Figure 5.60: 3D view of the deformed shape of the interior composite panel.....	187
Figure 5.61: Plan view of slab horizontal movement, flexible connection.....	188
Figure 5.62: Comparison of the -slab central deflection – composite panel.....	189
Figure 5.63: Horizontal crack development at interior primary edge beam – flexible connection	190
Figure 5.64: Comparison of the -beam central deflection – composite panel.....	191
Figure 5.65: Comparison of connection rotational displacement – composite panel	191

List of Tables

Table 2.1: Reduction factors for stress-strain relationship of carbon steel – elevated temperatures.....	14
Table 2.2: Class N values for the parameters of the stress-strain relationship of hot rolled and cold worked reinforcing steel at elevated temperatures	53
Table 2.3: Temperature distribution in slab – standard fire	58
Table 2.4: Bond strength values proposed by various researchers	62
Table 4.1: Joint details – test C3.....	92
Table 4.2: Material properties-steel reinforcement.....	94
Table 4.3: Assumed Boundary Condition.....	94
Table 4.4: Material properties – Group 4.....	105
Table 4.5: Assumed boundary condition – Group 4	107
Table 4.6: Material properties - FRACOF test	123
Table 5.1: Section properties – 9m x 6m panel.....	128
Table 5.2: Boundary condition for model-scale interior composite panel.....	130

Abstract

The connections in a steel-framed building are subjected to a complex set of forces in fire conditions. Large axial forces (compressive forces that later become tension as the steel softens from rising temperature) will affect the beams and their connections, in addition to the shear forces and bending moments caused by gravity loading. Therefore, the performance of a joint in response to such loads plays a key role in overall behaviour of the frame. Large deflections of composite slabs contribute significantly to the robustness of composite steel-framed buildings in fire. The composite slab contributes to the rotational stiffness of a joint through the tensile resistance of its reinforcement acting at a large lever arm from the centroid of the steel beam, adding to the hogging moment capacity of the connection. This clearly results in considerably higher rotational stiffness, but for the purposes of structural fire engineering design there should also be enough ductility in the reinforcement to provide sufficient rotation capacity to the joint. Adequate ductility in composite slabs is a requirement for the robustness of composite buildings in fire. Finite element analysis of steel frames in fire often assumes the slab to be continuous and the inevitable cracking that takes place is accounted for using smeared cracking approaches. At beam-to-column connections the presence of the slab increases the stiffness and strength of the joint, but existing analytical techniques do not adequately address the effect of cracking in the slab at these locations. In order to investigate the influence of the concrete slab on the joint performance, a method to allow for the development of discrete cracks in the concrete slab, largely as a result of the hogging bending moments over supporting steel beams and connections, has been developed. In order to avoid the complexities of generalized discrete cracking analysis, fracture at key locations is represented by the use of “break-elements”. The new break-element represents the crack development in the composite slab, mainly across internal beams on the column grid where it is assumed that cracks will initially occur. The model results in a localisation of the yield and ultimate strains in the rebar, enabling the crack width at which it fractures to be represented in terms of the local bond characteristics beyond the crack faces.

The approach is being implemented in the *Vulcan* software, which is capable of modelling geometrical non-linearity, also considering non-linear material behaviour at elevated temperature. The software has the advantage of combined static and dynamic solvers, which makes it possible to trace the structural behavior of a single member or a whole frame from initial static response, through local failure or instability, to stable post-buckling behaviour. The composite joint is modelled using the existing two-dimensional component-based model for bare steel connections, acting compositely with the 3D slab shell element through link elements representing shear studs. The newly developed break elements can be located at the perimeter nodes of every slab element across the entire floor slab area. This will enable a more accurate investigation of the crack development within a slab panel in fire scenarios. Once the break element fractures the dynamic solver can temporarily be activated to search for the next re-stabilization. After re-stabilizing, the analysis continues using the static solver.

Three series of previous experimental tests on composite joints at ambient temperature with different bare steel connections have been modelled in *Vulcan* software in order to validate the newly developed break element. The model is capable of predicting the occurrence of the initial cracks, tracing the behaviour of the mesh reinforcement represented at each break element and the sequence of failure of the reinforcement in the composite slab. Furthermore, the numerical model can represent the rotational response of composite joints with a reasonable level of accuracy, subject to the limitations of the current version of the software in modelling component-based connection elements.

A series of parametric studies was conducted in order to investigate the influence of reinforcement ratio, reinforcement material properties (characteristic yield strength), concrete material properties (characteristic compressive strength), composite slab thickness and the different aspect ratio on the overall performance of the composite panel. The outcome of the analysis has been presented in terms of the slab vertical deflection, rotational displacement of the connection and the horizontal movement of the slab edges (crack propagation). The calculated result from the updated version was compared with the result from the original software and appropriate discussion has been drawn.

Chapter 1

1. Introduction

1.1 Structural Fire Engineering

The ultimate limit state condition requires the structure to withstand the load against collapse with an adequate factor of safety. Specific aspects of passive fire protection must be considered to ensure the fire safety of the structure. Limiting fire spread and the adequate load bearing capacity are the main aspects to consider when designing the structure for fire safety purposes, these ensure the ability of the building to retain its stability in fire for a rational period of time [1]. Prevention of the catastrophic collapse of a structure in fire is the primary concern of structural fire engineering, therefore, it can be insured that there is always adequate time available to evacuate the building with no major hazard [1], [2].

1.1.1 Natural fire behaviour

The first step to understand structural behaviour in fire is to have adequate knowledge about how fire develops in a compartment. In general, there are three main components required to initiate a fire; ignition, fuel, and oxygen, which are also known as the fire triangle. The response of a natural fire in any compartment is depended on a series of factors, such as: the opening size, type of compartment, fuel amount and the ventilation. The typical development of a compartment fire can be divided into three phases: [3], [4]

Pre-flashover: is a transition point also known as the growth period, where all combustible materials within the compartment start to burn resulting in a rapid increase of temperature in the compartment

Post-flashover: this is the stage where the temperature within the compartment reaches its peak, provided that sufficient ventilation is available. The increase in the

rate of the temperature continues until the rate of generated volatiles is dropped below the level of the fuel consumption.

Decay: Once all the combustible materials burn out, the temperature will drop in the cooling stage (that is also known as the decay period). Refer to figure 1.1.

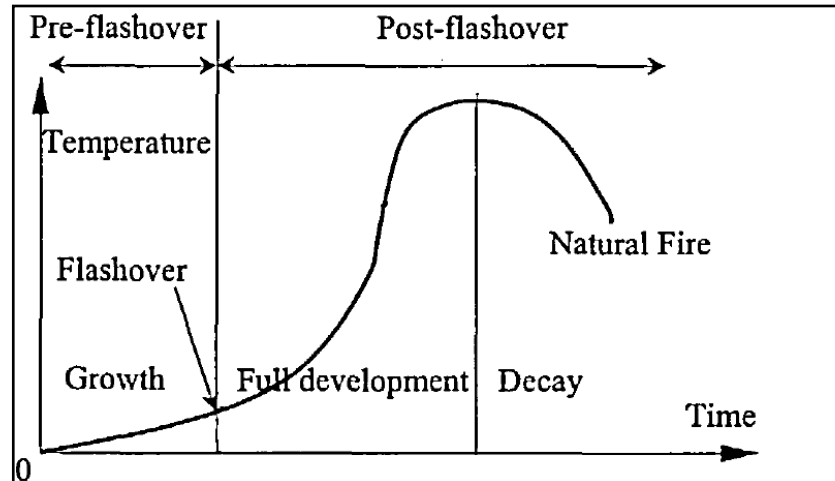


Figure 1.1: Development of natural fire in a compartment [6]

1.1.2 Standard fires

The development of a natural fire in a compartment is a complex phenomenon, since it depends on many different factors, which vary according to surrounding conditions. Therefore, in order to investigate the structural behaviour at elevated temperature it is more convenient to have a standard time-temperature curve for a fire to allow comparison of different structural member performance in a standard heating environment. This is also specified in Eurocode 4; “*required functions and levels of performance can be specified either in terms of nominal (standard) fire resistance rating, generally given in national regulations or, where allowed by national fire regulations, by referring to fire safety engineering for assessing passive and active measures*” [5]. Therefore, four nominal (standard) fire curves have been defined in Eurocode 1 [6].

1.1.2.1 ISO834 fire curve

The standard fire gas temperature curve (also known as ISO834) is the internationally accepted method of heating in order to test individual structural elements at high temperature. It should also be noted that there is some variation in the standard fire curves adopted in different countries. This can be explained by the difference in fuel types, the internal walls of the furnace and its geometry, which all can have an influence on the heat radiation and thus the amount of heat transferred to the specimen. The standard fire curve is presented in terms of time-temperature relationship as described by equation 1.1.

$$\theta_g = 20 + 345 \log(8t + 1) \quad (1.1)$$

Where, θ_g is the furnace temperature in °C and t is the time in minutes. A certain period of fire resistance is required for different structural members based on the function of the element in the building. The required resistance time is normally expressed in periods of 30, 60, 90 and 120 minutes. It should be noted that the cooling phase of the fire is not considered in the standard fire curve and ISO834 can only be used while the temperature is increasing inside the furnace.

1.1.2.2 Parametric fire curve

The standard fire curve is simple to use, however, the cooling phase of a natural fire is not included, and therefore, a new concept (a parametric curve) was introduced by EC1 to give better understanding of structural behaviour under fire. A linear cooling phase of the fire has been considered in the new fire curve, which provides a better estimation of the real fire behaviour. Equation 1.2 expresses the time-temperature relationship for the new curve.

$$\theta_g = 20 + 1325(1 - 0.324e^{-0.2t^*} - 0.204e^{-1.7t^*} - 0.472e^{-19t^*}) \quad (1.2)$$

Where, θ_g is the temperature inside the furnace in °C and t^* is the normalized time in minutes.

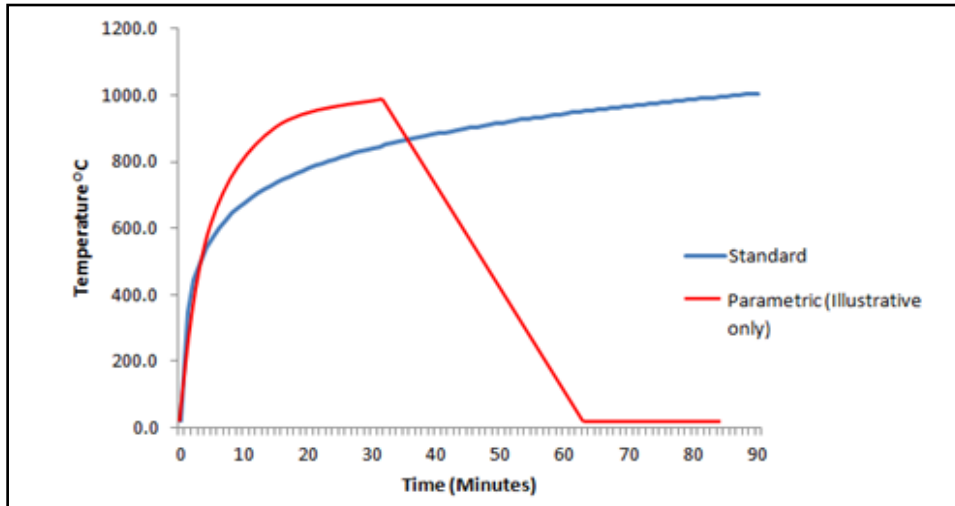


Figure 1.2: Parametric fire curve – ISO834 [6]

1.1.2.3 Other nominal fire exposure

There are two other fire exposures that have been introduced in EC1; the External fire curve and the Hydrocarbon fire curve. Equations 1.3 and 1.4 show the time-temperature relationship for the mentioned fire curves respectively and figure 1.3, illustrates different nominal fire curves defined in EC1. It should be noted that a uniform temperature distribution within the fire compartment is always assumed regardless of the type of nominal fire curve used.

$$\theta_g = 20 + 660(1 - 0.687e^{-0.32t} - 0.313e^{-3.8t}) \quad (1.3)$$

$$\theta_g = 20 + 1080(1 - 0.325e^{-0.167t} - 0.675e^{-2.5t}) \quad (1.4)$$

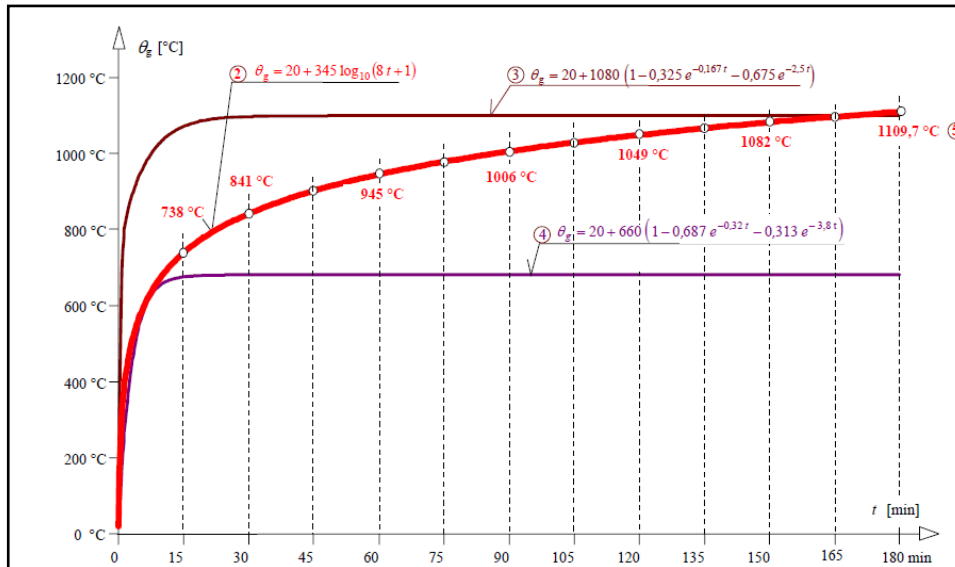


Figure 1.3: Nominal fire curves [6]

1.2 Connection behaviour and Structural Integrity

Any structure is only as strong as its weakest links but which is the weakest part is the matter of issue. Previously it was a common design practice to consider the main structural members first and to give connection design a secondary role with respect to stability issues in the design of steel structures. This process fails to recognize the fundamental influence of the connections on the performance of the structure as a whole [16]. Today, the importance of joints and connections has been widely recognized and it is generally believed that in many structures it is the connections that will be weaker than its connected components [17].

Different types of local failure cause different degrees of risk to a building. Progressive collapse can be the consequence of failure of a single load-carrying element. Joints are of particular importance since the progressive collapse of a steel framed structure can be critically influenced by the performance of joints, especially under accidental extreme loading such as fire attacks. The collapse of the twin towers of the World Trade Centre in 2001 clearly illustrates the importance of joints in the overall performance of a structure. The local damage caused by aircraft impacts and the high temperature effects from the running fire within the building, along with

poor performance of joints resulted in catastrophic collapse of the entire building. What actually happened in the twin towers is the loss of structural ability to transfer the load above the impact zone due to the combination of aircraft impacts and fire damage. Wang et al, 2011 [17] has also cited the report by NIST (National Institute of Standards and Technology) on progressive collapse of the WTC buildings, which suggested that connection failure initiated progressive collapse of the building. Regarding what NIST states, standard connection types typically used in steel structures may not be able to adequately redistribute loads in order to provide sufficient rotation and tensile strain to resist large deflections [18]. Furthermore, FEMA stated, *“the performance of the connections in steel structures is important for the building’s overall stability and often determines whether a collapse is localized or leads to progressive collapse. Thus, the issue of connection performance under fire exposure is critical to understanding building performance and should be a subject of further research”* [19]. Clearly the joint performance is critical at the time of extreme events such as fire. Apart from the danger of progressive collapse in the structure, joint failure in fire is crucial as any fracture of joints between beams and columns (or beams-to-beam) can lead to several undesirable effects such as spreading of fire to the upper floors through the gaps in cracked concrete slabs or lateral instability of a column resulting from a loss of connection to the beam and floor [20].

Generally there are three elements to be met in order to have a safely designed structure with respect to fire, namely Integrity, Insulation and load bearing capacity. The British Building Regulations states that *“The fire resistance of an element of construction is a measure of its ability to withstand the effects of fire in one or more ways, as follows:*

- a. resistance to collapse, i.e. the ability to maintain loadbearing capacity [...];*
- b. resistance to fire penetration, i.e. an ability to maintain the integrity of the element;*
- c. resistance to transfer of excessive heat, i.e. an ability to provide insulation from high temperatures”* [21].

Therefore, as mentioned above, in the event of fire, the overall stability of a building can be greatly influenced by the performance of joints within the structure. Despite the previous extensive researches on steel frame behaviour, there are still some aspects of joint behaviour that need be deeply investigated. This research aims to provide a better understanding of composite joint behaviour and develop a component-based model accounting for the slab behaviour on top of the joint.

1.3 Scope of the Research

The software *Vulcan* has been developed by the Structural Fire Engineering Research Group at the University of Sheffield for three-dimensional analysis of the structural behaviour of steel and composite buildings. The current version of the *Vulcan* software is based on the layered slab shell element that was previously developed by Huang [22], in which a smeared cracking approach was adopted to model the cracking and crushing of individual layers of the slab under large deflection. The main objective of this research is to develop a model to address possible fire compartment integrity failure caused by through-depth cracking of the composite slabs subjected to a large deflection. The presence of a concrete slab on top of a beam-to-beam or beam-to-column connection in the hogging region of the floor area can significantly influence the performance of the connection underneath and consequently the overall performance of the structural frame. The layered procedure for the slab element incorporating the smeared cracking model assumes perfect bond between the concrete and the steel reinforcement. Therefore, localised failure of the slab cannot be studied using the current model. The cracking behaviour decisively depends on the characteristics of the mesh reinforcement in the slab, including its ductility across discrete cracks. Therefore, any reasonable modelling of crack development over the steel beams becomes essential to investigate the influence of the slab on the overall performance of the composite joint.

The main threads of this research include:

- By applying an appropriate model to represent the continuity of the slab, the *Vulcan* software will be enhanced by allowing the horizontal relative movement of the concrete floors around the edges due to through-depth

cracking to be included in the analysis. Hence, further studies can be done on the behaviour of composite floor systems with discrete cracking around their edges.

- Performing parametric studies, in order to increase the depth of understanding of the effect of integrity failure of floor slabs due to excessive discrete cracking in extreme loading cases such as fire. The main areas to be investigated initially are:
 - tracing the failure pattern of the slab;
 - the overall performance of the floor area in terms of vertical deformation;
 - most importantly, the influence of slab discontinuity on the performance of steel connections and its subsequent effects on the overall behaviour of the structure.

1.4 Thesis Outline

The thesis is organized into six main chapters. Each chapter begins with an introductory section giving a brief outline of the contents of the actual chapter. At the end of the chapter, a concluding section reiterates the key findings and the results which have been obtained.

- **Chapter 1:** presents a general introduction about the research background and the scope and the outline of the thesis.
- **Chapter 2:** Contains an extensive literature review that provides a general introduction to the properties of different materials at elevated temperature, and then focuses on the performance of different structural elements in fire. The main issues are the large vertical deformation and the appearance of cracks within the composite slab due to membrane action. A section gives a brief introduction to the application of numerical analysis and gives a general understanding of the software *Vulcan*. The chapter finishes with a section explains the importance of appropriate modelling of the discrete cracks over the hogging regions of composite slabs.

- **Chapter 3:** This chapter discusses the numerical approach to model discrete cracking in composite slab. The chapter is then continues with the detailed theoretical and numerical development of the new element (“Break Element”) implemented in the *Vulcan* software.
- **Chapter 4:** This chapter evaluates the new element against experimental data. The element has been used to model a series of experimental works on composite joints at both ambient and elevated temperature. A particular emphasis is put on the development and tracing the behaviour of the cracks in composite slabs in the hogging region on top of the connection zone.
- **Chapter 5:** Presents an investigation of the application of using the break element in composite structures at ambient and elevated temperature. Parametric studies on major steel connections and composite slab parameters are conducted using the finite element model. The influence of the new element on the local and global behaviour of the model is discussed in detail.
- **Chapter 6:** Gives a review of the work carried out in this thesis. In addition, a summary of the main conclusions from this research are stated, followed by recommendation for future related research work.
- **Appendix I:** Implemented code in *Vulcan* Software

Chapter 2

2. Literature Review

2.1 Material Properties at Elevated Temperature

2.1.1 Properties of Steel at Elevated Temperature

Steel has been widely used in building construction for decades due to its prime benefits of high strength, light weight and high ductility. The mechanical property of steel is normally expressed by the stress-strain relationship. Figure 2.1 shows the stress-strain relationship of steel material for a standard specimen in tension at ambient temperature, recommended by EC3 [23].

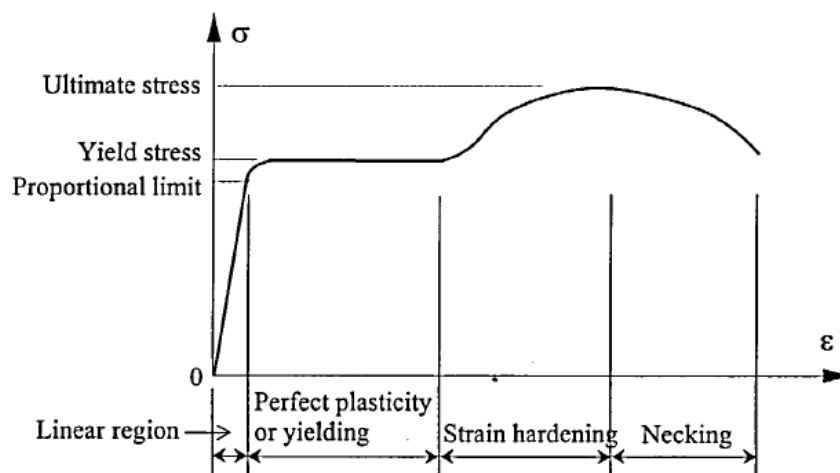


Figure 2.1: Stress-strain relationship for carbon steel – ambient temperature [23]

2.1.1.1 Degradation of structural steel

The mechanical properties of steel at elevated temperature are one of the most important aspects which influence their structural behaviour in fire. Extensive works have been done in the past to investigate the behaviour of structural steel at high temperature. Cooke [25] studied the mechanical properties of steel at elevated temperature in 1988. His work was further developed by Kirby and Preston [26] to investigate the mechanical properties of hot rolled structural steel at high

temperature. Badoo, 1999, also conducted a series of tests to study the behaviour of stainless steel in fire [24]. In contrast with its good performance at ambient temperature, the steel material is vulnerable if exposed to fire since its mechanical properties are temperature dependant. It goes through extensive loss of strength and stiffness at elevated temperature as a result of having very high thermal conductivity [27]. Therefore, excessive deformation in unprotected steel elements can lead to possible failure of the whole structure, depending on its circumstance such as: applied load, supporting condition and, of course, the fire severity. Two commonly used methods exist to determine the stress-strain characteristic for structural steel at elevated temperature; transient state test and steady state test. In the former method, the specimen is subjected to a constant load along with increasing temperature and the stress-strain curves are derived from a number of curves at different stresses. In the latter method, the specimen is heated up to a certain temperature and then tested in tension. The stress-strain curve for the tested specimen is derived through doing several tests at different temperatures.

Using both methods, extensive work has been done by Kirby and Peterson [26], to investigate the influence of increasing temperature on isolated steel members for typical grades of S275 and S355. The outcomes from their work revealed that the transient-state test generally indicates lower strength than the steady state test; however, their response provides a better representation of the actual behaviour. The test data from their work has been adopted in BS5950: part 8 and later in EC3: part 1.2. Figure 2.2 illustrates the stress-strain curves recommended by EC3 for a steel grade of S275.

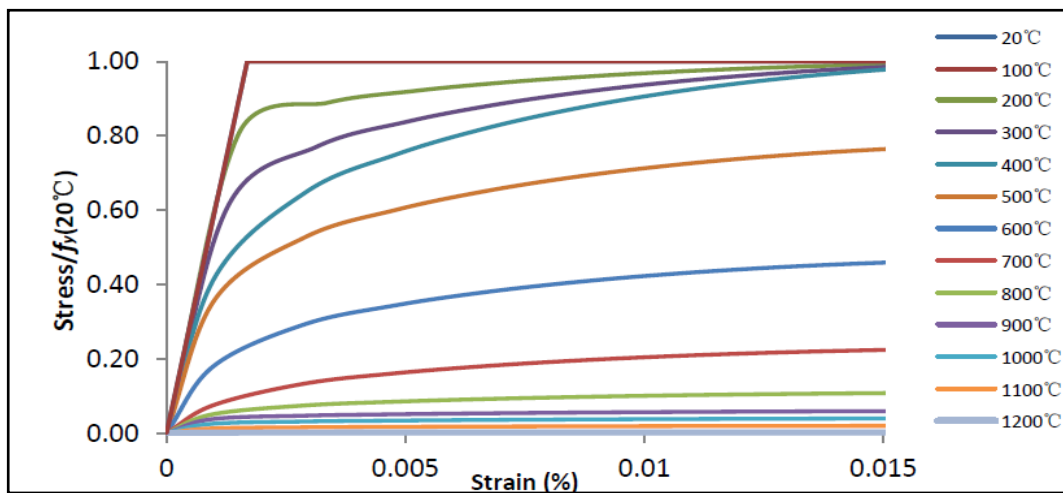


Figure 2.2: Stress-strain curve of steel material – elevated temperature [11]

2.1.1.2 Degradation of steel strength/stiffness

“Strength retention factor” is the term introduced by the design codes that basically refers to the changes in residual strength of steel at particular temperatures over its original yield strength at ambient temperature. The stress-strain characteristic of steel at ambient temperature is a bilinear behaviour with a clear yield plateau, however, as the temperature increases the bilinear behaviour is smoothed out, which makes it quite difficult to identify a yield point and elastic modulus. This problem has been overcome in design codes EC3 [10] and BS550 [11] by adopting a limiting strain for the steel material, therefore, the relationship between strength reduction factor and temperature is related to a specific strain (usually 0.5, 1 or 2%). Figure 2.3a and figure 2.3b represents the recommended retention factor from different design codes for degradation of strength and stiffness of steel respectively.

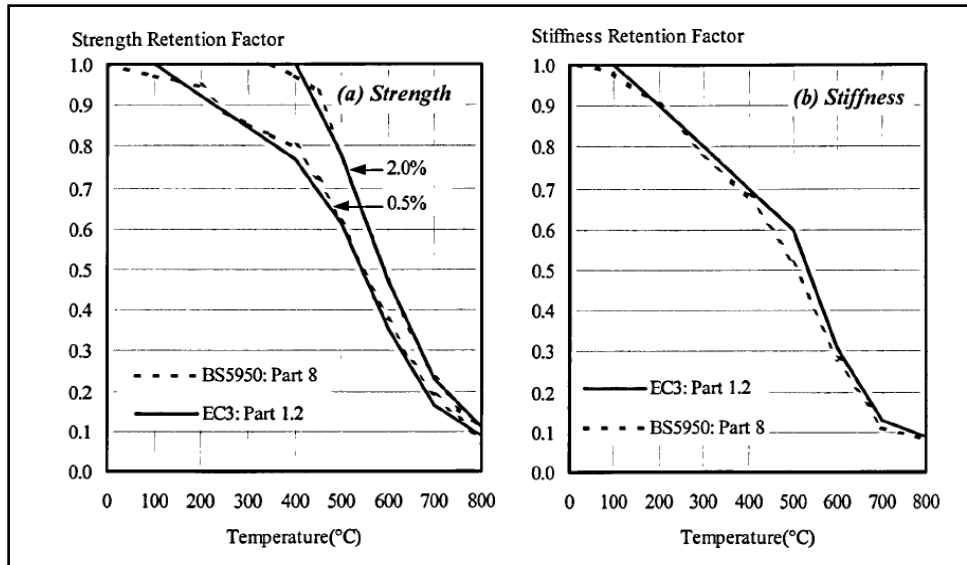


Figure 2.3: Degradation of strength and stiffness for steel at elevated temperature [11]

There is little change in the yield strength of steel at temperatures below 400°C. The rate of the reduction in the mechanical properties accelerates with almost constant rate when the temperature in steel is between 400°C and 800°C. Beyond this temperature, the strength's reduction continues at a more gradual rate, until the melting point is reached. Although the melting point of steel is about 1500°C, steel loses a considerable portion of its original strength when the surrounding temperature is between 600 °C and 900°C. Only 23% of the ambient temperature strength remains at 700°C, whereas, at 800°C strength this reduces to 11%, and at 900°C to just 6% [28]. Table 2.1 from [11] also provides the strength reduction rate of steel with temperature increments from ambient temperature of 20°C to an elevated temperature of 1200°C. It can be seen from the table below that the proportional limit and the Young's modulus (stiffness) of steel is assumed to decrease from 200°C, while the steel strength is reduced beyond 400°C, however, the rate of the strength reduction is faster than the other two parameters.

Steel Temperature θ_a	Reduction factors at temperature θ_a relative to the value of f_y or E_a at 20°C		
	Reduction factor (relative to f_y) for effective yield strength $k_{y,\theta} = f_{y,\theta}/f_y$	Reduction factor (relative to f_y) for proportional limit $k_{p,\theta} = f_{p,\theta}/f_y$	Reduction factor (relative to E_a) for the slope of the linear elastic range $k_{E,\theta} = E_{a,\theta}/E_a$
20°C	1,000	1,000	1,000
100°C	1,000	1,000	1,000
200°C	1,000	0,807	0,900
300°C	1,000	0,613	0,800
400°C	1,000	0,420	0,700
500°C	0,780	0,360	0,600
600°C	0,470	0,180	0,310
700°C	0,230	0,075	0,130
800°C	0,110	0,050	0,090
900°C	0,060	0,0375	0,0675
1000°C	0,040	0,0250	0,0450
1100°C	0,020	0,0125	0,0225
1200°C	0,000	0,0000	0,0000

NOTE: For intermediate values of the steel temperature, linear interpolation may be used.

Table 2.1: Reduction factors for stress-strain relationship of carbon steel – elevated temperatures [11]

Where,

$k_{y,\theta}$ is the reduction factor for effective yield strength of steel at relevant elevated temperature,

$k_{p,\theta}$ is the reduction factor for proportional limit,

$k_{E,\theta}$ is the reduction factor for the linear elastic range (Young's modulus).

2.1.2 Properties of Concrete at Elevated Temperature

Studying the behaviour of concrete at elevated temperature is complicated due to the variation in its constituent materials and changes in the properties of any of these will have a direct effect on the behaviour of concrete.

2.1.2.1 Degradation of concrete material

The elastic modulus of concrete reduces by 10-20% at temperatures above 100°C, when the free water inside of the concrete starts to evaporate. Concrete compressive strength is gradually decreased as the temperature reaches 500°C, beyond which, the rate of the reduction increases rapidly. By the time that the temperature of the concrete gets to 600°C, some types of aggregate (containing quartz) experience a crystalline transformation resulting in significant volume expansion, which in return causes cracking and spalling of the cement paste [29]. The compressive strength in concrete reduces to zero when the temperature reaches 1000°C. This is due to the decomposition of calcium carbonate and the loss of the free and absorbed water inside the concrete.

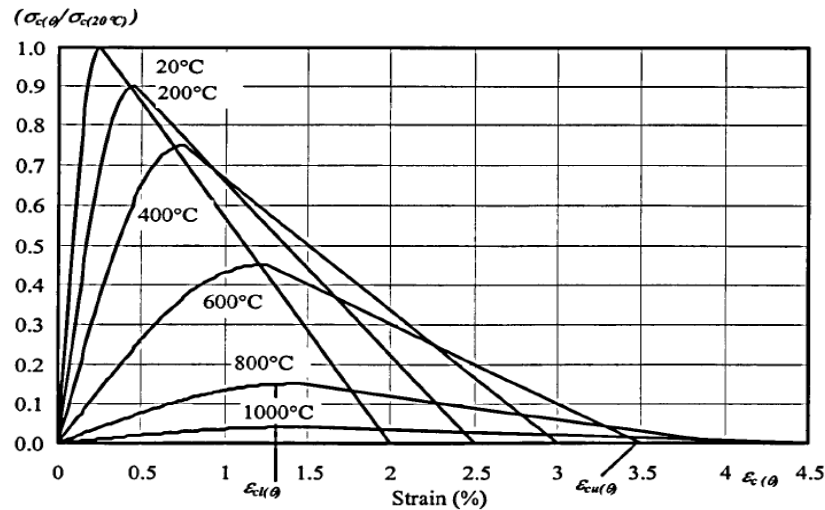


Figure 2.4: Stress-strain curves for concrete at elevated temperature [5]

The stress-strain characteristics of concrete at rising temperature have been developed based on the experimental data from the series of concrete compressive tests at elevated temperature. Figure 2.4 illustrates the stress-strain characteristics of concrete in fire recommended by EC4: part 1.2 [5]. The graphs show a gradual increase in the strain level as the compressive strength of concrete reaches its maximum value, beyond which it starts to decrease along with increase in the strain level. The concrete experiences a reduction in the load capacity for strain levels beyond 2% at room temperature. As can be seen from the graphs in figure 2.4, the strength level in concrete has dropped by more than 50% at approximately 600°C. The strength gets to zero as the temperature in the concrete reaches 1200°C. It

should be noted that unlike steel, the loss of strength in concrete as a result of rising temperature is permanent and there is no strength recovery of concrete in the cooling stage [30], [31].

2.1.2.2 Degradation of concrete strength/stiffness

Figure 2.5 represents the strength retention factor of concrete recommended by [5] for both normal-weight and light-weight concrete. Degradation of concrete strength is greatly influenced by the aggregate type used [30]. Therefore, the recommended degradation rate in EC4 is based on siliceous aggregate concrete, which represents the lower range of strength values for concrete. However, this assumption results in conservative strength retention factor for other types of concrete such as calcareous aggregate concrete.

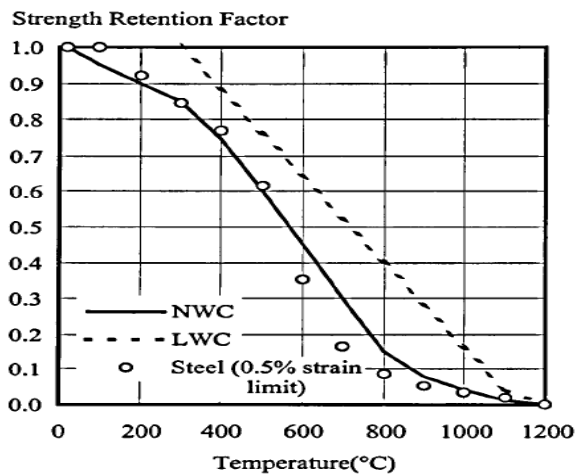


Figure 2.5: Degradation of concrete strength at elevated temperature [5]

Concrete is well known as a material of great compressive strength and its tensile capacity is normally ignored for the design purposes. Design codes such as Eurocode 2 [5] and Eurocode 4 [32] often suggest that the tensile strength of concrete should be ignored as a part of conservative design. However, if the tensile capacity needs to be considered, EC2 suggests a simplified reduction factor for particular temperature. The reduced tensile strength of concrete at different temperature can be obtained using equation 2.1.

$$f_{ck,t}(\theta) = k_{c,t}(\theta) \cdot f_{ck,t} \quad (2.1)$$

The reduction factor $k_{c,t}(\theta)$ can be calculated as:

For $20^{\circ}\text{C} \leq \theta_c \leq 100^{\circ}\text{C}$

$$k_{c,t}(\theta) = 1.0 \quad (2.2a)$$

For $100^{\circ}\text{C} < \theta_c \leq 600^{\circ}\text{C}$

$$k_{c,t}(\theta) = 1.0 - 1.0(\theta - 100)/500 \quad (2.2b)$$

2.1.3 Properties of Shear Studs at Elevated Temperature

The role of shear connection in composite structures is to ensure the proper contact between the steel beam and the composite slab. Studs are normally welded to the upper flange of steel beams through the steel decking and embedded in the concrete slab. Shear connectors provide composite action between the beam and slab by resisting the longitudinal shear and the tensile force perpendicular to the interface. The mechanical characteristics of the studs are not dramatically influenced at elevated temperature as they are generally protected by the surrounding concrete on top of the steel beam. Therefore, their behaviour at high temperature has not received much study; however, a series of tests has been conducted by Twilt and Kruppa [33], [34] to investigate the reduction rate in stud capacity at elevated temperature. According to their work the strength and stiffness retention factors for shear studs can be derived using the following equations:

For Strength Retention Factor

$$20^{\circ}\text{C} < t_{ss} \leq 200^{\circ}\text{C} \rightarrow SFR = 1.0 \quad (2.3a)$$

$$200^{\circ}\text{C} < t_{ss} \leq 400^{\circ}\text{C} \rightarrow SFR = 1.15 - 0.00075 t_{ss} \quad (2.3b)$$

$$400^{\circ}\text{C} < t_{ss} \leq 800^{\circ}\text{C} \rightarrow SFR = 1.717 - 0.002167 t_{ss} \quad (2.3c)$$

For Stiffness Retention Factor

$$20^{\circ}\text{C} < t_{ss} \leq 100^{\circ}\text{C} \rightarrow SFR = 1.0 \quad (2.4a)$$

$$100^{\circ}\text{C} < t_{ss} \leq 800^{\circ}\text{C} \rightarrow SFR = 1.44 \times 10^{-(0.0016t_{ss})} \quad (2.4b)$$

Where, t_{ss} = temperature of shear stud

The strength of the shear stud gradually reduces as the temperature at the stud's level increases beyond 200°C before a rapid reduction occurs at around 400°C [33], [34].

2.1.4 Thermal Expansion

2.1.4.1 Steel

Most materials experience some level of elongation when they are subjected to rising temperature, however, the rate of expansion depends on the material type and the chemical composition. The rate at which the material expands as a function of temperature is known as the coefficient of thermal expansion (α_s). Large internal forces can be produced as a result of thermal expansion in a restrained steel component. These forces can occur in buildings where there are complex structural interactions between elements which are not free to expand. BS5950: part 8 recommends the value of thermal expansion coefficient of $12 \times 10^{-6}/^\circ\text{C}$ and $14 \times 10^{-6}/^\circ\text{C}$ for ambient temperature and elevated temperature (200 to 600°C.) respectively. Significant changes in the expansion properties of steel occur at temperatures around 730°C due to a change in the phase diagram of the material (steel develops a denser internal structure). Equation 1.6 expresses a tri-linear thermal behaviour to determine the total expansion of steel (δ_s) recommended by EC3: part 1.2 [11]. The behaviour, including the temperature beyond the point of phase change is described by:

$$20^\circ\text{C} \leq t_s < 750^\circ\text{C}$$

$$\delta_s = (0.4 \times 10^{-8} t_s^2 + 1.2 \times 10^{-5} t_s - 2.416 \times 10^{-4}) l \quad (2.5a)$$

$$750^\circ\text{C} \leq t_s \leq 860^\circ\text{C}$$

$$\delta_s = (1.1 \times 10^{-2}) l \quad (2.5b)$$

$$860^\circ\text{C} < t_s \leq 1200^\circ\text{C}$$

$$\delta_s = (2.0 \times 10^{-5} t_s - 6.2 \times 10^{-3}) l \quad (2.5c)$$

2.1.4.2 Concrete

Concrete is a composite material containing different types of aggregate. Therefore its thermal expansion is a function of thermal properties of mineral compositions and structure of individual aggregates within the mortar mix of any particular concrete. Figure 2.6 illustrates the thermal expansion of steel and calcareous concrete at elevated temperature recommended by Eurocode 4: part 1.2 [5]. The graphs show a slightly higher strain level of steel at rising temperature between 20°C to 450°C. However, the concrete starts to expand with a faster rate compared to steel at temperatures beyond 450°C. Concrete elongation eventually stops at about 700°C as a result of irreversible chemical breakdown within the mortar mix, this has been shown in the following figure using flat line. This is also partly in parallel with the break down in the steel expansion due to the phase change of the material to a more compact crystal structure. Once the phase change completes, the steel resumes its expansion and continues to do so till it passes the maximum concrete expansion.

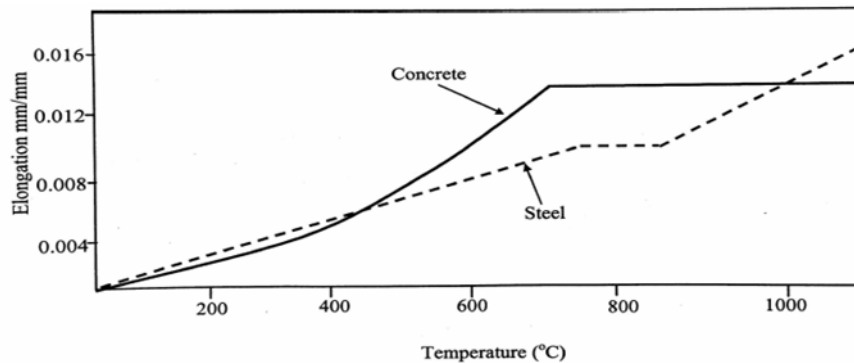


Figure 2.6: Comparison of thermal expansion of steel and concrete at elevated temperature

2.2 Connections in Steel Frames

Steel connections are a key component of any structure as they contribute to the overall stability of the building through linking other primary structural components. Predicting the behaviour of a structure in the connection zone is complex since there are a wide range of parameters involved in order to establish the behaviour of a connection. Therefore, extensive research has been conducted during the past

decades to provide a better understanding of steel connection behaviour and improvement of the design methods. Beam to column connections were traditionally assumed to be either rigid (full moment resistance) or pinned (no moment resistance). However, further investigations have shown that the actual connections in reality perform over a wide range between these two limits. In other words, it was found that the traditionally assumed pinned connections exhibit some rotational stiffness whereas the rigid connections show some level of flexibility. Therefore, it appears to be more reasonable to classify a wide range of connections as “semi-rigid” with pinned and rigid considered as lower and upper stiffness limits respectively.

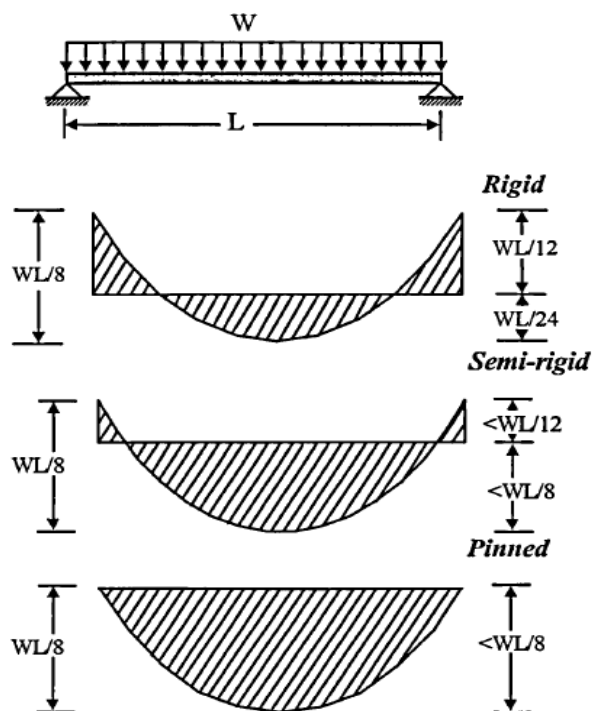


Figure 2.7: Effects of connections characteristics on beam behaviour [35]

Semi-rigid connections can be used to optimize the structural design of buildings through transferring some level of moments from adjacent beams to the supporting columns, which in turn results in lighter beam sections. Figure 2.7 illustrates the influence of connection flexibility on the beam response.

Connections are the key component responsible for transferring various types of forces (shear force, axial force) and moment (bending moment) between the adjacent structural members. The overall response of a structure can be greatly influenced by

the rotational behaviour of the beam-to-column connections [19]. Other joint's characteristics such as: shear and axial resistance are assumed to have less significant effect on the overall performance of structure compared to the rotational deformation of the joint at ambient temperature. Therefore, connections are generally required to safely transfer forces between structural elements and to prevent excessive deformation/slip in structure (as a result of the applied load/moment) by retaining adequate axial and rotational stiffness. The rotational characteristics of the joint can be accurately determined using experimental testing for different types of joint [36]. Moment-rotation relationships can be used to represent the rotational behaviour of any particular joint. Figure 2.8 illustrates the generated moment in the connection (as a result of the applied load) and the causing rotational displacement (ϕ), which is the relative angle between the beam's bottom flange and the adjacent column face.

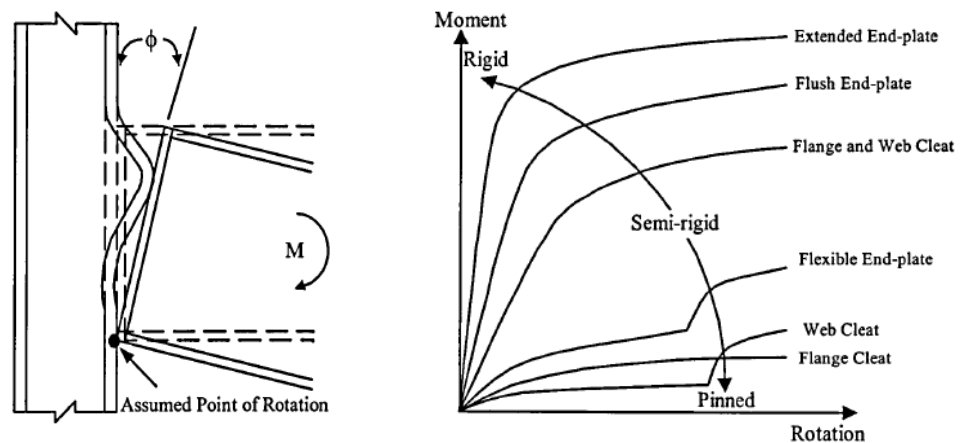


Figure 2.8: a) Rotational deformation of beam-to-column connection, b) Connection types – Rotational characteristics [36]

Several types of steel connections (web cleat, flange cleat, flexible end plate, flush end plate ...), are currently used in the construction industry. Figure 2.8b, illustrates the moment-rotation characteristics of different types of connections between the two extreme stiffness categories.

2.3 Behaviour of Different Structural Elements in Fire

2.3.1 Steel beam behaviour at elevated temperature

2.3.1.1 Simply supported beam

The performance of a steel beam in fire is generally assumed to be ruled by pure bending and the total vertical displacement of the beam at elevated temperature can be obtained by super positioning its mechanical deflection, which increases with rising temperature as a result of reduced bending stiffness, and the thermal bowing deflection, which is a function of temperature gradient within the beam cross-section. The latter has been found by Wainman and Kirby [37] to have little effect on the overall behaviour of the beam at the later stage of heating. The magnitude of the thermal bowing can be obtained using equation 2.6 suggested by [37].

$$\delta_{th} = \frac{\alpha \times \Delta T \times L^2}{8d} \quad (2.6)$$

Where, α is the coefficient of thermal expansion of steel, ΔT the temperature difference in °C between the lower and upper flanges, L the beam span and d is the depth between the centroids of the upper and lower flanges. Figure 2.9 is the schematic of simply supported beam showing its vertical deflection due to thermal bowing at elevated temperature.

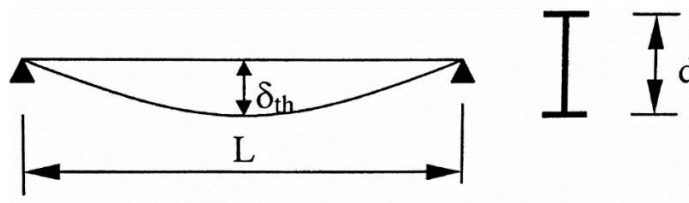


Figure 2.9: Thermal bowing in a simply supported beam [37]

The failure criteria of the steel beam is normally characterised using a deflection limit for its vertical displacement (typically span/20). Therefore, the ultimate fire resistance of the statically determinant beam can be calculated using the plastic bending moment capacity of the steel beam cross-section [20].

2.3.1.2 *Longitudinally and rotationally restrained beam*

Understanding the behaviour of a restrained beam at elevated temperature is complex as the beam is subjected to a set of complex non-linear geometrical, material and temperature interactions from the adjacent structure. When the steel beam forms part of a complete structure, its interaction with the surrounding structural elements provides longitudinal and rotational restraints to the beam. Therefore, the performance of such a beam at elevated temperature is considerably different from that of an isolated beam with no assumed restraints. Extensive works have been done in the past to investigate the behaviour of restrained beams in fire. The influence of thermal effects on structural performance at high temperature was studied by Usmani and Sanad [39], who have further developed their research by investigating the structural behaviour of restraint members in fire compartment subjected to different heating regimes [40]. Elghazouli and Izzudin [38] also investigated the numerical modelling of steel and composite structures in the past. Wang [20] summarised the general behaviour of a restrained beam during fire. Figure 2.10 is an illustrative stage by stage behaviour of an axially and rotationally restrained beam with rising temperature. Looking at the figure, it can be seen that the behaviour of the restrained beam during the fire has been divided into three different stages. During the first stage, part of the thermal curvature of the beam (as a result of rising temperature) is restrained by the boundary condition at the end of the beam in the form of hogging bending moments (M_h) along with the increase in vertical deflection (δ_v) due to the effect of thermal curvature over the unrestrained part of the beam. In parallel to the thermal curvature, the thermal expansion of the beam is also partly restrained by the presence of the adjacent structural elements at both beam ends causing compressive force in the beam (P). The unrestrained part of the beam also experiences some change in the length (δ_l) as a result of the beam's thermal expansion. Local buckling occurs at the ends of the beam as a result of sufficiently high compressive force. Once the local buckling takes place, the lateral displacement of the beam starts to gradually increase along with the reduction in the beam's length as a result of relieving the compressive force in the beam (stage 2).

The third stage is when the vertical deflection of the beam becomes sufficiently large, so the tensile force in the beam starts to develop and therefore, the beam will be under catenary action. Beyond this state, the bending moment capacities (M_h , M_s) of the beam are relatively small, which can be neglected but the applied force can still be resisted by the steel beam with no sign of “run-away” deflection as in simply supported beam [20].

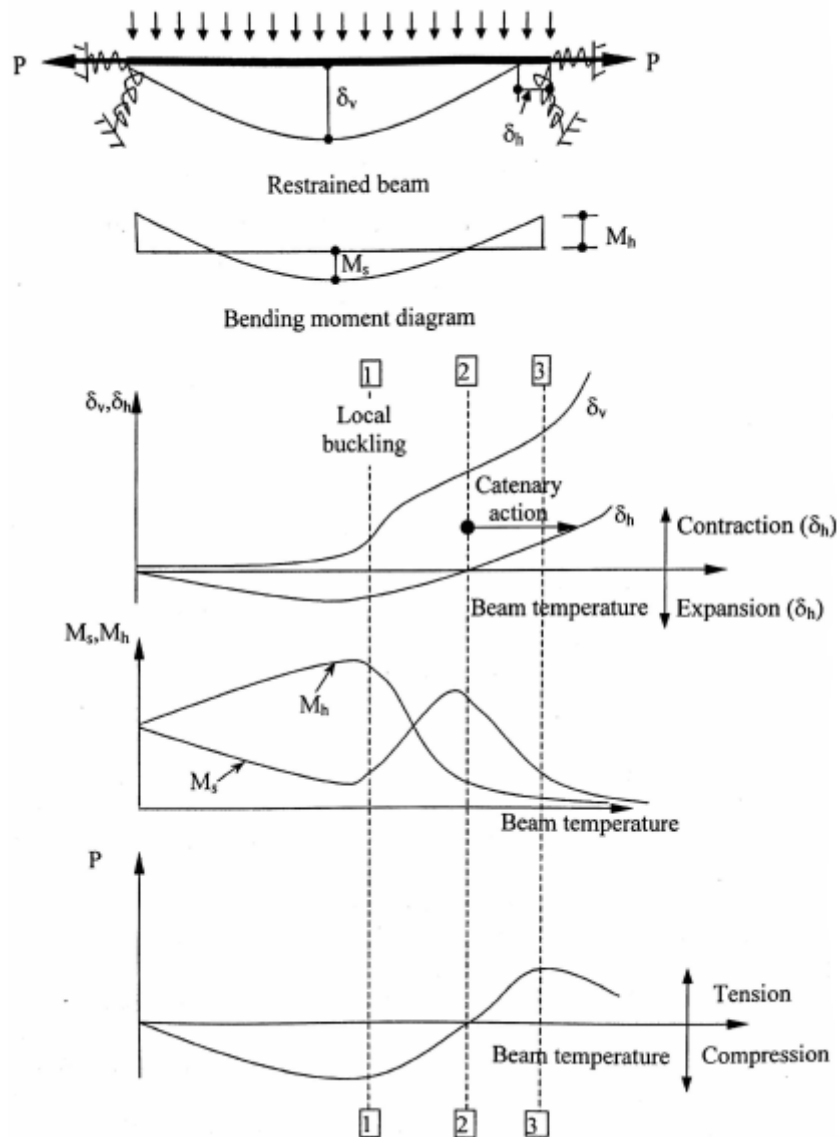


Figure 2.10: Illustrative behaviour of axially/rotationally restrained beam in fire [20]

Sufficient rotational capacity should be provided by the connections (adjacent structures) to resist the additional moment generated by the large mid-span deflection, which consequently results in reduced mid-span moment of the beam. Therefore, it is reasonable to state that the catenary action results in longer survival time of steel beams in fire, however, it requires sufficient connection resistance, since the behaviour of the beam is affected by the connection's ductility and stiffness [41].

2.3.2 Concrete Slab behaviour at elevated temperature

Yield line theory can be used to determine the ultimate load capacity of the slab at room temperature. The method is also applicable at elevated temperature by considering the effect of strength reduction of the reinforcing steel due to temperature. However, the method ignores the effect of membrane forces in the slab, which has been experimentally proved to significantly enhance the load capacity of the slab in fire.

2.3.2.1 Yield line theory

Yield line theory is a method for limit analysis, which can be used to establish the ultimate load capacity of a reinforced concrete (RC) slab at ambient temperatures. The method was initially developed by Johansen in the early 1960s, assuming that the slab's edges are simply supported allowing it to rotate [20]. Prager describes the theory as a simple and quick method to obtain the upper bound of the small deflection plastic failure loads of slabs. The yield line theory assumes the moments of resistance of the RC sections to be equal to the moments across the plastic hinges lines. Therefore, the load capacity of the slab can be determined by applying energy balance principle, i.e. equating the work done by external loads to the work dissipated across the yield lines. The yield line analysis considers the lowest resistance value for the collapse mechanism to occur. It adopts an upper bound solution on the basis that the applied load is always greater than or equal to the actual collapse load of the structure. Being an upper bound approach, the yield line method provides ultimate loads which are either correct or too high. Yield line theory offers a quick and simple way to design and check the performance of the concrete section.

However, despite of being useful in compiling floor loading design guides, the method does not include the enhancement due to the effect of membrane action.

2.3.2.2 *Compressive membrane action*

Compressive membrane action occurs immediately after yielding when the deflection of the slab is small. Vertical compressive forces are induced within the simply supported slab, acting from the bottom corners, to resist the downward applied load. With in-plane restraint of the slab present along its edges, and the vertical displacement not greater than the slab's depth, compressive membrane action will develop, as shown in figure 2.11. Once the vertical displacement exceeds this depth, the slab will lose its stability. As a result this phenomenon has a very limited range of permissible deflection.

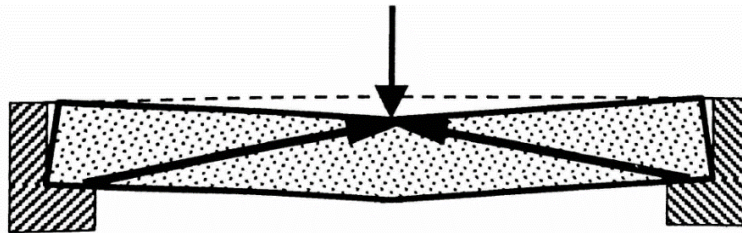


Figure 2.11: Compressive membrane action in fire [20]

The normal practice is to design slabs to withstand a maximum allowable deflection of half the slab depth. This means that for compressive membrane action to effectively carry the load, the slab needs to have adequate thickness. In reality, steel framed structures are usually designed with thin composite floor slabs, which in the case of fire will cause the deflection to go far beyond the slab's thickness [20]. Therefore, compressive membrane action exists only shortly before tensile membrane action takes its place.

2.3.2.3 *Tensile membrane action*

Extensive experimental and theoretical studies have been done in the past to investigate the behaviour of RC slabs at large vertical displacements. Wood, 1961 was the first to study the elastic and plastic properties of the slab for the design

purposes [44]. His work became the basis of the further studies on the development of membrane forces within the slab section area. Kemp, 1967 investigated the development of membrane forces beyond the yield of the square reinforced concrete slab [43]. Hayes, 1968 also studied the occurrence of membrane forces in post elastic phase of rectangular reinforced concrete slabs [42]. Wang, 2002, summarised the previous works on membrane forces in his book [20]. The results show that the ultimate load capacity of slabs at large deflection is considerably greater than those determined using the traditional yield-line theory (small deflection). This is mainly due the occurrence of tensile membrane action within the slab area, regardless of probable presence of horizontal restraint at the edge of the slab. At large deflection, the applied vertical load in the slab is resisted by the reinforcement net in tension. The magnitude of tension force in the reinforcement depends on the in-plane restraint at the edge of the slab. If sufficient horizontal restraint is available then tensile membrane forces will be resisted by the edge supports. Cameron and Usmani [45] assumed that the development of tensile membrane forces in slabs effectively depends on the provision of anchorage along the slab edges since most of the slab's bending capacity is lost at high temperature. Otherwise, if the in-plane restraint is neglected, the slab will resist the tensile forces in the reinforcement by forming a compressive ring beam around its edge. However, sufficient vertical support (small deflection) at slab perimeters should be retained in order to allow the compressive ring to be created [12]. This requirement has been justified by Bailey [46]. The absence of appropriate vertical support at slab perimeters (perimeter beams forming central plastic hinges by going through large deflection) leads to a single yield line collapse mechanism causing the floor slab to effectively fold along its yield line. Therefore, the membrane action cannot develop due to run-away deflection in the slab. Figure 2.12 shows the distribution of tensile membrane forces within the concrete slab subjected to different boundary condition

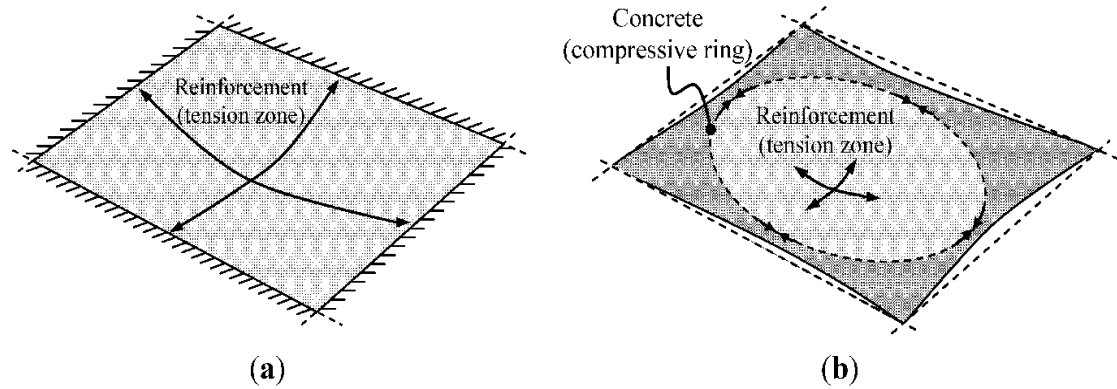


Figure 2.12: Different mechanism of tensile membrane action in slab [46]

Furthermore, it has been found by Bailey [46] that the horizontally restrained slab generally leads to a greater load-carrying capacity compared to the equivalent in-plane unrestrained floor slab. Figure 2.13 illustrates the load carrying mechanism for different restraint condition.

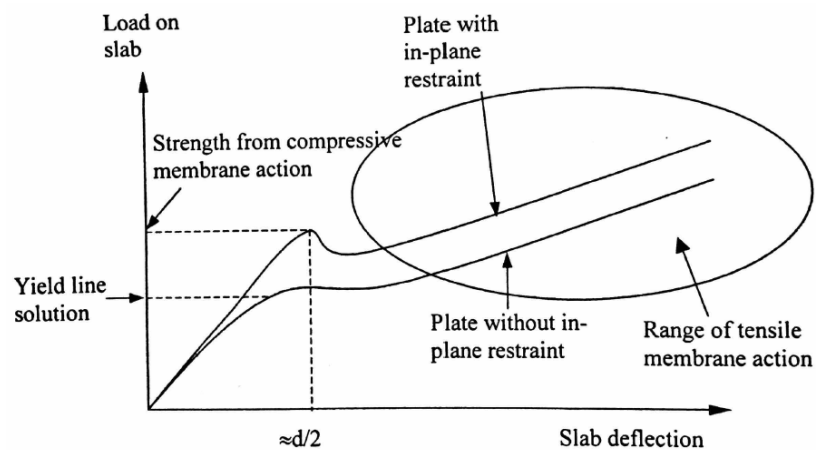


Figure 2.13: Load deflection of a slab [20]

2.3.2.4 Development of Bailey-BRE method

The Cardington fire tests on composite floor slab revealed that the increase in load carrying capacity of the slab is the direct result of the tensile membrane action being developed in the central area of the slab, assuming sufficient vertical supports are provided. The observation from these tests complies with the earlier studies on tensile membrane action at ambient temperature as discussed in section 2.3.2.3. A

new design method to establish the behaviour of slab at elevated temperature was developed by Bailey and Moore [47] based on the early work done by Hayes [42]. The Bailey-BRE method initially assumes two possible modes of failure of the slab at elevated temperature. The first mode considers a single full depth tension crack at the slab centre and parallel to the direction of the shorter span. The second mode considers the failure of the slab by incorporating two tension cracks from the intersections of the yield lines. The method was reviewed by Bailey in 2007 to include the compressive crushing of the concrete slab at its corners at ambient temperature (as a result of higher reinforcement ratio) [48]. However, according to Bailey's work no sign of compressive failure has been observed at elevated temperature. Figure 2.14 shows the possible failure mode recommended by Bailey [48]. Similar mode of failures was also suggested by Simms and Zhao [49].

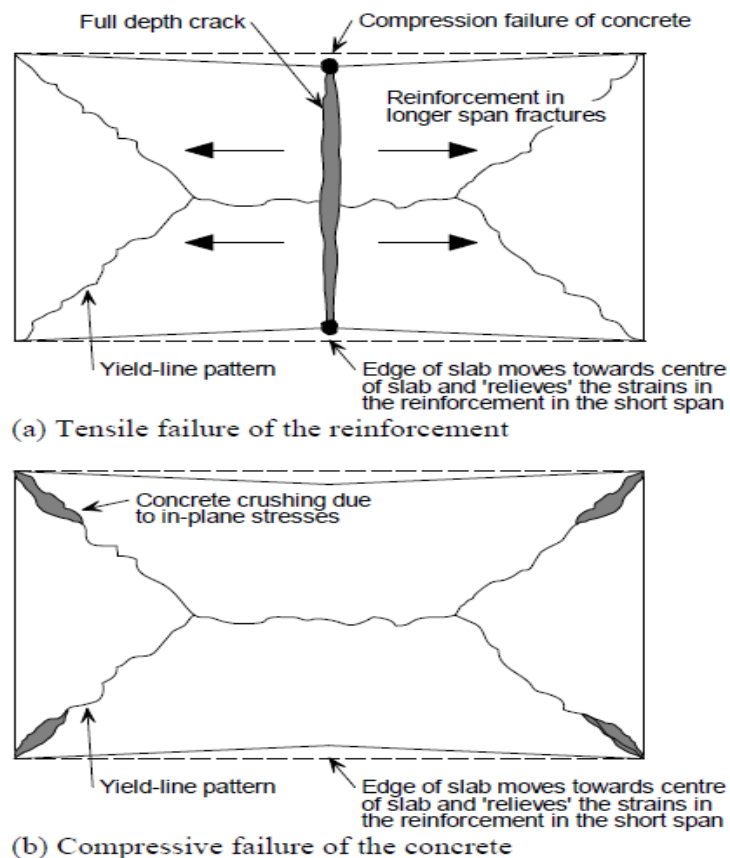


Figure 2.14: Failure mechanism of slab [48]

Figure 2.15 also illustrates the basic assumption of using the Bailey-BRE method, where, the floor area is divided into a series of square or rectangular composite slab

panels, with an assumption of unprotected secondary beams within the slab panel area and sufficient, stiff supporting beams at the perimeter.

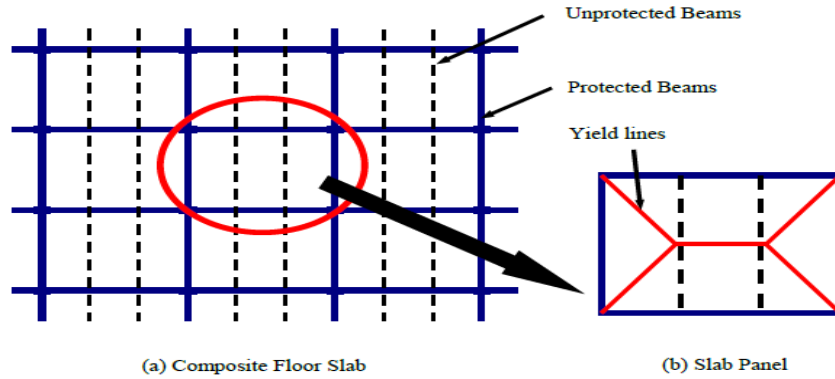


Figure 2.15: Schematic of floor division, Baily-BRE method [50]

Similar to the method recommend by Hayes [42], Bailey’s method is also based on the traditional yield line theory (rigid-perfectly plastic yield line theory), however this design method has been enhanced by considering the effect of tensile membrane action on increasing the load carrying capacity of the slab beyond the small deflection load capacity obtained from the traditional yield line theory. The overall load carrying capacity of a composite slab at rising temperature can be obtained using equation 2.6.

$$w_{p\theta} = e \left(\frac{\text{Internal work done by the composite slab in bending}}{\text{External work done by the floor per unit load}} \right) + \left(\frac{\text{Internal work done by the beams in bending}}{\text{External work done by the floor per unit load}} \right) \quad (2.6)$$

Where, $w_{p\theta}$ is the load carrying capacity of slab, and e is the slab enhancement factor which can be calculated by referring to Bailey’s work on different scale concrete structures at both ambient and elevated temperatures [48], [68]. Furthermore, the maximum allowable vertical displacement in fire (i.e. maximum deflection before fracture of reinforcement) can be calculated by combining the vertical deflection in the slab as result of thermal bowing and the deflection as result of the mechanical strain of the slab reinforcement. Simms and Zhao [49] suggests the maximum allowable vertical displacement of ‘shorter span/30’ for the deflection due

to mechanical strain limit of reinforcement. Equation 2.7 expresses the calculation of total vertical displacement of the slab at elevated temperature recommended by Bailey in his work [46], [48] on development of tensile membrane action.

$$\Delta_{\theta} = \frac{\alpha(T_2 - T_1)l^2}{19.2h} + \sqrt{\frac{0.5f_{sy}}{E_s} \times \frac{3L^2}{8}} \quad (2.7)$$

In which,

α is the coefficient of thermal expansion of concrete slab,

h is the effective thickness of slab,

f_{ys} and E_s are the reinforcement and Young's modulus,

L and l are longer and shorter span of the slab respectively,

T_2 and T_1 are the bottom and top reinforcement of the slab.

2.3.3 Connection behaviour at elevated temperature

Beam-to-column connections in structural steel or composite frames play a key role in the overall stability of the structure by transferring the induced load in horizontal elements (floor slab area, steel beams) to the supporting vertical elements (steel columns) and linking the principal structural members. The type and the magnitude of the transmitted forces from the connections to the supporting columns are governed by the type of the connection and its neighbouring condition. Therefore, depending on the type of the connection, different forces such as axial and shear forces or bending and torsional moment can be transmitted to the adjacent supporting member. For instance, torsional moment on individual members can be assumed to be negligible in composite structures as a result of the lateral restraint provided by the above concrete slab through the composite action. In the case of the moment resistance of connections, the transferred bending moments are the predominant factor influencing the joint performance compared to the transmitted axial and shear forces. In pin frames, using shear connections, in the design the generated shear force is the dominant factor influencing the joint performance.

It should be remembered that the behaviour of connections at ambient temperature can be significantly different under unusual circumstances such as rising temperature

as a result of severe fire. Observations from large scale experimental test frames have demonstrated the importance of joints and their great influence in improving the structural survival time. Steel beams experience large vertical deformation at high temperature but may still retain sufficient load carrying capacity. The load carrying performance of the heated beams can be enhanced if the adjacent connections are sufficiently capable of transferring the generated forces from the beams to the neighbouring cold structure. Figure 2.16 is schematic of a heated steel beam that goes through a significant deformation with a connection subsequently subjected to set of axial and rotational forces.

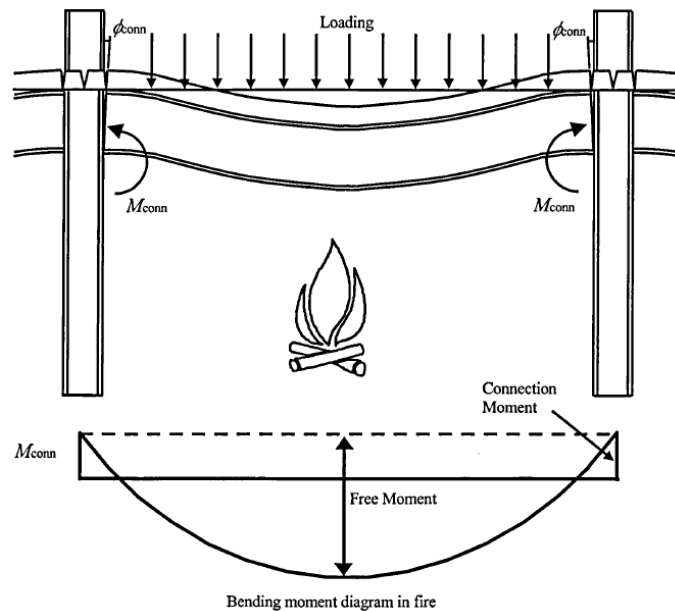


Figure 2.16: Behaviour of steel beam in fire condition [35]

In fire, structural elements will be subjected to a set of complex load combinations, in which axial force would most likely be of main concern (as a result of initial compression force from the beam thermal expansion followed by the induced tension force due to the beam catenary action). As illustrated in figure 2.16 above, the steel beam undergoes large deformation in fire, which consequently requires end connection to provide reaction against the resulting catenary action and induced end rotation. The hogging moment resistance of the nominally simply supported connections will reduce the mid-span moment in the deflected beam and therefore increase its load carrying capacity in fire. Observations from full-scale fire tests and

from damaged structures shows that the temperature in connection elements within the structural frame generally increases at a slower rate than other structural member, which can be reasoned by the shielded location of the connection (i.e. connections are normally located at the top of the protected steel column and beneath the composite floor). The composite slab in fire acts as insulation to the top part of the joint, shear studs and reinforcing mesh, which causes a reduction in their temperature and thus enhancing the characteristic fire resistance of the joint. This allows for the development of higher moments within the connection which in turn results in the reduction of the effective load ratio and hence the amount of fire protection required [35]. BS5950: Part 1 [10] assumes connections at elevated temperature perform similarly to how they behave at ambient temperature and gives no guidance on the design of beam-to-column connections under fire conditions. However, EC3: Part1.2 [11], suggests temperatures at joints of between 62% and 88% of that in the beam lower flange temperature at mid-span. Therefore, the performance of different structural elements under rising temperature is significantly influenced by ductility and strength of the connection elements since connections are the primary elements that make the whole assembly of structural members interact and work with each other. In other words, the connections in steel frames are required to be ductile enough to allow a reliable deformation of the floor's beams prior to its failure under fire conditions.

2.4 Numerical modelling

The basic and most reliable tool available to determine the moment-rotation curve of a composite connection is direct experimental measurement. Extensive experimental works were done on composite connection at both ambient and elevated temperature. Xiao and Nethercot [51], [52] conducted wide range of experiments on variety of different steel beam-to-column connections including composite joint at to assess the performance of the connections in terms of their moment and rotational capacity. Al-Jabri [35] and Lam [53] also did series of experimental tests to assess the performance of composite connection at ambient and elevated temperature. However, conducting experimental tests is an expensive task to do, particularly if a

series of variables needs to be considered. Thus modelling is a more reasonable approach to follow in order to investigate the behaviour of a structural joint. Component-based models divide a joint into different zones representing fundamental behaviour (such as compression, tension and shear) where the effect of each component within a specific zone is represented by springs based on a component's mechanical properties which are then assembled to generate the moment-rotation behaviour. The general behaviour of a joint modelled using the component-based technique is thus attained by assembling the individual stiffness of each component

2.4.1 Component-based method

Many numerical techniques are available to model the behaviour of individual structural members under different loading conditions. The component-based method considers the connection as an assemblage of series of individual non-linear springs, each representing the mechanical behaviour of a specific part of the connection in terms of force-displacement characteristic. Within this method, the stiffness and the corresponding maximum force for each component is combined together in order to represent the overall behaviour of the whole connection. Tschemmernegg [54], was the first to develop the component-based model for ambient temperature condition. The model was later adopted in Eurocode 3: part 1.8 [55] and since then, it has been successfully used by many researchers to model the overall behaviour of the connection, either as an isolated member or as a part of a structure which has been axially restrained. Leston-Jones [58] studied the influence of semi-rigid connection on the performance of steel structures at ambient and elevated temperature. The developed model for steel connection was in a good agreement with the experimental data at ambient temperature. Da Silva [59] investigated the behaviour of a steel joint in fire through a simple modelling of steel connection using component based method. Spyrou [56], [57] conducted series of experimental work to investigate the behaviour of steel connection at tension and compression zones. The experimental data was then used to investigate the behaviour of the tension and compression zones of the connection component model at rising temperature. Al-Jabri [60] has further developed the Spyrou's work to predict the degradation of connection characteristics

for both steel and composite joint at elevated temperature. Block [61] has also developed a component based connection element for endplate connections in fire based on the previous developments by Spyrou and Al-Jabri. Figure 2.17 illustrates a typical flush end-plate connection modelled using the component-based method, where the overall behaviour of the connection has been modelled through the assemblage of series of spring components representing different part of the connection [61].

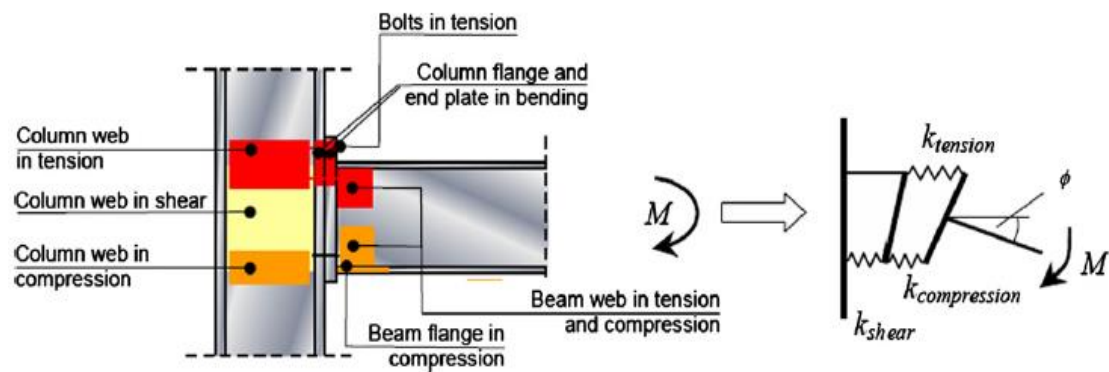


Figure 2.17: Typical beam-to-column joint – component model [61]

As mentioned, different component of a connection can be characterised using as spring element with specific force-displacement behaviour. The behaviour of these springs can be defined using elasto-plastic, bi-linear, multi-linear or non-linear response. Eurocode 3: Part 1.8 [55] assumes elastic- perfectly plastic behaviour to link the initial stiffness K with the design resistance force F_{Rd} . Therefore, the resulting moment-rotation relationship of the whole joint can be obtained by assembling the response of the individual components. Equation 2.8 expresses the moment resistance $M_{j,Rd}$ of a joint recommended by EC3: part 1.8 [55].

$$M_{j,Rd} = \sum_{i=1}^n F_{ti,Rd} z_i \quad (2.8)$$

Where, $F_{ti,Rd}$ represents the design resistance of individual bolt row in tension zone and z_i is the distance between the i^{th} bolt row and centre of the compression zone. For the bolt rows within the connection, the resistance is determined by the weakest component in that row or by considering the performance of either the compression

component or the shear panel [63]. Once the spring model of the connection is completed, the rotational stiffness of the joint can be simplified using an equivalent spring to represent the stiffness of each bolt row.

$$k_{et,i} = \frac{1}{\frac{1}{k_{cwt,i}} + \frac{1}{k_{cfb,i}} + \frac{1}{k_{bt,i}} + \frac{1}{k_{cep,b,i}} + \frac{1}{k_{bwt,i}}} \quad (2.9)$$

The overall moment-rotation response of the joint can be presented using bi-linear or curvilinear characteristic, which are recommended in EC3: part 1.8 [55]. Furthermore, in order to avoid complexity arising from complete non-linear modelling, a tri-linear force-displacement response is recommended by Al-Jabri in his work [63] for the ease of calculation. This is presented in the figure 2.18 to model a semi-rigid joint at elevated temperature.

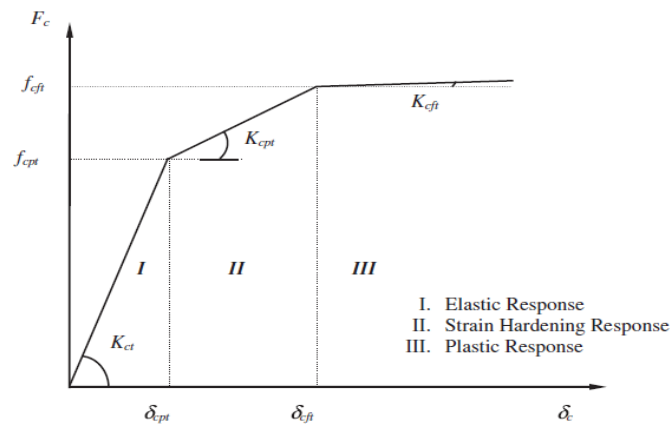


Figure 2.18: Tri-linear force-displacement representations of joint component [63]

Component method is generally capable of modelling the joint behaviour at ambient and elevated temperature with a reasonable level of accuracy, therefore it is widely used to study the behaviour of the steel and composite connections at rising temperature, either in isolation or as a part of a complex structure.

2.4.2 VULCAN program

Vulcan is a highly specialised three-dimensional non-linear finite element analysis software developed at the University of Sheffield over the last two decades. The capability of the software to perform non-linear analysis of different types of

structure under fire conditions has been extensively validated over the years using experimental data from a series of full-scale fire tests. Huang and Burgess [64] modelled a series of full scale fire tests using *Vulcan* and the results has successfully been validated against the experimental data. Development of membrane action of concrete slabs in composite buildings in fire was also modelled and validated against the relative experimental data using *Vulcan* software [65], [66]. The overall fire resistance behaviour of composite floors subjected to compartment fires was also modelled in *Vulcan* and the results from the numerical model were extensively validated using experimental data [67]. The current version of the software includes a three-noded beam-column element, a nine noded slab element and a two-noded special element (spring and shear connector element) in addition to a two-noded component based connection element. The elements are defined at the common reference plane in the software, which is assumed to coincide with the mid-surface of the slab element (if represented), otherwise it is the centroid of steel beam-column element.

2.4.2.1 *Non-linear procedure*

The main purpose of conducting finite element analysis is to work out the displacement of a structure under different load conditions taking the effects of geometric and material properties in to account. The basic finite element stiffness equation for an element for static analysis can be obtained by:

$$K.U = R \quad (2.10)$$

The main issue in non-linear analysis is to establish the equilibrium state of a structure in correspondence to the applied load. This means that when the structure is externally loaded, the internal force generated need to balance the applied load. Reaching this equilibrium state in a single step is not achievable in non-linear analysis therefore, unbalanced forces are generated. As a result, incremental nodal displacement is necessary in an iteration process until the unbalanced forces are small enough to be neglected. Equation 2.11 expresses the basic mathematical derivation used to conduct non-linear finite element analysis:

$$\left({}^tK_L + {}^tK_{NL} \right) \cdot \Delta U = {}^{t+\Delta t}R - {}^tF \quad (2.11)$$

where, tK_L and ${}^tK_{NL}$ are the incremental stiffness matrix for the linear and non-linear-strain respectively, ΔU is the vector for incremental nodal point displacement, ${}^{t+\Delta t}R$ is the vector of externally applied nodal point loads at time $t+\Delta t$ and tF is the vector of nodal point forces equivalent to the element stresses at time t .

2.4.2.2 Beam element modelling

The cross-section of each beam element is comprised of a number of segments. Each segment is capable of having individual material properties and temperature along with an independent stress-strain relationship. Perfect bond is assumed between the segments, therefore no slip is allowed between segments. Each segment within the beam element is represented by three degrees of freedom (one longitudinal stress and two shear stresses) and the plane section is assumed to remain plane under flexural deformation. The reference axis of the element can be located anywhere across the depth of the beam in order to represent the offset effect when composite action between the slab and the beam is considered. Figure 2.23, shows the configuration of the three-noded beam element in *Vulcan*.

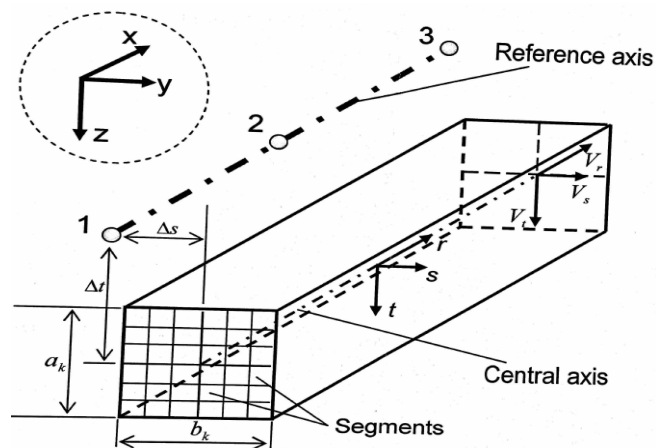


Figure 2.19: Three noded- beam element configuration [1]

2.4.2.3 Slab element modelling

Basic principles

Concrete slabs in *Vulcan* are modelled as an assembly of finite plate elements, which are in the form of four-sided isoparametric element with nine-nodes as described by da Silva [59]. The slab shell element is assumed to have layered properties representing concrete and reinforcing mesh. Several assumptions had been made within the layered procedure approach:

- Perfect bond is assumed between the plane concrete layers and the steel reinforcement layers, therefore, no slip between layers is assumed.
- Orthotropic properties have been assumed for the concrete layers after cracking.
- The reinforcing mesh in the orthogonal directions is modelled using uniaxial stiffness in the direction of the reinforcing bars.
- The cross-section area of the reinforcement layer is the equivalent of the total area of reinforcing bars in the appropriate direction.

The temperature of individual layers can differ, but must be uniform within each layer of an element. Figure 2.20 illustrates the configuration of the slab shell element incorporated in *Vulcan*

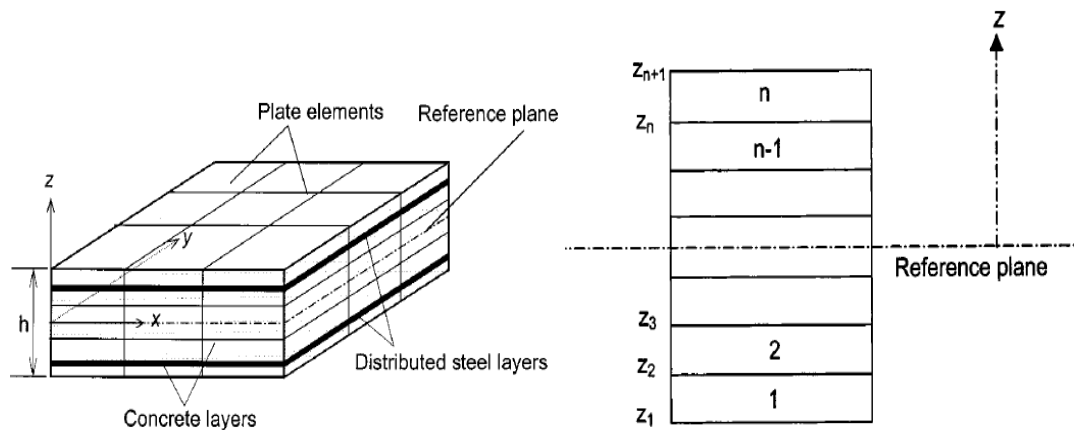


Figure 2.20: Concrete slab configuration in *Vulcan* [65]

Quadrature Gauss integration points can be used to evaluate the stiffness matrix $[K]$ (which represents the material properties of slab element) for a nine noded

quadrilateral slab element [65]. Each slab element contains nine different Gauss point across its surface area and close to the actual geometrical coordination of the slab nodes. Therefore, the changes in material properties of the slab element (stiffness, strength, thermal expansion) around the perimeter nodes can be accurately determined by considering the adjacent Gauss integration point. This property of the slab will be used in the next chapter in order to identify the occurrence of the tension failure in a composite slab element as a part of the implementation of the new “Break Element”.

Biaxial failure envelop of concrete

The mechanical properties of concrete under uniaxial loading are generally assumed to be quite different compared to the two or three-dimensional stress analysis. Composite slabs generally have a large span to depth ratio, since the thickness of the slab is much smaller than its other two dimensions, therefore the slab element can be assumed to be in a plane stress state for the purpose of numerical modelling [66]. In Vulcan bi-axial failures envelope has been assumed to identify the initiation of plane concrete failure within a slab element. Figure 2.21 shows the bi-axial failure envelope for the concrete material used in the software. In this model, the cracking or crushing of concrete is identified when the stresses (σ_{c1} and σ_{c2}) in the concrete reaches the peak value in the corresponding principal direction at that point. The boundary between cracking and crushing failures in the modes is determined by the relationship of $0.75f_{c\theta}$ and the compressive stress.

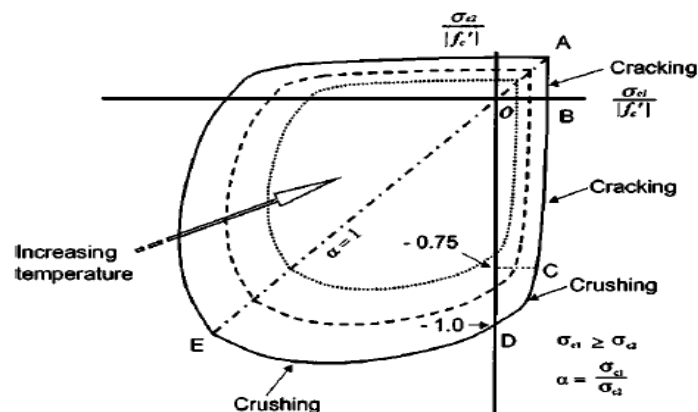


Figure 2.21: Concrete bi-axial failure envelopes at elevated temperature [65]

Smearred cracking model

Strain softening in concrete occurs when the stresses within the concrete surface reaches the failure criteria and beyond this point the strength of concrete starts to decrease along with progressive straining. It is generally agreed that strain softening is more likely to be a structural property than a material property and represents the progressive changes in member geometry, uniformity and homogeneity [70]. Initiation of the strain softening phenomenon is directly a function of localised failures, i.e. tensile cracking and compressive crushing in concrete. There are currently two approaches available to model the tensile cracking: discrete cracking and smeared cracking. The former method assumes the cracks to occur along the element interface and in the latter method the cracks are assumed to be smeared over the area within the element. Jirasek, 2001 reviewed different approaches to deal with the subsequent discontinuities of concrete after the initiation of cracks. The methods include: re-meshing, Elements with embedded discontinuities (FED) and the extended finite element method (XFEM). It was concluded that these discrete methods are computationally time consuming and therefore, smeared cracking approach would be a better technique to model and deal with tensile cracking of concrete [69]. Despite the importance of appropriate modelling of strain-softening in concrete, extensive research has also been conducted to develop failure surfaces for concrete since concrete is generally assumed to have poor performance in tension. Some mathematical models have been developed in the past by Chen [70] and Ohtani [71] to provide appropriate modelling of the concrete surface failure, however, using these models for the purpose of finite element analysis results in a non-symmetric stiffness matrix.

Vulcan software is not currently capable of performing analysis based on non-symmetric stiffness matrix; therefore a smeared crack model has been adopted in the software *Vulcan* to represent the behaviour of concrete in tension [65]. Concrete is assumed to be cracked once its stress in the principal directions reaches the failure surface either in the biaxial tension region (segment AB in figure 2.21) or the combined tension-compression region (segment BC in figure 2.21) at any Gauss point over the area of the element. Once the first crack occurs the concrete is working as an orthotropic material with two principal axes normal and parallel to the

direction of the crack. Linear elastic behaviour and uniaxial stress-strain relationships are assumed for the concrete (parallel to the crack direction) when it is subjected to a tension force and the compression force respectively [72]. As the singly cracked concrete is further loaded, a second set of cracks form normal to the direction of the first crack. Figure 2.22 represents the simplified strain-softening model, which has also been adopted in Vulcan software by [65]. The model shows a linear elastic behaviour up to the point when concrete reaches its ultimate tensile capacity, beyond which the tensile stress gradually decreases along with increasing strain.

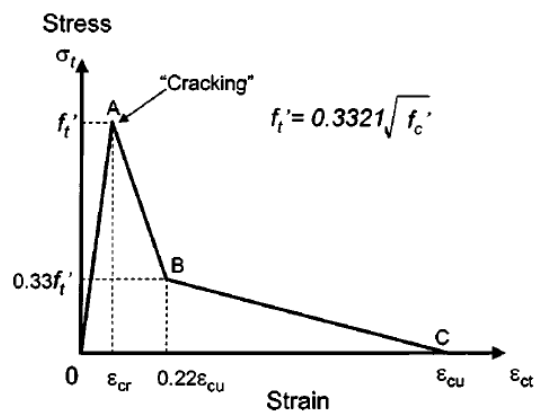


Figure 2.22: Bi-linear smeared concrete crack model used in *Vulcan* [65]

2.4.2.4 The static-dynamic procedure

Most numerical analysis software for modelling the structural behaviour in fire are capable of doing static analysis using static solver. This type of analysis ignores the inertial effect aroused from the variation of loading and temperature. Static analysis traces the equilibrium behaviour of the structure at both ambient and elevated temperature until instability occurs due to the failure of one or more members within the structure. However it is clear that numerical failure does not necessarily indicate a real structural failure, since this may be due to a temporary instability, such as buckling of a column, local cracking of a concrete slab or the fracture of components in connections, which is then balanced by redistribution of forces within the remaining structure. At this point the analysis becomes divergent after this limit point and the solver is unable to find the next equilibrium point and fails to converge because of the numerical singularity, consequently the analysis will be terminated.

Progressive collapse in fire is a highly nonlinear and discontinuous process, within which a sequence of structural instabilities, material degradation and discrete fractures occur. The numerical problems associated with these nonlinearities, discontinuities and instabilities need to be solved in order to predict the real structural collapse process. Static-dynamic solver was developed by [73] in *Vulcan* software at University of Sheffield in order to overcome the instability issues in numerical problem as a result of using conventional static analysis. The new procedure was extensively validated against experimental data on progressive collapse of the structure [74]. The main characteristics of the solver are listed below:

- The inertial forces are calculated on the basis of a lumped-mass assumption;
- The dynamic procedure adopts an explicit direct time integration method since the implicit dynamic procedure requires formation and inversion of the global stiffness matrix, more disk space and memory are needed compared to the explicit dynamic process;
- Viscous damping was assumed in the dynamic solver for the ease of solution (velocity-proportional damping);
- Small time increments must be used since for the ease of convergence in dynamic stage accompanying acceleration for all degrees of freedom need to be nearly constant during an increment.

This combined static-dynamic procedure is capable of modelling both stable and unstable structural behaviour in fire. Conventional static analysis is adopted to track the stable equilibrium behaviour at both ambient and elevated temperatures. After instability is identified in the analysis, the dynamic procedure will be activated to continue the analysis. This switch happens within a single temperature-increment step, using the criterion that static analysis has failed to converge. The switch back from dynamic to static analysis depends on the kinetic energy of the structure. If, during the following dynamic motion, stability is regained, the static solution process is reactivated to continue the analysis under changing temperature. The static analysis is continued while the stability of the structure is recovered. These alternate analyses are continued until the final global failure of the structure is indicated by a divergent increase of kinetic energy over a series of time steps at very high

deflections. Figure 2.23 illustrates the general procedure of the application of static-dynamic solver incorporated in *Vulcan*.

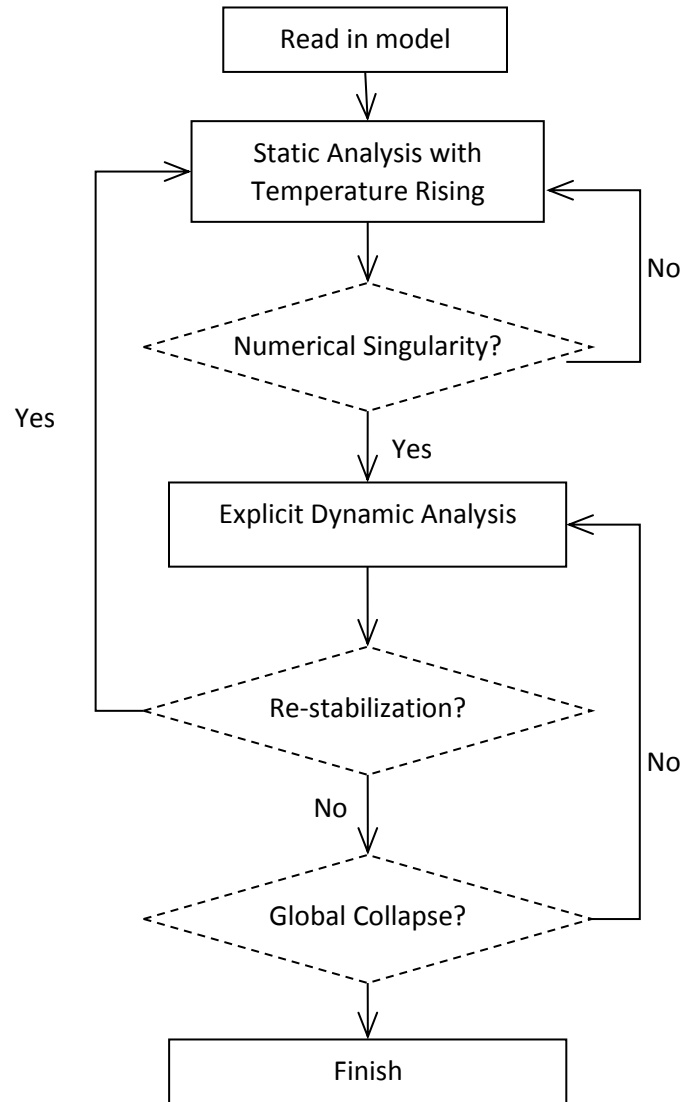


Figure 2.23: General procedure of static-dynamic solver in *Vulcan* [74]

2.5 The Importance of Composite Slab Break Element

2.5.1 Behaviour of composite slab in hogging regions

In the case of a fire heating up a structure, the connections in a steel framed building are subjected to a complex set of forces. Large axial forces (compressive forces that later become tension as the steel softens from rising temperature) result from developing catenary action will affect the structure in addition to the standard shear and bending moments raised from gravity load. Therefore, the performance of the joint to withstand these loads plays a key role in overall behaviour of the frame. Composite joints are one of the most common types of joint used in the structure where a composite slab and the steel connection are working together to withstand the gravity load and the generated horizontal load from axial restraint. Extensive works have been done in the past to investigate the performance of different types of bare steel connection over the last two decades. Al-Jabri [35] developed a component based model for flexible and extended bare steel connections at ambient temperature. Brown and Anderson [75] investigated the structural properties of major axis end plate connections and developed a simple component based model accordingly. Block [61] has further developed the implemented steel connection model in *Vulcan*. Sarraj [62] has also developed a numerical finite element model for fin plate connections in fire. But there are fewer works investigating the influence of the composite slab on the joint performance at elevated temperature. Composite joints are one of the most common types of joint used in current structures. Extensive work has been done to investigate the performance of different types of bare steel connection over the last two decades, but little work has been done to investigate the influence of the composite slab on joint performance at elevated temperature.

A composite slab contributes to the rotational stiffness of the joint by means of its resistance to tensile force due to hogging bending moment at the top surface of the slab. The presence of composite slab increases the lever arm within the joint, which consequently results in higher rotational stiffness. But for the purpose of fire engineering safety design it should also be ductile enough to provide sufficient rotation to the joint. Composite slabs are relatively thin (100-150mm) compared to

conventional reinforced concrete slabs, therefore, in case of fire it is assumed that the stiffness of the slab is governed by its tensile stiffness rather than the bending stiffness since the depth of the slab is very small compared to the span. According to the Bailey-BRE method, the top surface of slab on its edge is mainly under tension as a result of hogging bending moment and tensile membrane action of the slab [47]. In the Bailey method, rigid supports are considered to vertically support the slab. The method assumes the large hogging moments generated at the edges cause failure of the slab reinforcement over the edges and accounts for no continuity with adjacent panels. Therefore, this analysis is based on an isolated slab panel and on the assumption that the protected edge beams have sufficient vertical restraint throughout the fire exposure [76]. But in fact The Bailey method neglects two important aspects for the design of a slab in fire. The method states that the supports around the edge are considered ideally rigid vertically but are not restrained horizontally and rotationally. This means that the influence of the edge beams is not taken into account. Work done by Stadler at the Technical University of Munich shows that the deformation of edge beams along with thermal elongations and the interaction with adjacent slab panels have an effect on the distribution of the force in the slab [77]. Taking his work into account, deformation of steel beams, both intermediate and edges, results in reducing hogging bending moment at the top surface of the slab. Figure 2.24a illustrates the distribution of compressive/tensile membrane force across the slab panel. The influence of the edge beams and the interaction with the adjacent slab are presented in figure 2.24b.

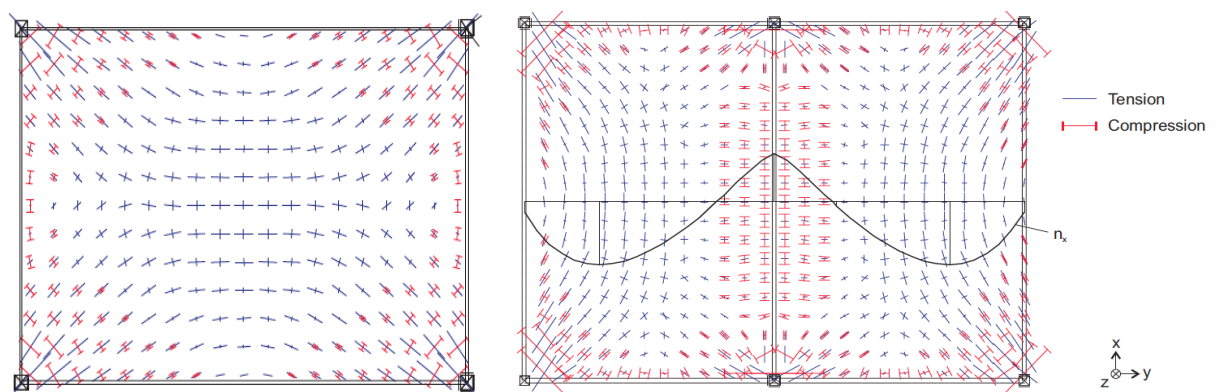


Figure 2.24: a) membrane forces of single slab, b) membrane forces of two adjacent slabs [77]

It can be seen from the above figure that the presence of the steel beams and the adjacent slab clearly contribute to the distribution of membrane forces over the slab area i.e. in the example above, the maximum deflection occurred at one-third of the short span at the middle of the slab rather than the slab centre. This also consequently influences the distribution of hogging bending moment in tensioned areas, where the top surface of the slab above the steel beams cracks in the transverse direction as a result of pure tensile force due to the vertical deflection of the slab.

2.5.2 Integrity and insulation criterion of composite slab in fire

Experimental work done by Stadler (DASt project) at Munich University in Germany [77] and Simms and Zhao (FRACOF project) [49] on composite floors show that discrete cracks can occur right above the intermediate beam in composite structures (as a result of low reinforcement ratio in composite slabs) where the hogging moment is maximum. It should be noticed that, even the failure of a slab around the edge results in no structural collapse and structural stability is retained, but it has to be appreciated that in fire not only should a structure remain stable, it should also satisfy the integrity condition so the fire does not spread through openings in any structure. In the large compartment test at Cardington, the test frame survived various fire tests while no sign of structural stability was observed, however, some local failure occurred. Figure 2.25 represents a gaping crack in the composite slab at the location close to one of the columns and right above the beam-column connection in one of the demonstration fire tests at Cardington.



Figure 2.25: Cracked floor slab around the connection [49]

The crack occurred as a result of thermal contraction of the composite floor slab during the cooling stage. Although the opening in the slab caused no safety failure as it occurred while the structure was cooling down but it is not always the case when dealing with the real structure, where there could be a risk of fire and smoke spread to the floor above if the fire enclosure is still hot and producing smoke [20]. Furthermore, the development of crack at the corners of the composite slab panel during fire can result in reduced rotational capacity of the steel beam-column connection below the composite slab, which consequently cause the joint to be overloaded and therefore, the joint failure is possible (failure of load bearing capacity criteria “R”). Despite the risk of the progressive collapse in the structure, joint failure can also led to structural failure in terms of insulation “I” and integrity “E” by passing the fire to the upper floor through the gaps in the cracked zone. Two full scale fire tests on membrane action in fire were also conducted by [77] in Munich, Germany as a part of DAST research project (the project aimed to investigate the behaviour of intermediate beams between two slab panels) [78]. During the first Munich test on conventional reinforced concrete slab, discrete cracks occurred in the concrete slab right above the intermediate beam and also at a very close distance from the protected intermediate beam along the first lattice girder. These are shown in figure 2.26.

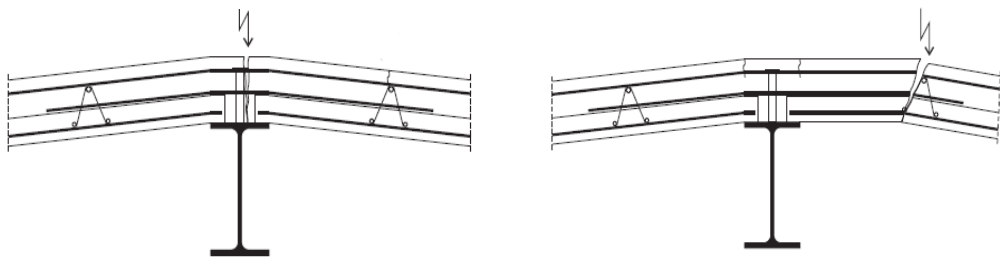


Figure 2.26: Cracked section of the first Munich test [77]

The first cracks occurred at the top of the intermediate beam as a result of large hogging moment and tensile forces generated by the applied mechanical load and the restraint thermal elongation. The second crack occurred at the location of the first lattice girder, which provides a weakening in the structure. The gaping cracks have been developed during the test so that the top reinforcement reached its ultimate strain and ruptured. The width of the crack at these positioned was reported to be

several centimetres over the whole depth of the slab. Figure 2.27 shows the gaping crack adjacent to the intermediate beam. The opened crack caused the smoke streams to the upper side of the slab resulting failure in terms of integrity “E” and insulation criterion “I” of the slab. On the other hand, the developed crack above the intermediate beam caused no integrity failure of the structure as smoke could not get to the upper side of the slab due to the present of the steel beam beneath the slab.



Figure 2.27: Gaping crack, first Munich test [77]

The second Munich test was focused on the behaviour of the composite concrete slab in full scale structure at elevated temperature. Figure 2.28 illustrates the plan view of the typical floor layout for this test.

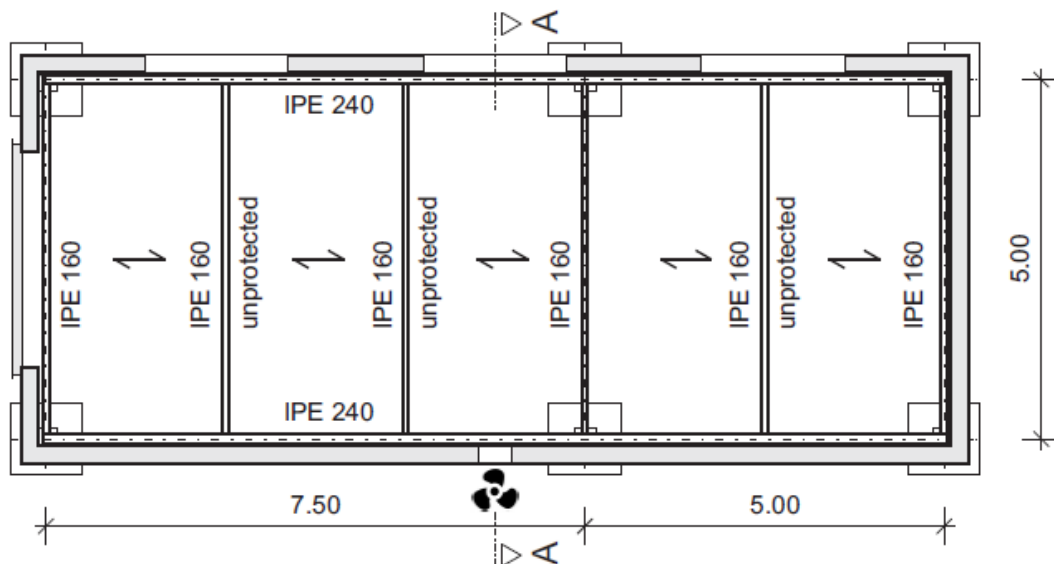


Figure 2.28: Plan view of the compartment arrangement, second Munich test [78]

Similar to the previous test, the temperature within the compartment in the second Munich test also reached 900°C, where the maximum vertical deflection of the slab panels were measured to be about 255 mm and 190 mm at larger panel and smaller panel respectively. A single crack occurred across the whole slab on top of the intermediate beam as it is shown in figure 2.29.

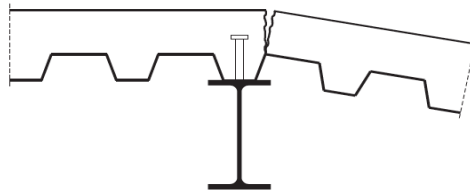


Figure 2.29: Crack location at the edge of composite slab – second Munich test [77]

The width of the gaping crack remained relatively small during the test and no reinforcement has been ruptured. This is mainly due to the large vertical deformation of the intermediate beam which in turn causes small rotation in the slab above. The width of the crack was reported to be several millimetres but it did not lead to any structural failure of the slab [77]. However, the reinforcement could be fractured and the structural failure was likely to occur if the intermediate beam had been stiffer. Furthermore, the installed thermocouple on the top surface of the composite slab (right at the crack position) recorded the maximum temperature of 135°C, which was lower than the specified limit for the insulation criterion “I” according to the DIN EN 1994-1-1 [79]. Also no sign of smoke or flames was observed to pass through the crack at the top surface of the slab, therefore, all safety criteria (“R, E, I”) were satisfied for the whole test.

2.5.3 Remarks

Many factors such as: non-uniform compacting of the concrete or inaccurate reinforcement overlapping can cause local weakening within the slab floor area in the real structures. The two Munich fire tests are good examples to prove that it is not conservative to state that the failure in structure can be excluded by using composite/concrete slab. In all currently available simple calculation models for slab

capacity such as Bailey BRE method [14], [47] the contribution of the mesh reinforcement has been ignored and the slab floor area is considered as an isolated slab panel since in these methods it is assumed that the reinforcement at the slab edges are indeed ruptured. But within these methods it is also assumed that the fracture of the reinforcement do not lead to any sort of failure, the fact that has already been proved not so accurate. Hence, it is important for the slab to meet the safety criteria “R”, “E”, “I” that are load bearing capacity, structural integrity and insulation respectively, thereby ensuring that no smoke or flames can penetrate to the floor above [5]. These all illustrate the needs for the revise in the current fire engineering approach, which can be achieved either by developing a more rational fire safety engineering approach to provide a design method for the required reinforcement amount around the slab edges in order to prevent the failure at this location or through appropriate modelling of the crack development at the slab perimeters specially at the locations close the connections to consider the effect of horizontal restraint from the mesh reinforcement and the possible effects reinforcement failure on the overall stability of the structure.

2.6 Factors Influencing Composite Slab Break Element

2.6.1 Minimum reinforcement area

Brittle failure in a lightly reinforced concrete section can occur if the required force to induce the first crack in the concrete is higher than ultimate strength of the rebar. This type of failure usually happens suddenly and should be avoided by providing the minimum reinforcement area according to the relevant design code. According to EC2, a minimum amount of bonded reinforcement needs to be considered in the design of a reinforced member in order to control cracks in the tensioned areas. The following formula has been recommended by Eurocode2 to calculate the amount of reinforcement required to control cracking.

$$A_{s,min} \cdot \sigma_s = K_c K_{ct,eff} \cdot A_{ct} \quad (2.12)$$

Where,

$A_{s,min}$ is the minimum area of reinforcement in tensile zone

A_{ct} is the area of concrete in tension.

$f_{ct,eff}$ is the mean value of concrete tensile strength, $f_{ct,eff} = f_{ctm}$

K is the reduction coefficient of restraint forces, $K = 1$ for $h < 300mm$

K_c is a coefficient representing the stress distribution within the section prior to cracking; for pure tension the value of $K_c = 1$.

It should be mentioned that in order to calculate the effective tension area of concrete in a composite slab equivalent, an rectangular area has been assumed based on a formula given by Annex D of BS-EN 1994-1-2.[5]

$$h_{eff} = h_1 + 0.5h_2 \left(\frac{l_1 - l_2}{l_1 + l_3} \right) \text{ for } h_2/h_1 \leq 1.5 \quad (2.13)$$

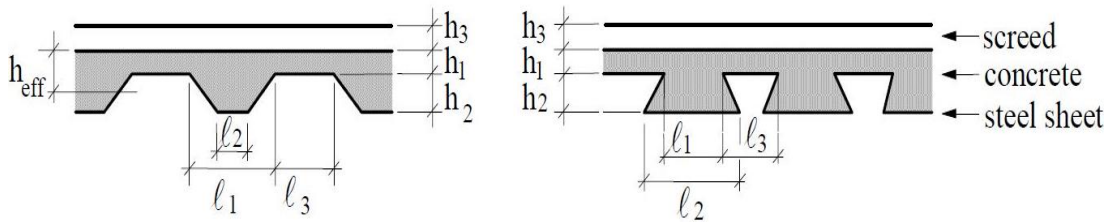


Figure 2.30: Geometrical notation of steel decking according to EC4 [5]

2.6.2 Temperature

Structural material properties are affected by changes in temperature. Structural members may behave in a different manner at high temperature due to the changes in the constituent material properties under rising temperature resulting in a reduced level of strength and stiffness for the structural element.

2.6.2.1 Steel reinforcement

In the case of a fire, the temperature in a composite section distributes through the depth of the section, where the highest and the lowest temperature is at the bottom and top surface of the section respectively; the temperature in the section decreases through the depth of the cross-section. Therefore, the mesh reinforcement near the top surface of the slab experiences a much lower temperature than the bottom face,

but it is important to know what temperature the reinforcement is likely to reach so that the effect of rising temperature on the material properties of the reinforcement steel can be accounted for. Annex D of BS-EN1994-1-2 [5] introduces a simple model for the calculation of the temperature distribution along the depth of unprotected composite slab exposed to fire based on the standard temperature-time curve. According to BS-EN 1992-1-2 [90], the mechanical properties of steel rebar remain unaffected at elevated temperature of up to 400 °C. However, beyond that point the strength and stiffness of steel rebar reduce with the increase of temperature starting with loss of the strain-hardening effect. Table 2.2 and figure 2.31 from Eurocode 2 illustrate the reduction of the characteristic strength of tension reinforcement (class N) as a function of temperature for different tension and compression reinforcements, where curve 1 and 2 refers to the tension reinforcement with strain less than 2% and greater than 2% respectively, and curve 3 refers to the compression reinforcement [5], [90].

Steel Temperature θ [°C]	$f_{s,y,\theta} / f_{yk}$		$f_{sp,\theta} / f_{yk}$		$E_{s,\theta} / E_s$	
	hot rolled	cold worked	hot rolled	cold worked	hot rolled	cold worked
1	2	3	4	5	6	7
20	1,00	1,00	1,00	1,00	1,00	1,00
100	1,00	1,00	1,00	0,96	1,00	1,00
200	1,00	1,00	0,81	0,92	0,90	0,87
300	1,00	1,00	0,61	0,81	0,80	0,72
400	1,00	0,94	0,42	0,63	0,70	0,56
500	0,78	0,67	0,36	0,44	0,60	0,40
600	0,47	0,40	0,18	0,26	0,31	0,24
700	0,23	0,12	0,07	0,08	0,13	0,08
800	0,11	0,11	0,05	0,06	0,09	0,06
900	0,06	0,08	0,04	0,05	0,07	0,05
1000	0,04	0,05	0,02	0,03	0,04	0,03
1100	0,02	0,03	0,01	0,02	0,02	0,02
1200	0,00	0,00	0,00	0,00	0,00	0,00

Table 2.2: Class N values for the parameters of the stress-strain relationship of hot rolled and cold worked reinforcing steel at elevated temperatures [90]

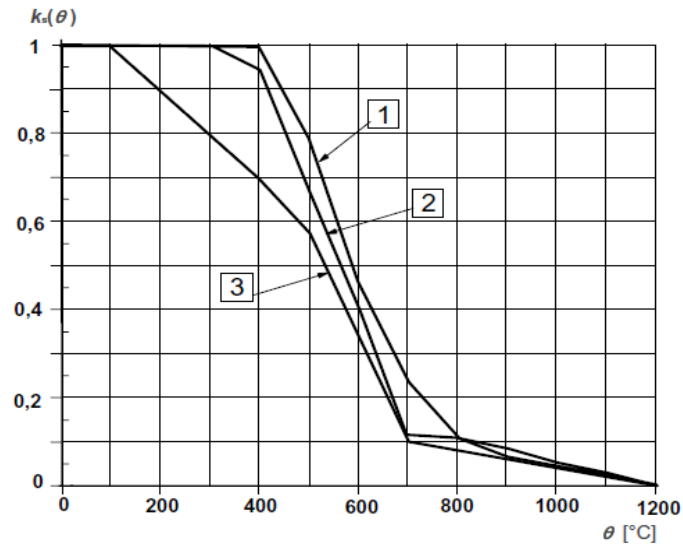


Figure 2.31: Coefficient $k_s(\theta)$ allowing for decrease of characteristic strength (f_{yk}) of tension and compression reinforcement (Class N) [90]

This can be further justified by experimental investigations. For instance, changes in mechanical properties of steel rebar due to temperature have been investigated by [91]. Steel rebar of 10mm and 16mm diameter in S220 and S420 grades were tested at elevated temperature up to 900 °C. The results revealed that there is no significant change in the mechanical properties of the rebar due to rising temperature up to 500 °C. The result is almost 100 °C beyond the limit suggested by BS-EN 1994-1-2 and BS-EN 1992-1-2 [5], [90]. Figure 2.32 is the comparison of the stress-strain curve of the rebar S420 at different temperature.

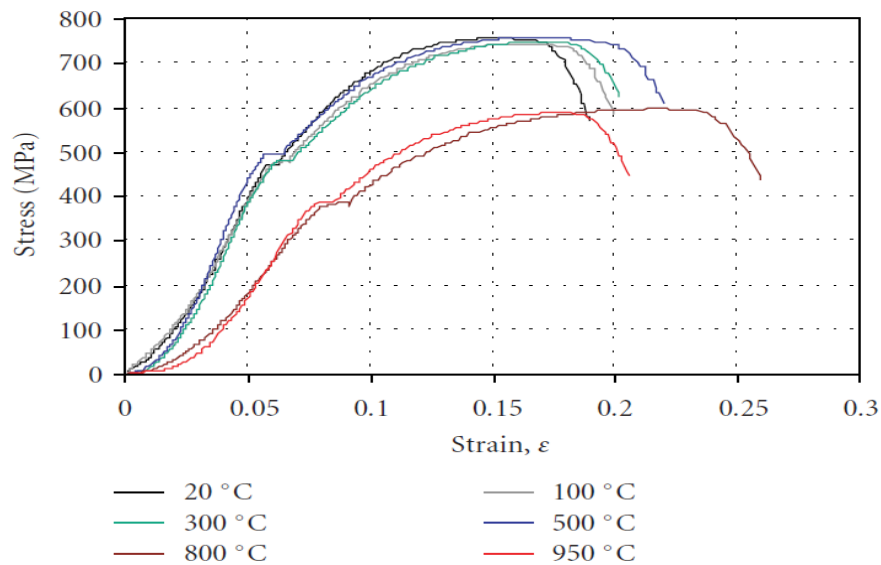


Figure 2.32: Stress-strain of rebar at different temperature [91]

The rate of degradation of the yield strength for both types of steel reinforcement is shown in figure 2.33 [91]. The figure shows that there is no variation in the yield strength of both types of the reinforcement (S220 and S420) at different temperature up to 300 °C. This is in accordance with the limits recommended by EC2. Furthermore, it can be seen from the graph that even the rebars are grades S220 and S420, the average yield strength for both type of rebars at room temperature are approximately 100Mpa above the expected values. This can explain the better mechanical performance of the tested rebars at elevated temperature, similar to figure 3.6, where there was no significant changes in mechanical properties of the rebars at elevated temperature up to 500 °C

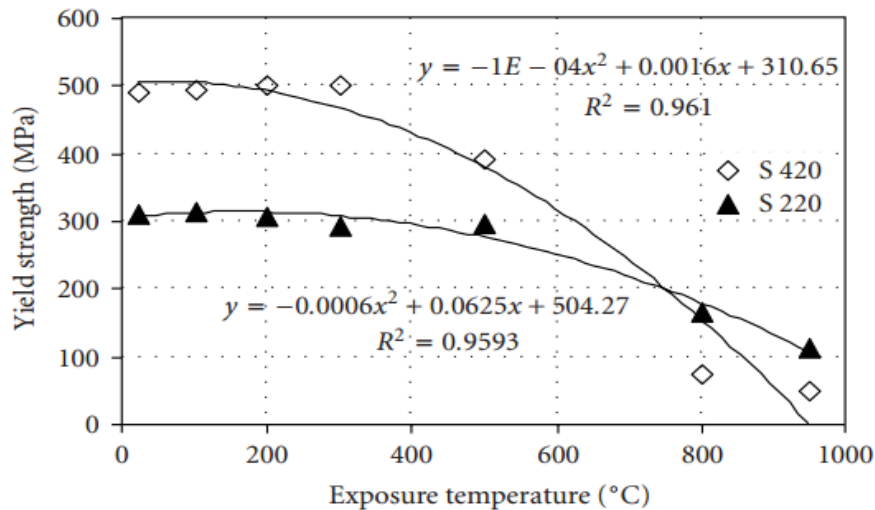


Figure 2.33: Tensile strength of steel rebar – temperature [91]

Munich test

The test conducted by [77] at Technical University of Munich was part of a DASt research project on composite slabs under fire with re-entrant trough profile steel sheeting. The main objective of the test was to generate data that can be used to calibrate numerical models and design methods. A welded mesh size of grade S500 was used as top reinforcement providing a reinforcement area of 188 mm²/m in both directions; approximately equal to 8mm diameter bars spaced every 200mm. The maximum temperature the slab reached during the test was about 750 °C [77].

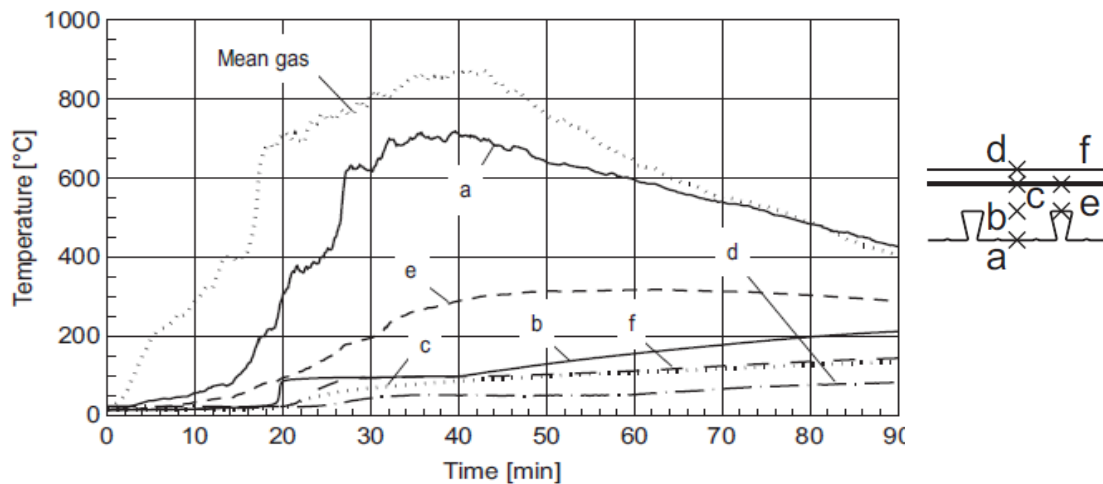


Figure 2.34: Temperature distribution in slab-Munich [77]

Figure 2.34 illustrates the temperature development across the depth of the composite slab. The dotted line “C” shows the change in temperature at the top reinforcement over 90 minutes of the test. It can be seen that the reinforcement stayed relatively cold during the test with a temperature of less than 150°C. This suggests that when modelling the break element in fire the effect of temperature on the reinforcement is likely to be negligible.

FRACOF test

A full-scale test to investigate membrane action was performed in Metz-France as part of the Fire Resistance Assessment of Partially Protected Composite Floors project (FRACOF) [49]. An open trough profile steel sheeting was used in the composite slab with a top reinforcement of 7mm diameter bars of grade S500 at 150mm centres that provides a total reinforcement area of 257mm²/m. The test was successfully run for 150 minutes following the standard fire curve. Figure 2.35 represents the distribution of temperature over time. It is clear from the figure that the top reinforcement (placed at points “E” and “F”) reached a maximum which is temperature of 250°C and 350°C respectively [49]. These values are well below the temperature limit of 400°C recommended by EC2, above which the strength and the stiffness of the steel reduce significantly [5], [90].

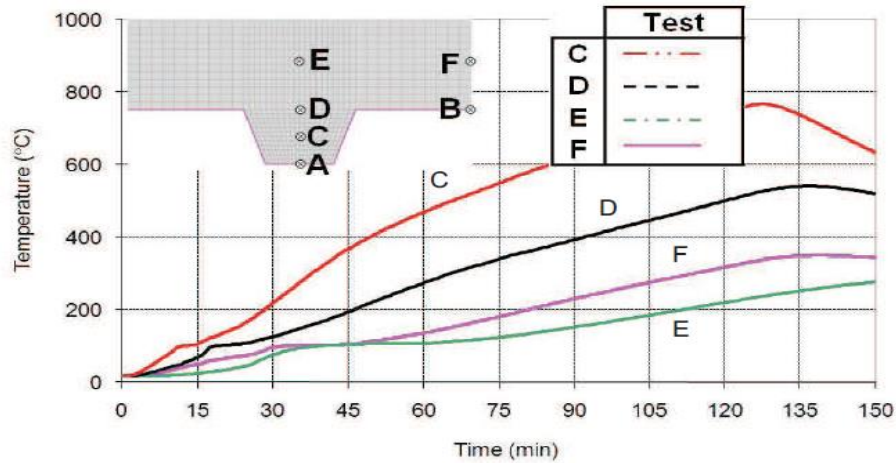


Figure 2.35: Temperature distribution in slab-FRACOF [49]

2.6.2.2 Concrete

Although concrete is commonly considered to be fire resistant, it should be noted that the characteristic strength (f_{ck}) of concrete reduces at temperatures beyond 100 °C. The rate of the reduction in the compressive strength of concrete can be found in section 4.2a of BS EN 1992-1-2. Figure 2.36 demonstrates the changes in concrete compressive strength at elevated temperature based on the standard fire test curve. Curve 1 and curve 2 represent the characteristic strength of normal and lightweight concrete respectively.

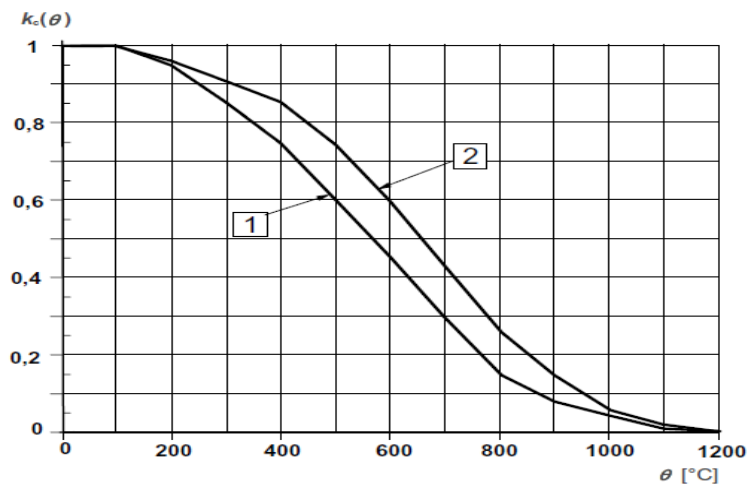


Figure 2.36: Characteristic compressive strength (f_{ck}) against temperature [90]

Distance x [mm]	Temperature in the concrete slab θ_c [°C]				
	30 min	60 min	90 min	120 min	180 min
2.5	681	837	918	973	1048
10	509	682	778	844	933
20	345	519	621	694	796
30	233	395	497	571	677
40	156	300	398	470	577
50	106	228	318	388	492
60	76	172	254	320	420
70	56	130	203	263	359
80	42	101	161	217	307
90	33	80	129	178	262
100	27	64	104	146	224
110	24	51	86	121	191
120	22	42	71	101	163
130	21	35	60	86	140
140	21	30	50	74	122
150	20	27	43	64	107

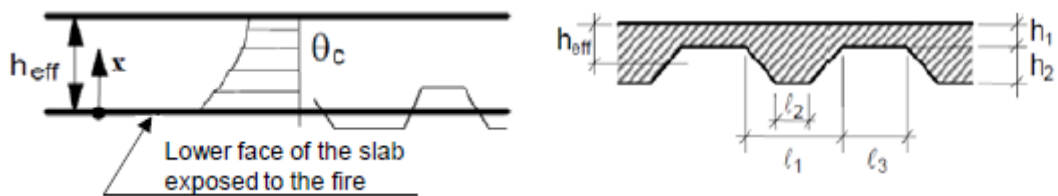


Table 2.3: Temperature distribution in slab – standard fire [92]

Part 4.4.2 of EN 1994-1-2 introduces a calculation technique to determine the temperature distribution through the depth of the composite slab by considering the actual shape of the concrete slab including the metal deck. However, an alternative method to determine the temperature distribution within the slab was established by [92] as part of the FRACOF project. In this method, the spreading of the temperature under a standard fire is determined based on the calculation of the effective height (h_{eff}) of the slab recommended by Annex D of EN 1994-1-2 and in accordance with EN 1992-1-2 and its National Annex. Table 2.3 demonstrates the temperature distribution in a slab with effective height of 150mm (typically, composite slab

depths are in the range of 110-150mm) for standard fire exposure of 30, 60, 90, 120 and 180 minutes.

2.6.3 Bond Strength

2.6.3.1 Bond failure modes

There are two types of failure modes under monotonic loading. The first type is associated with pull-out of the bar which is mostly likely to occur in elements with sufficient cover/confinement as a consequence of concrete shearing between the lugs of the steel reinforcement. It is worth noting that the rebar geometry and its surface condition, together with compressive strength of the surrounding concrete, are the factors with the most influence on the pull-out failure.

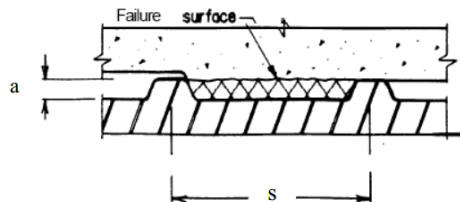


Figure 2.37: Shearing of concrete between the lugs in pull-out failure

The second type is the splitting mode failure. This occurs when there is insufficient concrete cover or confinement present. This failure originates as a result of the wedging action of ribs when the bar moves with respect to concrete, as shown in figure 2.38. In other words this failure is a direct result of stresses that are developed from lug bearing forces. It is assumed that no concrete cover and bond interaction is remained when splitting approaches the edges of the member.

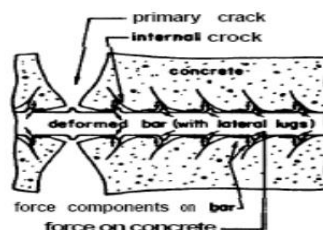


Figure 2.38: Wedging action causing splitting failure

2.6.3.2 *Parameters affecting the bond strength*

Several factors influence the bond strength between the steel bar and concrete. These factors are listed below along with a brief description of each:

- Concrete compressive strength: The tensile and shear strength of concrete correlate well with compressive strength. In RC members, force is mainly transferred between steel and concrete by bearing against the lugs. When the transferred force exceeds either the concrete tensile strength or shearing strength failure occurs by means of tensile splitting or pull-out (shearing of concrete), respectively.
- Bar sizes: The quality of the bond interaction can be influenced by the geometry of the bar and its surface pattern. As the bar size increases, larger bond forces are required to be transferred over a certain length (the development length). Hence, there is a reduction in the ultimate bond stress with increase in the size of the bar.
- Anchorage length: Average bond strength decreases with increase in anchorage length.
- Rib geometry: Bond performance is also influenced by the rib geometry. The larger the bearing to shearing area ratio, the higher is the initial bond stiffness and performance.
- Transverse reinforcement: This plays an important role in preventing splitting failure after cracking of a member and provides confinement.

2.6.3.3 *Bond-slip models*

Over the years a number of bond-slip models have been developed. These models are split into two major categories: (1) micro-models and (2) macro-models. In micro-models the steel-concrete interface is modelled by using the relationship between local bond stress and local slip in a numerical model. Using micro-models for the purpose of numerical analysis can replicate the bond interaction with a good level of accuracy [93]. However there is a major drawback associated with these models that is their iterative nature leading to time-consuming running processes. Macro-models

on the other hand are based on the relationship between the tensile forces and bar slip. These models are also referred to as element models in the literature and often assume a uniform or stepped bond stress over the development length of the reinforcing rebar. It is worth noting that, although macro-models are efficient computationally, they can only be applied to members with the same conditions [93]. Some examples of micro-models and macro-models are presented below.

Micro model

Figure 2.39 presents a nonlinear local bond τ - s relationship based on the findings of extensive experimental program for both pull-out and splitting failure modes [94]

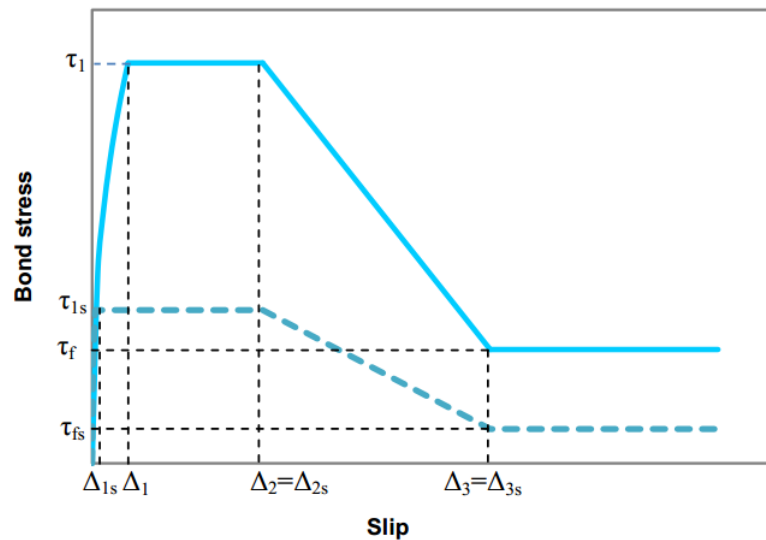


Figure 2.39: Bond-stress and slip relationship [94]

τ_1 is the peak bond stress and Δ_1 is the corresponding slip, which is then followed by a plateau section ($\tau_2 = \tau_1$) up to Δ_2 . The next section is descending linearly to the ultimate frictional bond stress τ_f at a slip that is denoted as Δ_3 on the figure. The last section contains a constant horizontal profile for bond stress and is equal to τ_f . Splitting failure is shown with thick dashed lines on the above figure and resembles the relationship between τ - s where τ_{1s} is the peak bond stress in splitting failure and Δ_{1s} is the corresponding slip. Δ_{2s} is the end of the slip plateau with bond stress equal to τ_{2s} . τ_{fs} is the peak frictional bond strength in splitting failure. Following relations expressions compare the bond strength with slip at splitting and pull-out failure in different stages:

$$\begin{aligned}
\tau_{1s} &\leq \tau_1 & \Delta_{1s} &< \Delta_1 \\
\tau_{1s} &= \tau_{2s} & \Delta_{2s} &= \Delta_2 \\
\tau_{fs} &\leq \tau_f & \Delta_{3s} &= \Delta_3
\end{aligned}
\tag{2.14}$$

The proposed bond-slip models by [94] were adopted in CEB-FIP (MC90) [95] with slight changes in bond stresses and slips. Different slips and bond stresses are specified for different levels of confinement and bond conditions as shown in table 2.4.

Table C.4 Bond stress-slip values for different bond conditions (CEB-FIP(MC90) (1993))

	Unconfined concrete		Confined concrete	
	Bond conditions		Bond conditions	
	Good	All other cases	Good	All other cases
s_1 (mm)	0.6	0.6	1.0mm	
s_2 (mm)	0.6	0.6	3.0mm	
s_3 (mm)	1.0	2.5	clear rib spacing	
α	0.4		0.4	
τ_{\max} (MPa)	$2\sqrt{f'_c}$	$1\sqrt{f'_c}$	$2.5\sqrt{f'_c}$	$1.25\sqrt{f'_c}$
τ_{\max} (MPa)	$0.15\tau_{\max}$		$0.40\tau_{\max}$	

Table 2.4: Bond strength values proposed by various researchers [95]

Bond strength values proposed by various researchers

Various researchers have suggested different values of bond strength for different bond and confinement conditions in normal strength concrete. The peak and average bond strength for moderately confined steel which remains in the elastic range was determined by [94] to be $2.5\sqrt{f'_c}$ and $1.8\sqrt{f'_c}$, respectively. An average bond strength of $0.4\sqrt{f'_c}$ was suggested by [93] for yielded steel. Lehman and Moehle [96] and Sezen [97] used the values $1.0\sqrt{f'_c}$ of and $0.5\sqrt{f'_c}$ for elastic and yield bond strength. [95] Recommends the bond strength values of $1.0\sqrt{f'_c}$ and $1.25\sqrt{f'_c}$ for unconfined and confined respectively in poor bond conditions. These values are doubled in good bond conditions.

Macro model

Various analytical models have been developed over the years to represent the interaction between the steel and concrete subjected to tensile load. Ostani and Sozen [99] presented a macro-model and modelled the deformations at the ends of an RC member due to bar slip by assuming a uniform bond stress along the development length. This model is more representative of the elastic range since linear elastic behaviour of the reinforcing steel was considered. An average uniform bond stress of $u_b = 0.54 \sqrt{f_c}$ MPa was assumed for embedded bars in tension, where f_c is the concrete compressive strength. Strain in the bar was assumed to decrease linearly with embedment distance and becomes zero at the end of the development length, as shown in figure 2.40.

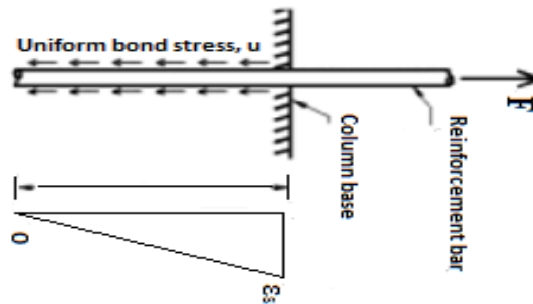


Figure 2.40: Bar stress-slip model by [99]

The equilibrium of the forces acting on the bar can be calculated using the following equation:

$$A_s f_s = u_b \pi d_b l_d \quad (2.15)$$

Using the equilibrium equation, the bar stress which can be developed because of a particular development length can be evaluated. This can be applicable to conditions when the bars do not achieve yielding and fail in splitting or pull-out. The bar stress is given by following equation:

$$\sigma_s = \frac{4u_b l_d}{d} \quad (2.16)$$

Where;

ϵ_s = Strain in the bar (elastic)

l_d = development length

u_b = bond strength

f_s = bar stress

E_s = Modulus of elasticity of steel

The slip of the reinforcing bar over development length is given by;

$$Slip = \frac{\varepsilon_s l_d}{2} = \frac{f_s l_d}{2E_s} = \frac{f_s^2 d_b}{8E_s u_b} \quad (2.17)$$

Another analytical model has also been developed by Sezen at the University of California-Berkeley [97]. The model offers efficient and reliable calculation of the reinforcement slip by assuming bi-uniform bond stress over the embedded length, which accounts for both elastic and inelastic phases of rebar. See figure 2.41.

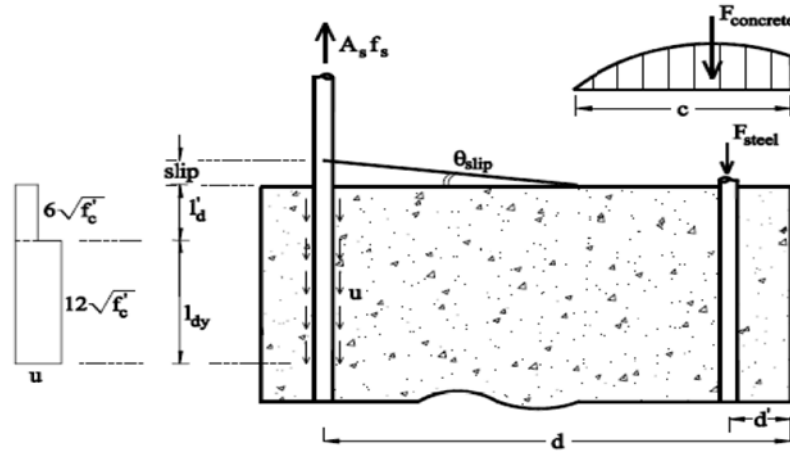


Figure 2.41: Bar slip model [97]

Following the model, the displacement can be calculated by integrating the strain over the development length.

$$Slip = \int_0^{l_d+l'_d} \varepsilon(x) dx \quad (2.18)$$

Where, l_d and l'_d are the development lengths for the elastic and plastic phases of the bar, and can be determined by:

$$l_d = \frac{f_s \cdot d_b}{4u_b} \quad , \quad l'_d = \frac{(f_s - f_y) \cdot d_b}{4u'_b} \quad (2.19) \text{ \& \ (2.20)}$$

Therefore;

$$Slip = \frac{\varepsilon_s \cdot l_d}{2} \quad \varepsilon_s \leq \varepsilon_y \quad (2.21)$$

$$Slip = \frac{\varepsilon_y \cdot l_{dy}}{2} + \frac{l'_d}{2} (\varepsilon_s + \varepsilon_y) \quad \varepsilon_s > \varepsilon_y \quad (2.22)$$

The plastic-slip equation 2.23 can be evaluated by inputting equation 2.19 and 2.20 in equation 2.22.

The mechanics behind the bond stress values go back to the work done by Alsiwat and Saatcioglu [100], in which they proposed an analytical procedure for the force deformation relationship of an embedded rebar in concrete. According to their model, the elastic development length of the bar can be calculated by:

$$l_d = \frac{f_s \cdot d_b}{4u_b} \quad \text{where} \quad u_e = \frac{f_y \cdot d_b}{4l_{d,ACI}} \quad (\text{MPa}) \quad (2.23)$$

Where $l_{d,ACI}$ is the basic development length recommended by ACI committee 408 (1979) as:

$$l_{d,ACI} = \frac{400A_s}{K\sqrt{f'_c}} \frac{f_y}{400} \quad (2.24)$$

Similar to many practical applications and as suggested by ACI committee, Alsiwat has taken the value of $K=3d_b$. Therefore, if $A_s = \pi \cdot d_b^2/4$, the uniform bond stress in the elastic phase of the bar can be determined by substituting into the above equations, and the value of u_e would be approximately equal to $0.86\sqrt{f'_c}$, which can be compared to the bond stress of $1\sqrt{f'_c}$ recommended by Sezen in his model. The same value had also been proposed by [96]. The model proposed by [100] introduces a yield plateau region beyond the elastic phase and just before entering the strain-hardening region. Since the bar has yielded in this region, large local deformations are expected, that consequently results in crushing the concrete between lugs of the reinforcement bar, and therefore, the local bond stress over yielding plateau can be estimated using the frictional bond stress. Extensive work has been done by [101] on frictional bond stress. The result of his work states that frictional bond stress is a function of surface texture and the geometry of the bar. The following expression was recommended by [101] in order to determine the frictional

bond stress. The equation takes the effect of bar geometry into account. The same magnitude of bond stress also used in the strain-hardening phase of model.

$$u_f = \left(5.5 - 0.07 \frac{S_L}{H_L}\right) \sqrt{\frac{f'_c}{27.6}} \quad (2.25)$$

Where, S_L and H_L are the clear spacing and height of reinforcement lugs respectively. The calculated bond stress in the plastic region of the bar using the above expression is of the similar order to the bond stress value proposed by [96], [97]. Figure 2.42, shows the uniaxial steel material model and the comparison of calculated reinforcing bar stress-slip relationship done by different analytical models. According to the graph, all models used the same slip equation similar to equation 2.21 upon to the yield point but with different magnitude of the average elastic bond stress u_b . Beyond the yield point the models behave slightly differently from each other, which can be reasoned as the difference in the assumption of development length and the uniform bond stress. (1 ksi = 6.895 MPa, 1 in. =25.4 mm)

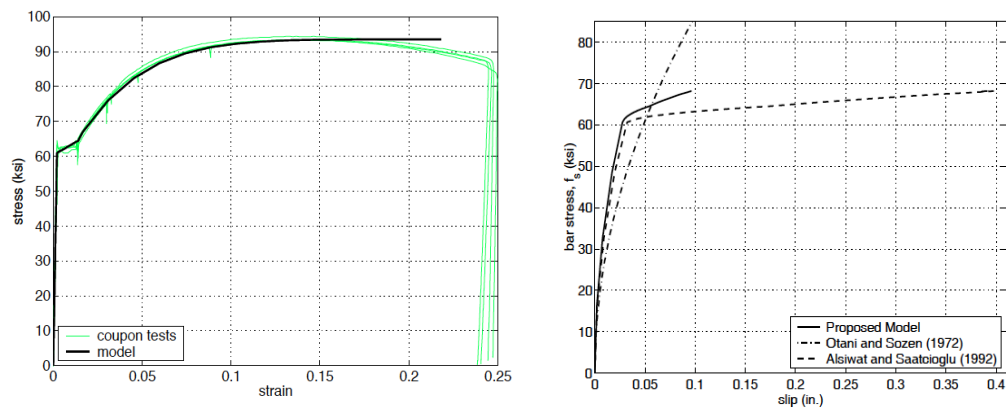


Figure 2.42: Uniaxial stress-strain relationship [52]

2.6.3.4 Bond strength at elevated temperatures

Extensive work has been carried out to investigate the bond interaction between steel reinforcement and concrete at ambient temperature (refer to section 2.6.3.3). Comparatively, only a few experiments have been conducted to investigate the bond performance under the influence of rising temperature [103]. Bazant and Kaplan [104] gathered test data from previous work on bond performance at elevated temperature. Figure 2.43 is a comparison of bond performance for different types of

steel reinforcement at elevated temperature. As can be seen from the graph, the bond strength has an inverse relationship with the increasing temperature. Furthermore, it is noticeable that ribbed/deformed bars generally result in less reduction in bond strength at elevated temperature than plain/smooth bars. However, [104] has also concluded that the experiential procedure used during these tests along with the variation in concrete cover to the reinforcement affects the bond tests at high temperature.

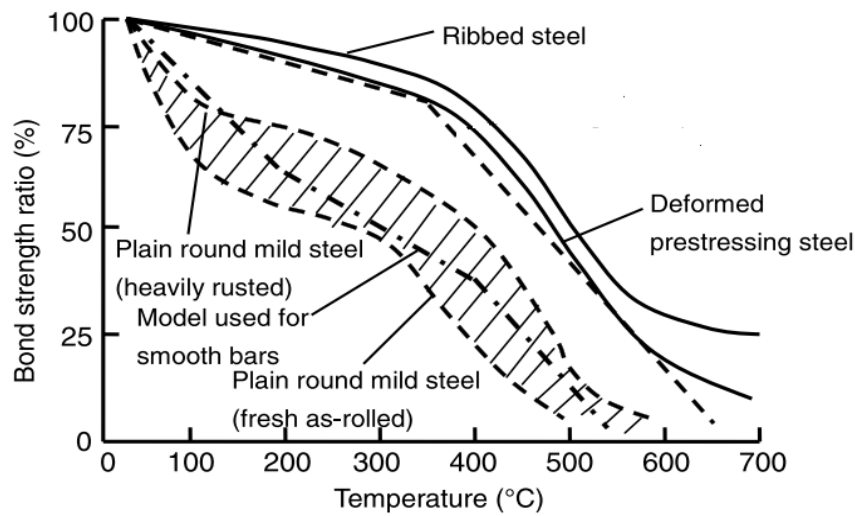


Figure 2.43: Degradation of bond strength between concrete and reinforcing steel bar at elevated temperatures [104]

The anchor point contributes to the anchorage of the steel rebar if the embedded length is not enough to develop the tensile force in the steel. In this case the anchor point works similar to a hook, so when the applied force cannot be sustained by the assumed bond stress through the embedded length, the anchor point will take part of the force [97], [102]. The force in the anchor point can be easily determined by deducting the resisted force in the elastic and inelastic regions of the embedded length (straight length) from the total applied force.

$$P_{anchor\ point} = A_s \cdot f_s - (\pi \cdot d_b \cdot l_d \cdot u_b) - (\pi \cdot d_b \cdot l'_d \cdot u'_b) \quad (2.26)$$

Therefore, it can be stated that for anchored steel rebar with insufficient embedded length, the magnitude of slip under tensile force is slightly less compared to the case of a steel rebar with sufficient development length subjected to the same level of load. This can also be reasoned due to the direct relationship between the

development length and the slip of the embedded bar as shown in equation 2.21 and equation 2.22.

2.7 Component- based composite joint model

Following the component method recommended by EC3-1.8 [55]; the composite connection includes two parts: the composite slab and the bare-steel connection (which may itself be modelled from a number of springs). In this approach the composite slab is modelled as an additional single spring element on top of the bare-steel joint, which represents the influence of the mesh reinforcement and shear studs on the overall performance of the composite joint. In this model the tensile capacity of the concrete can be neglected and it is assumed that the mesh reinforcement is the only component that resists the internal tensile force at the top of the connection. Furthermore, the effect of shear studs in the hogging moment region also needs to be considered when calculating the stiffness of the composite joint. However, further investigation of the work done by previous researchers reveals some limitations in modelling the composite joint in this way. Early work to study composite joints was conducted by Zandonini [80] and focused on developing criteria and a suitable method for design and analysis of semi-continuous composite frames. He modelled the slab as a spring in the connection in order to represent the influence of the concrete slab on the joint performance. Lee Leston-Jones [58] also modelled the composite slab as an additional spring located above a bare-steel connection. The results from his work on bare steel connections showed a close correlation with experimental data at ambient temperature but the composite joint model performed significantly differently from the test data in respect of the rate of degradation at elevated temperature [35], [58]. Da Silva et al. [59] also proposed a component model for elevated temperature which was in a good agreement with test data; however, his model was restricted to one type of bare steel connection. Following Jones' work, Spyrou [56] developed a simple component model, figure 2.44, which

was a successful representation of tension and compression zones of the connection.

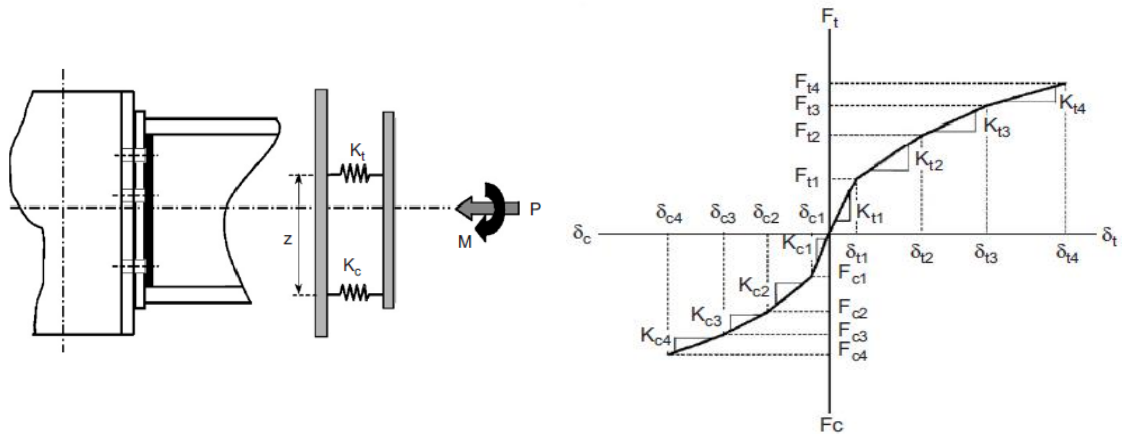


Figure 2.44: Behaviour of joint subjected to axial

His work has been further developed by Block [61] to include the bending of the column flange and the attached end plate into the component model and hence derive a more realistic response of the steel joint. Al-Jabri adopted a similar approach to model both bare steel and composite joints. These models were reasonably accurate at ambient temperature, but the rates of degradation of its components were different from the experiments and more experimental data were required to draw a positive conclusion [60].

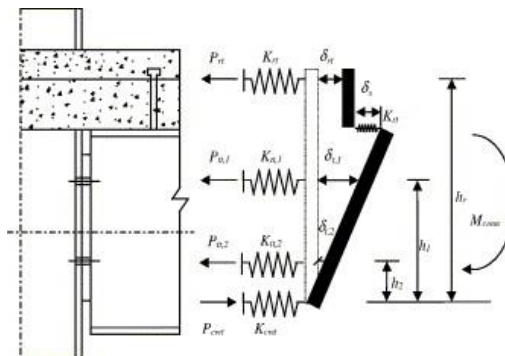


Figure 2.45: Idealised representation of composite connection component model [60]

Although the component model of a bare steel connection can be considered as a 2D model that contains a series of springs representing active components within the joint, the slab is a member which is three-dimensional in nature. Therefore, an additional spring element on a 2D joint model should accurately represent the lumped properties of the slab. The bending stiffness of the slab in hogging is a function of its cross-section, and the presence of reinforcement and shear studs must

also be accounted for in order to provide full or partial composite action. Therefore, the width of the slab over the joint plays an important role in providing the joint rotational stiffness since it determines the amount of reinforcement and number of shear studs within the section. When the composite beam deflects, the slab works as a compression flange of the beam within a certain width. In theory plane section remains plane, which means that the effect of shear strain is neglected. But in fact, the slab has some in plane flexibility, which leads to a small relative displacement between the beam and slab when the section is loaded; this small displacement is due to the “Shear lag” effect [81]. The presence of shear lag causes a variation in longitudinal stress across the section which decreases as the distance from the web increases. This would suggest gathering most of the reinforcement near to the column within the limits of practicality. In such a system the actual width of the flange is not fully effective in resisting the compression; therefore, an “Effective width” concept is used to approximately account for in plane flexibility [82]. A simple formulation to calculate the effective width is given in section 5.4.1 of Eurocode 4 for simply supported beams [83], however a recent experimental study shows that the effective width actually increases as the load increases, approaching the width of the whole slab near collapse [84]. The simple formula recommended by EC4 can be used to determine the effective width of the slab. However, the determination of effective widths in EC4 is actually based on compressive stress within the compressive flange i.e. the sagging bending moment distribution, whereas, the width of slab over the joint should be determined with respect to the applied tension and hogging bending moment. Therefore, calculation of the effective width of composite joint in the hogging region is complex. The presence of a composite slab clearly provides considerable stiffness to the rotational behaviour of a joint in ambient-temperature semi-rigid design but it is not yet established that its ductility is adequate in the robustness of composite buildings in fire. This means that the calculated effective width by EC4, which is recommended for design purposes, is not necessarily applicable in the global analysis of the structure in fire and it is certainly not appropriate for the purpose of fire safety engineering design. Furthermore, as mentioned above, all the component-based connection models, including those modelled in *Vulcan* are two dimensional, whilst the composite slab is three

dimensional. Therefore, even if a reasonable assumption can be made to determine the effective width of the composite joint, the behaviour of the slab beyond the length of the effective width and over the length of the steel beam, as well as its influence on the global behaviour of the structure, cannot be properly addressed.

In addition to the issue of determining the effective width of the slab, the limitation of the software also needs to be considered. A composite slab is currently modelled in *Vulcan* as a simply supported slab and accounts for continuity over the internal beams using a smeared crack method [65]. Therefore, even if the effective width of the slab over the joint can be determined, the problem arises as to whether the slab presence has been accounted for twice in the analysis, once as part of the joint and secondly as a three dimensional layered shell element, which accounts for continuity by using smeared cracking technique.

2.8 Conclusion

Vulcan is highly specialized software developed at the University of Sheffield and is being continuously enhanced. The software is capable of modeling geometrical non-linearity and considers non-linear material behavior at elevated temperature. The software models the slab as three-dimensional layered shell elements, which is capable of modeling membrane and bending affects. Like most of the commercial FE software, the current version of *Vulcan* also accounts for the continuity of the slab element over the length of the internal beams through the entire structure and uses smeared cracking for the purpose of analysis. The concrete slab contributes to the overall performance of the structure through its composite action with the joint and connected steel beams in resisting the joint's horizontal and rotational movements. Therefore, any reasonable modelling of crack development over the steel beams becomes essential in order to investigate the influence of the slab continuity on the overall performance of the composite structures especially over the connection zone. The development of pre-defined crack patterns in the concrete slab has been characterised using a new element, so-called "Break Element"

Chapter 3

3. Methodology

3.1 Bare steel connection with 3D slab shell element

Unlike using the component-based method to consider the influence of slab ductility on the overall performance of the structure (as described in section 2.7), the presented approach incorporates the technical advantages offered by *Vulcan* software. As mentioned before, the software represents a composite slab as a three-dimensional layered shell element with different temperatures for each layer to model the temperature distribution through the slab thickness. Furthermore, different types of beam to column connections can be modelled with acceptable level of accuracy using an EC3-based method.

The main idea behind this approach is to produce a simplified model of the behaviour of the composite slab within the tension area, which represents the continuing concrete slab and its reinforcement in modelling the beam-to-column and beam-to-beam connections. In order to avoid the limitations of the component-based approach, the new approach suggests the composite joint may be modelled using the existing two-dimensional component-based model for the bare steel connection along with the 3D slab shell element resting on top of it and connected to the beam with link elements representing shear studs. With this method the limitations from the first approach can be overcome since the effect of the concrete slab will be applied to the joint directly, not as a single spring element with certain mechanical characteristics but as a three-dimensional layered shell element. Therefore, working out the effective width of the slab and the assumption of slab continuity are no longer issues. As mentioned in the literature, the stiffness of a composite slab is a function of its tensile strength rather than the bending stiffness. The top surface of the slab around its perimeter is mainly subjected to tensile forces resulting from vertical deflection at the slab centre, the restrained thermal elongation of the edge beams and the adjacent cool structure. The concrete slab on top of the steel beams is under axial tension/compression forces. Of course it is not easy to say where on the slab is in

tension, compression or both since the stress is non-uniformly distributed in transverse and longitudinal directions. Furthermore, the distribution of tensile and compressive force on the slab is greatly influenced by the support conditions around the edge. As stated before, the tensile force resulting from hogging bending moments causes failure of the slab around its edge by cracking of the concrete followed by fracture of the mesh reinforcement. Concrete in tension is limited by its low tensile strength, once the concrete in the composite slab reaches its tensile strength, the concrete cracks and the stiffness of the slab is reduced. The concrete slab contributes to the overall performance of the structure through its composite action with the joint and connected steel beams with respect to the joint's horizontal and rotational movements. Therefore, reasonable modelling of the crack development over the steel beams becomes essential in order to investigate the influence of the concrete slab on the overall performance of the composite joint.

Adopting this approach, the development of pre-defined crack patterns (as a result of maximum hogging bending moments on top of the steel beams) in the concrete slab will be characterised with a new spring a so-called "Break Element". The new element will be placed and used to connect the slab panels across the length of internal beams on the column grid, which is initially assumed to be the location where the cracks occur. Since the concrete slab and the steel beams beneath it are assumed to act fully compositely with each other, by applying this method a more realistic behaviour of the slab and its effects on the joint performance can be investigated.

3.2 Characterisation of Break Element

Using a component-based model technique each element within the joint is evaluated by its mechanical characteristics. The moment-rotation curve is then a function of the force-displacement response of the components and its accuracy is greatly influenced by the quality of the characteristics of the load-deformation behaviour of each component [32]. Therefore, in order to investigate the influence of the concrete slab on the joint performance the new "Break Element", which in fact is the representation of the crack development in the slab, needs to be characterised by the force-deformation behaviour of a reinforced concrete section cracking under pure

tension. The first step to characterising the new element is to understand how exactly a crack behaves in a composite slab. As mentioned before, considering the effect of the steel beams around the perimeter, the composite slab is tensioned as a result of hogging bending moments due to horizontal restraint along with the large deflection arising from tensile membrane action [72], [87]. At ambient temperature when an RC slab is under tension, cracking of the section causes a reduction in the stiffness of the slab but even after the crack occurs the adjacent uncracked concrete segments tends to regain a certain level of stiffness that is beyond the theoretical value for a cracked concrete slab. This is usually called “tension stiffening” [88]. The cracking behaviour is very dependent upon the available reinforcement in the slab. The tension stiffening effect is quite pronounced for an RC member with a large reinforcement ratio. After the first crack occurs the applied force carried by the rebar will be transferred to the concrete through bond between the steel and concrete and causes the second crack. But a concrete slab with a low reinforcement ratio (composite slab) behaves in a different manner. Stadler proposed a simplified model for the cracking behaviour of a reinforced section in his doctoral thesis [77], which is based on the work done by Diaz et al [89]. Figure 3.1 represents the behaviour of a lightly reinforced member. As can be seen, the first crack occurs when the concrete reaches its tensile strength after which the total force has to be carried by the light rebar inside; but since the section is lightly reinforced the rebar has a lower load capacity than the force that was required to induce the first crack. So the reinforcement in the crack is unable to transfer enough force into the concrete in order to induce a second crack. Therefore, just one discrete crack occurs in the section before the reinforcement in the crack yields and finally ruptures at its ultimate strength.

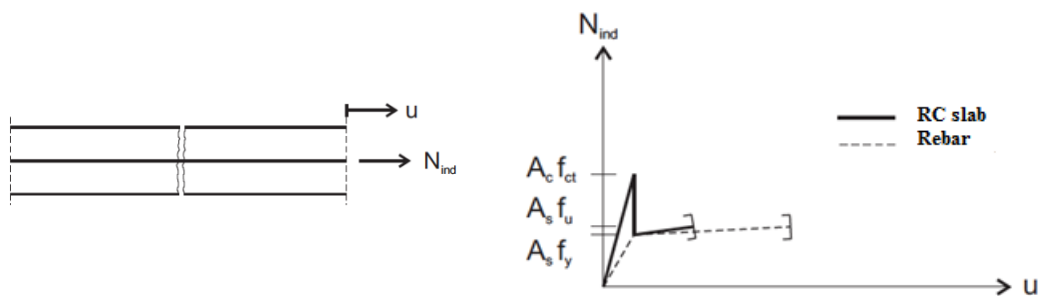


Figure 3.1: Idealised representation of composite connection component model [60]

The top surface of a composite slab around its edge and over the supporting steel beams is subjected to tensile force at elevated temperatures. This is due to the generated hogging bending moment at the edge of the slab as a result of large vertical deflection at the centre of composite slab; therefore, a transverse crack occurs on the tension surface of the slab. Additionally, as previously discussed a slab incorporating low reinforcement ratio can only develop one single crack as a result of direct tensile force within the tensioned area. This behaviour is in fact analogous to the real pull-out test of a reinforced concrete section. In this condition the embedded rebar in the concrete is subjected to axial tensile force that can fail in one of two ways: pull-out failure or splitting failure. Accordingly, it is possible to investigate the whole process of crack development in the slab by accurate modelling of the pull-out effect in RC members.

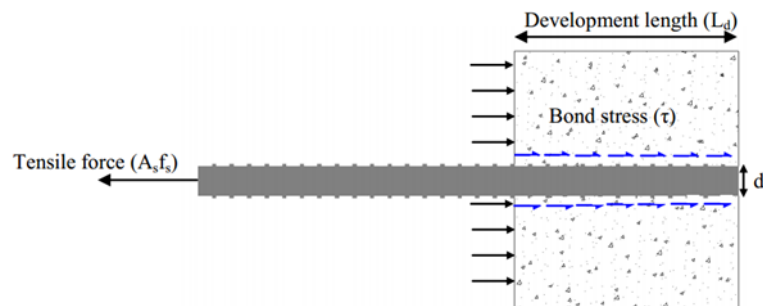


Figure 3.2: Transfer of tensile forces through bond stresses

3.2.1 The effects of shear bond interaction

In a reinforced concrete section subjected to a tensile force, accumulated strain over the embedded length of the rebar results in relative displacement between the concrete and the rebar. The bond interactions between the steel and concrete develop due to the direct application of the tensile force to the free end of a rebar surrounded by concrete. The bond stresses need to develop under two main conditions: either in the presence of anchorage, where the rebars are terminated, or when a variation in bending moment is experienced along the member leading to a change of force along the length of rebar. At the same time it is necessary for the bond to maintain the

contact between the steel and concrete at the cracks permitting “tension stiffening” to occur.

Bond-slip model: in order to consider the effects of shear bond stress on the crack development in a composite slab, the analytical bond-slip model by Sezen [97] was assigned to the newly developed break element to represent the bond interaction between the concrete and the embedded rebar and its influence on the accumulative strain of the rebar at the crack face. The selected analytical model has been discussed in detail in chapter 2.

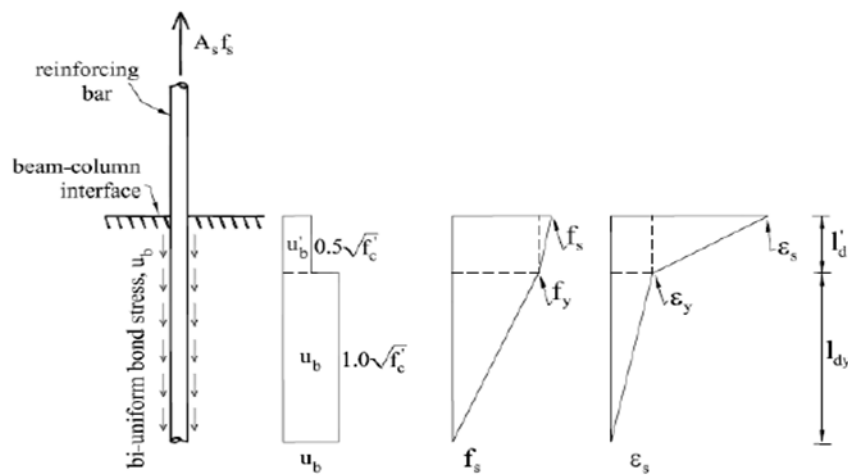


Figure 3.3: Bar slip model [97]

The model offers efficient and reliable calculation of the reinforcement slip by assuming bi-uniform bond stress over the embedded length, which accounts for both elastic and inelastic phases of rebar.

$$Slip = \frac{f_y^2 d_b}{8E_s u_b} + \frac{(f_s - f_y) f_y d_b}{4u'_b E_s} + \frac{(f_s - f_y)^2 d_b}{8u'_b E_h} \quad (3.1)$$

u_b and u'_b are the uniform bond stress for elastic and plastic portion of the bar and approximated as $1\sqrt{f'_c}$ and $0.5\sqrt{f'_c}$ (MPa)). It should be noted that in the proposed break-element model the distance between the predefined crack and the first anchor point (the point that longitudinal and transverse reinforcement are welded to each other) limits the development length l_d for the assumed bond stress.

3.2.2 The effects of temperature

Steel reinforcement: Based on these previous experimental investigations (refer to section 2.6.2), it can be stated that the mechanical properties of steel reinforcement in the composite slab is not influenced by fire as the temperatures in the mesh reinforcement never exceed the limit recommended by the EC2 [90]. Therefore, characterisation of the new element “Break Element” can be based on the assumption that the material properties of the mesh reinforcement close to the top surface of slab are not significantly influenced by rising temperature; hence the degradation in strength of the steel reinforcement can be neglected in the development of the new element.

Concrete: As discussed in section 2.6.3, the characteristic strength of concrete is important for the purpose of modelling the crack in a composite slab since it directly influences the quality of shear bond between concrete and rebar. The influence of reduced concrete strength at elevated temperature on the bond-slip model for the embedded rebar is considered in the following section. As the empirical equation to determine the uniform bond stress is a function of concrete strength, therefore the characteristic strength of concrete at ambient temperature can be easily replaced by its reduced value at elevated temperature, which consequently results in the reduction of available bond between steel and concrete. In the current model for crack development, the effect of increasing temperature on the bond quality has been taken into account by applying the appropriate retention factor to the characteristic compressive strength variable in the slip equation.

3.3 Development of 2D Break Element

In nonlinear analysis the basic problem is to find the equilibrium states of a body corresponding to the applied loads i.e. a balance between the externally applied loads and the internal stress-related forces. Due to the non-linearity, the initial stiffness of the structure used to generate the deformation and resulting internal forces results in a set of forces which are not in equilibrium with the applied loads; unbalanced forces are generated and an increment in the nodal point displacements is required. This

update of the nodal displacements in the iteration continues until the unbalanced forces are negligible. This response is calculated by the governing finite element equations:

$$(K_L + K_{NL}).\Delta U = R - F \quad (3.2)$$

Where,

K_L is the linear-strain incremental stiffness matrix

K_{NL} is the nonlinear-strain incremental stiffness matrix

ΔU is the vector of increments in the nodal point displacements

R is the vector of externally applied nodal point loads at time $t + \Delta t$

F is the vector of nodal point forces equivalent to the element stresses at time t

As discussed above, the iterative analysis is a way of solving nonlinear problems. The most frequently used iteration scheme is the Newton-Raphson method, in which a new tangent stiffness matrix is calculated and updated for each iteration. It is evident that, if the tangent stiffness matrix does not change sharply, and if the current result is sufficiently close to the solution, convergence can be obtained rapidly. Normally, in order to reach convergence more easily the primary process is to decrease the magnitude of the load step. This is based on using an exact tangent stiffness matrix. The correct stiffness matrix will result in lower numbers of iterations before convergence is reached. Hence, its calculation plays an important part in FEM. In *Vulcan*, the Newton-Raphson method is applied as the iteration scheme for the solution of the nonlinear finite element equations.

3.3.1 *Vulcan* Programming

As discussed in chapter 2, for composite floor system analysis in *Vulcan*, it is assumed that the nodes of the elements representing concrete slabs and steel beams are defined as lying in a common reference plane, which is assumed to coincide with the mid-surface of the concrete slab shell element as shown in figure 3.4. The concentric circle represents the break element, where the two nodes of the element are located at far ends of the outer circle. The break element is used to connect the slab elements around its edge to the adjacent steel beams; therefore, the nodes of the

new element are also defined at the common reference plane. However, the position of the reference plane can be adjusted in the input file of the program, so the behaviour of the crack along the depth of the composite slab can be investigated.

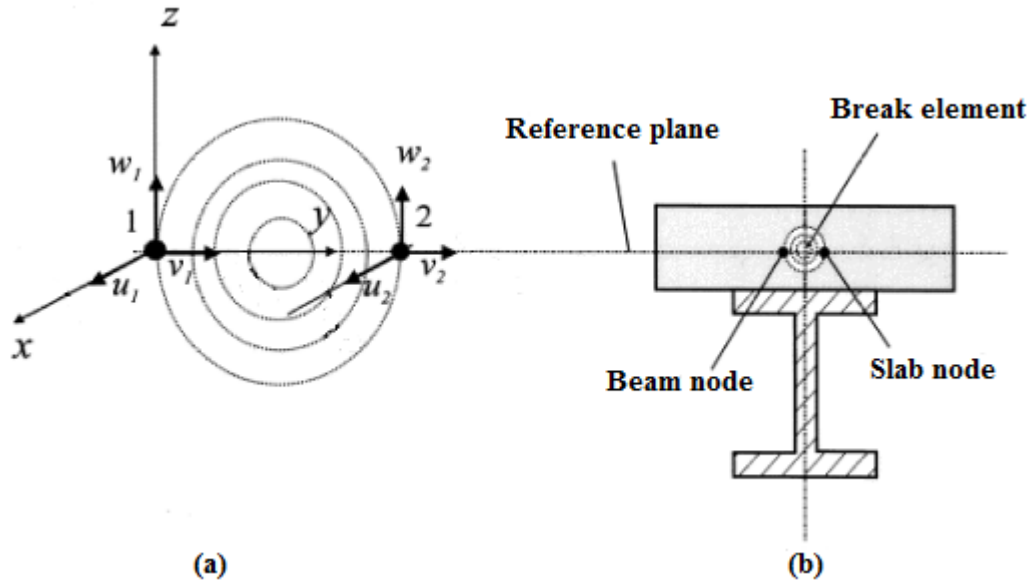


Figure 3.4: Element arrangement in *Vulcan*

In *Vulcan*, the concrete slabs are modelled as an assemblage of finite plate elements, which are of the quadrilateral nine-noded high-order isoparametric element type described by Huang [65]. Slab elements are divided into several layers representing concrete and reinforcement mesh. In the context of this layered approach several assumptions have been made as follows:

- Slab elements are considered to consist of plane concrete layers and steel reinforcement layers, without slip between them.
- Reinforcement steel bars in the orthogonal mesh directions are modelled by equivalent smeared steel layers with uniaxial stiffnesses in the directions of the reinforcing bars. The cross-section of the reinforcing steel layer is equal to the total area of rebar in the appropriate direction. In addition, the bond between the steel layers and the concrete surrounding them is assumed to be perfect.
- The temperature of individual layers can differ, but must be uniform within each layer of an element.

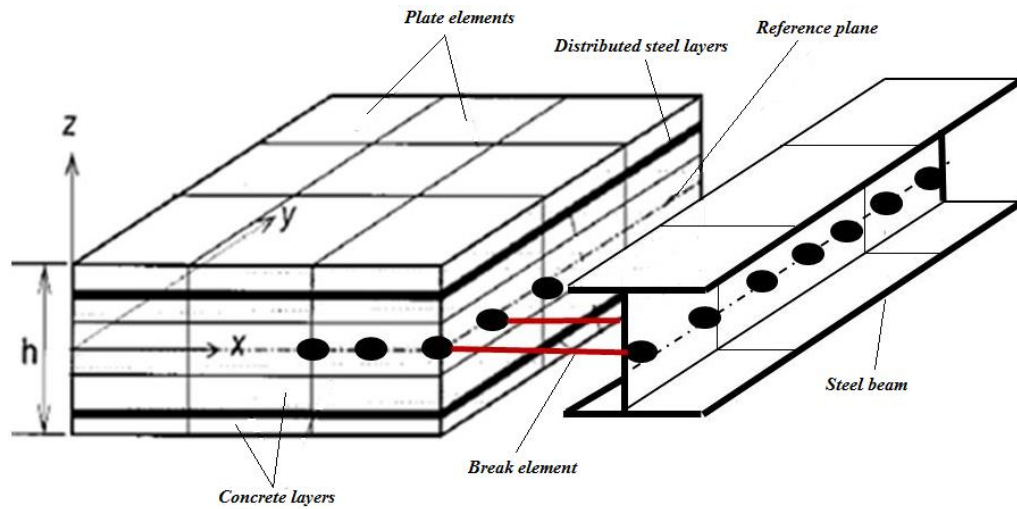


Figure 3.5: 3-D representation of floor compartments in *Vulcan*

Figure 3.5 shows the schematic three-dimensional arrangement of a typical floor system compartment in *Vulcan*. The system includes 9-noded layered slab shell elements, 3-noded beam line elements and the 2-noded break elements. As mentioned before, the break element connects the slab perimeter nodes to their adjacent steel beam nodes around the edges of the composite slab floor area. It should be noted that the position of the reference plane in the software *Vulcan* can vary according to the user preference, this gives the advantage of investigating the behaviour of the crack development (using the break element) through the depth of the concrete slab floor area. Break elements may be located across the floor area and at the perimeter nodes of every slab element across the slab area representing defined lengths of the floor slab at its edge. The break elements connecting to the mid-node of the slab elements to the adjacent beam represent half the length of the slab in that particular direction, the corner break elements represent a quarter of the slab length, and the common break elements between the adjacent slab elements represent the accumulated length of the slab elements at their corners. Figure 3.6 shows divisions of the typical slab element area corresponding to the corner and the mid length break elements. This enables a more accurate investigation of crack development within a slab panel. Once concrete at the top surface cracks following fracture of break elements, a dynamic solver can temporarily be activated to search for the next re-stabilization. After re-stabilizing, the analysis continues using a static solver [74].

Figure 3.7 illustrates typical layouts of composite floor structure modelled in *Vulcan*, with break elements between slab and beam nodes.

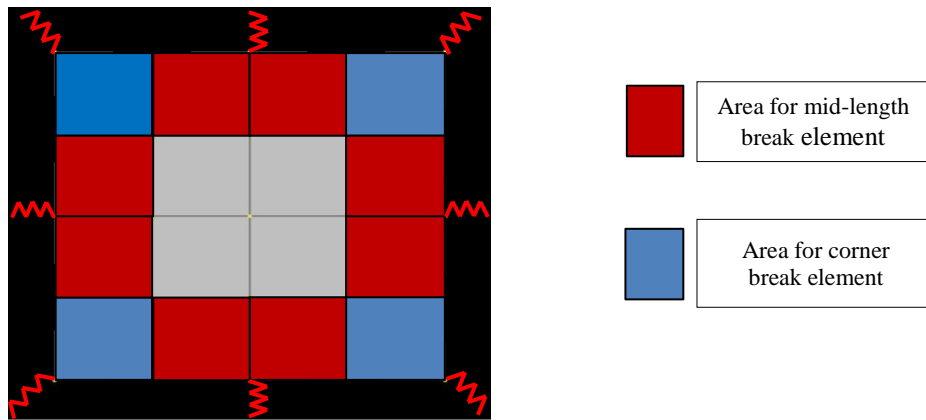
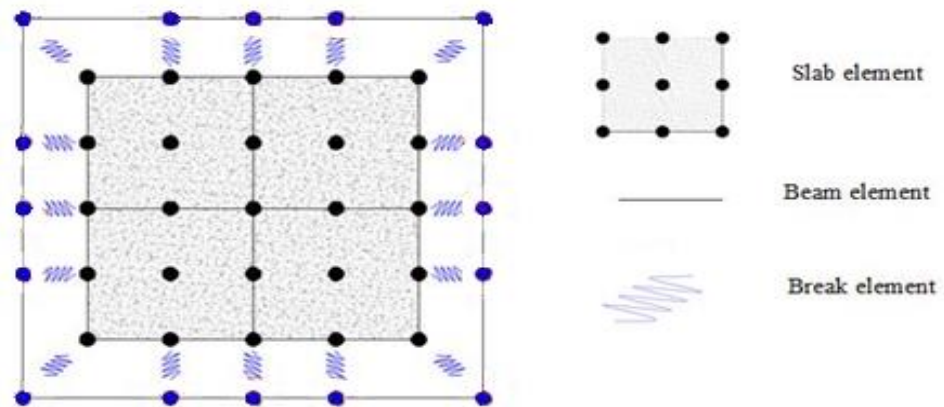


Figure 3.6: Corresponding slab area for individual break element in *Vulcan*



(a)

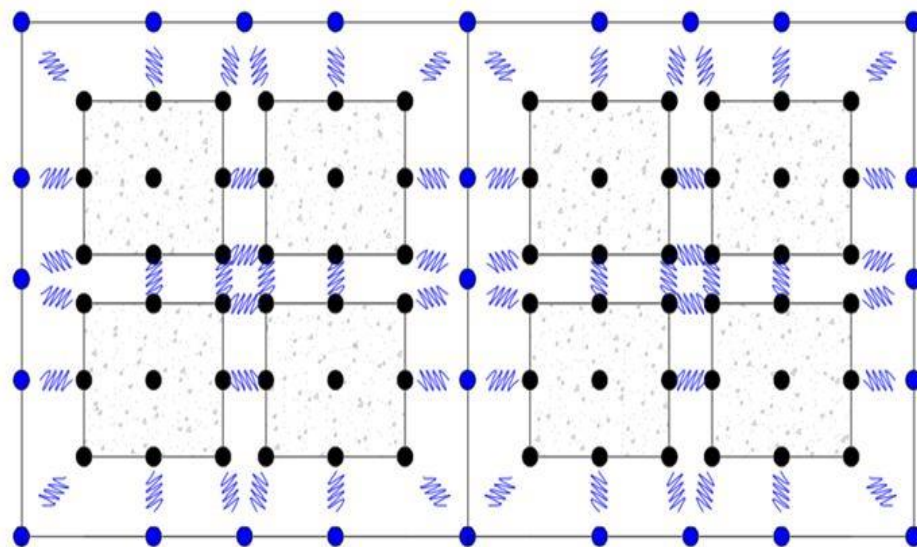


Figure 3.7: Elemental arrangement- *Vulcan*

3.3.2 Force-Displacement Relationship

The new element has been implemented in *Vulcan* with a multi-linear force-deformation characteristic. The first part of the curve represents an un-cracked concrete section with negligible relative displacement. As mentioned in chapter 2, *Vulcan* software uses a smeared cracking approach in order to account for the micro-cracking within the slab area [105]. Using this technique makes it possible to identify the tensile failure of the concrete material at different layers of the slab shell element. Tensile failure of concrete in the break element is assumed, once the concrete layers just above and below the mesh reinforcement layer (depending on the position of the reinforcement layers) within the slab shell element has been cracked. The second (elastic) phase starts as soon as concrete has cracked across the depth of the slab. Beyond this point, the shear bond interaction between the steel reinforcement and concrete is the influencing factor that regulates the crack behaviour. The third phase is the plastic region where the embedded rebar is yielded and a reduced shear bond has been applied. The final part of the characteristic introduces the failure criterion for the break element, at which the ultimate strain of the assumed reinforcement is reached. Figure 3.8 is a multi-linear schematic representation of the force-displacement relationship.

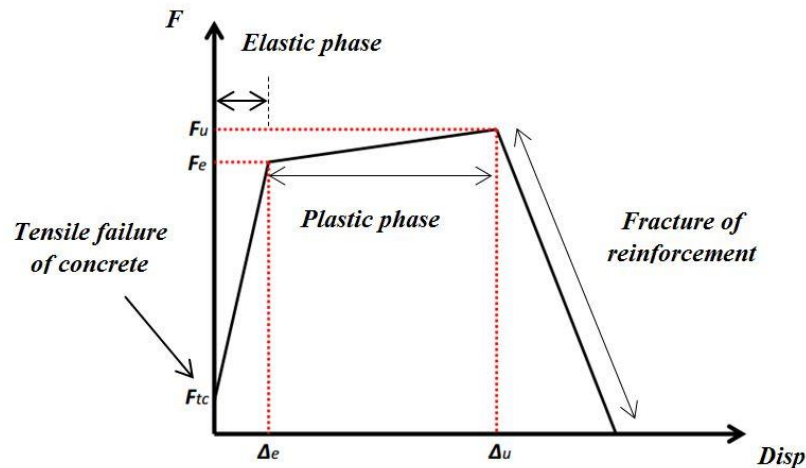


Figure 3.8: Multi-linear force-displacement relationship – break element

The magnitude of the different characteristics in the force-displacement relationship i.e. yield stress (f_y), ultimate stress (f_u), yield strain (ϵ_y) and ultimate strain (ϵ_u) level, are model dependant, therefore, the magnitudes of the force-displacement behaviour

in the break element is a function of the steel and concrete material properties. These material properties are user-defined within the input file of the *Vulcan* program.

3.3.3 Stiffness Matrix

The break element shown in Fig 3.4 is implemented in *Vulcan* as a specialized two-noded element of infinitesimally small length, which has three translational degrees of freedom u , v , w and three rotational degrees of freedom θ_x , θ_y , θ_z at each node. Beyond the cracking of concrete in tension, the axial stiffness coefficient of the element at the longitudinal direction of the break element (k_1 or k_2 for the x and y direction respectively) is obtained by dividing the applied force at the reinforcement level (break element) over the calculated slip from the bond-slip relationship model proposed by [97], [98], [100] in equation 2.21 and 2.22. The horizontal stiffness in the transverse direction to the element as well as the vertical shear stiffness k_3 is obtained from the cross section properties of the equivalent level of mesh reinforcement at the crack face.

$$k_3 = \frac{12E\pi r^4}{L^3} \quad (3.3)$$

The break element is assumed to be fairly rigid before the appearance of the crack at the top surface of the concrete floor with stiffness similar to that of the adjacent uncracked slab element. Once the crack in the concrete has been picked by the software, it is still reasonable to assume that the two nodes of the element, which are in fact connecting the concrete slab and steel beam element together, have identical rotation around x and y directions while the concrete section at two sides of the crack face are still in contact (figure 3.9). In this case k_4 , k_5 and k_6 , which represent the rotational stiffness of the new element around x , y and z direction respectively are assumed to have infinite magnitude. Once the bottom contact of the crack faces disappears, the rotational stiffness is obtained by multiplying the lateral stiffness and the lever arm.

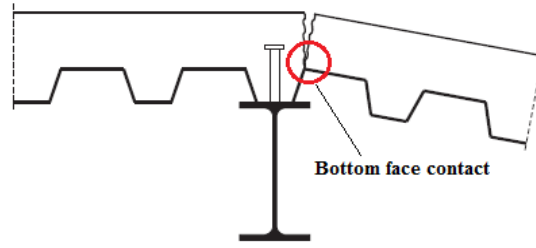


Figure 3.9: Possible crack location & bottom face contact

In order to simplify the analysis it is also assumed that there is not coupling of effects due to different degrees of freedom for the break element. This means that the force and its related nodal displacement in each direction of the break element are only influenced by the stiffness and displacement related to that particular degree of freedom respectively. This method has been effectively used in the previous developments of *Vulcan* software to model other types of two nodes elements [103], [106]. Therefore, in local co-ordinates, the nodal force can be related to its nodal deformation using the equation below:

$$\Delta F_i = k_i \cdot \Delta U_i \quad (3.4)$$

Figure 3.10 represents the increment of internal force ΔF_i for each degree of freedom related to the increment of slip, ΔU_i by the tangent stiffness relationship.

$$\begin{Bmatrix} \Delta F_{x,1} \\ \Delta F_{y,1} \\ \Delta F_{z,1} \\ \Delta M_{x,1} \\ \Delta M_{y,1} \\ \Delta M_{z,1} \\ \Delta F_{x,2} \\ \Delta F_{y,2} \\ \Delta F_{z,2} \\ \Delta M_{x,2} \\ \Delta M_{y,2} \\ \Delta M_{z,2} \end{Bmatrix} = \begin{bmatrix} k_1 & 0 & 0 & 0 & 0 & 0 & -k_1 & 0 & 0 & 0 & 0 & 0 \\ 0 & k_2 & 0 & 0 & 0 & 0 & 0 & -k_2 & 0 & 0 & 0 & 0 \\ 0 & 0 & k_3 & 0 & 0 & 0 & 0 & 0 & -k_3 & 0 & 0 & 0 \\ 0 & 0 & 0 & k_4 & 0 & 0 & 0 & 0 & 0 & -k_4 & 0 & 0 \\ 0 & 0 & 0 & 0 & k_5 & 0 & 0 & 0 & 0 & 0 & -k_5 & 0 \\ 0 & 0 & 0 & 0 & 0 & k_6 & 0 & 0 & 0 & 0 & 0 & -k_6 \\ -k_1 & 0 & 0 & 0 & 0 & 0 & k_1 & 0 & 0 & 0 & 0 & 0 \\ 0 & -k_2 & 0 & 0 & 0 & 0 & 0 & k_2 & 0 & 0 & 0 & 0 \\ 0 & 0 & -k_3 & 0 & 0 & 0 & 0 & 0 & k_3 & 0 & 0 & 0 \\ 0 & 0 & 0 & -k_4 & 0 & 0 & 0 & 0 & 0 & k_4 & 0 & 0 \\ 0 & 0 & 0 & 0 & -k_5 & 0 & 0 & 0 & 0 & 0 & k_5 & 0 \\ 0 & 0 & 0 & 0 & 0 & -k_6 & 0 & 0 & 0 & 0 & 0 & k_6 \end{bmatrix} \begin{Bmatrix} \Delta u_1 \\ \Delta v_1 \\ \Delta w_1 \\ \Delta \theta_{x,1} \\ \Delta \theta_{y,1} \\ \Delta \theta_{z,1} \\ \Delta u_2 \\ \Delta v_2 \\ \Delta w_2 \\ \Delta \theta_{x,2} \\ \Delta \theta_{y,2} \\ \Delta \theta_{z,2} \end{Bmatrix}$$

Figure 3.10: Nodal force vector – local co-ordinates

3.4 Conclusion

Theoretical development and the elemental material properties for the newly break element was discussed in details. The new element has been successful implemented into the software Vulcan and is used in the next chapter to model some experimental work of previous researchers in order to validate the new element and determine the level of accuracy that it provides. Upon successful validation of the element a series of parametric studies is conducted to investigate the influence of the new element on the analysis.

Chapter 4

4. Numerical Modelling and Validation

Evaluating the finite element model is an essential task before any trust can be placed in the model's output or it can be decided to use the model in further studies. Therefore, wherever possible, numerical simulations should be validated against experimental results. The evaluation process for the new developed break element comprises two stages i) evaluation of the new element against a theoretical model ii) comparison of the FE model containing the new developed break element against series of experimental data from composite joint with both cantilever and cruciform test arrangements. The numerical modelling of structural elements in this study was carried out using the finite element analysis program *Vulcan*, which has been progressively developed at the University of Sheffield for some years.

4.1 Convergence and Sensitivity Study

When dealing with finite element method, appropriate element sizing (mesh density) becomes essential in order to obtain accurate results. Finer element mesh results in a more accurate behaviour especially when local effects such as discrete cracking within the slab floor area need to be studied. However, the down side of this is the longer processing analysis, therefore, finding the most efficient element sizing is essential to determine the appropriate balance point in finite element software such as *Vulcan*.

Slab element

In order to test the accuracy of using different element sizes, a 6m x 6m slab has been modelled using four different square element sizes of 3m, 1.5m, 0.5m, 0.25 m as shown in figure 4.1. All the panels were modelled using the same assumption in terms of boundary condition, temperature and dimensions. It is normally expected that the smaller element sizes result in a more accurate result but with a longer running time, therefore, the optimum solution is to have a mesh which can provides sufficiently accurate results in a reasonable time.

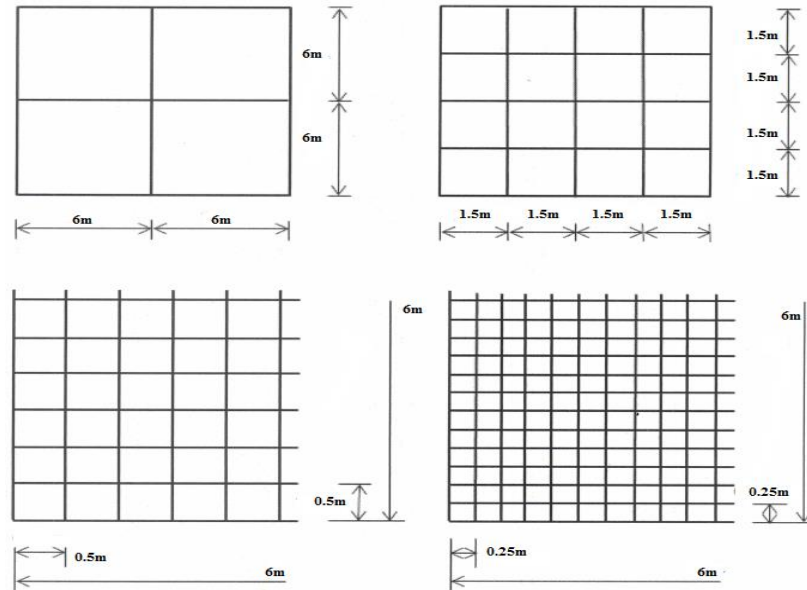


Figure 4.1: Slab panels with identical overall dimensions

Figure 4.2 illustrates the overall performance of the modelled floor slab at elevated temperature using different element sizes. As it seen from the graphs, apart from the model with the element length of 3m, the results in terms of slab central deflection for other meshes are very similar. Comparing the result of the two denser meshes it is evident that despite doubling the element sizes the difference between the resulting vertical displacements for these model are negligible, therefore, considering the computational cost and the convenience of meshing slab panel, the recommended range of element sizes to obtain accurate result within the reasonable time is between 0.5 to 1m.

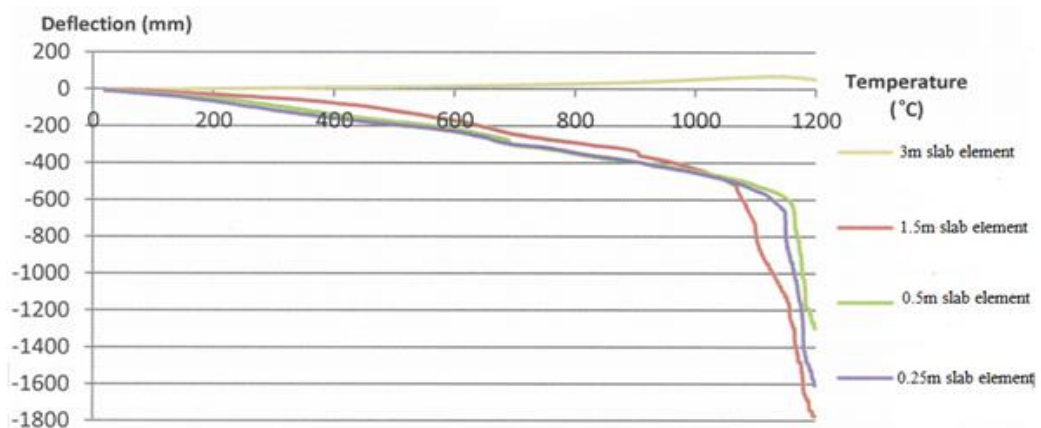


Figure 4.2: Mesh sensitivity study - slab central deflection

Break element

The accuracy of using different element sizes was studied through modelling a 6m by 9m composite panel using different numbers of 2-noded break element in *Vulcan*. As is evident the number of break element used in the model is purely depends on the mesh density of the modelled slab. Figure 4.3 shows the plan view of the modelled composite panel in *Vulcan* using different number of break elements to represent the discrete cracking across the edges of the panel.

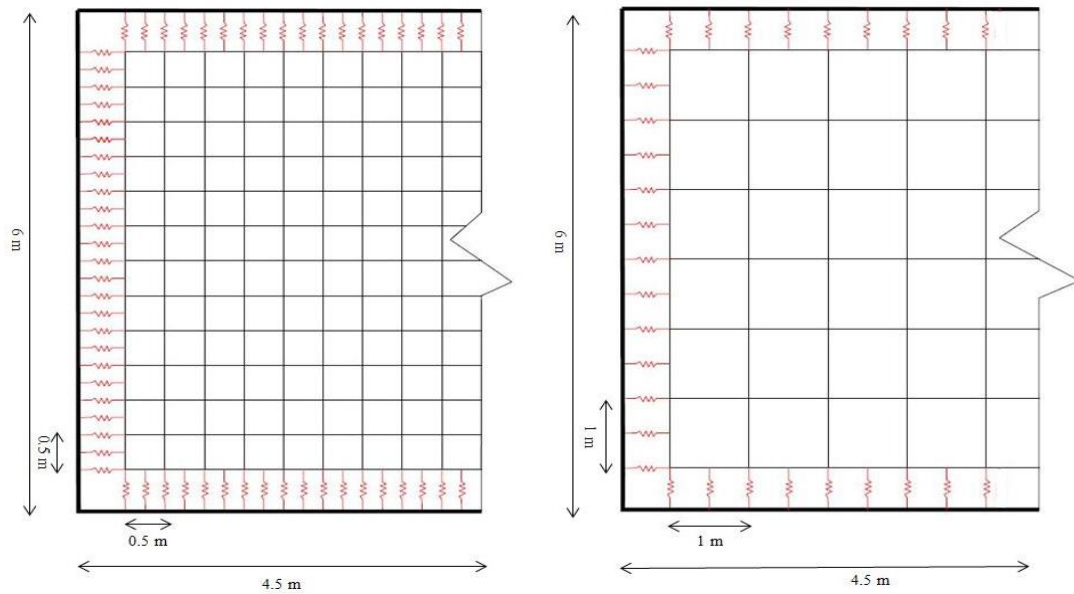


Figure 4.3: Composite lab panels with break element - identical overall dimensions

Figure 4.4 illustrates the crack development in concrete across the longer edge of the modelled composite panel using two different element sizes. The result from the analysis clearly indicates the importance of element sizing on the overall performance of the structure. The composite panel with slab element size of 0.5m results in significantly more accurate/realistic crack propagation at high temperature. As the temperature increases, a reasonable crack development can be observed in model with the finer mesh, whereas, the model with coarser slab element size of 1m shows no significant changes in the crack propagation even at high temperature of 800°C. Extra two sensitivity studies were also carried out for the same composite model using slab element sizes of 0.25m and 2m. The result from the model with finer mesh of 0.25m is very similar to that of the model with slab element size of 0.5m. No result could be obtained from the model with the coarser mesh of 2m (per slab element) as the failure of the first break element

resulted in rapid instability of the structure due to its coarse element sizes. In order to provide a reliable/realistic representation of discrete crack development in composite structures it is recommended that an individual slab element should represent at least 10% of the total length of floor area

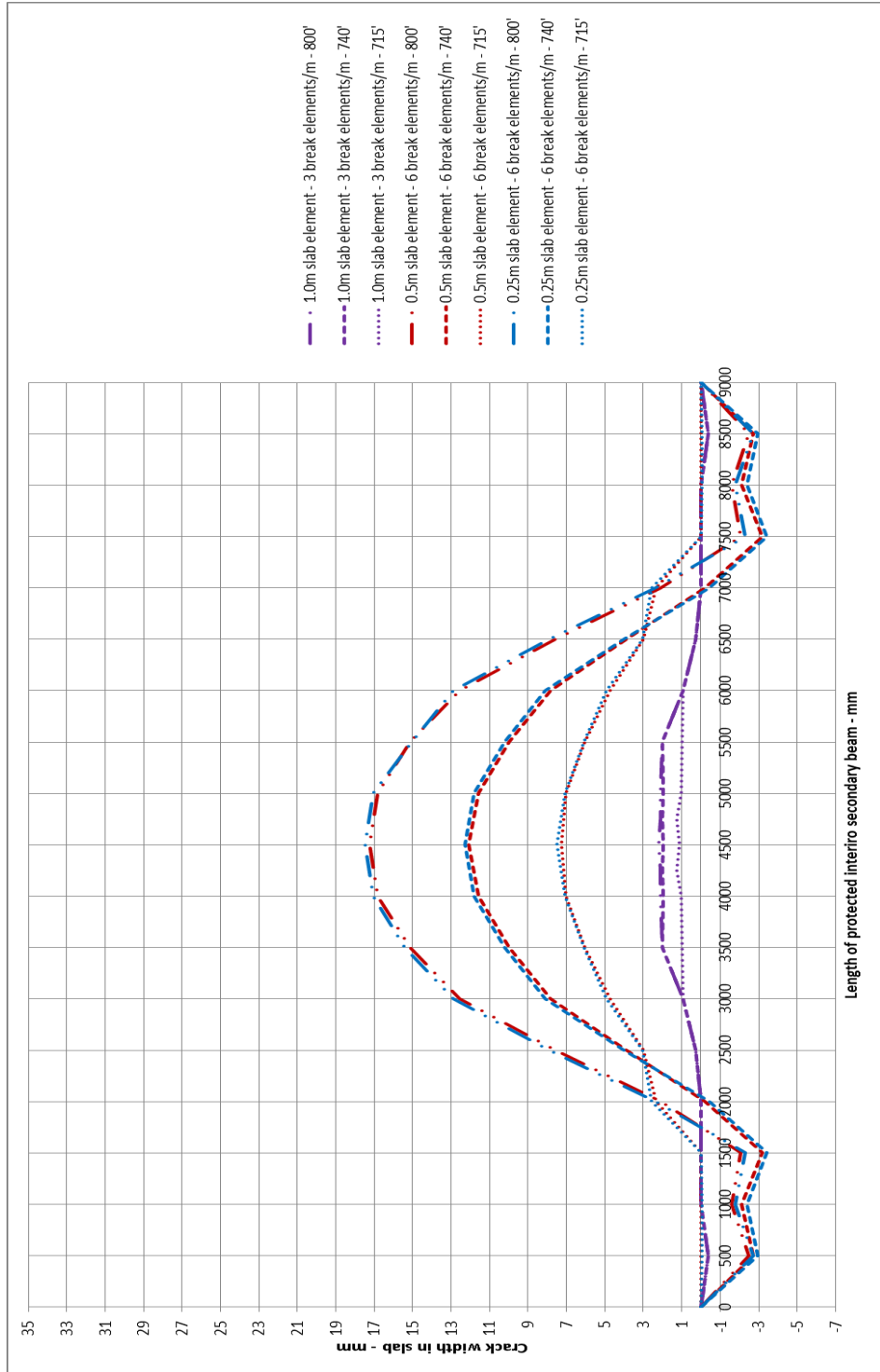


Figure 4.4: Mesh sensitivity study - slab crack development

4.2 Evaluation of Break Element against Theoretical Model

As mentioned in the previous chapter, it is possible to investigate the entire process of crack development in a slab by accurate modelling of the pull-out effect in RC members. This has been taken into account by using an analytical model developed at the University of California-Berkeley [97]. A simple evaluation of the proposed bond-slip model (see equation 3.10 and 3.11) against the implemented break element in *Vulcan* has been done. Figure 4.5 illustrates the pull-out phenomena using the theoretical and numerical models.

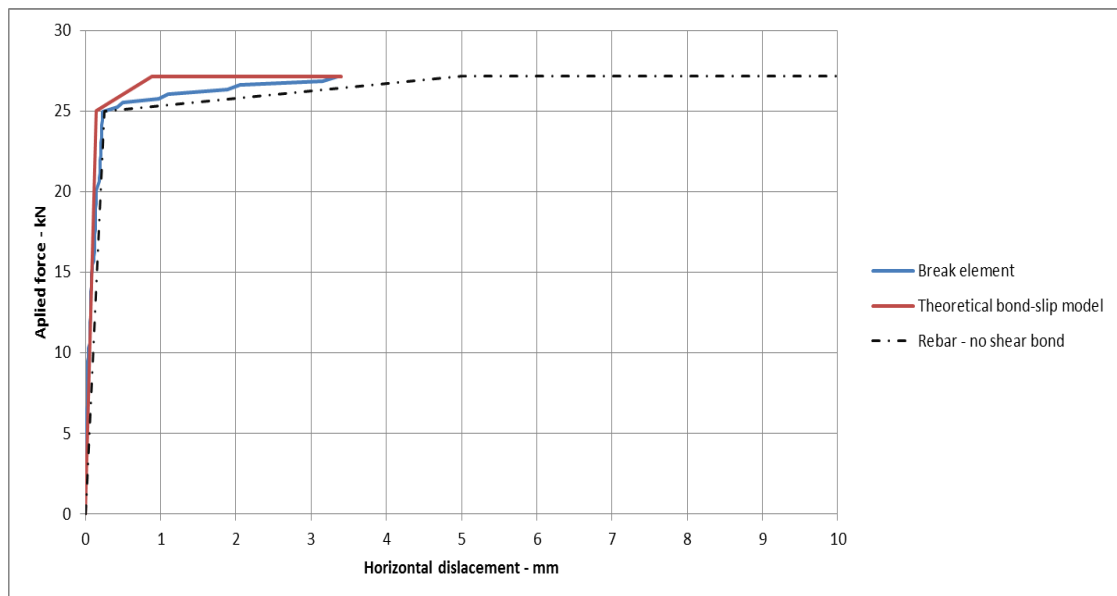


Figure 4.5: Comparison of theoretical and numerical model for lateral displacements – pull out test

A simple numerical model was created in *Vulcan*. The model represents a 10cm length of embedded rebar in concrete grade (C35) subjected to pure tensile force, with a total reinforcement area, $A_s = 50.2 \text{ mm}^2$, yield strength of $f_y = 500 \text{ N/mm}^2$ and ultimate strain of $\epsilon_u = 20\%$. It can be seen from the graph that the numerical model behaves very similarly to the theoretical model. As the applied load in the bar at the crack face passes the yield stress, the embedded length of rebar close to the crack face becomes plastic with a reduced uniform bond strength, which results in greater relative displacement of the rebar at the crack face. Since in composite slabs the embedded length of rebar is limited to the gauge length, where the longitudinal and

transverse reinforcement are welded together, therefore, termination of the test is due to the rupture of the steel reinforcement rather than pulling out of the rebar from the concrete.

4.3 Comparison of the FE model with experimental data

4.3.1 Seat Cleat Composite Joint Experiment

Davison et al. [107] conducted experiments to investigate the influence of the presence of a composite floor slab on the performance of steel beam-to-column connections. The test program included 19 tests to examine the effect of various parameters on the joint behaviour, such as deck direction, column orientation, internal or external column position, and slab reinforcement. This comprehensive experimental research forms the basis for the evaluation of the current FE model. In order to investigate the influence of the composite slab on joint, the beam-to-column connection was initially tested without the presence of the composite deck. In this way a fair comparison between the bare steel and composite joint could be made. Test S2 and C3 of Davison's experiment for bare steel and composite joint respectively were chosen to be compared with the numerical model in Vulcan. Figure 4.6 and figure 4.7 show the test arrangement for a cantilever specimen.

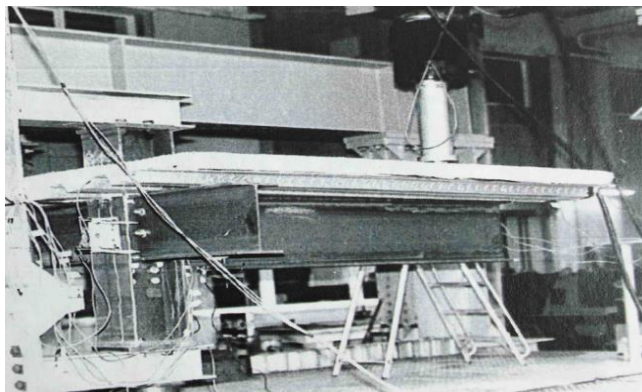


Figure 4.6: Cantilever composite joint – C3 test arrangement [107]

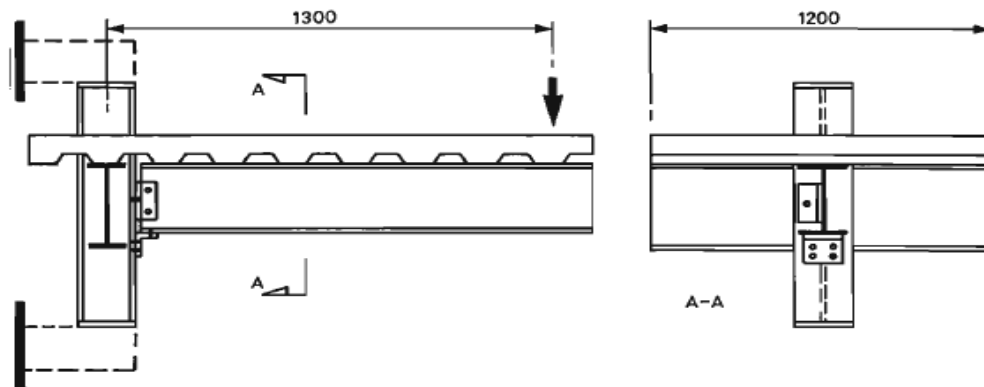


Figure 4.7: Dimensions of typical test specimen [107]

Test C3 featured a lightweight composite slab reinforced with only a single layer of A142 mesh to represent the minimum required level of reinforcement present in composite floors. The test has been conducted using 356 x 171 UB67 as the main beam, and 305 x 165 UB46 as the stub, with a slab depth of 120mm and a metal deck of 1.2mm thickness running perpendicular to the direction of the cantilever beam. The joint arrangement details are shown in table 4.1.

Main Beam	356 x 171 UB67
Stub Beam	305 x 165 UB46
Column	203 x 203 UB46
Dimension	1300 x 1200 mm
Axis	External (major)
Deck Span (to cantilever beam)	Perpendicular
Reinforcement	A142 mesh
Ultimate Strength of Reinforcement	635 N/mm ²
Mean Concrete Compressive Strength	46.0 N/mm ²
Mean Concrete Tensile Strength	5.7 N/mm ²

Table 4.1: Joint details – test C3

4.3.1.1 Finite Element Model

A model-scale composite joint was created in *Vulcan* using an assemblage of finite elements. A quadrilateral 9-noded slab element was used to model the area of composite slab from the C3 test. In order to take the effect of rib direction into account, the effective stiffness model for a slab element [108] has been used with the

main stiffness parallel to the direction of the steel deck. The effective stiffness model is valid at ambient temperature; however, it has been found in *Vulcan* that the model also works reasonably accurately at high temperature [108].

Extensively validated three-noded line element was used to represent the cantilever/stub steel beam/column in the numerical model. The composite action between the beam and slab element is provided through the break element, which represent the shear connector and mesh reinforcement in the experiment. As mentioned in chapter two, *Vulcan* is coded/developed in *FORTTRAN* language using *Microsoft Power Station 94/95* as a compiler. This version of the compiler is old and it is no longer supported by the Microsoft development team. The main limitation of using this type of compiler was the lack of required memory space to execute the program. *Vulcan* has been developed for over 2 decades at the University of Sheffield and the current version of the Program is over forty five thousand lines of code, which is at the border line of the maximum provided memory space by the compiler. Unfortunately, adopting a new compiling platform was not possible since the new generation of *FORTTRAN* compilers are more restricted with coding regulations compared to their old versions. Therefore, the current version of the *Vulcan's* code needed to be modified/revised in order to be compatible with a new compiler but modifying the current program is a long time consuming task and requires an extensive knowledge of programming and a deep understanding of the program itself, since the code has been developed by different people over a long time. Modifying the whole code was beyond the time limit of this research. A temporary solution was to identify and remove the unnecessary parts of the code in order to free up some memory space. Thus the program has been modified and some features such as super element, bond element and a recent component based connection element [103], [110] have been removed from the program. Therefore, a predefined semi-rigid connection element is used in the numerical model, which replicates the stiffness of the actual web cleat connection between the beam and column from the test. The model was created based on the available information from the experimental data shown in table 4.1. A layer of steel reinforcement has been placed at half depth of the slab element at the reference plane to represent the meshing reinforcement. Another single layer of steel reinforcement has been placed

at the bottom of the slab shell element to present the metal deck in terms of its tensile stiffness at ambient temperature. In order to represent the crack development in the composite slab, a series of break elements has been placed over the length of the main and the stub beams, where the cracks are most likely to happen. As mentioned above, the web-cleat connection in the experiment has been modelled in *Vulcan* using a semi-rigid connection element. The rotational stiffness for the bare steel joint in the current model has been worked out from the moment-rotation curve for the bare-steel connection in test S2. Unfortunately the material properties for the mesh reinforcement have not been provided in the reporting of the experiments. Therefore, it has been decided to use the typical stress-strain curve for steel reinforcement at the time of the test. In the early 1990's it was common for the mesh reinforcement to be wire and drawn, which results in higher ultimate strength. BS8110 and BS4461 are the relevant code of practice for application of steel reinforcement. Table 4.2 shows the material properties for the wire reinforcement recommended by BS8110.

<i>Material Type</i>	<i>Yield Strength N/mm²</i>	<i>Ultimate Strength N/mm²</i>	<i>Yield Strain %</i>	<i>Ultimate Strain %</i>
Wired Rebar	600	635	0.3	5

Table 4.2: Material properties-steel reinforcement

4.3.1.2 Loading and Boundary Condition

In order to illustrate the real test condition, the nodes of the slab elements were set to be unrestrained in all DOF except for rotational movement around the z-direction (θ_z). The same arrangement applied to the nodes of the beam line elements, where the only restraint to the elements comes from the presence of a connection element and the composite action from the slab above. Also the column element set to be short, only 1m in length, and it has been assumed to be fully rigid at both at the top and the base. Denoting 0 as no-restraint and 1 as restrained, the following table summarises the boundary condition for the numerical model.

<i>DOFs</i>	<i>9-noded Slab Element</i>	<i>3-noded Beam Element</i>	<i>3-noded Column Element</i>	<i>Top/Base Column Element</i>
x y z θ_x θ_y θ_z	000001	000001	000001	111111

Table 4.3: Assumed Boundary Condition

The vertical point load of 45kN was applied at the end of the beam cantilever element through a series of fine load increments. This load is enough to generate the applied moment at the connection similar to the one recorded by the experimental moment-rotation curve of test C3.

4.3.1.3 Numerical Analysis- Experimental data

Bare-steel Joint, S2

Numerical analysis has been conducted and compared against the experimental results for the bare steel and the composite joints. Figure 4.8 illustrates the moment-rotation behaviour of the web cleat connection for the bare-steel joint. The bare steel connection from the S2 test has been represented by the existing 2-noded spring connection element in *Vulcan*, with the rotational stiffness equal to the average stiffness of the seat cleat connection from the experiment S2 (figure 4.6). Therefore, the analytical model results in a lower level of resisting moment compared to the experiment between 0 and 30mrad. Bolt slip occurred in the connection at the early stages of the test followed by an increase in rotational capacity due to the presence of the seat cleat under the bottom flange of the cantilever beam [107]. This has not been modelled.

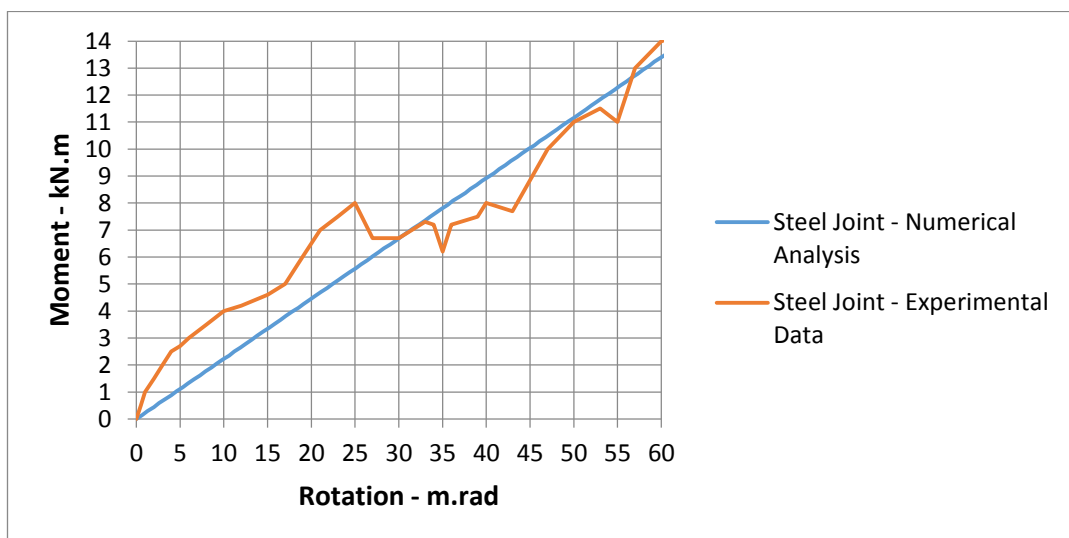


Figure 4.8: Moment-rotation curve of S2 – comparison of numerical analysis with experimental data

Composite joint, C3

The model-scale composite joint was created in *Vulcan* based on the technical specification given in table 4.1 and table 4.2. Figure 4.9 compares the rotation of the web cleat connection from experimental data with the numerical analysis. According to the experimental report, bolt slip occurred gradually with little increase in moment after the appearance of the first crack. Bolt slippage is not reflected in the numerical analyses due to the fact that a semi-rigid connection element with an average rotational stiffness was used in the model instead of a component based connection element.

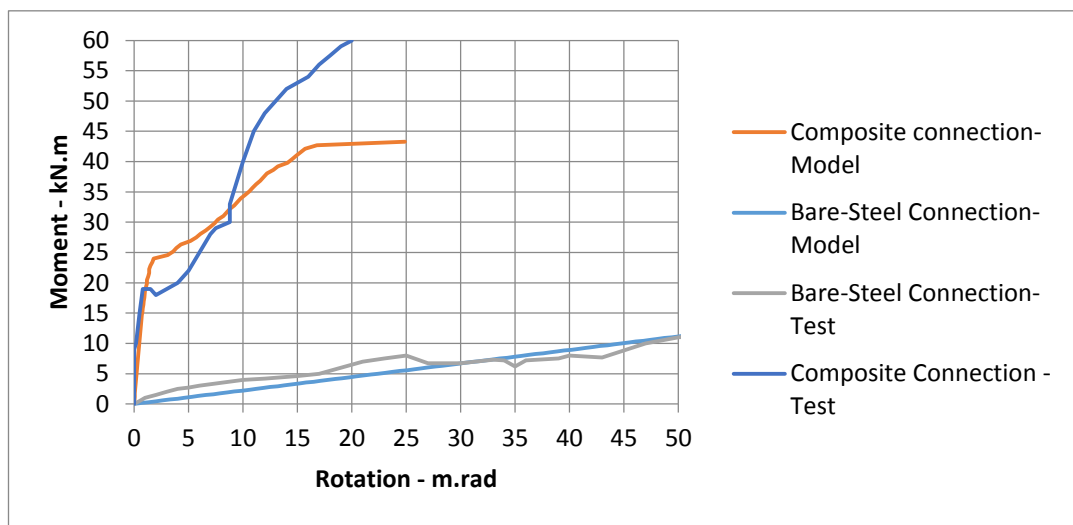


Figure 4.9: Moment-Rotation Curves of S2/C3 – comparison of test data with numerical model

It is evident from this result that the rotational displacement predicted by *Vulcan* matches the experimental data with a good level of accuracy between 0 and 15mrad. Beyond this range the numerical model starts to behave differently in comparison to the test data. This is due to the significant loss in stiffness of the slab element as a result of the concrete being cracked or crushed in both principal directions due to extensive smeared cracking. Furthermore, in *Vulcan*, the model suggested by [65] has been used to model tensile strain-softening of concrete and that results in lower tensile capacity than the model proposed by BS EN-1992: Part1. The initial cracks in the numerical model occur at an earlier stage compared to the experimental data; this results in a greater vertical displacement of the slab, since the stiffness of the slab element beyond the crack is only provided by tensile stiffness of the mesh reinforcement carrying the load. In general, it can be stated that the numerical model

incorporating the break element is capable of representing the influence of the composite slab and ductility of the mesh reinforcement on the overall performance of beam-column connection.

Crack Development, C3

Experimental data of test C3 shows the first crack to appear at the back of the column at the early stage of the loading. Figure 4.10 from [107] shows the formation of the crack in the composite slab during the test. A large crack opened across the slab at the back of the column when the moment reached 60kN.m, with a width up to 3mm.

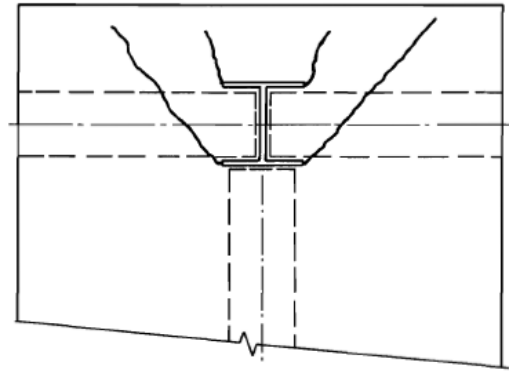


Figure 4.10: Formation of cracks around column [107]

In order to represent the initiation/development of the crack over the length of the composite slab, a series of break elements was used in the numerical model to connect the slab element to the beam where the crack is most likely to happen. The model is capable of predicting the occurrence of the initial cracks, tracing the behaviour of the mesh reinforcement represented at each break element and the sequence of the failure of the reinforcement in the composite slab. Figure 4.11 shows the plan view of the composite joint from the experimental data modelled in *Vulcan*. The FE model is the arrangement of a series of slab elements acting compositely with the cantilever/stub beams through break elements. The cantilever beam connected to the column flange using a semi-rigid connection element with the rotational stiffness of similar magnitude to the joint from test C3.

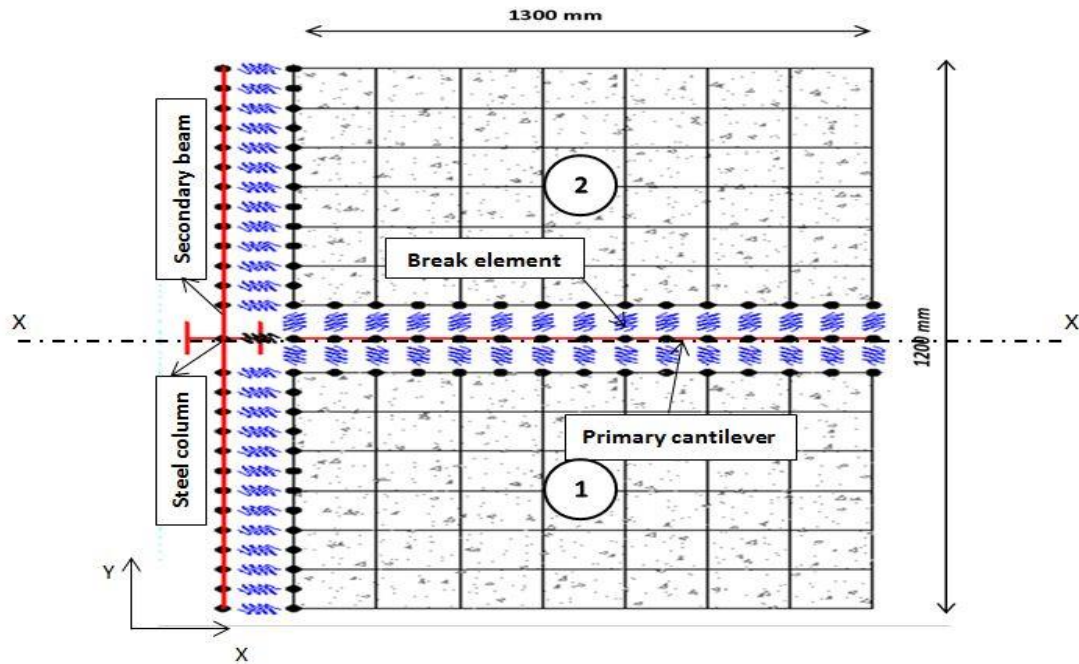


Figure 4.11: C3 composite joint – numerical model for *Vulcan*

Figures 4.12 and 4.13 are the schematic of the magnified lateral displacement of the composite slab modelled in *Vulcan* at 30kN.m and 60kN.m (half loaded and fully loaded) respectively. In order to place the break elements over the length of both stub and cantilever beams, the composite joint has to be divided into two separate parts on the right and left hand side of the cantilever beam. Figure 4.12 shows the lateral displacement of the concrete slab at both sides of the loading beam when the moment at the connection reaches 30kN.m. The numerical model shows the maximum crack width of 0.2mm close the column. The numerical model indicates that the first crack occurs at the edge of slab on both sides of the cantilever beam close to the column. The same behaviour was reported during the test C3. Based on the material properties of the reinforcement mentioned in section 4.3.2, the steel reinforcement would have an ultimate elongation of 0.27mm at an ultimate stress level of 635 N/mm^2 . Therefore, it can be seen that the mesh reinforcement is not ruptured yet and the opening of the crack width is the result of bond interaction between the embedded rebar and concrete.

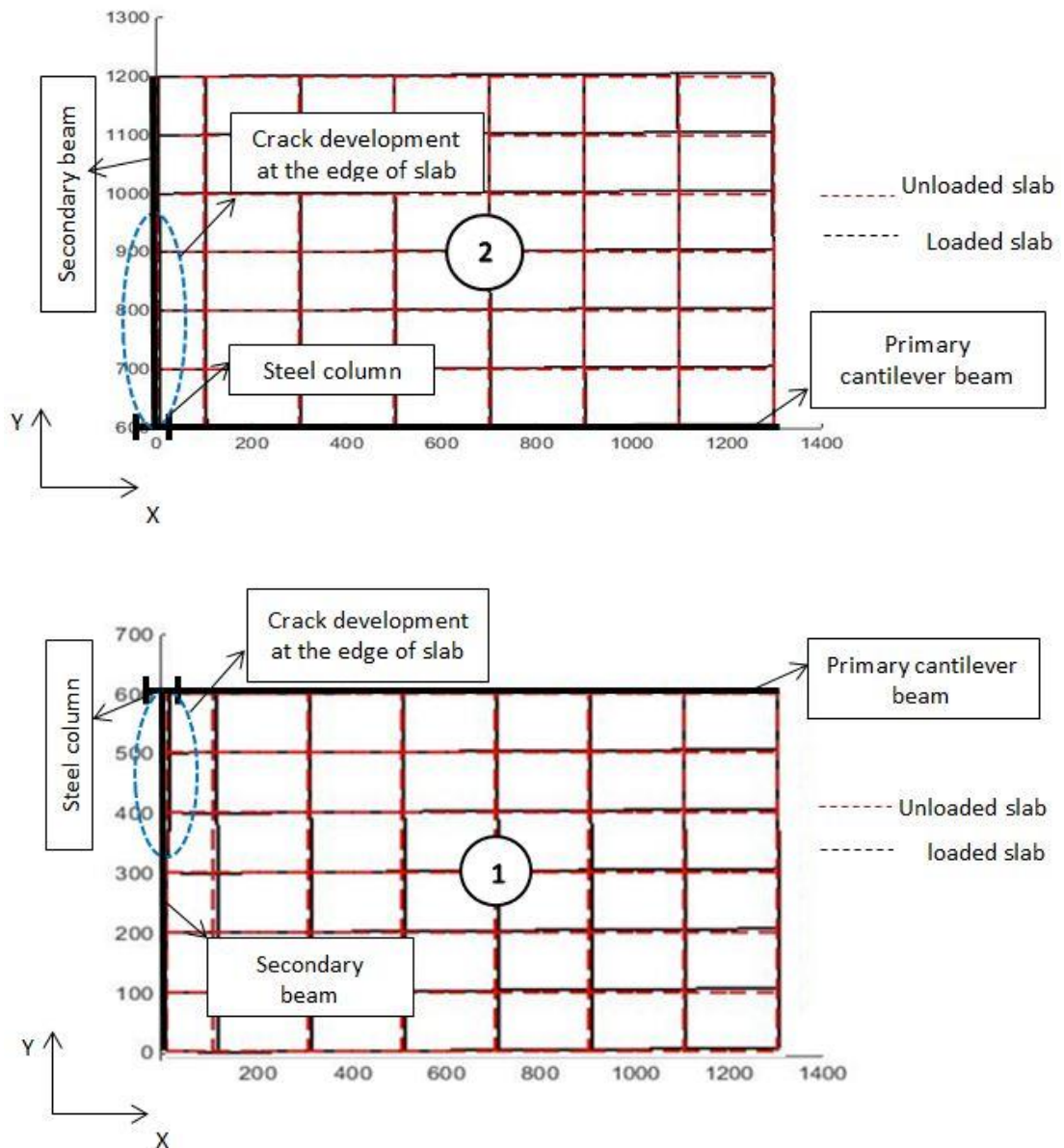


Figure 4.12: C3 test - lateral displacement of composite slab from *Vulcan* 30kN.m

Figures 4.13 illustrate the lateral displacement of the model when the moment at the connection reaches 60kN.m. As can be seen from these figures, after the initiation of the first crack around the column the crack then develops over the length of the stub beams followed by the fracture of the mesh reinforcement. The maximum crack width from the test was expected to be at the location close to the column where the tensile force at the top surface of the slab is maximised as the result of the large lever arm between the connection and the mesh reinforcement. The maximum crack width of 1.2mm has also been picked up by the FE model at 100mm away from the column at the left hand side of the cantilever beam and reduces going towards the end of stub

beam. However, the model shows a uniform development of the crack at the right hand side of the loaded beam.

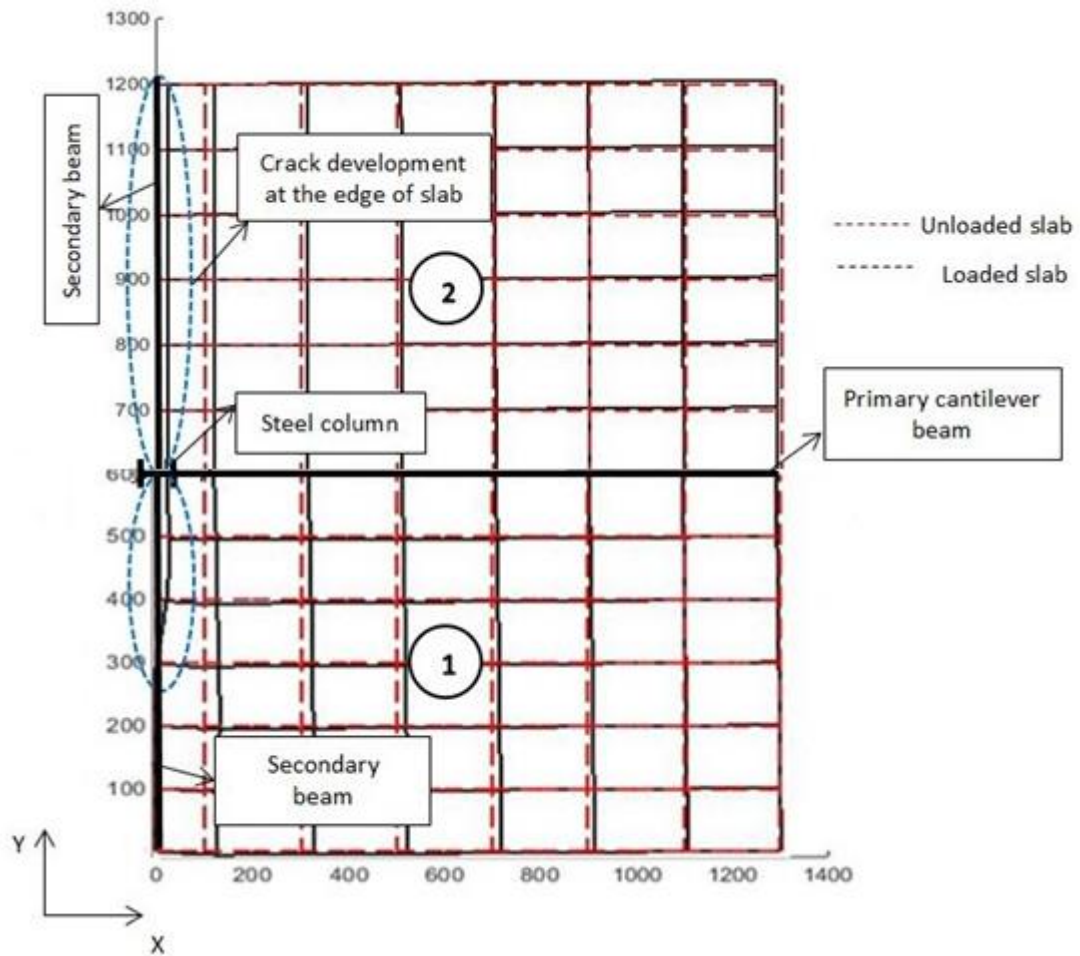


Figure 4.13: C3 test - lateral displacement of composite slab from *Vulcan* at 60kN.m

Figure 4.14 illustrates the horizontal displacement of the composite slab along the length of the stub beams. The development of the crack over the length of the slab is the result of relative movement between the slab and beam nodes at different load steps. The unsymmetrical development of the crack in concrete and the failure of the break elements across the length of the stub-beam in the above *Vulcan* model can be explained by the occurrence of the numerical error during the analysis. The Newton-Raphson iteration is the solution method currently adopted in the *Vulcan* program. The method is controlled by making steps of load (stress) and calculating the resulting strain. Therefore, the unsymmetrical development of the crack pattern along the length of symmetric model can occur as a result of earlier fracture of a break element on one side of the model than the other symmetric side. Note that these

fractures occur at different iteration numbers within a single load step of the analysis. There is no clear evidence in the experimental report to show the actual location of the maximum crack and also no statement has been made in the report regarding the fracture of the mesh reinforcement. Based on the details of the test specimen, drawn wire with a smooth surface was used as the mesh reinforcement and the composite slab was reported to be continuous beyond the column for a very short length, where it was assumed to be a free end with no lateral/rotational restraint. Therefore, it is most likely that the development of the crack around the column in the test happened as a result of reinforcement being pulled out from the concrete due to insufficient length of the embedded rebar in the concrete beyond the column and the poor bond interaction between the smooth surface of the mesh and concrete.

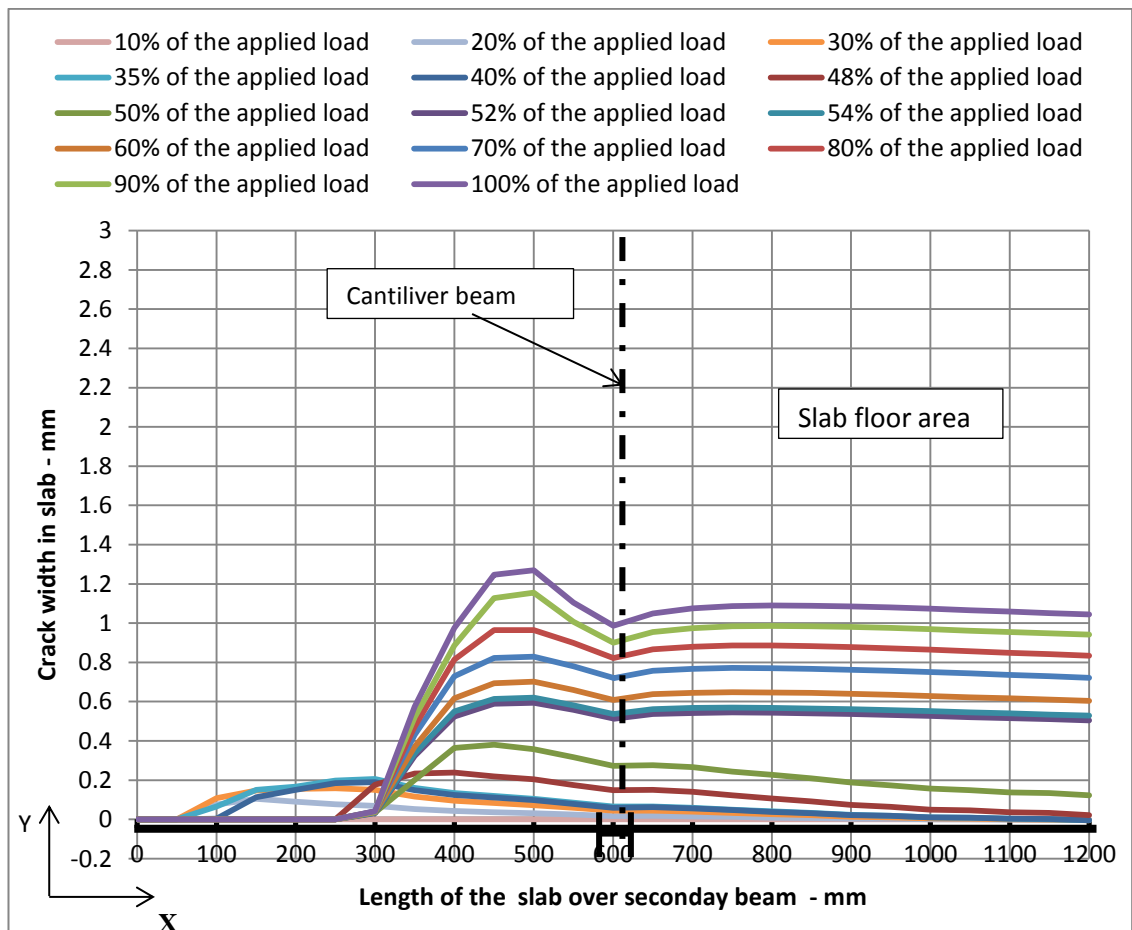


Figure 4.14: Comparison of crack development in the slab at different load levels

As has been mentioned in chapter 2, the break element in *Vulcan* is modelled based on the assumption that sufficient gauge length is always provided so the pull-out

phenomenon never occurs and the failure of the break element is only due to axial tensile force reaching the ultimate tensile capacity of the break element. Therefore, what happened in test C3 in terms of crack development cannot be accurately modelled since the failure of the test was the result of local de-bonding of the reinforcement from the concrete as a result of insufficient development length. Furthermore, it should be remembered that concrete is not a homogeneous material, so predicting its behaviour and the development of a crack is problematic as it can be the result of a single local effect (i.e. imperfection of bond interaction between aggregates and cement, curing condition, etc.). This local effect currently cannot be modelled accurately by common commercial software and the smeared cracking approach has been widely applied in numerical analysis. Crack distribution has also been addressed in *Vulcan* using the smeared cracking properties. Using this approach the effect of the occurrence of the crack on the slab performance is reflected by the means of uniformly reduced axial and bending stiffness of the slab element. The smeared cracking approach is acceptable to use when the global behaviour of the structure is considered but it is not a reliable technique to use when we dealing with local effects such as the development of cracks in the concrete.

4.3.2 Flexible End Plate Composite Joint

Extensive studies have been carried out by Al-Jabri [35] on the performance of steel/composite connections at ambient and elevated temperatures. Tests on bare steel connections were performed based on the previous work done by Jones [58] at the University of Sheffield with the extended scope of study to include the effect of member sizes and different types of connection on the overall performance of joints and the possible failure mechanisms. Similar to the work done by [107], Al-Jabri also used the experimental data of tested steel connections to study the influence of composite slabs on joint performance. The experimental work [35] was divided in to five groups; the purpose of the first three groups was to study the rotational rigidity of flush end plate connections, and the tests for the other two groups were designed to investigate the influence of existing composite slabs and its reinforcement on the overall performance of the joint and to establish the moment-rotation relationship for

the composite joint using flexible end plate connections. Flexible connections are generally categorised as semi-rigid connection, however, they also can be considered as a nominally pinned connection with limited level of rotational rigidity. The ease of construction for these type of connection makes them financially benefice and therefore, more attractive to use in construction. The steel connections used in the section of the work are based on the experimental data of the connection at ambient temperature reported by Boreman *et al.* [109]. The tests were designed to investigate the performance of the connections utilised in the Cardington full-scale test. The experimental works for all groups has been performed in a symmetric cruciform arrangement with a central column of 2.7m height connected to two cantilever beams of 1.9m length on two sides of the column flanges using flexible end plate connection. Figure 4.15 illustrates the experimental layout of the flexible end-plate connection test used in group four and five.

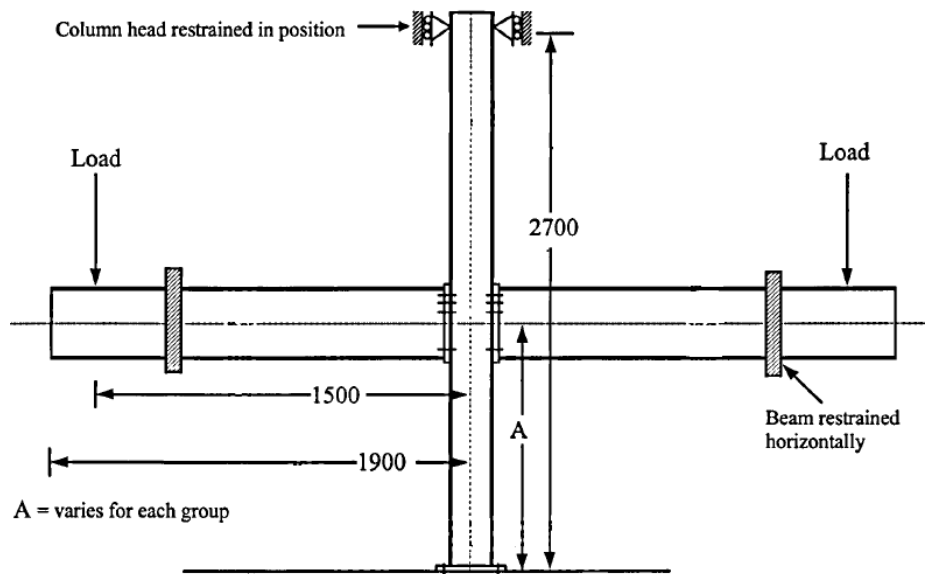


Figure 4.15: Cruciform arrangement –bare steel connection [35]

4.3.2.1 Composite joint test- Group 4

This type of connection was selected to provide a comparison between the steel and composite connection at ambient temperature. Figures 4.16 and 4.17 show the detail of the composite joint tested.



Figure 4.16: Flexible end plate composite connection detail – Group 4 [35]

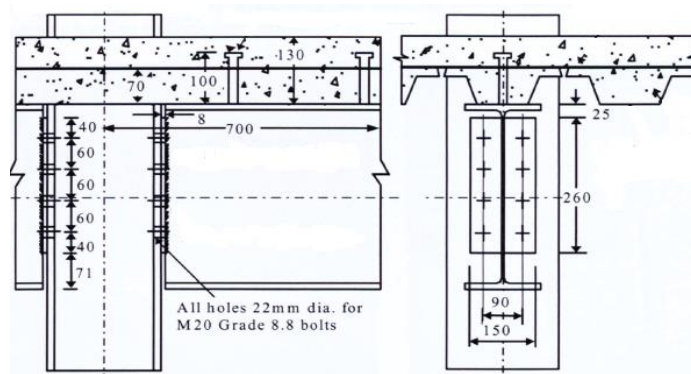


Figure 4.17: Flexible end plate composite connection detail – Group 4 [35]

Tests in group 4 featured a lightweight composite slab with COMFLOR C70 decking of 1mm thickness, parallel to the direction of primary beams, and overall depth of 130mm, which was reinforced with A142 mesh to represent the minimum required level of reinforcement present in composite floors. The test was conducted using a 254 x 254 x 89UC, and 356 x 171 x 51UB. The length of continuous slab across the connection was 1400mm and its width was 1200mm. The length of the slab was enough to allow two 100mm by 19mm diameter shear studs at 300mm centres on

each cantilever beam. Table 4.4 presents the material properties and the joint arrangement for group 4.

Specimen size	356 x 171 x 51UB	254 x 254 x 89UC	Reinforcement	Concrete
σ_y (N/mm ²)	415.5	426	487	-
σ_{ult} (N/mm ²)	552	573	552.6	-
E (kN/mm ²)	196	196	200	-
ε (%)	25.4	27.7	20.2	-
f_t (N/mm ²)	-	-	-	3.97
f_{ck} (N/mm ²)	-	-	-	63

Table 4.4: Material properties – Group 4 [35]

Finite Element Model

Bare steel and composite joints for the above joint arrangement were created in *Vulcan*. The models were created based on the available test data shown in table 4.4. Similar to the model for the seat cleat connection, the numerical model for the flexible end plate connection was also created as an assemblage of a series of finite elements, containing break elements which represent slab continuity beyond the crack, slab shell elements and beam line elements. Figure 4.18 shows the plan view of the composite joint modelled in *Vulcan*. Unfortunately, due to some technical limitations of the software and insufficient memory space when using the compiler it was not possible to include the previously validated component-based model of the connection [110] for the purpose of this analysis. As was mentioned before, a flexible end plate connection is generally assumed as a pin connection with only a limited level of rotational rigidity; therefore, a semi-rigid connection element with a bilinear rotational stiffness property may be used to represent the equivalent rotational stiffness of the joint in both the elastic and plastic zones up to the failure of the mesh reinforcement in tension. The rotational stiffness for the connection element was calculated from the moment-rotation curve of the bare steel connection test of group 4. Break elements have been placed along the width and the length of the composite slab in both directions to represent the slab continuity before and after the failure of concrete in tension.

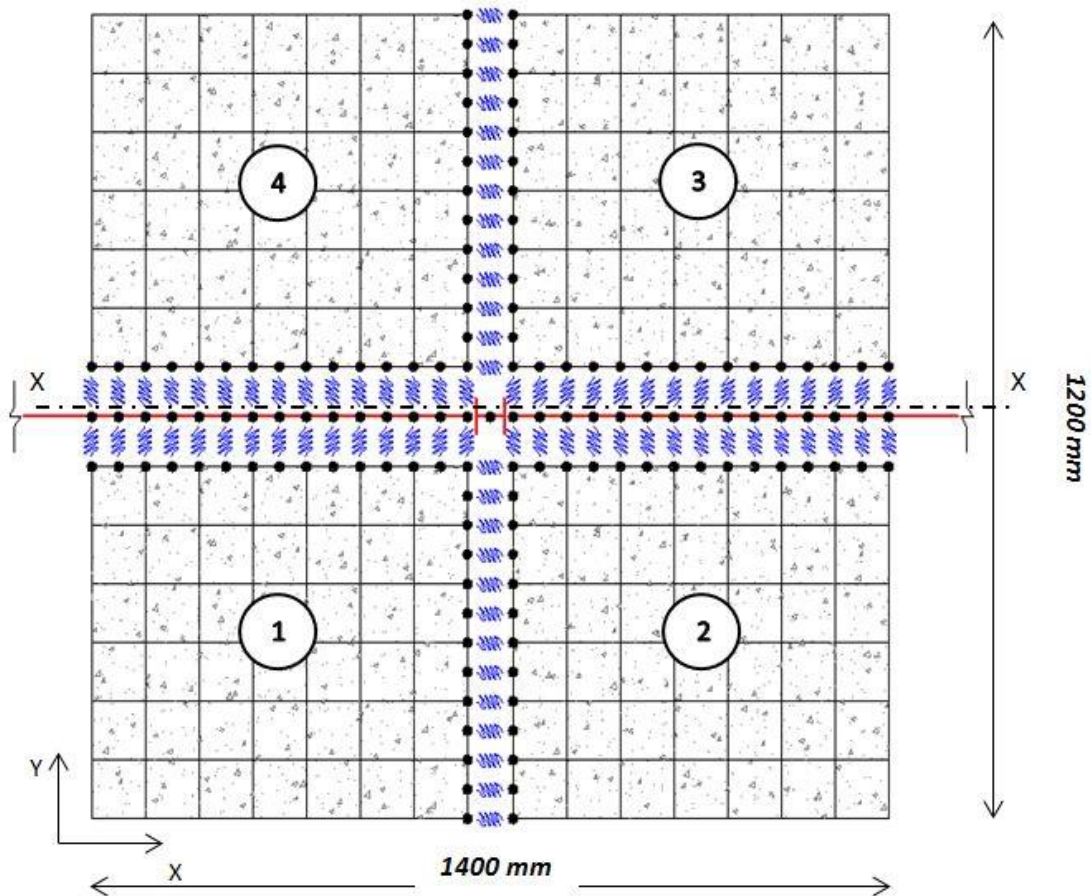


Figure 4.18: Composite joint – Group 4 – Numerical model, *Vulcan*

Loading and Boundary conditions

Appropriate boundary conditions need to be applied to the finite element model to ensure that the model is a true representation of the experimental work. Similar to the numerical model for the seat cleat connection, the slab element is also set to be free in all DOF except for the rotational movement around the z axis (θ_z) as this is the default assumption for the successful convergence of the slab shell element in *Vulcan* software. The cantilever beam elements are restrained horizontally at the far end of the beams to represent the horizontal restraint of the beams during the test. The composite action between the steel beams and slab is included in the model by using the break element between the slab and beam elements over the length of the cantilever beams. Furthermore, a series of break elements has also been placed along the minor axis of the column to represent the continuity of the composite slab through the cruciform arrangement. Column elements are also modelled using the

appropriate column section which is set to be fully fixed at the base and axially free at its top end in order to allow vertical movement. Assigning 0 to no-restrain and 1 to denote restrained, the following table summarises the boundary conditions for the numerical model.

<i>DOFs</i>	<i>9-noded Slab Element</i>	<i>3-noded Beam Element</i>	<i>End – Beam Element</i>	<i>3-noded Column Element</i>	<i>Top/Base Column Element</i>
x y z θ_x θ_y θ_z	000001	000000	110000	000001	110111 / 111111

Table 4.5: Assumed boundary condition – Group 4 [35]

The total vertical point load of 77kN was applied on the cantilever beams at a distance of 1350mm away from the column face through a series of load increments. This load is enough to generate a similar magnitude of applied moment at the connection to the one measured in the test.

Numerical Analysis – Experimental Data

Similar to the previous validation part for the seat cleat connection, the numerical analysis has been compared with the experimental results from the work done by Al-Jabri [35] on composite joints with flexible flush end plate connections. Similar to the previous validation part for the seat cleat connection, the numerical analysis has been conducted with the experimental results from Al-Jabri's work [35] on a composite joint with a flexible flush end plate connection. Considering the limitations of the program, the validation of the developed model against the test data was conducted using a predefined semi-rigid connection element with a bi-linear rotational stiffness characteristic. The magnitudes of the rotational stiffness of the steel connection for the elastic and plastic phases were assumed to be equal to the average stiffness of the tested bare steel joint for the elastic and plastic zone respectively. The composite joint model was created in *Vulcan* based on the technical specification given in figure 4.17, table 4.4 and table 4.5. Figure 4.19 compares the moment-rotation response of the composite and bare steel connection from the experiments with the numerical model created in *Vulcan*.

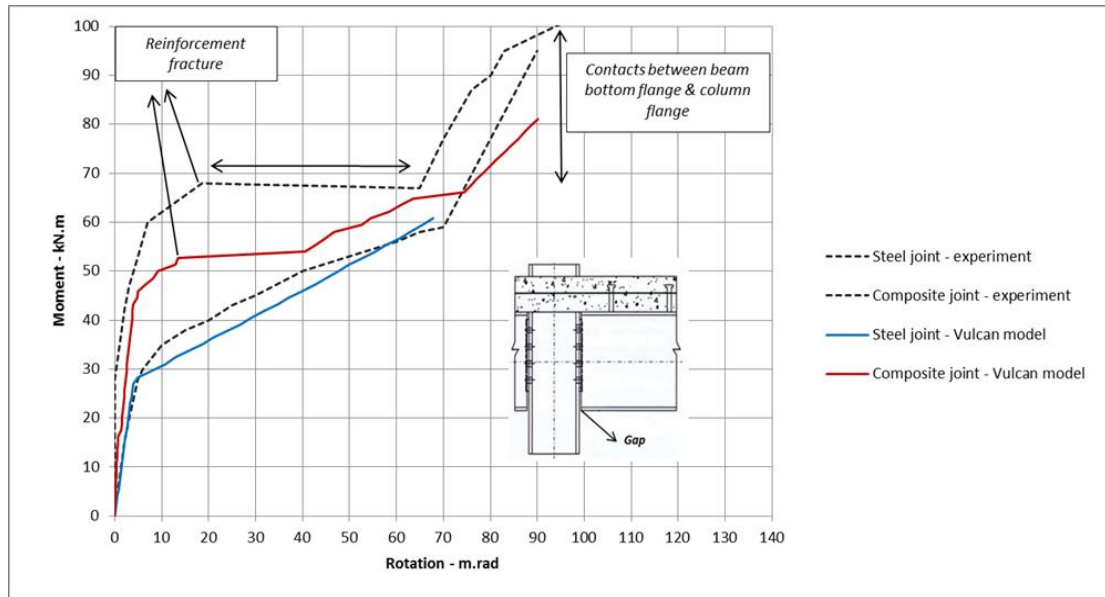


Figure 4.19: Moment- rotation of composite joint – Group 4

As is evident, the experimental curve for the composite joint shows a linear behaviour up to the moment of 46kN.m. This indicates an enhanced stiffness of the composite connection compared to the corresponding bare-steel connection. The appearance of the crack in composite slab was reported by Al-Jabri [35] at the moment of 50kN.m. As the load increased the width of the crack at the column faces were also increased up to the moment of 69kN.m. At this point, the concrete slab became unable to support any further loading within the connection due to the tensile failure of some reinforcing bars as a result of increased crack width at the face of the column flange perpendicular to the cantilever beam. Therefore, the whole load is transferred to the end-plate, which consequently results in extreme end-plate deformation. This is indicated by the flat-plateau in the above moment-rotation curve. Upon the failure of the composite slab, the connection tends to behaves as a bare steel connection. The connection regained some of its initial stiffness along with further rotation once the bottom flange of the beam came into contact with the column flange. The predefined moment-rotation characteristic of the connection element successfully replicates the behaviour of the steel joint from the test data with elastic rotational stiffness up to 5mrad followed by reduced linear stiffness to represent the behaviour of the joint in the plastic zone. With regards to the bilinear behaviour of the modelled steel connection, it is also evident that the response of the numerical model for the composite joint is in a good agreement with the collected

data from the experiment. The numerical model shows an enhanced moment capacity of 50kN.m within its elastic region which is due to the presence of the concrete slab and its reinforcement at the top of the steel joint. This is comparable with the obtained moment of 60kN.m from the test. Once the concrete at the top surface of the slab cracks (i.e. the stress level in the concrete exceeds the tensile strength), the steel reinforcement in the slab contributes to the overall rotational behaviour of the composite joint through its longitudinal stiffness. The behaviour of the numerical model beyond the elastic region also provides a reasonable representation of the tested composite joint from the experiment, where the connection experiences a large rotational displacement as a result of the reinforcement being yielded/ fractured at the top of the steel joint. The numerical model indicates the maximum moment capacity of 65kN.m at the rotation displacement of 65mrad, this is very close to the obtained moment capacity of 67kN.m at the same level of rotational displacement during the test. The numerical model illustrates a softer manner compared to the experimental curve beyond the yield of the reinforcement within the plastic region; this is due to the lower rotational stiffness of the steel connection element compared to the steel connection rotational response from the experiment. The model shows a reduced rotational stiffness of the composite joint beyond the tensile failure of the reinforcement, which is very close to the stiffness of the bare steel connection element. This is a direct result of the break element failure (reinforcement failure) at the locations close to the connection element.

The changes in rotational stiffness of the predefined semi-rigid connection element in the above numerical model was assumed to be the same for all rotational DOFs, which means that the rotational stiffness characteristic of the connection element is assumed to be the same in all directions (X, Y, Z) regardless of the main direction of the steel joint in the model. Therefore, the influence of structural interaction between the steel joint and the composite slab in all directions apart from the main working direction of the joint was investigated using the existing numerical model. In this model the rotational stiffness of the steel connection around its main working direction (x-direction) was also the same as the experimental data of joint response in that direction, however, the stiffness of the joint around all other directions (y and z

directions) were assumed to be rigid during the analysis. This represents the full interaction between the steel joint and the slab in those directions.

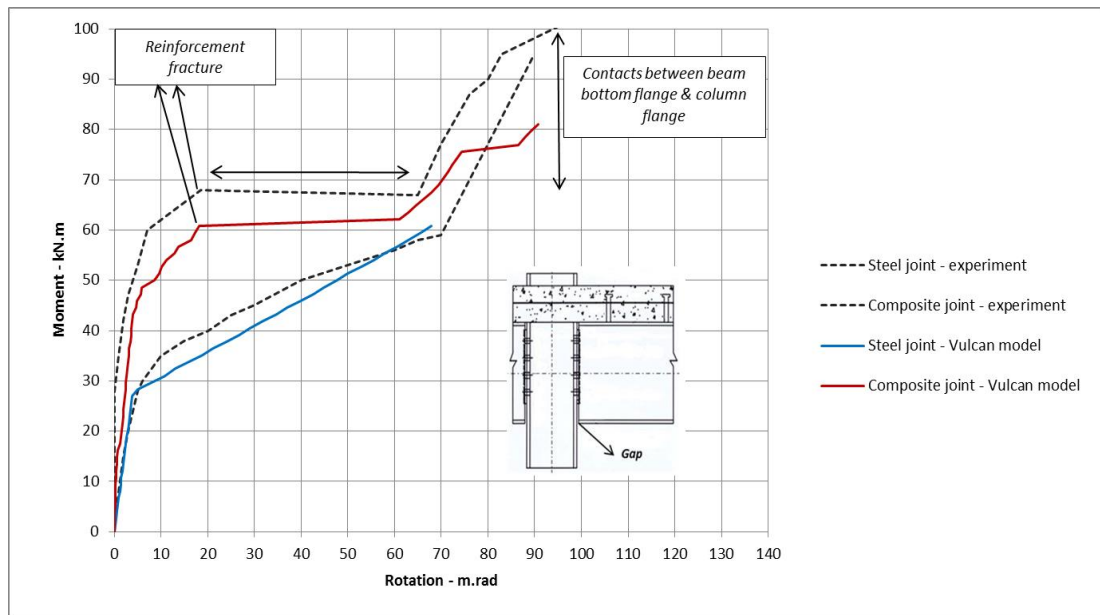


Figure 4.20: Moment- rotation of composite joint – Enhanced - Group 4

Figure 4.20 compares the response of the updated numerical analysis (which represents the full interaction between slab and beam along off-directions of the steel joints) with experimental data [35]. It is evident from the graph that the presence of full interaction between the steel joint and the composite slab along the off directions of the connection clearly results in a greater enhancement factor for the composite connection in the numerical model. The magnitude of the moment capacity from the updated model in the elastic region up to 5mrad is identical to that of the model in figure 4.17. However, the new model indicates a higher moment-rotation response within its plastic zone compared to the initial model, where the moment capacity of the connection reaches the value of 60kN.m at the rotational displacement of 18mrad.

Crack Development

Experimental data of group 4 shows that failure in the concrete slab occurred first followed by failure of the flexible end-plate. In the concrete slab a large crack propagated from the face of the column flange parallel to the primary beam, resulting in fracture of some reinforcing bars and exposure of shear studs. Figure 4.21 shows typical crack locations in the composite slab during the test.

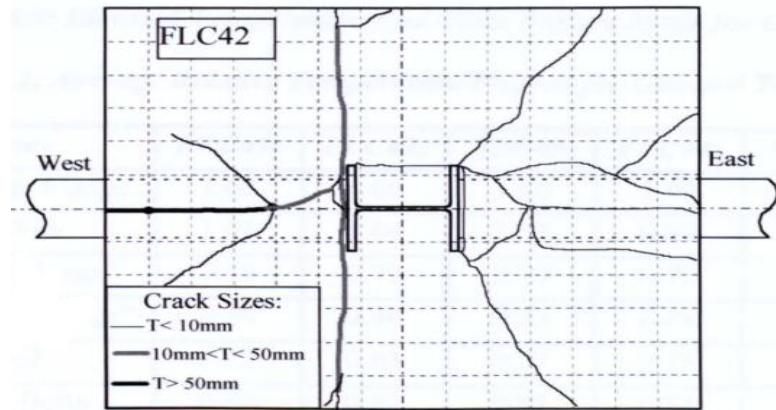


Figure 4.21: Slab crack locations in Group4 [35]

This crack occurred due to a pulling through of shear studs within the concrete slab. This pattern of failure is mainly due to an insufficient number of shear studs on each cantilever beam as only one third of the beam span was constructed as composite (to allow the specimen be fitted in the oven). Two major secondary cracks were also observed perpendicular to and continuous across the connections on both sides of the slab. These cracks occurred as a result of considerable end plate deformation which imposed high tensile strains on the decking and slab. Al-Jabri [35] reported the crack width ranging between 10 to 50mm perpendiculars to the primary beams. This pronounced cracking occurred as a result of further loading of the beam. The developed numerical model for the analysis of experimental data of group4 is also capable of predicting the occurrence of the initial cracks, tracing the behaviour of the mesh reinforcement represented at each break element and the sequence of the failure of the reinforcement in the composite slab. Figures 4.22 is schematics of the magnified lateral displacement of the composite slab modelled in *Vulcan*. In the following figure, the dashed red lines represent the unloaded slab and the continuous black lines shows the deformed slab at ultimate loading. The results from the numerical model have been divided into 4 parts each representing one quarter of the actual composite slab. Similar to the group 4 experiment, the finite element model of the test also results in development of large cracks perpendicular to the primary beams, over the width of the composite slab at higher load levels.

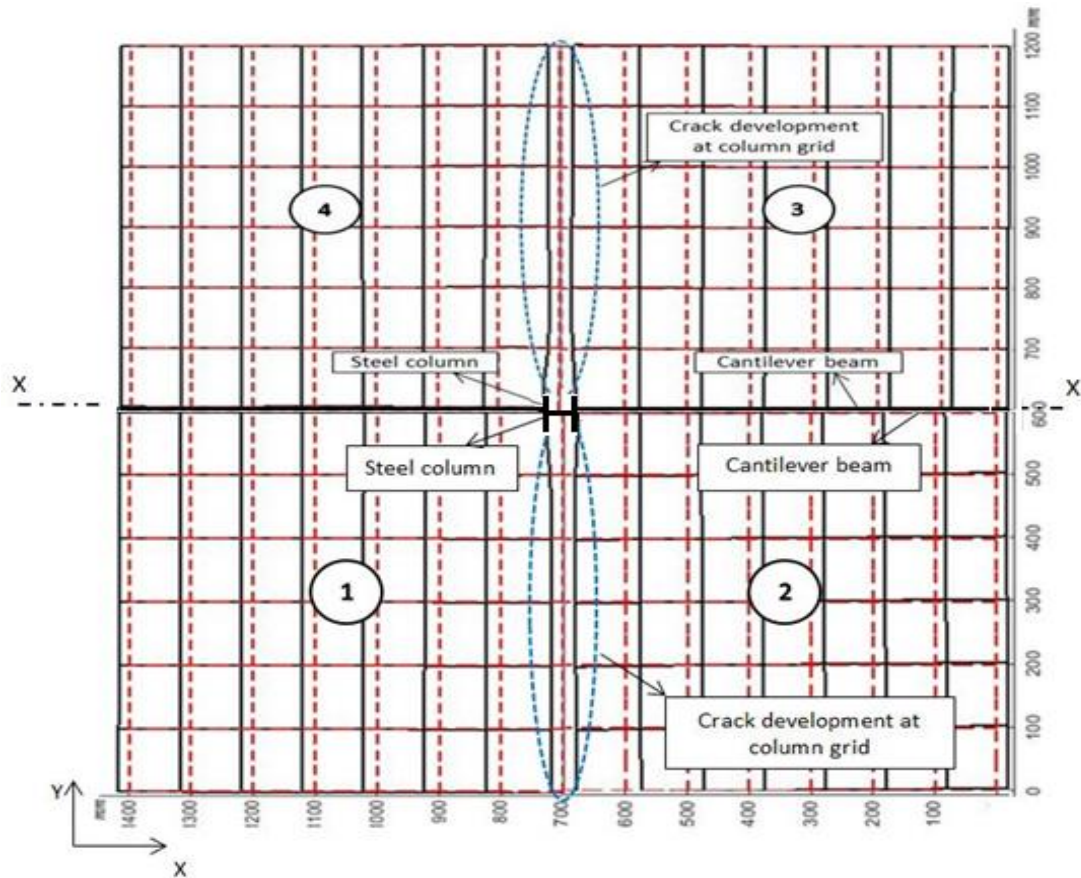


Figure 4.22: Group4 test - lateral displacement of composite slab from *Vulcan*

Figure 4.23 illustrates the results from the *Vulcan* model for crack development along the width of the composite slab at different load increments through the analysis. As is evident from the figure, the crack has initially occurred at locations close to the column, and it has been developed towards the edge of the slab perpendicular to the cantilever beams. As the loading increased a sudden failure of the reinforcement happened along the width of slab, which consequently resulted in a sudden increase in the crack width. Based on the numerical data from the model, the composite slab has also been cracked in the direction parallel to the primary beams but no failure of the break elements has been identified in this direction during the analysis. This is mainly due to the fact that full shear interaction has been assumed between the steel beams and composite slab during the analysis; therefore, no pulling through of shear studs occurred as a result of the large shear force.

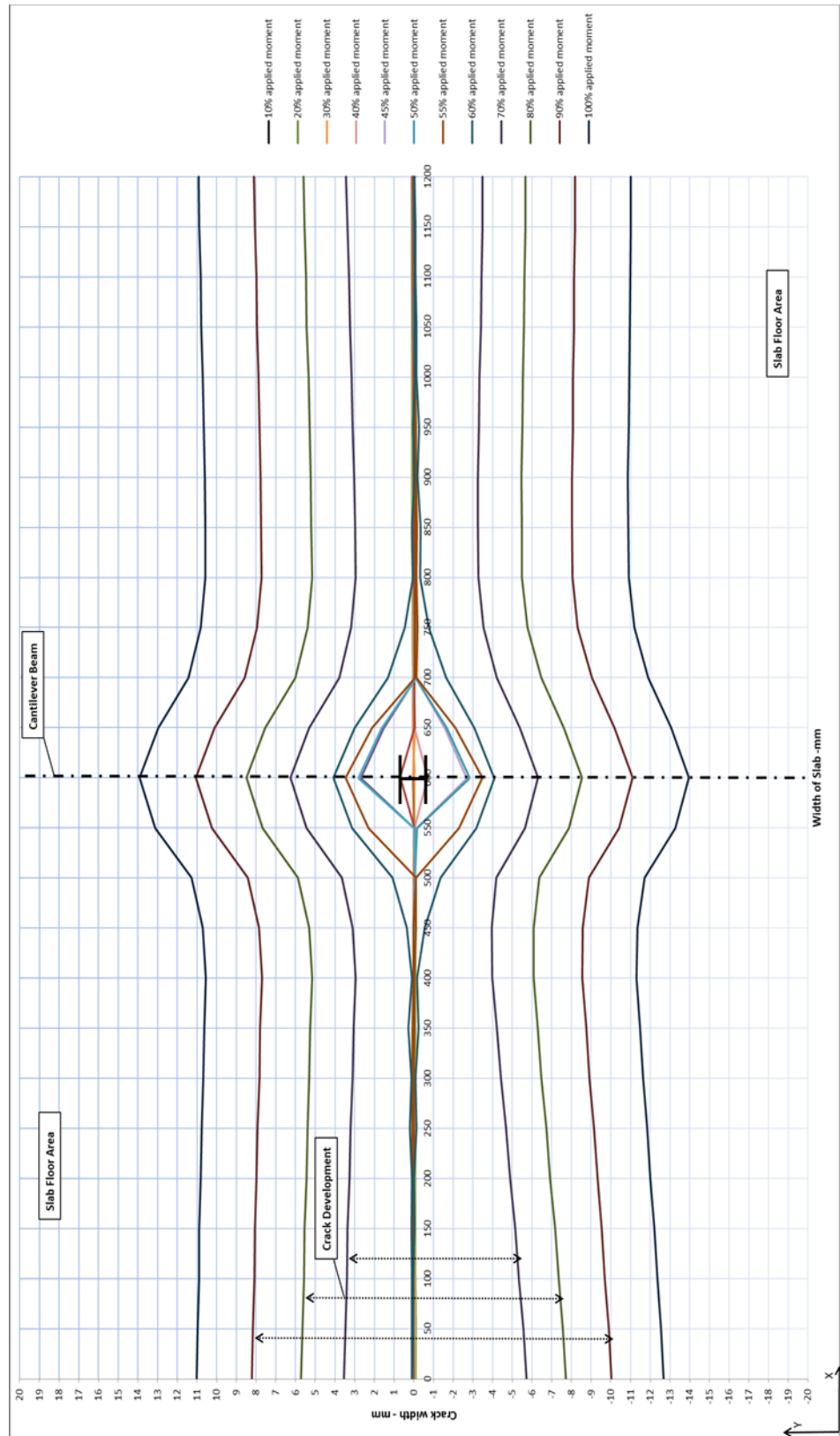


Figure 4.23: Crack development in composite slab – Group 4 - Vulcan

Force-displacement response- break element

As explained in the methodology chapter, the mechanical characteristic of the newly developed break element has been implemented in the *Vulcan* using a force-displacement relationship. Figures 4.24 and 4.25 show the force-displacement response of random break elements, which were positioned along the width of the composite slab to model the experimental test group 4.

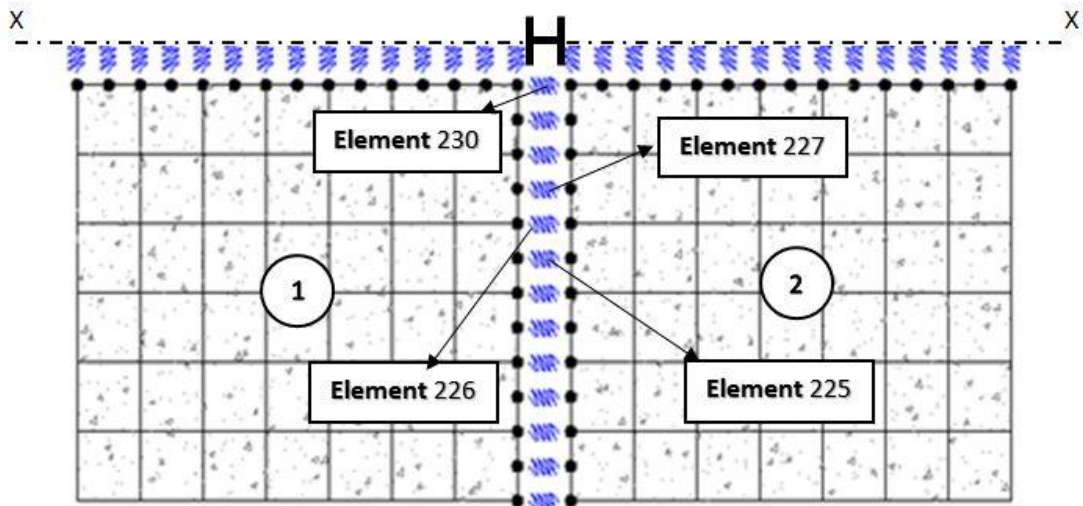


Figure 4.24: Plan view of specimen arrangement, Group 4 - *Vulcan*

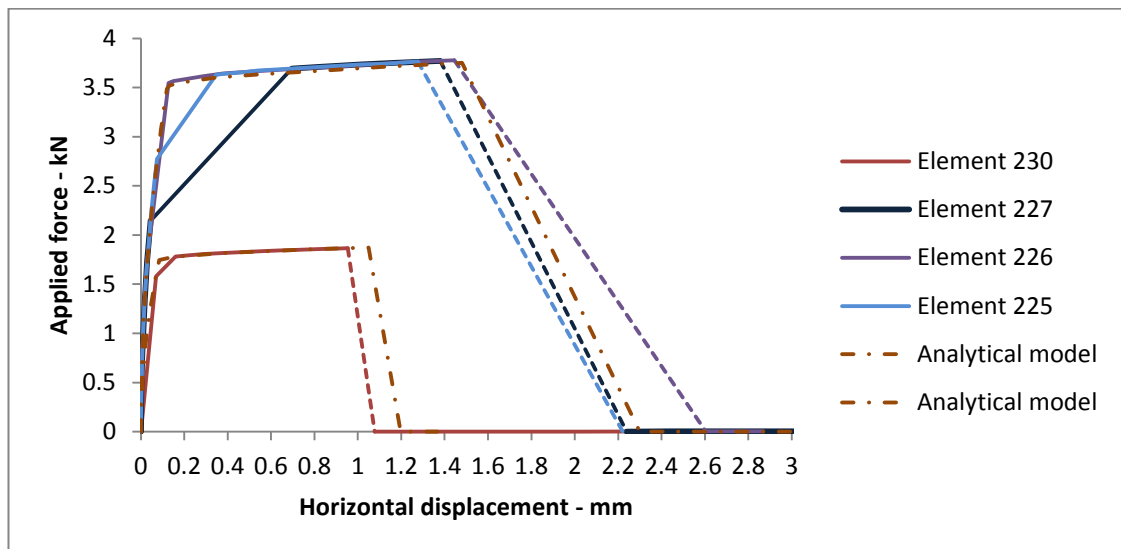


Figure 4.25: Force-displacement of break elements - *Vulcan*

Figure 4.25 illustrates the force-displacement response of one corner break element and three other elements along the width of the slab. As is evident, element 230 (the corner element) reached the ultimate capacity at a lower level of both applied force and the displacement compared to the other elements. This is due to the fact that the

corner break elements represent lower equivalent levels of reinforcement area than the other break elements since the strength capacity of break element is directly related to the provided area of reinforcement (see section 3.3.3). Looking at the figure, it can be stated that the force-displacement response of different elements from the numerical model is in line with analytical calculations. The sudden changes in the displacement response of some of the elements are because of the insufficient number of load steps of the applied load and it can be sorted using smaller load increment through the analysis.

4.3.2.2 Composite joint test- Group 5

The test arrangement for group 5 tests was exactly the same as the specimens tested in group 4, but using a stronger connection and different section sizes. Figures 4.26 shows the detail of the composite joint tested in group 5.

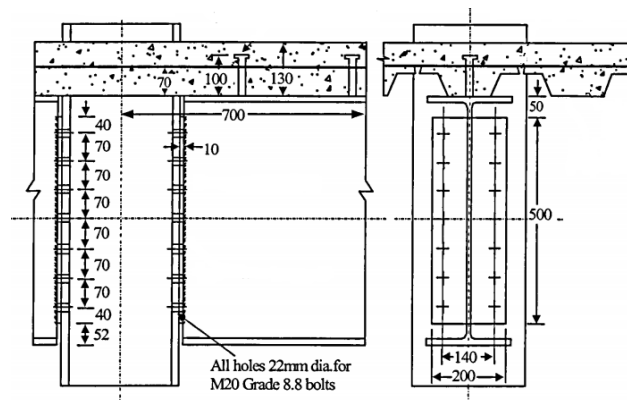


Figure 4.26: Flexible end plate composite connection detail – Group 5 [35]

The test was conducted using a 610 x 229 x 101UB and a 305 x 305 x 137UC. The length of continuous slab across the connection was identical to that of group 4. The material properties of the different components are also similar to the data provided in table 4.4.

Finite Element Model

Based on the available information a model of the bare steel and the composite joint for the above joint arrangement were created in *Vulcan*. The arrangement of the numerical model is identical to the model created for group 4.

Loading and Boundary condition

The total vertical point load of 125kN was applied on the cantilever beams at a distance of 1350mm away from the column face through a series of load increments. This load generated a similar magnitude of applied moment at the connection to the one measured in the experiment.

Numerical Analysis – Experimental Data

Similar to the previous validation part for the group 4 specimens, a numerical analysis has been done and compared with the experimental results from [35] on composite joints with a flexible flush end plate connection. Figure 4.27 compares the moment-rotation response of the composite and bare steel connection from the experiments with the numerical model created in *Vulcan*.

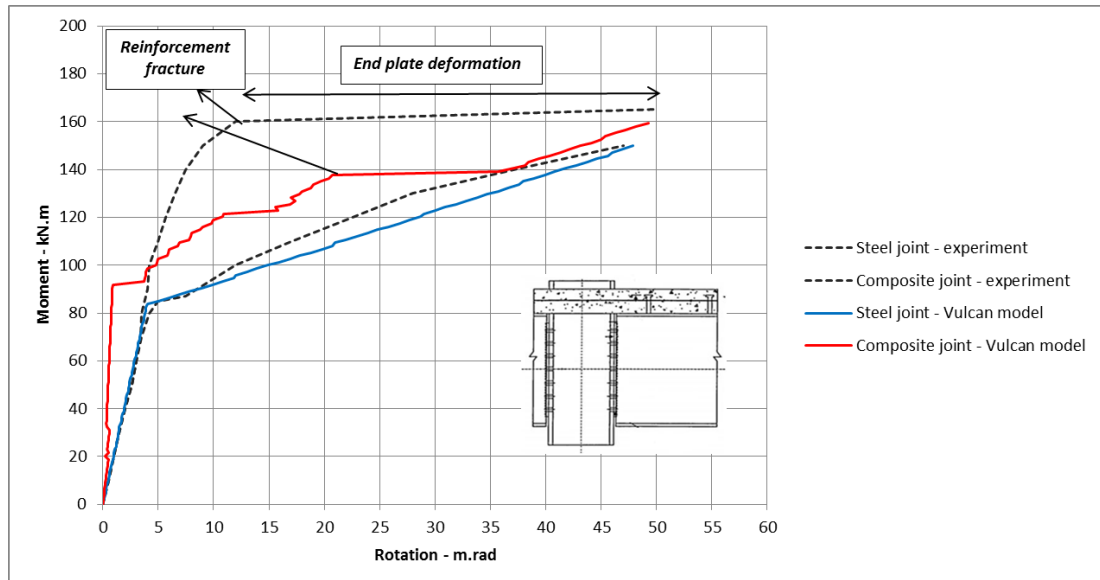


Figure 4.27: Moment- rotation of composite joint – Group 5

As is evident, the experimental curve for the composite joint shows a linear behaviour up to moment of 130kN.m. This indicates an enhanced stiffness of the composite connection compared to the corresponding bare-steel connection. A similar form of crack pattern in concrete was observed by Al-Jabri [35] at the moment of approximately 130kN.m. As the load increases the width of the crack at the column faces were also increased up to the moment of 155kN.m, where tensile failure of some reinforcing bars occurred as a result of increased crack width at the face of the column flange perpendicular to the cantilever beam. Therefore, the

whole load is transferred to the end-plate, which consequently results in extreme end-plate deformation. This is indicated by the flat-plateau in the above moment-rotation curve. Unlike the connection in group4, no enhanced behaviour of the bare steel joint has been observed beyond the failure of the slab as result of premature failure of the joint. The reason for the premature failure of the connection was further investigated by Al-Jabri [35] and, the overestimation of the connection capacity was found to be the cause of this premature failure since the connection design method by Boreman [109] was mainly based on the extensive contribution of bolt strength to the performance of the connection. As mentioned in part 4.3.2.1, the connection element used in the numerical analysis is a nominal pin connection with limited bilinear rotational stiffness equivalent to the average magnitude of the moment-rotation response of the tested joint in both elastic and plastic regions. The numerical model for the composite joint of group 5 also shows an enhanced stiffness compared to the corresponding model for the bare steel connection. The *Vulcan* model behaves in a slightly stiffer manner compared to the experimental curve at low levels of rotation up to approximately 5mrad. The difference in performance between the numerical model and the experimental data can be explained by the inhomogeneous property of concrete and therefore, the variation in concrete compressive/tensile strength of the slab in the test (the average compressive strength of concrete from the test was used for the purpose of numerical modelling in *Vulcan*). This is further indicated by the slightly higher moment capacity of the connection at the crack in the numerical model (90kN.m) compare to the moment capacity of the tested joint (80kN.m), which also causes a sudden increase in the rotational displacement of the joint up to 5mrad. The behaviour of the numerical model beyond the elastic region also provides a reasonable representation of the tested composite joint from the experiment, where the connection experiences a large rotational displacement as a result of the reinforcement being yielded/ fractured at the top of the steel joint. The *Vulcan* model identifies the fracture of some steel reinforcement in the composite slab at a moment of 120kN.m. The small flat-plateau in the numerical curve for the composite joint (between 10-15mrad) occurred as result of a number of break elements being fractured at the location close to the column face, which indicates the fraction of reinforcement close to the column faces from the experiment. As the load further

increased the second flat-plateau in the numerical model occurred at the moment of 140kN.m which is the direct result of a large number of break elements being fractured at the higher load level. The *Vulcan* model behaves in a softer manner compared to the experimental curve within the plastic region; this is due to the lower assumed rotational stiffness of the steel connection element compared to the joint rotational response from the experiment. The numerical model indicates the maximum moment capacity of 150kN.m at the rotation displacement of 45mrad, this is very close to the obtained moment capacity of 162kN.m at the same level of rotational displacement during the test. The stiffness of the model composite connection in group 5 also reduces to the stiffness of the steel connection beyond the tensile failure of the reinforcement. This is also a direct result of the break element failure (reinforcement failure) at the locations close to the connection element. Similar to the FE model for group 4, the influence of structural interaction between the steel joint and the composite slab in all directions apart from the main working direction of the joint was also investigated using the existing numerical model.

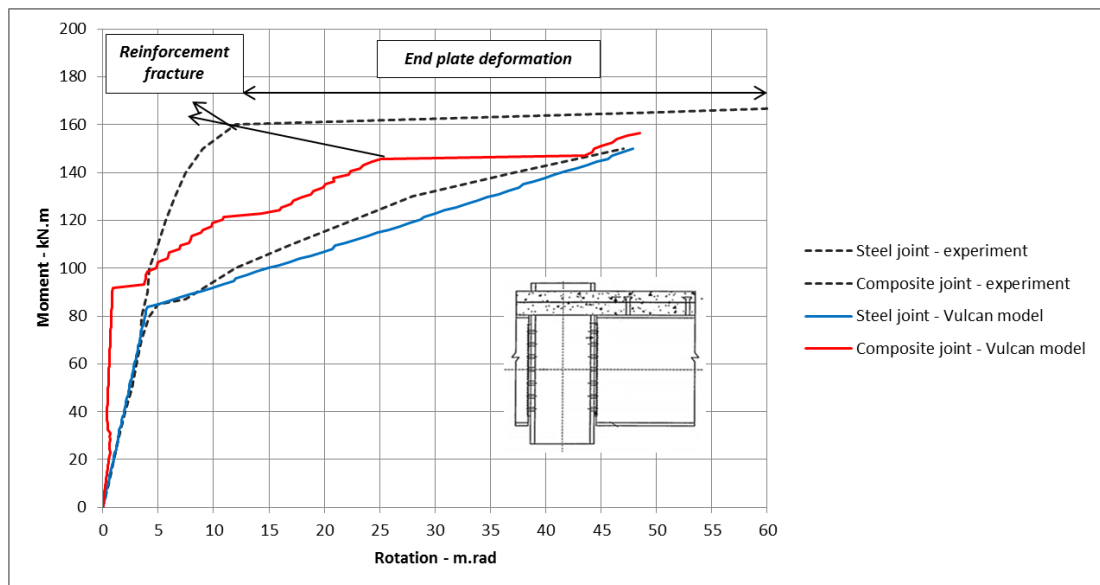


Figure 4.28: Moment- rotation of composite joint – Enhanced - Group 5

It is evident from the graph in figure 4.28 that the presence of full interaction between the steel joint and the composite slab along the off directions of the connection clearly results in a greater enhancement factor for the composite connection in the numerical mode. Similar to the numerical model for group 4, the updated model of group 5 also shows an identical magnitude of the moment capacity

of the joint in the elastic region up to 5mrad. The maximum moment capacity obtained by the model is also very similar to that of the initial model in figure 4.25. However the new model indicates a higher moment capacity within its plastic zone compared to the initial model especially at the second flat-plateau, where most of the reinforcement around the joint is fractured due to reaching its tensile capacity. The moment capacity of the connection at the flat-plateau reaches the value of 145kN.m at the rotational displacement of 25mrad.

Crack Development

The failure pattern of the composite slab for group 5 tests is of the similar behaviour to the composite joints tested in group 4. Figure 4.29 shows typical crack locations in the composite slab during the test of group 5 [35].

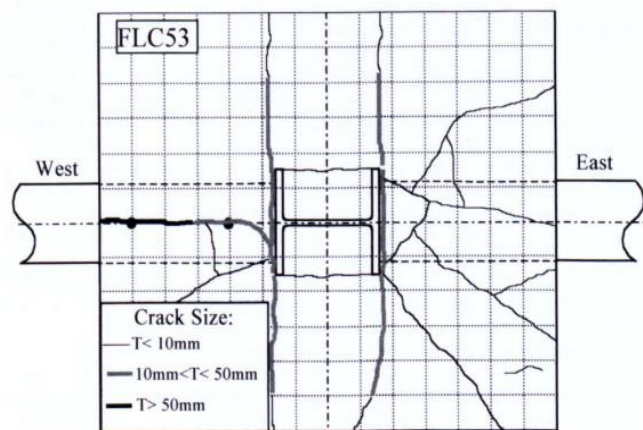


Figure 4.29: Slab crack locations in Group5 [35]

Two large cracks were observed in concrete in the direction perpendicular to the steel connection on both sides of the column. This is in addition to the primary crack developed over the length of the cantilever beam as a result of large shear force (the crack occurred as a result of flexible composite action between the steel beam and the concrete slab). Figures 4.30 is the schematic of the magnified lateral displacement of the composite slab in group 5 modelled in *Vulcan*. The finite element model of the test also results in development of large cracks perpendicular to the primary beams, over the width of the composite slab at higher load levels. However, the required moment to generate a similar magnitude of cracks was higher for the numerical model due to the fact that the connection element used in the model

had a linear elastic stiffness during the analysis, which was similar to the initial elastic stiffness of the steel connection from the test data.

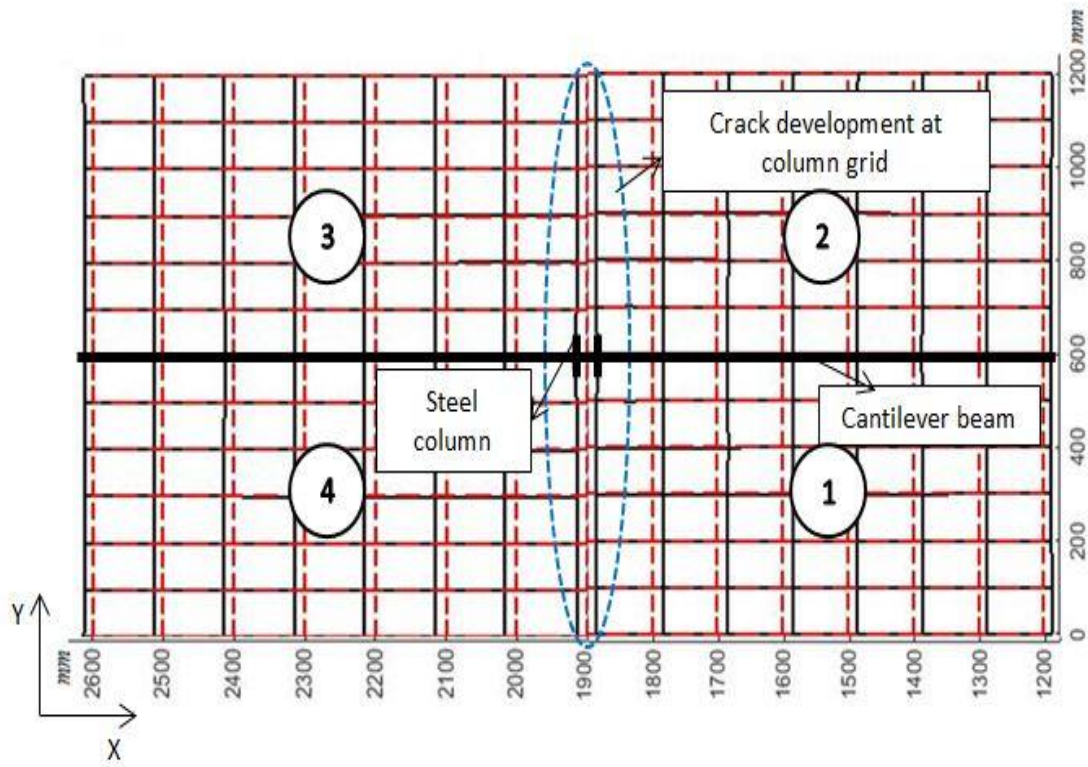


Figure 4.30: Lateral displacement of composite slab - Group 5 - Vulcan

Figure 4.31 illustrates the results from the *Vulcan* model for crack development along the width of the composite slab at different load increments through the analysis. As is evident from the figure, the crack has initially occurred at locations close to the column, and developed towards the edge of the slab perpendicular to the cantilever beams. As the loading increased a sudden failure of the reinforcement happened along the width of slab, which consequently resulted in a sudden increase in the crack width. Based on the numerical data from the model, the composite slab has also cracked in the direction parallel to the primary beams but apart from tiny cracks along the length of the beam no failure of the break elements has been identified in this direction during the analysis. This is mainly due to the fact that full shear interaction has been assumed between the steel beams and composite slab during the analysis, therefore, no pulling through of shear studs occur as a result of large shear force.

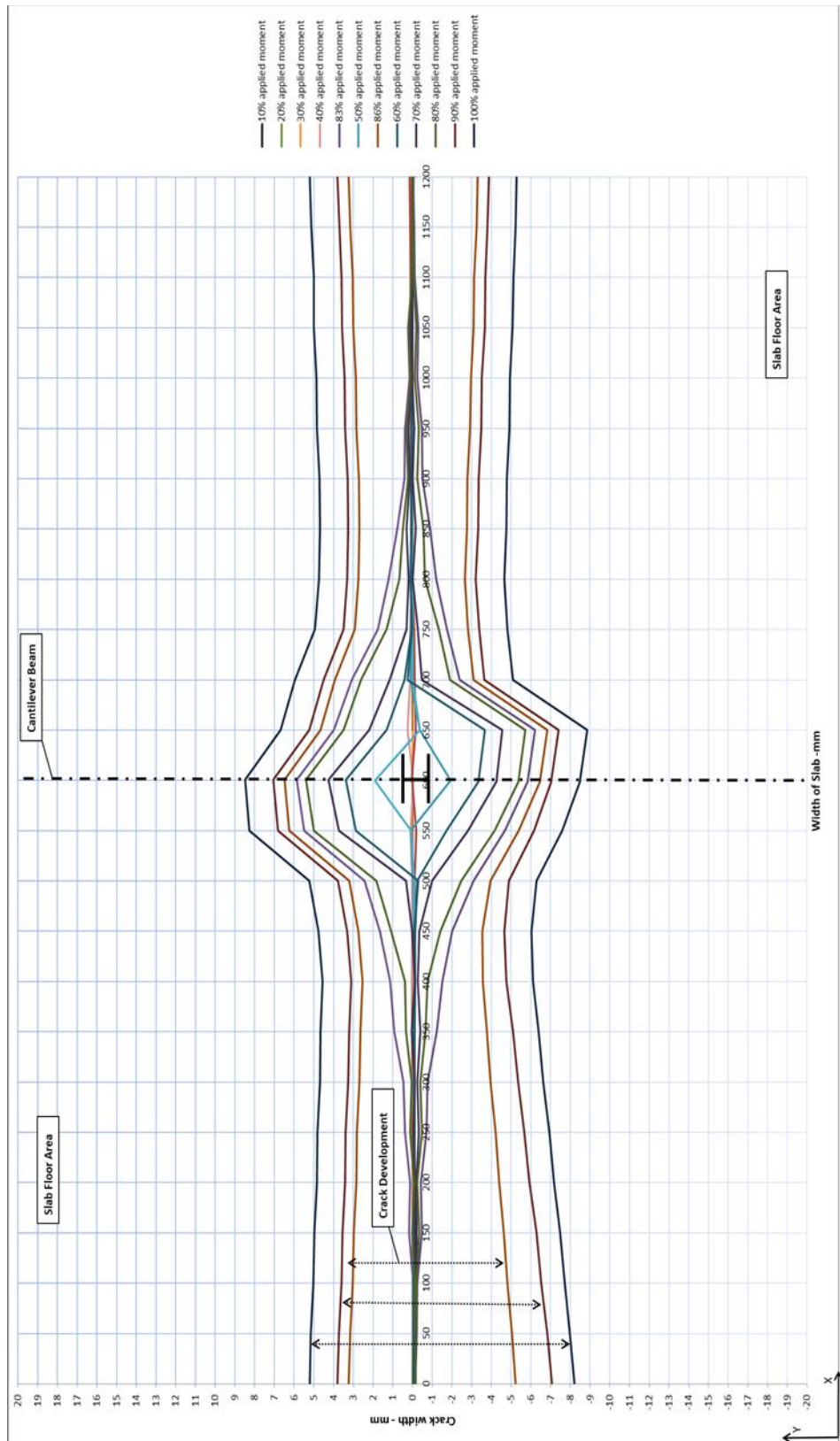


Figure 4.31: Crack development in composite slab – Group 5 - Vulcan

4.4 Qualitative comparison

4.4.1 FRACOF test

Further investigation on the performance of the newly developed break element was carried out by comparing the results from *FRACOF* test [49] with a numerical model of the actual test in *Vulcan* software. The test was part of the project which aimed to investigate of membrane action. The main purpose of the project was focused on the development of membrane forces within a slab floor area on top of the unprotected secondary beams at high temperature. Since only a general review of the crack development along the edges of the panel was provided in the test report, no quantitative comparison was possible thus a qualitative comparison was done to compare the performance of the developed numerical model incorporating break element with the general behaviour of the tested composite floor area at the crack face.

Test arrangement

A single composite slab panel was tested with a longer span of 8.735m, a shorter span of 6.660m and a total depth of 15.5 cm. The test featured a normal weight concrete composite slab with galvanised *Cofraplus60* profiled steel sheeting with a thickness of 0.75mm. The top reinforcement was placed 50mm below the top surface of the slab. The mesh reinforcement consisted of 7mm diameter bars, at 150mm spacing with a steel grade S500, which provided a reinforcement area of $257\text{mm}^2/\text{m}$ in both directions.

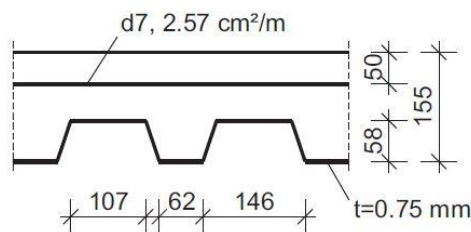


Figure 4.32: Slab cross-section of FRACOF test [49]

Two primary beams bridged the short span which consisted of IPE 400 hot-rolled sections, steel grade S355. Four secondary beams ran in the longitudinal direction and consisted of IPE 300 sections in S235. The beams were connected to short steel columns at all four corners which provided a clear height below the slab of 80cm.

End plate connections were used in the test to connect the beam and column at corners. The plan view of the specimen is shown in figure 4.33.

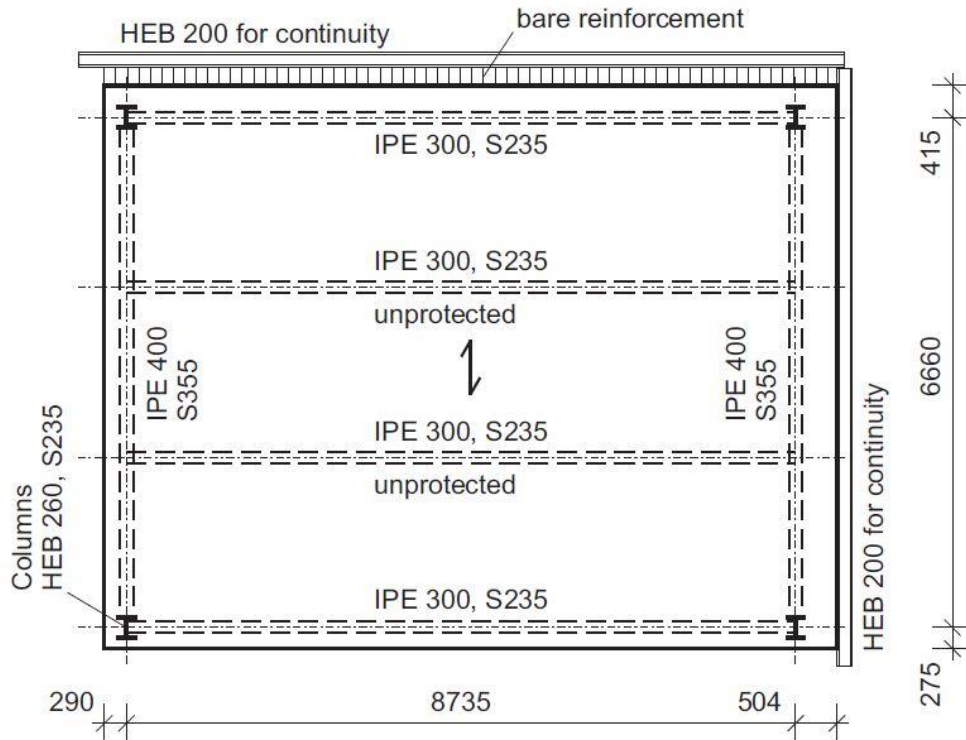


Figure 4.33: Plan view of FRACOF test [49]

The reinforcement mesh was welded to steel beams at two edges of the slab to simulate an interaction with adjacent slab panels. On the longitudinal edge the reinforcement projected out of the slab and was not covered by concrete for several centimetres before it was welded to the beam. This part of the reinforcement buckled during the test and therefore did not have the expected effect. Table 4.6 presents the material properties and the loading conditions of the test.

	IPE 300	IPE 400	Reinforcement	Concrete
σ_y (N/mm ²)	311	423	594	-
ε (%)	-	-	20	-
f_{cm} (N/mm ²)	-	-	-	36.7
Distributed load	7.12 N/mm ²			

Table 4.6: Material properties - FRACOF test [49]

Finite element model

The numerical model was created based on the available test data from [49]. The model is an assemblage of a series of finite elements, containing break elements which represent slab continuity beyond the crack, slab shell elements and beam/column line elements. Figure 4.34 shows the plan view of the composite slab panel modelled in *Vulcan*. The break elements have been placed along the perimeter of the floor slab area in both directions to represent the slab continuity before and after the failure of concrete in tension.

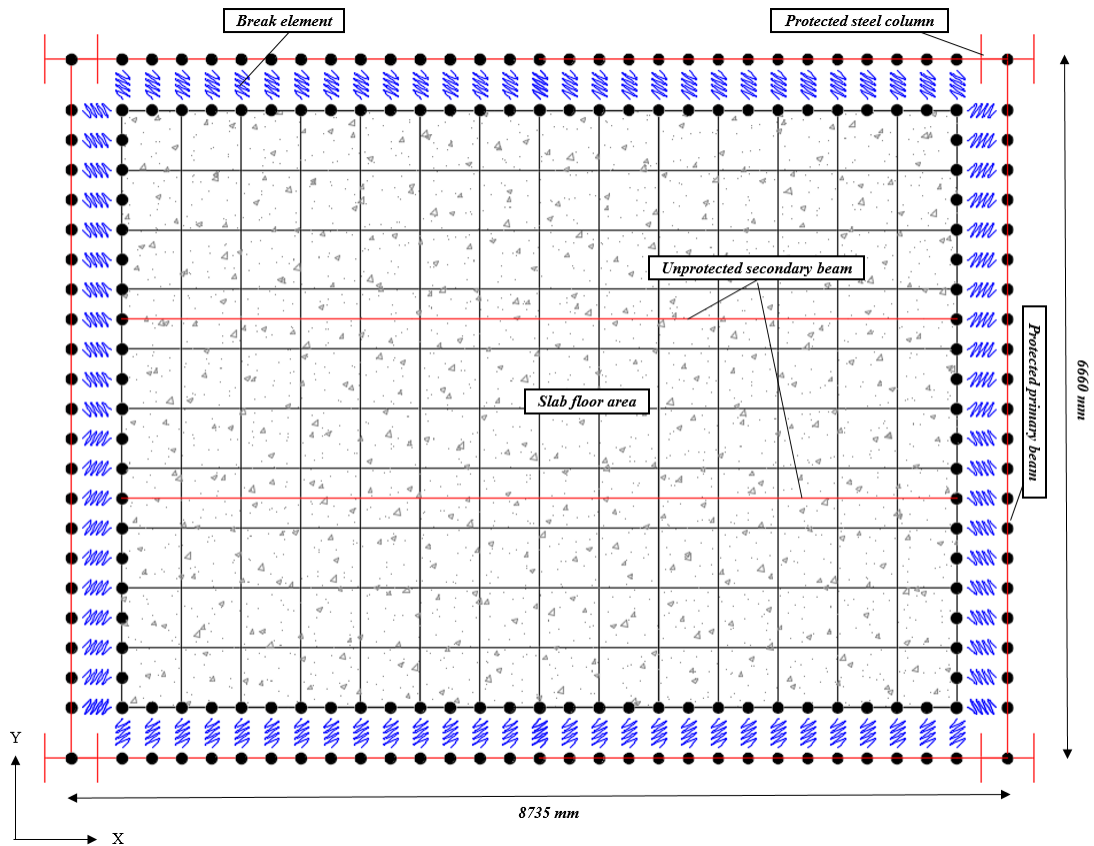


Figure 4.34: Numerical model of FRACOF test, *Vulcan*

Loading and boundary conditions

Appropriate boundary conditions were applied to the FE model to ensure that the model is a true representation of the experimental work. Therefore, the slab element in the model was set to be free in all DOF except for the rotational movement around the z-axis (θ_z). In order to include the effect of continuity in the structure in the model, the steel protected primary beam at the right-hand side of the tested panel was restrained along the x-axis (X) and against rotation around the y-axis (θ_y).

Furthermore, one of the edge protected secondary beams was also restrained horizontally along its y-direction as well as against rotation around the x-axis (θ_x). The intermediate secondary beams were left unprotected. Additionally, the short columns at all corners were modelled using the appropriate column section which was set to be fully fixed at the base and axially free at its top end in order to allow vertical movement. The total distributed load of 7.12N/mm² was applied across the floor slab area; this load is the same as that applied load to the test.

Numerical Analysis – Experimental Data

The experimental data from the test indicates an early initiation of diagonal cracks across all corners of the panel. The cracks were continued to develop during the test but did not lead to any reinforcement failure thus no structural failure occurred due to the propagation of the corner cracks. The test was successfully run up to the temperature of 800°C, when a large crack at the centre of the slab occurred and the test had to be stopped as the crack spread over the whole slab depth. Improper welding of the mesh reinforcement was explained to be the reason for the crack to occur at the centre of the slab. Figure 4.35 illustrates the composite panel response from the numerical model.

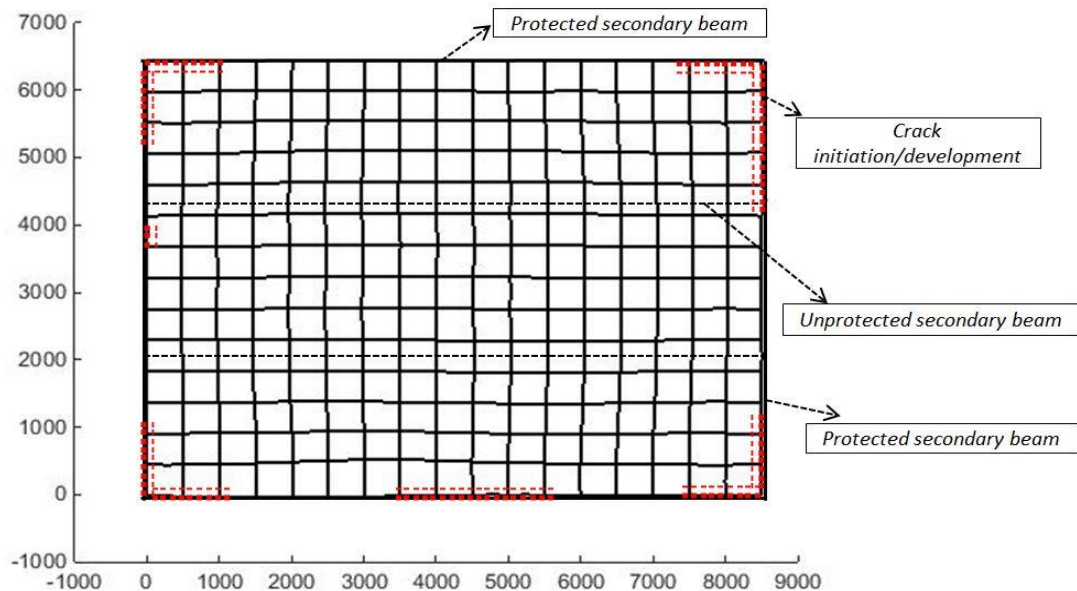


Figure 4.35: Crack development of FRACOF test, *Vulcan*

The numerical model of the test in *Vulcan* also identified the initiation of cracks in concrete across all corners of the floor area. The cracks in the model continued to develop at rising temperature; however, no fracture of reinforcement was occurred during the analysis. This is very similar to the behaviour observed during the test. As mentioned before, the main purpose of the FRACOF test was to further investigate the development of membrane forces within the slab area; therefore, no detailed information of the crack development within the tested panel was provided in the test report [49]. Although no quantitative comparison in terms of crack propagation was possible between the model and the test data, yet the numerical model incorporating the newly developed break element could successfully identify/trace the occurrence/development of the cracks around the edges of the composite floor panel.

4.5 Conclusion

Three series of experimental tests on composite joints at ambient temperature with different bare steel connections have been modelled in *Vulcan* software in order to validate the newly developed break element. The developed numerical model for the analysis of the experimental data is also capable of predicting the occurrence of the initial cracks, tracing the behaviour of the mesh reinforcement represented at each break element and the sequence of the failure of the reinforcement in the composite slab. A flexible end plate connection is generally assumed to be a pin connection with only a limited level of rotational rigidity; therefore, a semi-rigid connection element with bilinear rotational stiffness property was used to represent the equivalent rotational stiffness of the tested joints in the experiments in both the elastic and plastic zones up to the failure of the mesh reinforcement in tension. The rotational stiffness for the connection element in all numerical models was calculated from the moment-rotation curve of the tested steel connection. The performance of the newly developed break element was further investigated through a qualitative comparison between the *FRACOF* floor test [49] and the numerical model in *Vulcan*.

The numerical model of a composite connection in *Vulcan*, incorporating the newly developed break element, is capable of predicting the rotational response of the composite joint with a reasonable level of accuracy.

Chapter 5

5. Parametric Studies

Upon successful validation of the new break element, a parametric study was conducted in order to investigate the influence of discrete cracking on the overall performance of a structure in terms of maximum vertical deflection, developed crack width and rotational displacement of the beam-to-beam and beam-to-column composite connections. Two scenarios are considered in this chapter.

5.1 Case study I: Composite frame with rigid connections

The first study contains a composite-steel panel as a part of a conventional flooring system incorporating metal decking and composite beams. Figure 5.1 illustrates the plan view of the composite frame used by [107] in his study.

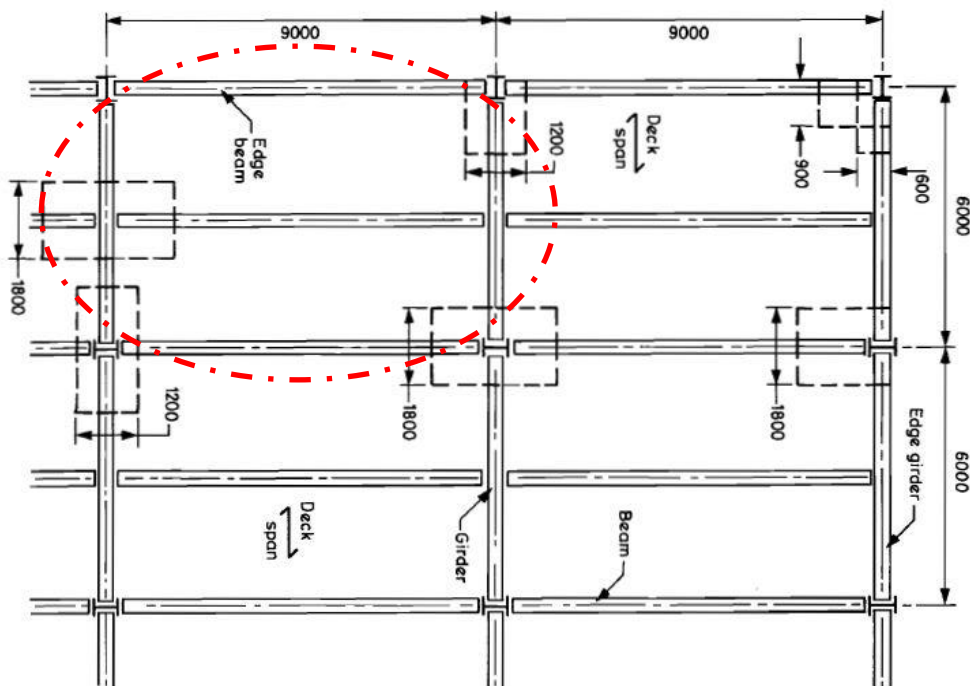


Figure 5.1: Composite floor arrangement [107]

In order to investigate the influence of the new element, the model-scale composite frame of a single panel, as indicated by the red-dotted line in the above figure, has been created in *Vulcan* using an assemblage of finite plate slab elements acting

compositely with the steel beam line elements beneath them through a series of break elements placed along the length of the edge beams. The model was based on the 9m x 6m slab panel and an applied uniform load of 10kN/m^2 . The load was applied to the model over a few incremental load steps (25 steps) at the beginning of the analysis at ambient temperature before increasing temperature in accordance with the standard fire curve (ISO834). The supporting edge beams were assumed to be protected (primary beams remain at the temperature of 20°C , during the analysis) and the increasing temperature was applied to the bottom face of the concrete floor area and the unprotected secondary beam at the middle of slab area. Table 5.1 represents the material properties used in the model.

Concrete compressive strength (f_{ck})	35 N/mm ²
Slab thickness	120mm
Mesh reinforcement	A142
Yield strength of reinforcement	500 N/mm ²
Primary edge beam	305 x 165 x 46UB
Secondary edge beam	356 x 171 x 67UB

Table 5.1: Section properties – 9m x 6m panel

The model was created in *Vulcan* using a mesh size of 216 slab elements (element length of 0.5m), as suggested by the convergence study presented in chapter 3, section 3.1. According to that, the mid-span vertical deflection of the floor area is not significantly influenced with element size of less than 0.5m

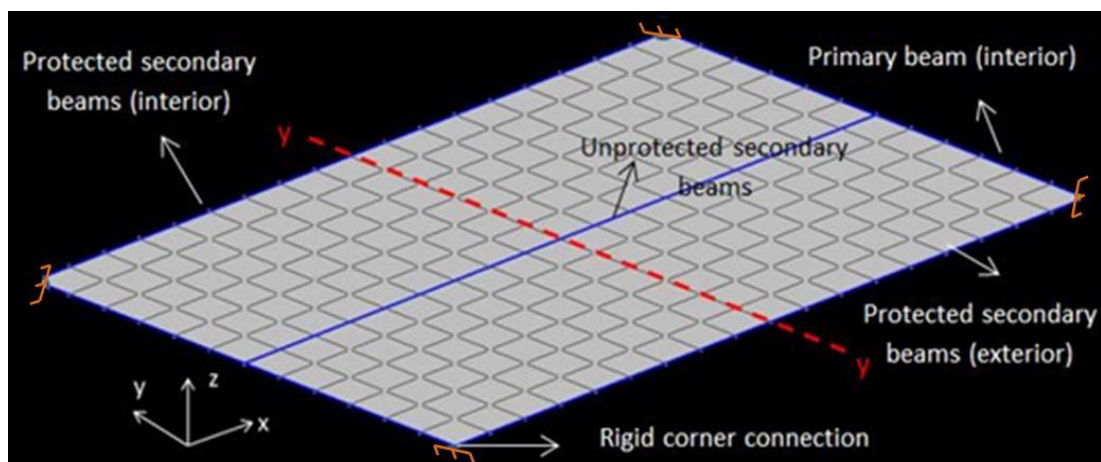


Figure 5.2: 3D isometric view of full floor slab area with 864 elements

5.1.1 Boundary conditions

The numerical model for the composite panel was horizontally and rotationally restrained in the x-direction and around the y-direction respectively along the length of the primary edge beams at the shorter span of the panel to represent the continuity of the composite frame beyond the primary beams. The frame has also been restrained horizontally and rotationally in y-direction and around x-direction respectively along the length of interior secondary edge beam over the longer span of the panel. The other secondary beam along the longer span is set to be free in all directions to represent the exterior behaviour of the edge beam. Furthermore, the slab elements were set to be free in all degrees of freedom except rotation around z-direction, since this is a required by the software to prevent unnecessary instability during the analysis. Figure 5.3 represents the external boundary condition applied at different structural members within the numerical model. Table 5.2 shows the detailed of the applied boundary condition to the created model in *Vulcan*.

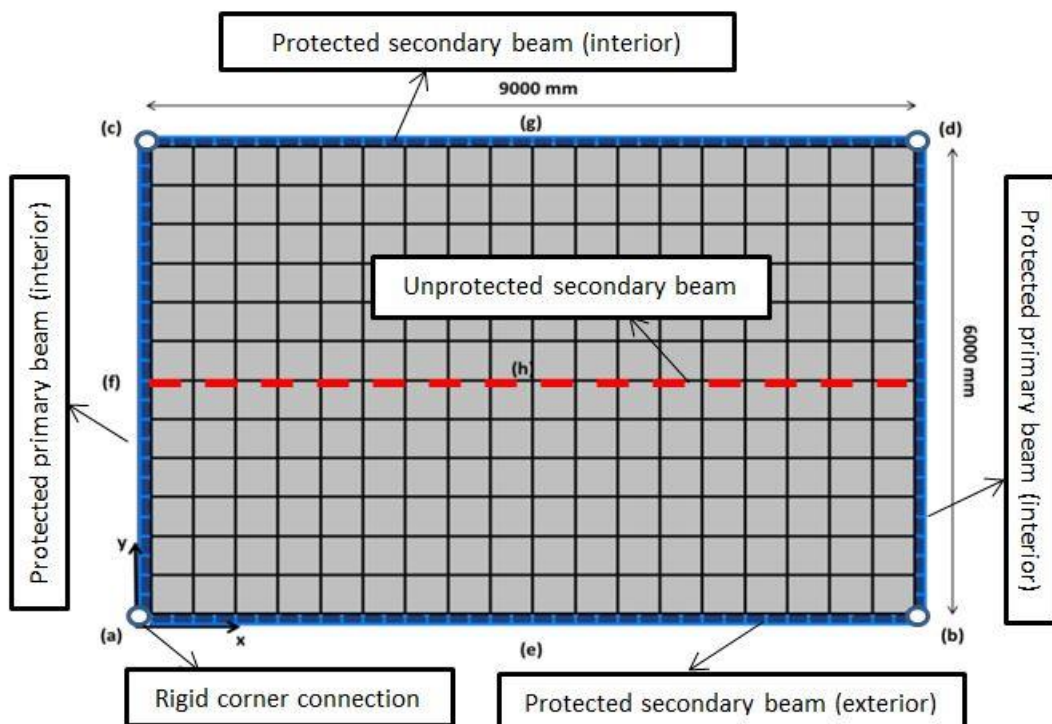


Figure 5.3: Boundary conditions for model-scale interior composite panel

(a)	δ_x	fixed	δ_y	fixed	δ_z	fixed	θ_x	fixed	θ_y	fixed	θ_z	fixed
(b)	δ_x	fixed	δ_y	fixed	δ_z	fixed	θ_x	fixed	θ_y	fixed	θ_z	fixed
(c)	δ_x	fixed	δ_y	fixed	δ_z	fixed	θ_x	fixed	θ_y	fixed	θ_z	fixed
(d)	δ_x	fixed	δ_y	fixed	δ_z	fixed	θ_x	fixed	θ_y	fixed	θ_z	fixed
(e)	δ_x	free	δ_y	free	δ_z	free	θ_x	free	θ_y	free	θ_z	free
(f)	δ_x	fixed	δ_y	free	δ_z	free	θ_x	free	θ_y	fixed	θ_z	free
(g)	δ_x	free	δ_y	fixed	δ_z	free	θ_x	fixed	θ_y	free	θ_z	free
(h)	δ_x	free	δ_y	free	δ_z	free	θ_x	free	θ_y	free	θ_z	fixed

Table 5.2: Boundary condition for model-scale interior composite panel

Due to the computational time and effect of modelling a full sized composite frame (9m x 6m), it was decided to model half of the panel. Using the symmetric line y-y as shown in figure 5.2; the full sized model was divided into 2 equal halves with dimensions of (4.5m x 6m), each with 108 slab elements. The boundary condition of the model at the line of symmetry (y-y) was chosen in order to represent the same condition as the full-scale model. Therefore, the slab nodes at the symmetry line were fixed against moving in the direction perpendicular to the line y-y as well as rotation around it. The same arrangement was applied to the boundary condition of the central beam element along the longer span of the panel.

5.1.2 Influence of reinforcement ratio on vertical deflection/ crack development of composite panel

The influence of reinforcement ratio on the overall performance of the floor area, and in particular the effect of different reinforcement ratios on the crack development around the edge of the slab, were studied through numerical modelling of the composite panel using different standard isotropic reinforcing mesh sizes of A142, A252 and A393. These are meshes with 6mm, 8mm and 10mm diameter of reinforcing bars at 200mm centres with yield strength of 500 N/mm² and ultimate strain of 5%. To comply with the design assumption from [107] the position of the reinforcing bars was assumed at half depth of the slab elements, which coincides with assumed reference plane of the model in *Vulcan* analysis. Therefore, figures in

this chapter are constructed based on the behaviour of different structural members at the position of the reference plane. In order to provide a better understanding of the influence of the recently developed break element on the structural behaviour a comparative analysis has been calculated using the original version of the software *Vulcan* (called *Vulcan1* from now on) along with the updated version of the software incorporating the break element (*Vulcan2*).

5.1.2.1 Composite panel with A142 mesh reinforcement

The results of the comparative analysis between *Vulcan1* and *Vulcan2* in terms of the slab vertical deflection and the horizontal crack development for A142 reinforcement are shown below. Figure 5.4 and 5.5 illustrate the slab 3D vertical deflection and the magnified horizontal displacement of the modelled composite panel respectively.

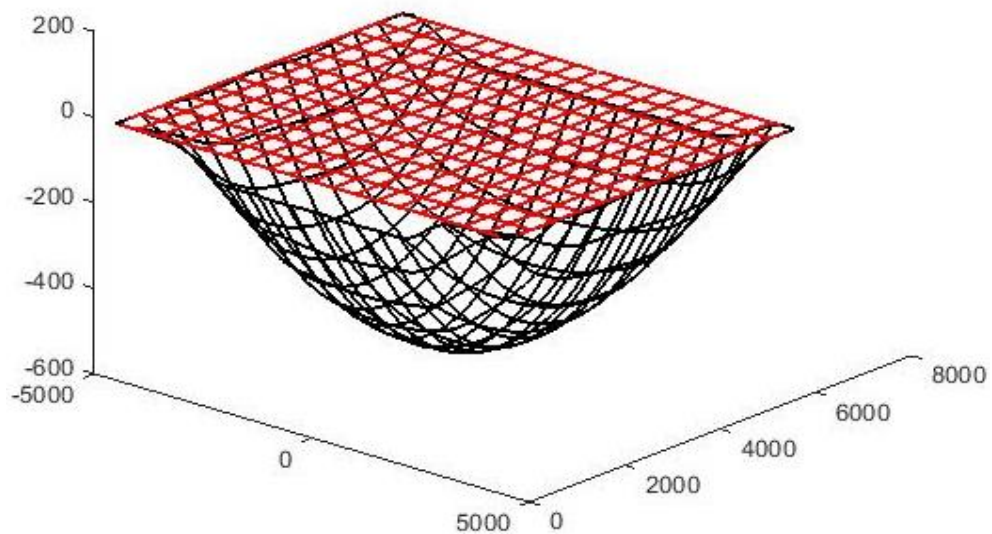


Figure 5.4: 3D view of the deformed shape of the A142 interior composite panel

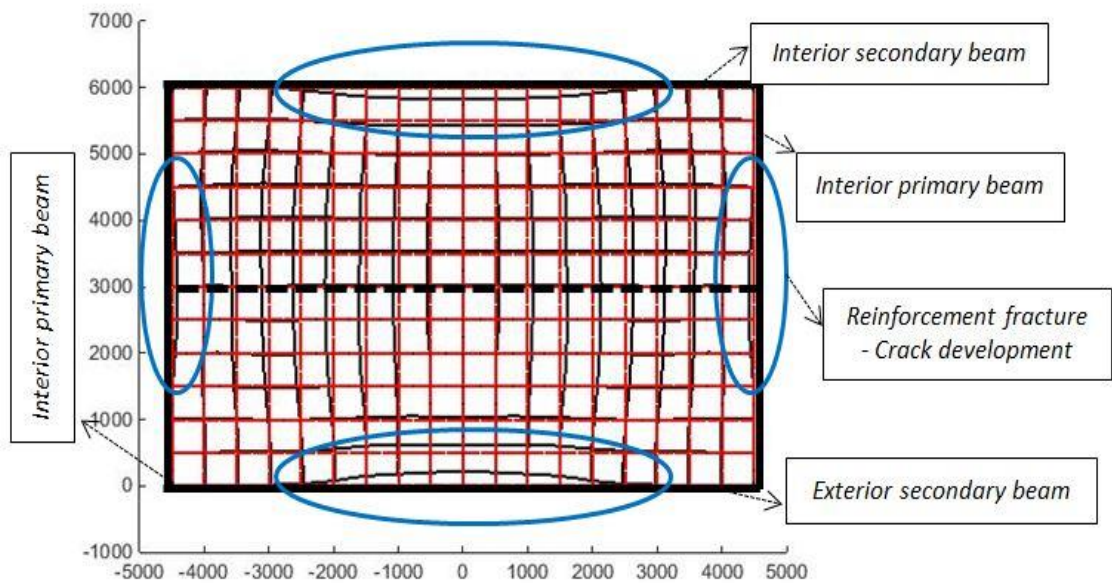


Figure 5.5: Plan view of slab horizontal movement, A142 interior composite panel

The A142 composite slab was cracked across the protected edge beams as the secondary unprotected beam at the middle of the slab loses significant stiffness under rising temperature causing large vertical deflection at the centre of the slab. As it has already been explained in section 3.4.1, once the concrete at the top of the protected beam cracks as a result of the generated hogging bending moment, the available reinforcement ratio is unable to fully transfer the load within the section and therefore only one discrete crack occurs, consequently, the load carrying capacity of the section reduces and the crack width starts to develop along with the rebar being de-bonded from the surrounding concrete and ruptures once it reaches the ultimate strain level. Figure 5.6 represents the central vertical displacement of the slab under elevated temperature. Comparison between the graphs from *Vulcan1* and *Vulcan2* clearly indicates the influence of discrete cracking around the edge on the overall vertical deflection of the panel in particular for the range of temperature beyond 720°C, where there is sudden increase in the vertical deflection of the panel. The vertical deflections from the software have also been compared against the well-known span/20 limit at elevated temperature.

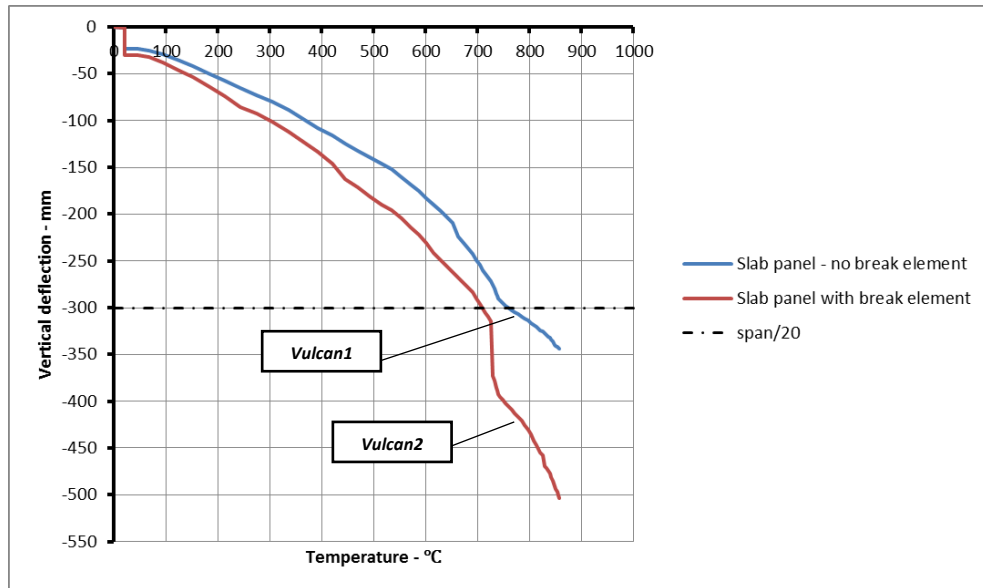


Figure 5.6: Comparison of the A142-slab central deflection from *Vulcan1* and *Vulcan2*

As vertical deflection of the panel increases, some of the reinforcement at the edges of the slab will be fractured as a result of pure tensile forces in this region. Figures 5.7 to 5.9 illustrate the crack development along the edges of the slab in both directions. As is evident from the figures, the crack along the internal secondary beam starts to develop at temperatures around 400°C, where the vertical deflection of the slab is about 150mm. The crack then widens as the temperatures increases and it reaches the maximum crack width of approximately 25mm when the temperature at the bottom flange of the unprotected secondary beam is about 858°C. Along the length of the exterior edge beam the first failure of reinforcement occurred at around 700°C and the crack width developed beyond this temperature. Figure 5.9 shows the horizontal movement of the slab at its edge along the interior primary edge beam. It can be seen that the centre of the shorter span is in compression during the analysis up to the temperature of approximately 600°C, which can be explained by the compression force generated from the thermal expansion of the unprotected secondary beam.

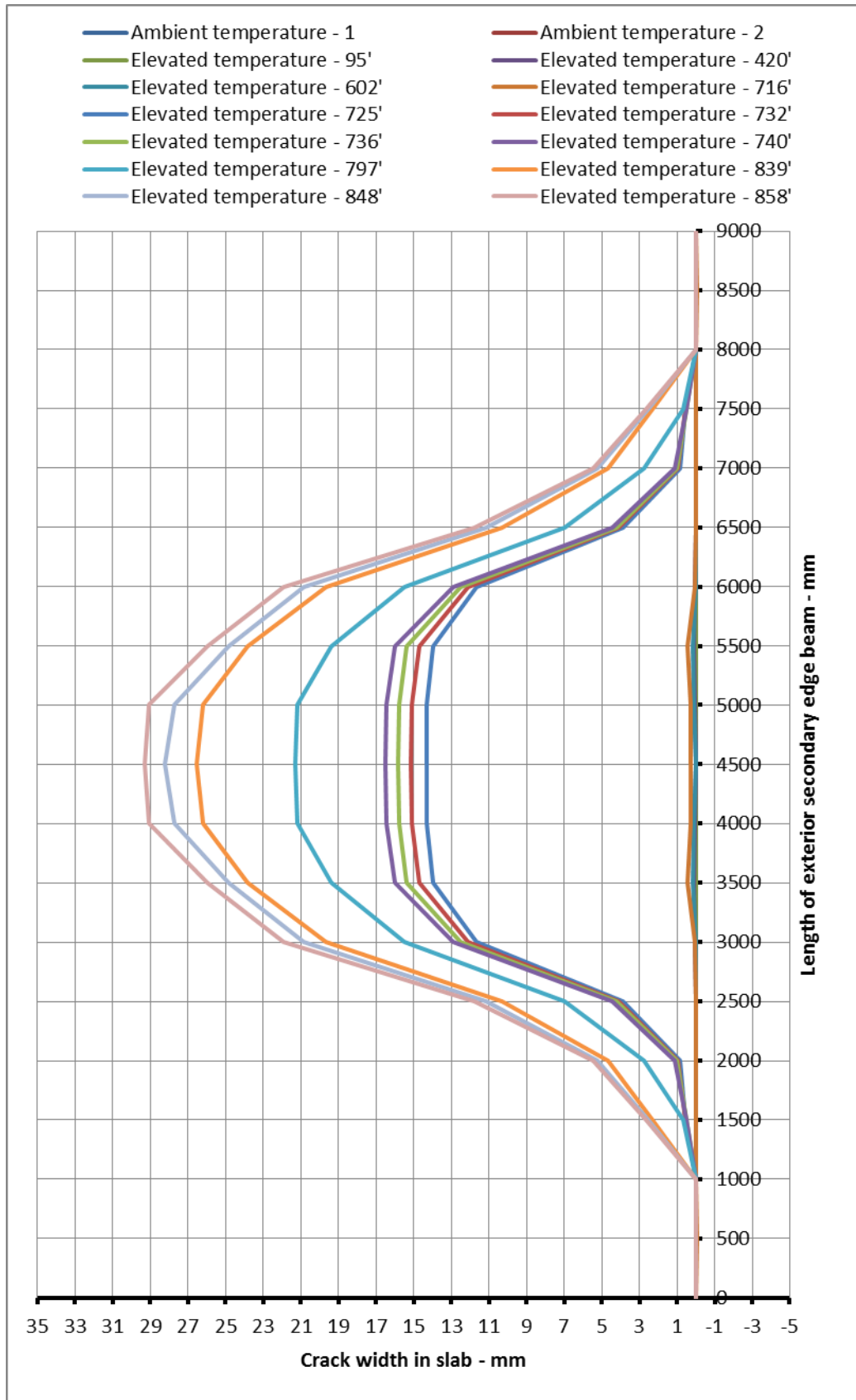


Figure 5.7: Horizontal crack development – exterior secondary edge beam, A142 panel

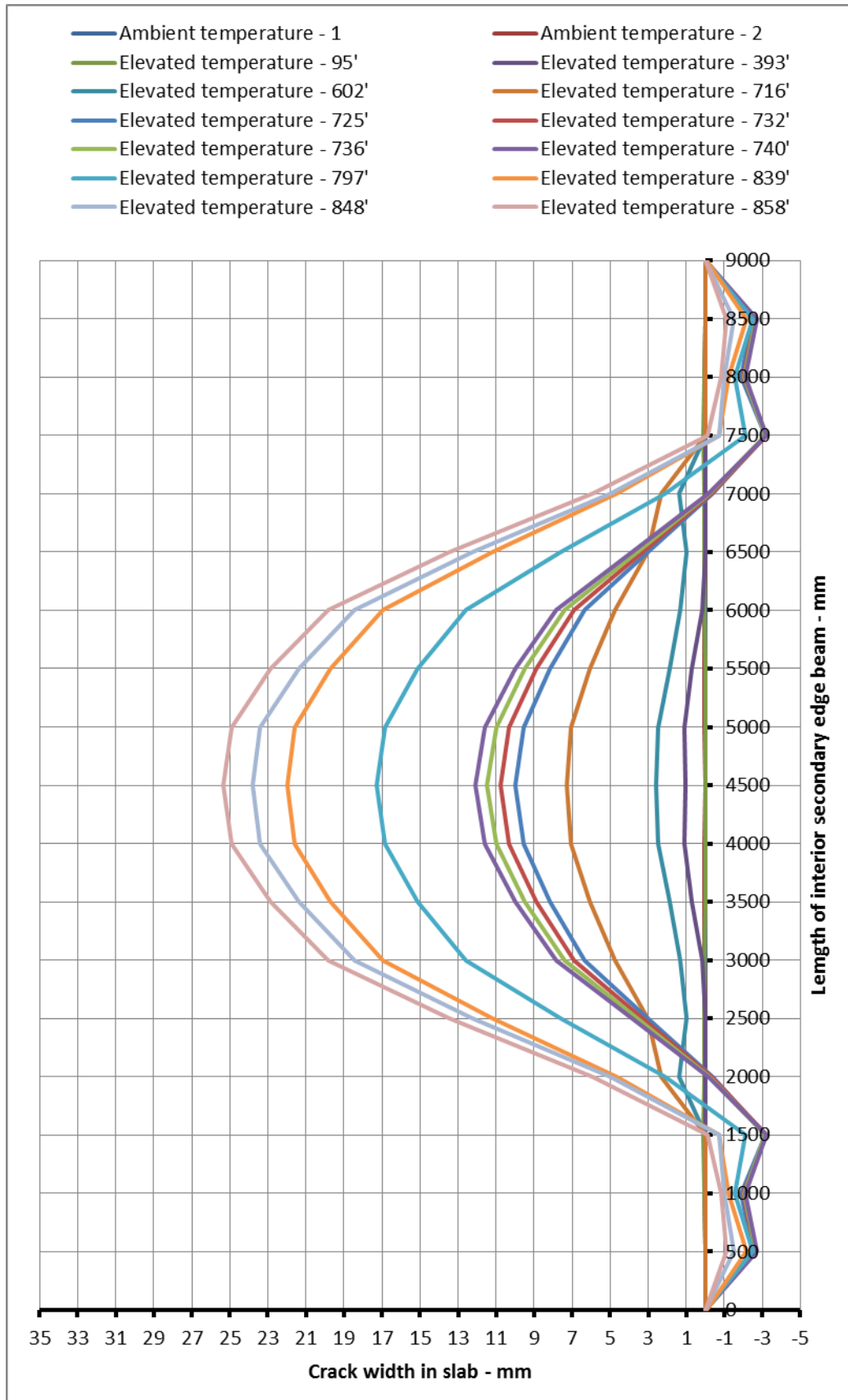


Figure 5.8: Horizontal crack development – interior secondary edge beam, A142 panel

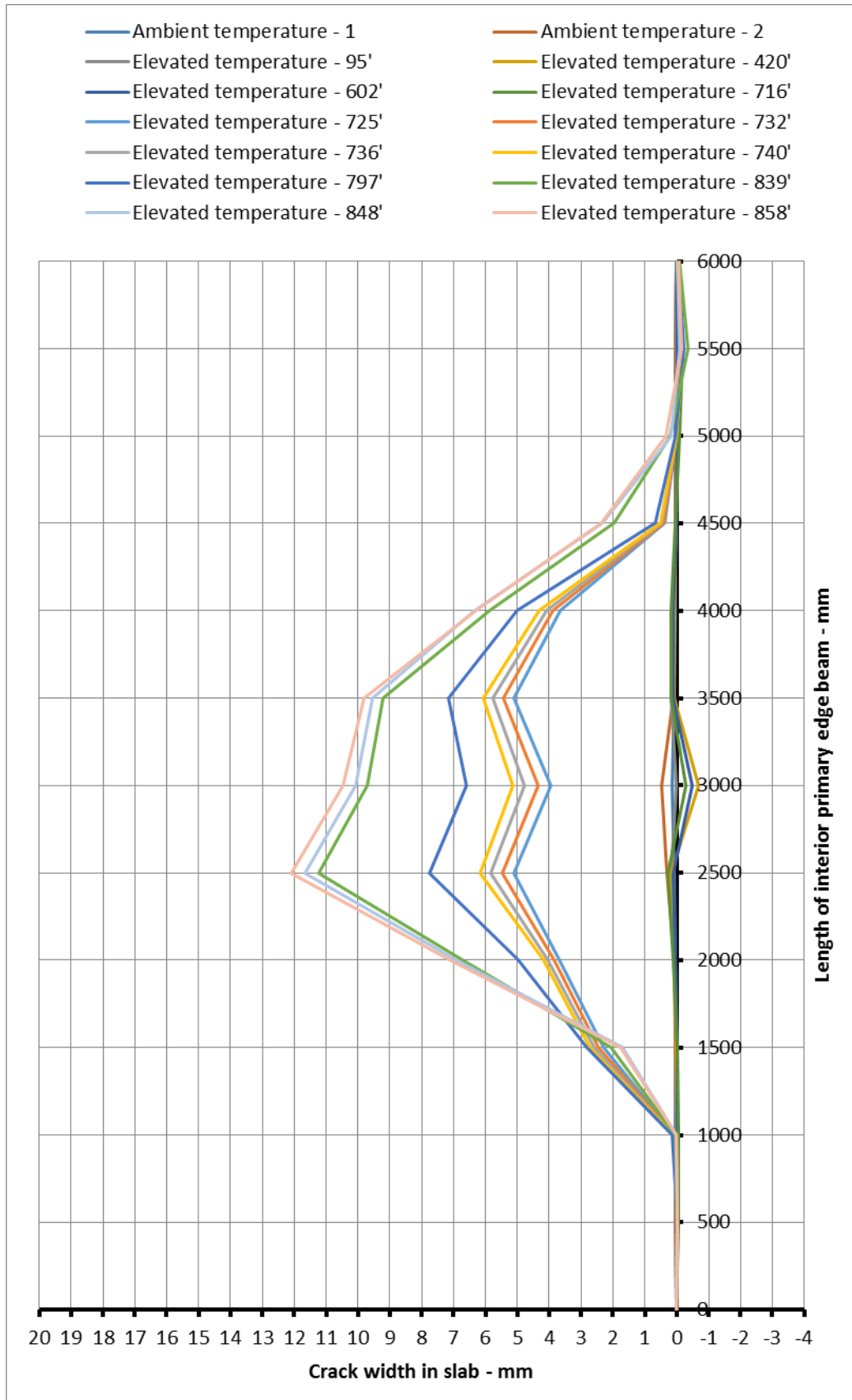


Figure 5.9: Horizontal crack development – interior primary edge beam, A142 panel

It is normally expected that no crack would occur along the length of the exterior beam as there is no horizontal restraint to limit the out of plane movement of the beam and therefore, the slab and steel beam are expected to move together towards the centre of the slab when the slab goes through large deflection. Further investigation was carried out to understand why in figure 5.7 the composite slab cracked along the length of its exterior beam. An identical model-scale composite panel was created in the commercial version of *Vulcan* which has the advantage of graphical representation of the structural behaviour. Figure 5.10 is a graphical representation of the similar composite panel modelled in *Vulcan* interface version, showing the distribution of the membrane force at the top surface of the slab floor during the time that the temperature at the secondary unprotected beam reaches 900°C.

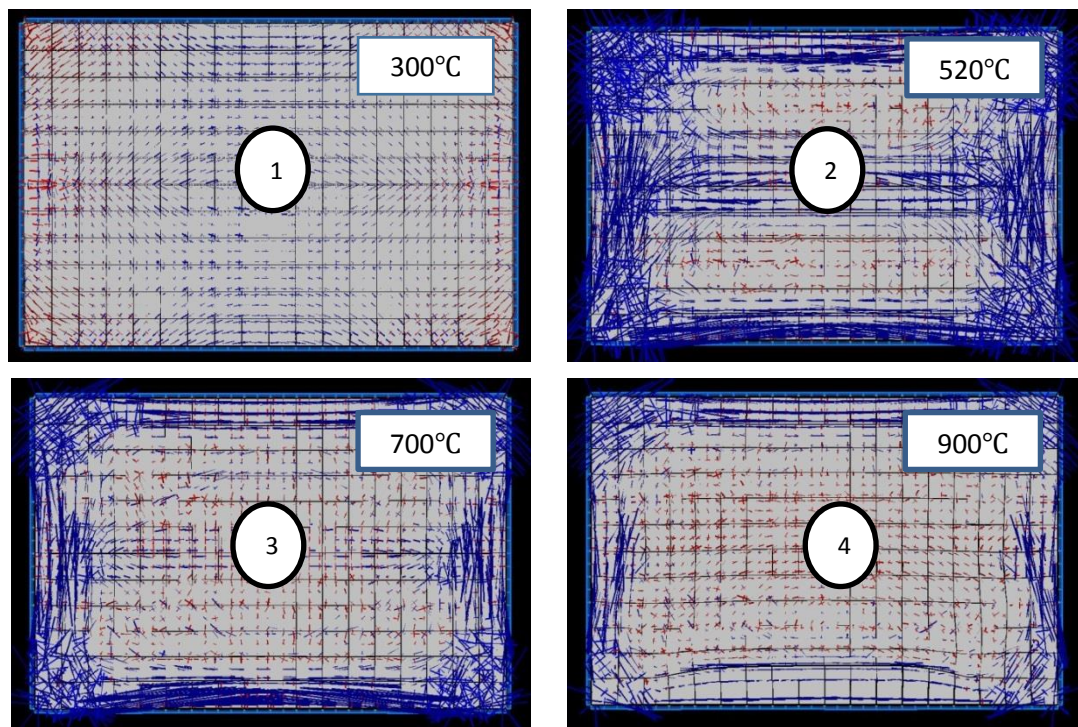


Figure 5.10: Distribution of membrane forces – A142 composite panel

The above figure shows the distribution of membrane forces at the top surface of the slab panel at four different temperature stages of the analysis. Looking at part 2 and 3 of the figure shows that tensile forces are developed over the length of the exterior secondary beam. The magnitude of these tensile forces are maximum at fire temperatures around 720°C, which is very close to the temperature curve of 725°C in

figure 5.7, where a series of reinforce bars are fractured simultaneously as a result of developed tensile membrane forces over the exterior edge of the slab. However, if a higher reinforcement ratio was available no fracture of the reinforcement (and consequently no extensive crack width) would have occurred along the exterior edge of the slab since the slab would be strong enough to pull the exterior steel beam with itself towards the centre of the slab. This also can be seen in part 4 of the above figure (since full composite action was assumed between the slab and the beam). Furthermore, in figure 5.10 the edges of the slab panel, especially around the corners, are subjected to compression forces almost constantly during the analysis. The corner compressive forces are the result of simultaneous inside movement of the slab edges over its longer spans along with pulling forces applied by the secondary unprotected beam. This also explains the developed compressive displacement at the far ends of the interior secondary edge beam as illustrated in figure 5.8.

5.1.2.2 Composite panel with A252 mesh reinforcement

As a part of the parametric study on the effects of the reinforcement ratio on the overall performance of composite structure, the same composite panel as section 5.1.2.1 with A252 mesh reinforcement was modelled in *Vulcan*. The composite panel model was also being analysed using *Vulcan1* and *Vulcan2*. The 3D view of the slab overall deflection and the magnified relative horizontal movement of the A252 composite panel are shown in the following figures.

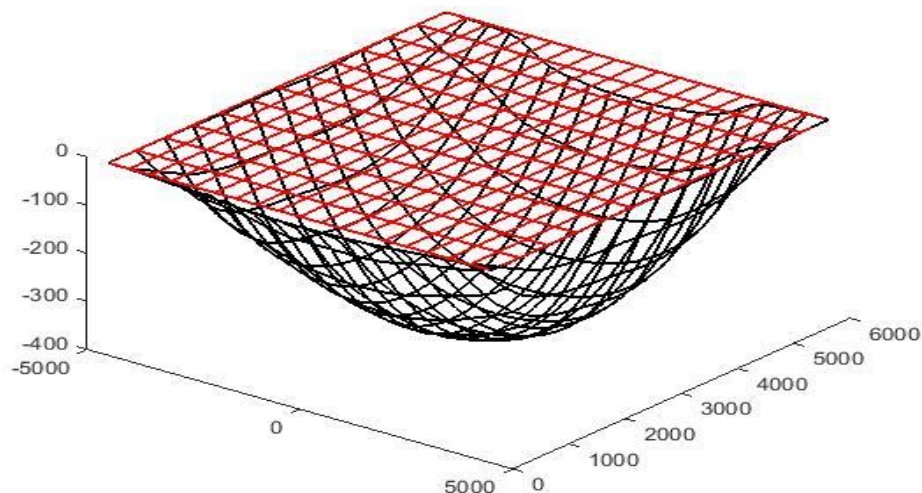


Figure 5.11: 3D view of the deformed shape of the A252 interior composite panel

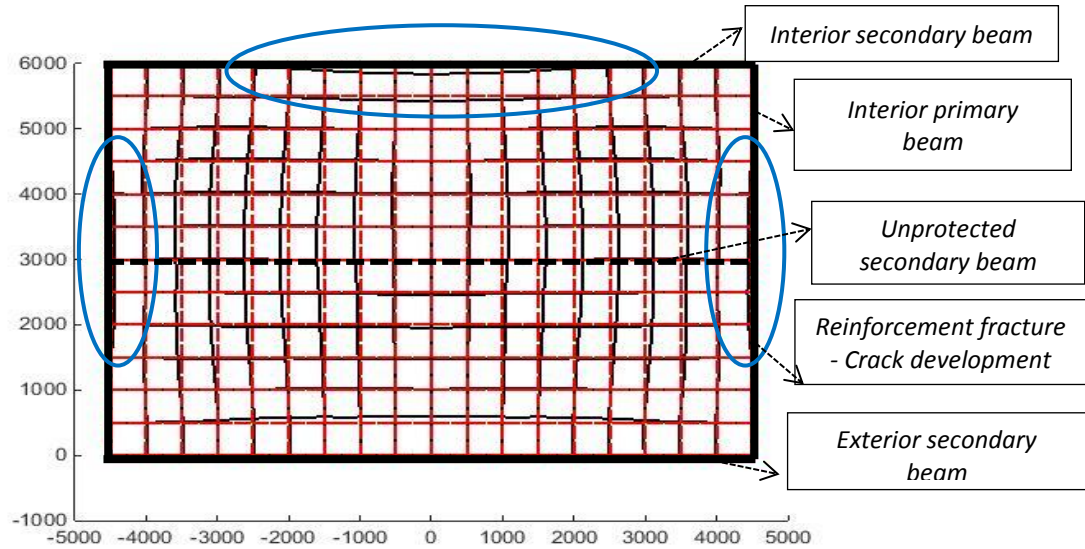


Figure 5.12: Plan view of slab horizontal movement, A252 interior composite panel

Similar to the composite panel with 6mm isotropic reinforcement, cracks in concrete in A252 composite panel also occur as result of edge hogging moment due to the increasing vertical deflection of the floor area. Once concrete at the edge of the panel cracks, the reinforcing mesh starts to extend in length as concrete gets de-bonded from the steel rebar due to tensile membrane forces developed within the slab area. Several reinforcing bars fracture simultaneously as the slab goes through large deflection due to significant loss of stiffness in the unprotected secondary beam. Figure 5.13 illustrates the central deflection for the A252 composite panel at rising temperature.

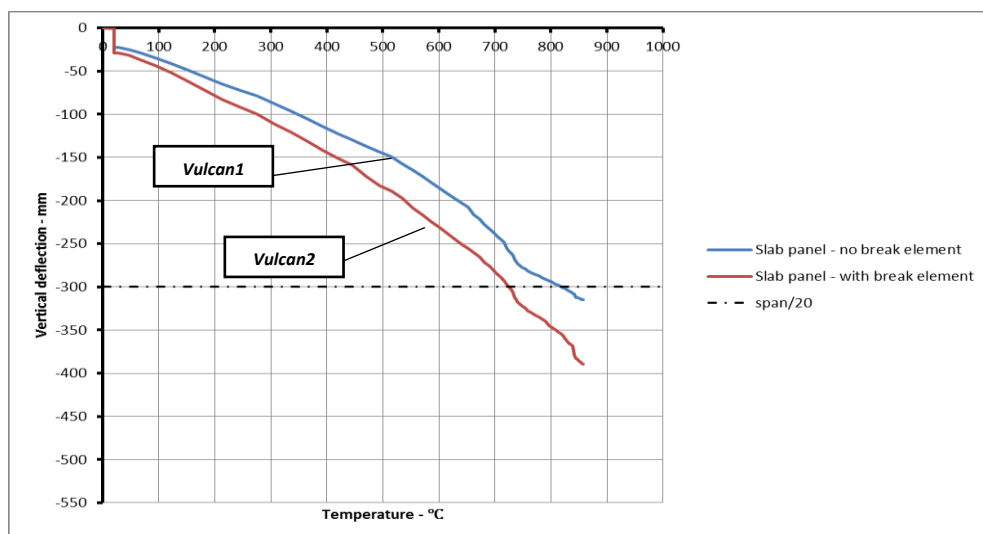


Figure 5.13: Comparison of the A252-slab central deflection from *Vulcan1* and *Vulcan2*

Similar to the A142 panel, comparison between *Vulcan1* and *Vulcan2* clearly shows the influence of discrete cracks in hogging moment areas on the overall vertical deflection of the A252 composite panel. The vertical deflections presented in figure 5.13 follow the similar pattern as those shown in figure 5.6 but with smaller magnitude. This is mainly due to a higher ratio of mesh reinforcement in composite slab, which in turn makes the slab stiffer and consequently result in less vertical deflection. Both calculated vertical displacements from *Vulcan1* and *Vulcan2* for the higher reinforcement ratio did not exceed the BRE limit however they passed the typical span/20 limit in fire condition.

Figures 5.14 to 5.15 show the relative horizontal movement of the composite slab around the edges and towards the centre of the panel. As is evident from the graph in figure 5.14 the maximum crack width along the interior secondary beam shows the value of around 17mm at just over 855°C, where the slab central deflection reaches the maximum of 393mm. Furthermore, looking at the plan view in figure 5.12 it can be observed that unlike the composite panel with A142 mesh, no fracture of the reinforcement (excessive crack) occurred along the edge of the slab over the exterior secondary beam. The reason has been previously discussed in section 5.1.2.1. These also explain the negligible compressive displacement (unlike figure 5.8) at far ends of the longer interior beam. The slab along the exterior beam remains in compression, since no failure of the reinforcements occurred at this edge (figure 5.10). Therefore, the composite panel has been pulled in from three directions (interior secondary beam and the two exterior primary beams) rather than four directions similar to that of A142 composite panel. As a result no significant outward movement occurs at the corners of the slab.

Another set of cracks also developed at the shorter spans of the panel along the protected interior primary beams. The crack in concrete in this direction starts to develop at temperature around 730°C, which is the temperature that unprotected secondary beam starts to lose most of its bending capacity as a result of rising temperature. This can also be identified in figure 5.13, where the graph from *Vulcan2* shows a rapid change in rate of increasing vertical displacement beyond the temperature of 720°C. Several reinforcing bars fractured simultaneously at higher

temperature resulting in the maximum crack width of 6.7mm to occur. Unlike the crack development along the direction of the longer spans, it can be seen from figure 5.15 that the maximum crack width in this direction did not occur at centre of the shorter span. This can be explained by the thermal expansion at far ends of the secondary unprotected beam that result in applying compressive forces in the slab at the top of the beam-to-beam connection.

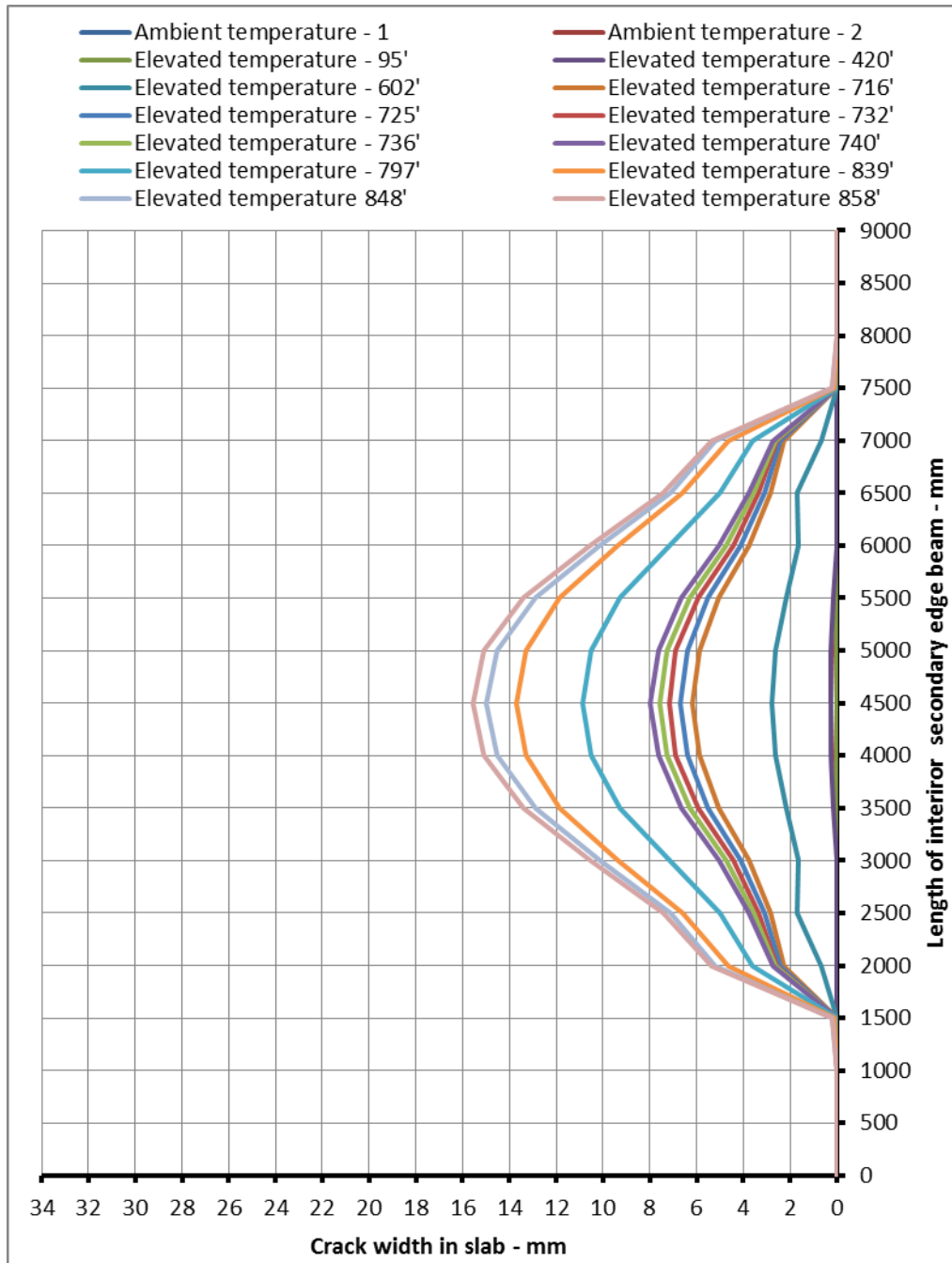


Figure 5.14: Horizontal crack development – interior secondary edge beam, A252 panel

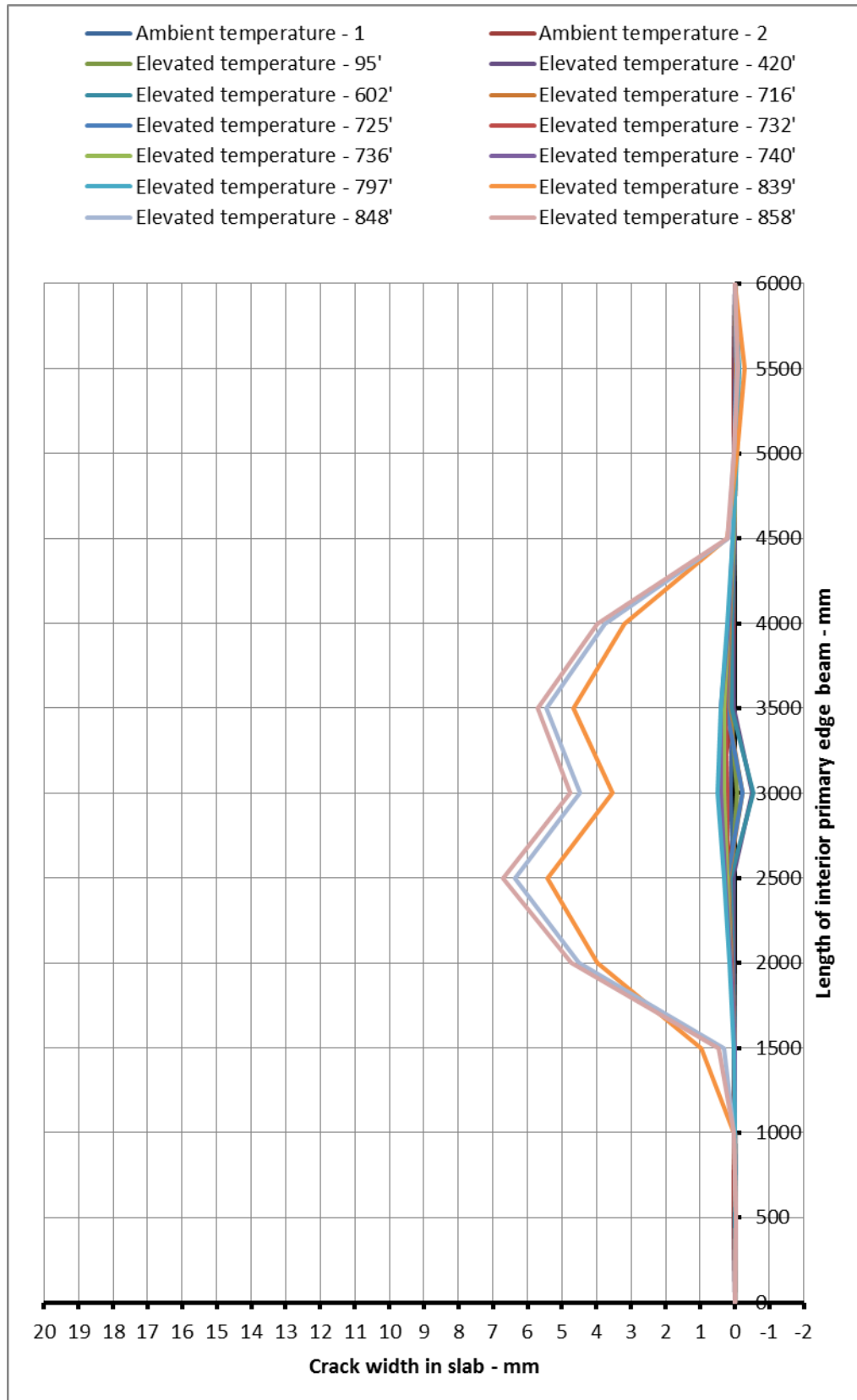


Figure 5.15: Horizontal crack development – interior primary edge beam, A252 panel

5.1.2.3 Composite panel with A393 mesh reinforcement

The above model for composite panel at elevated temperature was also analysed with a greater isotropic reinforcement of A393, which means having 10mm diameter bars spacing at 200mm centre to centre along both directions. Figure 5.16 illustrates the comparison between the resulting vertical deflections of the A393-composite panel at elevated temperature from *Vulcan1* and *Vulcan2*.

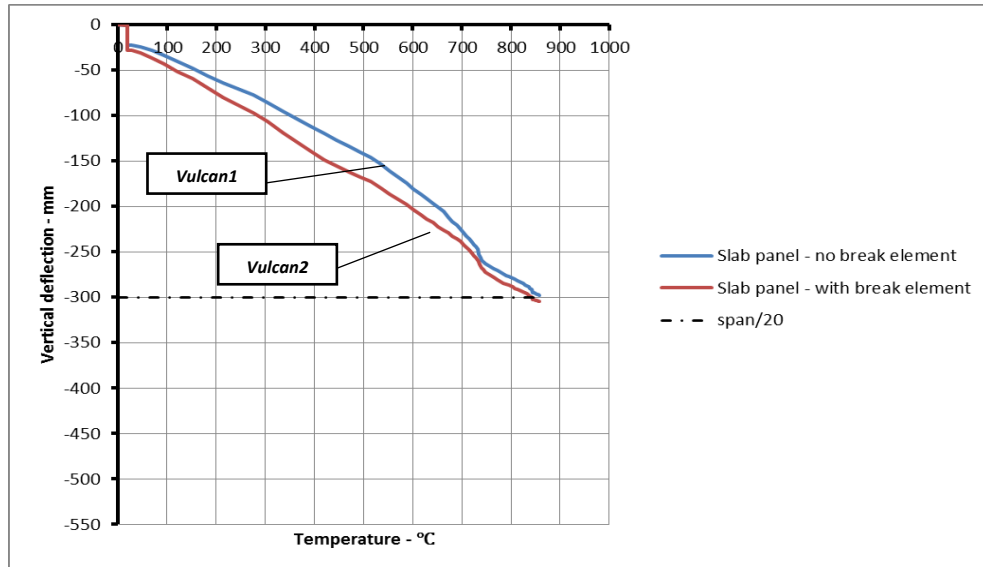


Figure 5.16: Comparison of the A393-slab central deflection from *Vulcan1* and *Vulcan2*

As it is noticeable from the graphs in the above figure, despite the fact that the presence of higher reinforcement ratio results in smaller vertical deflection of the slab panel, the plotting data from both versions of the software generally behaves similarly during the analysis both in terms of pattern and magnitude.

With regards to the development of the crack along the edges of the panel, the concrete at the hogging moment areas was cracked once the tensile force in slab (as a result of developed hogging moment) at the top of the protected beam exceeds the tensile capacity of the concrete, however, no fracture of the reinforcing mesh (failure of the break element) was identified by the software during the analysis. This is mainly due to the fact that composite panel with higher reinforcement ratio are generally stiffer in bending with an enhanced load carrying capacity, therefore, even the concrete failed in tension, the width of the crack was negligible as presence of stronger reinforcement result in less vertical deflection of the slab and consequently less tensile forces.

5.1.3 Influence of reinforcement ratio on connection performance of composite panel

In order to gain a better understanding about the importance of reasonable modelling of discrete cracks in composite structure the influence of different reinforcement ratio on the rotational performance of the beam-to beam connection in composite structure was also studied. In the model-scale composite panel in section 5.1, the secondary unprotected beam along the longer span of the panel was attached to the adjacent protected primary beams at its two ends using simple pin connection. Using pin connection means that the resisting rotational capacity at the beam-to-beam connection in the analysis is purely due to the presence of composite slab on top of the connection. Therefore, appropriate modelling of the slab continuity in this region can be significantly important when considering the overall behaviour of the composite frame. Figure 5.17 to 5.19 show the rotational displacements of the pin connection used in the numerical model with different reinforcement ratio of A142, A252, and A393 at elevated temperature respectively.

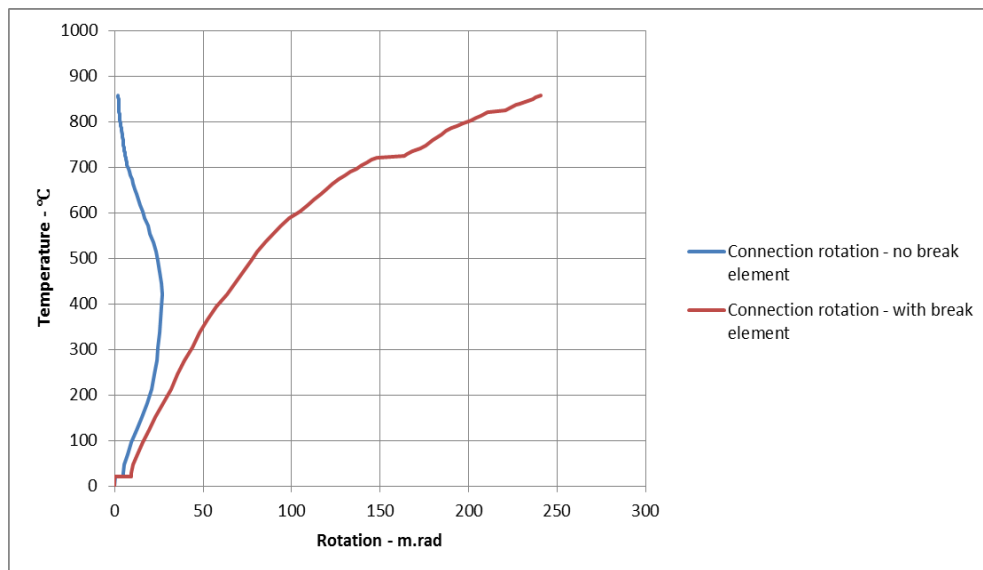


Figure 5.17: Comparison of rotational displacement at connection- A142

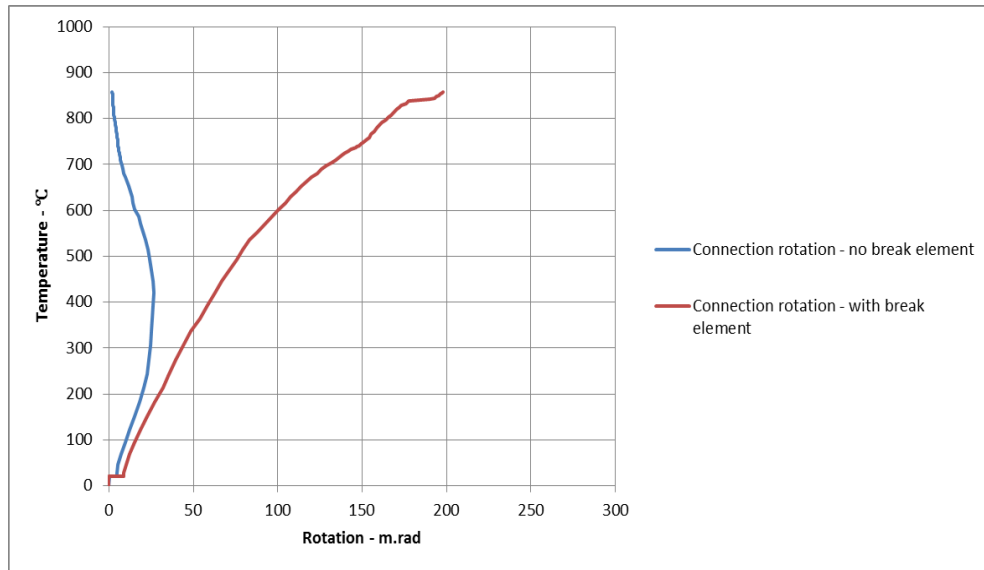


Figure 5.18: Comparison of rotational displacement at connection- A252

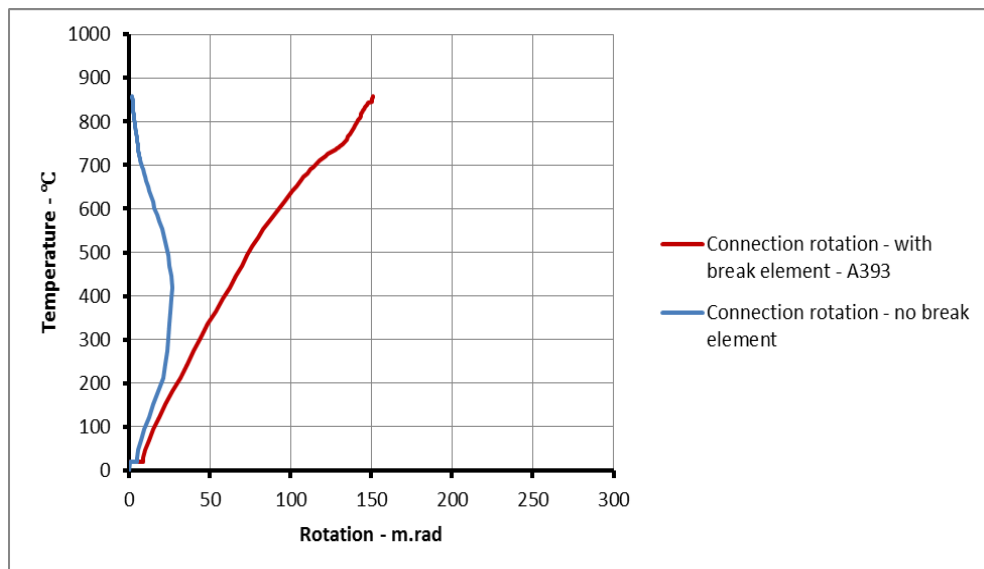


Figure 5.19: Comparison of rotational displacement at connection- A393

Looking at the above plots, it is evident that the appropriate modelling of the slab continuity and the possible crack development in hogging moment regions can significantly influence/alter the rotational behaviour of the steel connection. Once the concrete cracks in tension, the rotational capacity of the composite connection is reduced and the available reinforcement at the crack face will contribute to the overall rotational capacity of the steel connection. Therefore, any increase in the reinforcement ratio would enhance the rotational capacity of steel connection below the slab, which in turn results in reduced rotational displacement at the connection.

This has been clearly presented by the results from *Vulcan2* (red solid lines) in the above figures. The blue lines in these figures are the calculated rotational response of the connection from *Vulcan1* (the original version of the software with no break element included); where the continuity of the slab on to top of the connection was assumed using smeared cracking approach. The backward rotational movement of the connection from *Vulcan1* at high temperature can be explained by the presence of different temperature regimes over the structural members. The unprotected secondary beam is attached to the protected primary beams at its two end. As the temperature within the floor area increases, the unprotected secondary beam starts to experience both vertical deformation and thermal expansion, while the primary beam at the other end of the connection stays cold during the analysis. At the same time the continuous composite slab on top of the connection will also start to move outward as compressive membrane forces develops along the edges of the slab panel. Therefore, the connection becomes subjected to an upward rotation. Considering the results from *Vuclan1* it can be seen that changes in the reinforcement ratio has very little effects on the rotational response of the connection. This is mainly due to the assumption of permanent continuity of the composite slab during the analysis, which in turn results in unrealistic rotational capacity of the connection.

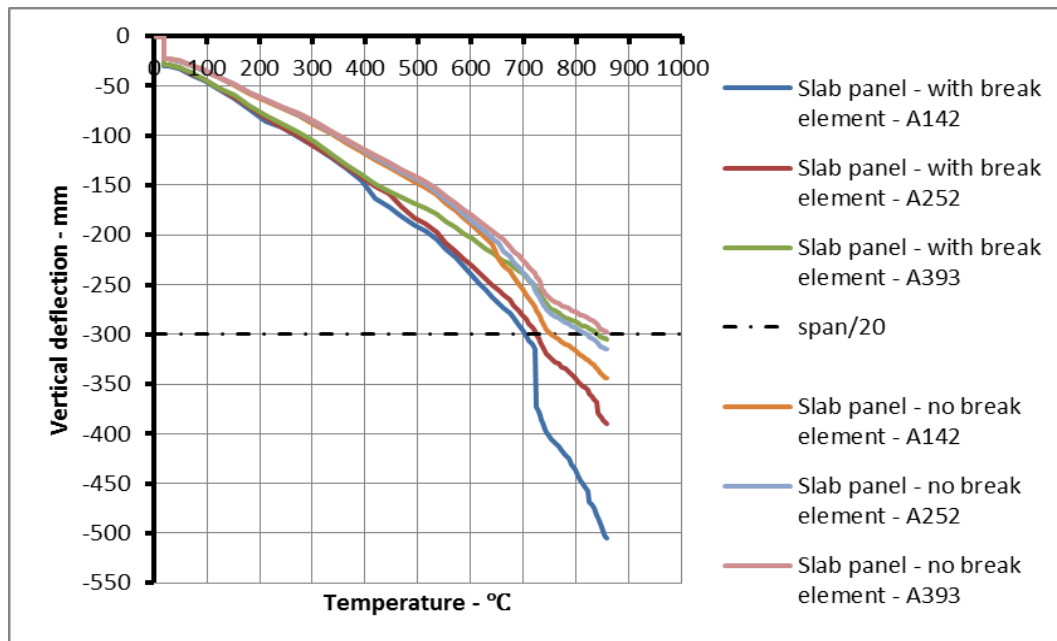


Figure 5.20: General comparison of slab central deflection from *Vulcan1* and *Vulcan2*

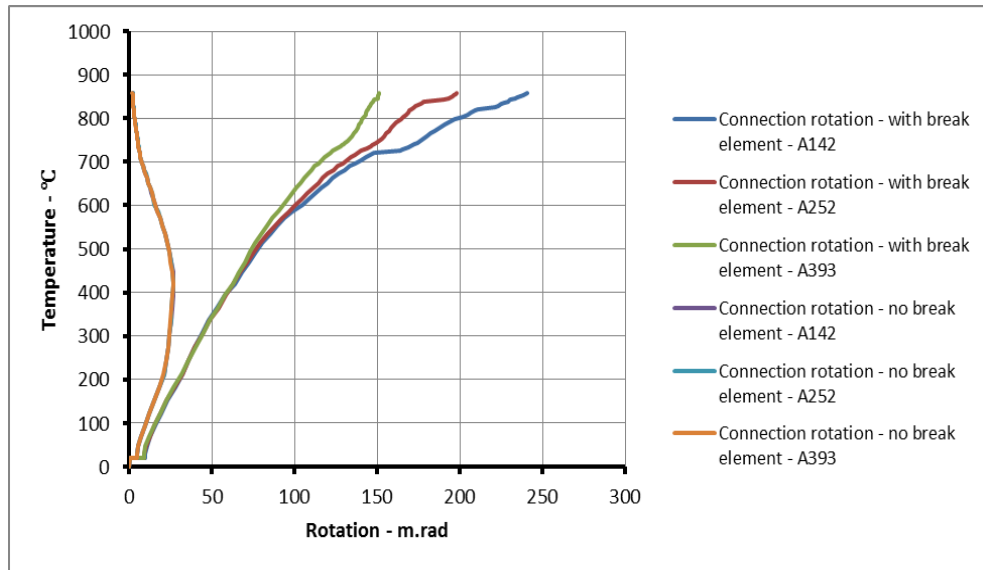


Figure 5.21: General comparison of connection rotational displacement from *Vulcan1* and *Vulcan2*

5.1.4 Influence of reinforcement material properties on vertical deflection/ crack development of composite panel

The influence of reinforcement material properties on the overall performance of the floor area, and in particular its effect on the overall deflection of the slab and the crack development around the edge of the slab, were studied through numerical modelling of the composite panel using different material properties for the steel reinforcement. Therefore, the same composite panel as section 5.1.2.1 was modelled using A142 reinforcement. This mesh has 6mm diameter of reinforcing bars at 200mm centres. However, in order to study the influence of different material properties of steel reinforcement on the composite panel performance a higher yield strength of 600 N/mm^2 along with an ultimate strain of 20% were assigned to the reinforcement of the modelled composite panel. To comply with the design assumption from [107] the position of the reinforcing bars was assumed at half depth of the slab elements, which coincides with the assumed reference plane of the model in *Vulcan* analysis. Therefore, figures in this section are constructed based on the behaviour of different structural members at the position of the reference plane.

Figure 5.23 and 5.24 illustrates the slab 3D vertical deflection and the magnified horizontal displacement of the modelled composite panel respectively.

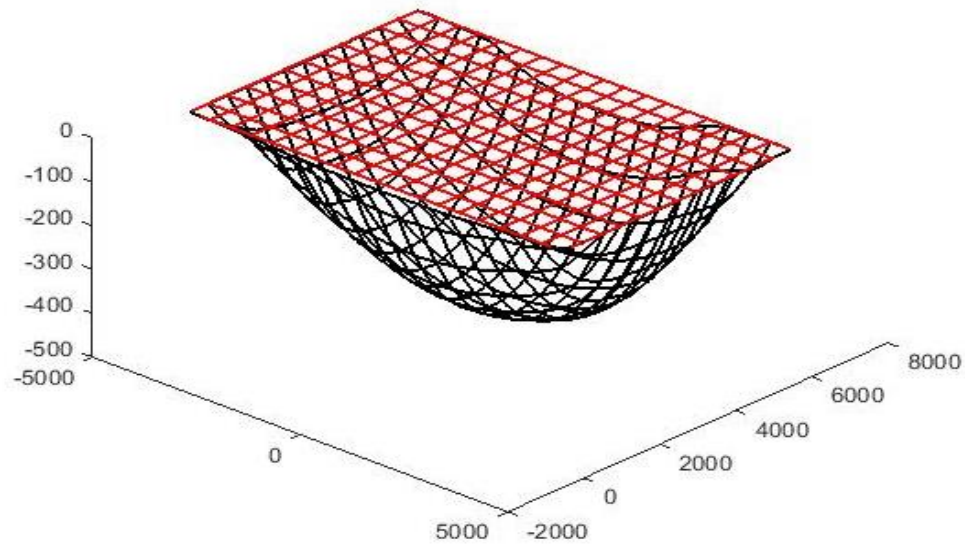


Figure 5.22: 3D view of the deformed shape of the A142 interior composite panel- $f_y=600\text{N/mm}^2$

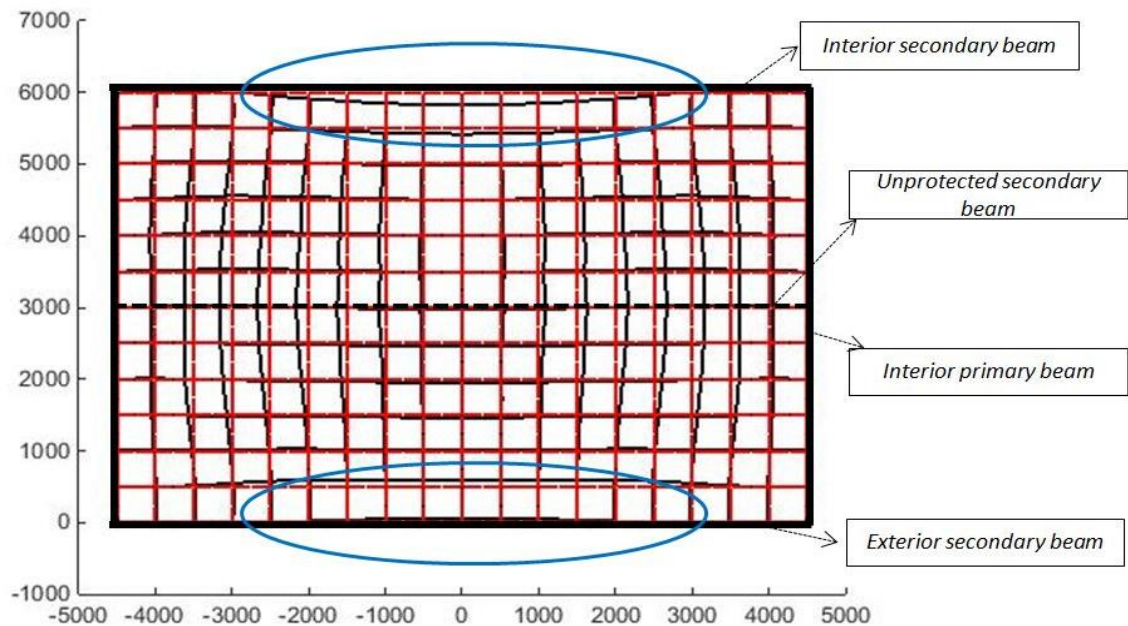


Figure 5.23: Plan view of slab horizontal movement, A142 interior composite panel- $f_y=600\text{N/mm}^2$

As mentioned before, the secondary unprotected beam at the middle of the slab loses a significant amount of its initial stiffness under rising temperature above 500°C . A large vertical deflection occurs at the centre of the slab due to the presence of full composite action between the slab and the unprotected secondary beam through the shear studs. Therefore, the cracks at the top surface of the slab occur due to the presence of the maximum hogging bending moment at the edges of the composite panel as a result of the large vertical deflection in composite slab. The results of the

comparative analysis between *Vulcan1* and *Vulcan2* (the versions with and without break element respectively) in terms of the slab vertical deflection and the horizontal crack development for the slab panel with A142 reinforcement and the higher reinforcement strength/strain capacity are shown below.

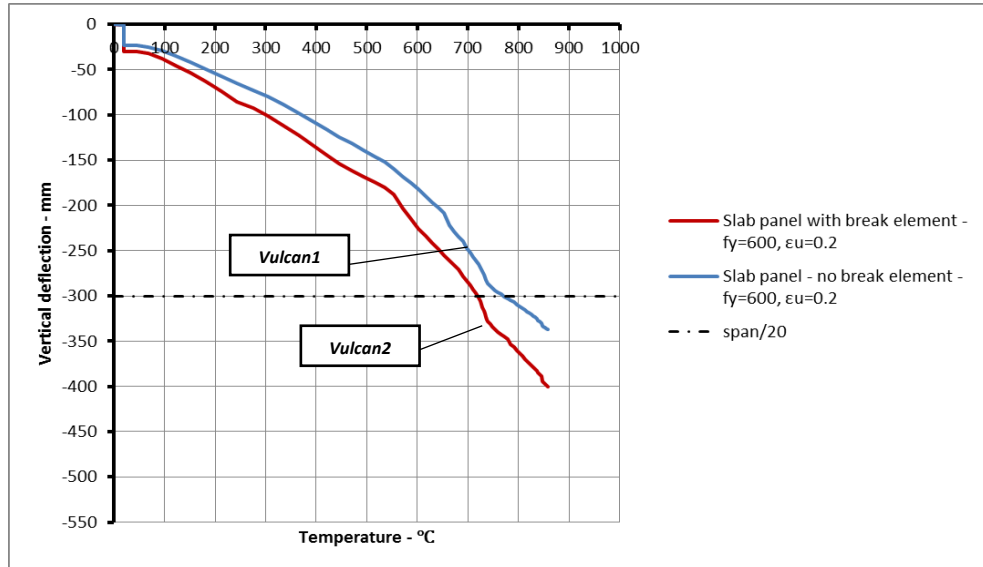


Figure 5.24: Comparison of the A142-slab central deflection from *Vulcan1* and *Vulcan2*

Comparison between the graphs in figure 5.24 clearly indicates the influence of discrete cracking around the edges of the slab on the overall vertical deflection of the panel. The presence of discrete cracking (failure of break elements) results in a larger vertical deflection in the numerical model from *Vulcan2*. The change in magnitude of vertical deflection of the slab became more obvious for the range of temperature beyond 720°C, where there is sudden increase in the vertical deflection of the panel. The vertical deflections from the software have also been compared against the well-known span/20 limit at elevated temperature. Figure 5.25 compares the vertical deflection of the modelled composite panels in section 5.1.2.1 (A1 model, with A142 mesh reinforcement, $f_y=500\text{N/mm}^2$) and section 5.1.4 (A2 model, with A142 mesh reinforcement, $f_y=600\text{N/mm}^2$). As is evident from the graphs, the presence of reinforcement with higher strength capacity can significantly influence the ultimate vertical displacement of the slab, especially at the temperature above 720°C, where the sudden increase in the vertical displacement has been altered. The numerical model with a higher yield strength of the steel reinforcement of $f_y=600\text{N/mm}^2$ (A2

model) indicates the maximum vertical deflection of 400mm at elevated temperature of 858°C, whereas, the maximum vertical deflection obtained by the A1 model is just over 500mm at the same temperature. The comparison between the two numerical models clearly indicates the importance of material properties of steel reinforcement on the overall behaviour of the slab panel, where the 20% increase in the yield strength of the reinforcement results in 25% reduction in the maximum vertical deflection obtained by the numerical model.

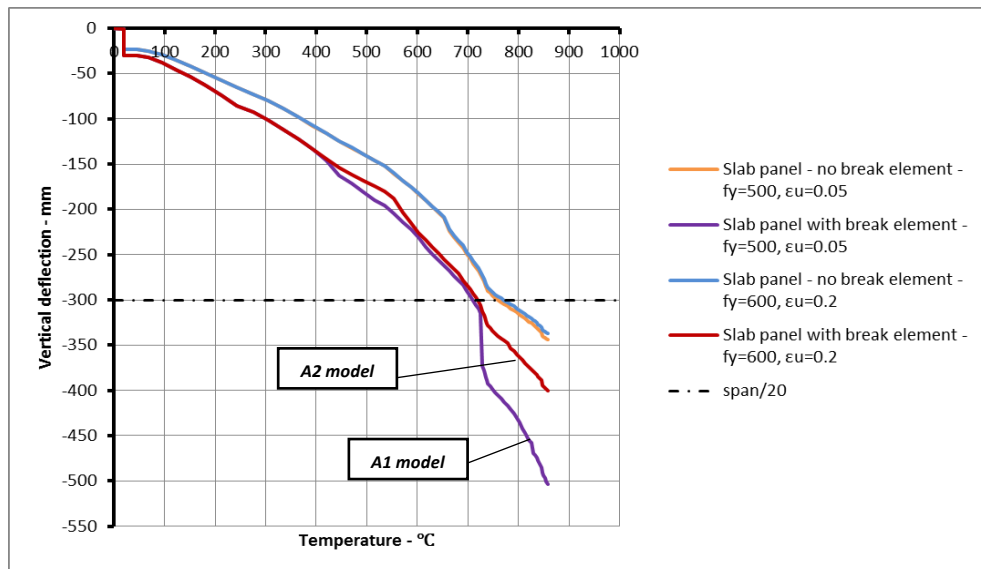


Figure 5.25: Comparison of the A142-slab central deflection from A1 and A2

Figure 5.27 to 5.29 illustrates the crack development along the edges of the slab in both directions for the A2 model. As is evident from the figures, the crack along the internal secondary beam in the A2 model starts to develop (beyond the fracture of some reinforcement) at temperatures around 600°C, where the vertical deflection of the slab is about 225mm. The edge of the slab along the internal secondary beam in the A1 model experienced the crack development (beyond the fracture of some reinforcement) at a temperature around 400°C with the vertical displacement of 140mm. This is also reflected in figure 5.25 where the vertical displacement from the A2 model is less than the displacement from the A1 model between the temperatures of 400°C to 600°C. The A2 model also indicates the maximum crack width of 18mm along the internal secondary beam at the maximum temperature of 858°C, whereas, the maximum crack width of 25mm was picked up by the A1 model at the same

temperature. Along the length of the exterior edge beam in A2 model the first fracture of reinforcement occurs at temperature of 797°C, whereas, the A1 model shows the first fracture of reinforcement along the same edge to occur at temperature of 725°C. The crack continued to develop beyond these temperatures in both models, where the maximum crack width of 29mm and 5mm were recorded by A1 model and A2 model respectively. As explained in section 5.1.2.1 it is normally expected that no crack would occur along the length of the exterior beam as there is no horizontal restraint to limit the out of plane movement of the beam and therefore, the slab and steel beam are expected to move together towards the centre of the slab when the slab goes through large deflection.

Comparing figure 5.27 and figure 5.7 from A1 and A2 models shows that unlike the A1 model where a series of reinforcing bars were fractured simultaneously as a result of developed tensile membrane forces over the exterior edge of the slab, the A2 model indicates the lower number of reinforcing bar to be fractured at the ultimate temperature of 858°C, which can be reasoned by the assumption of stronger material characteristics for the steel reinforcement in the model. A smaller crack width of the slab along the exterior edge in the A2 model also explains the outward movement of the slab over this edge. The exterior corners of the slab are subjected to large compressive forces as the slab starts to pull the exterior steel beam with itself towards the centre of the slab. This is the direct result of stronger material characteristics of steel reinforcement as the reinforcement in the slab is now strong enough to maintain the composite action between the slab and the steel beam below. The A2 model also indicates no failure of reinforcement along the interior primary edge of the composite panel (figure 5.29).

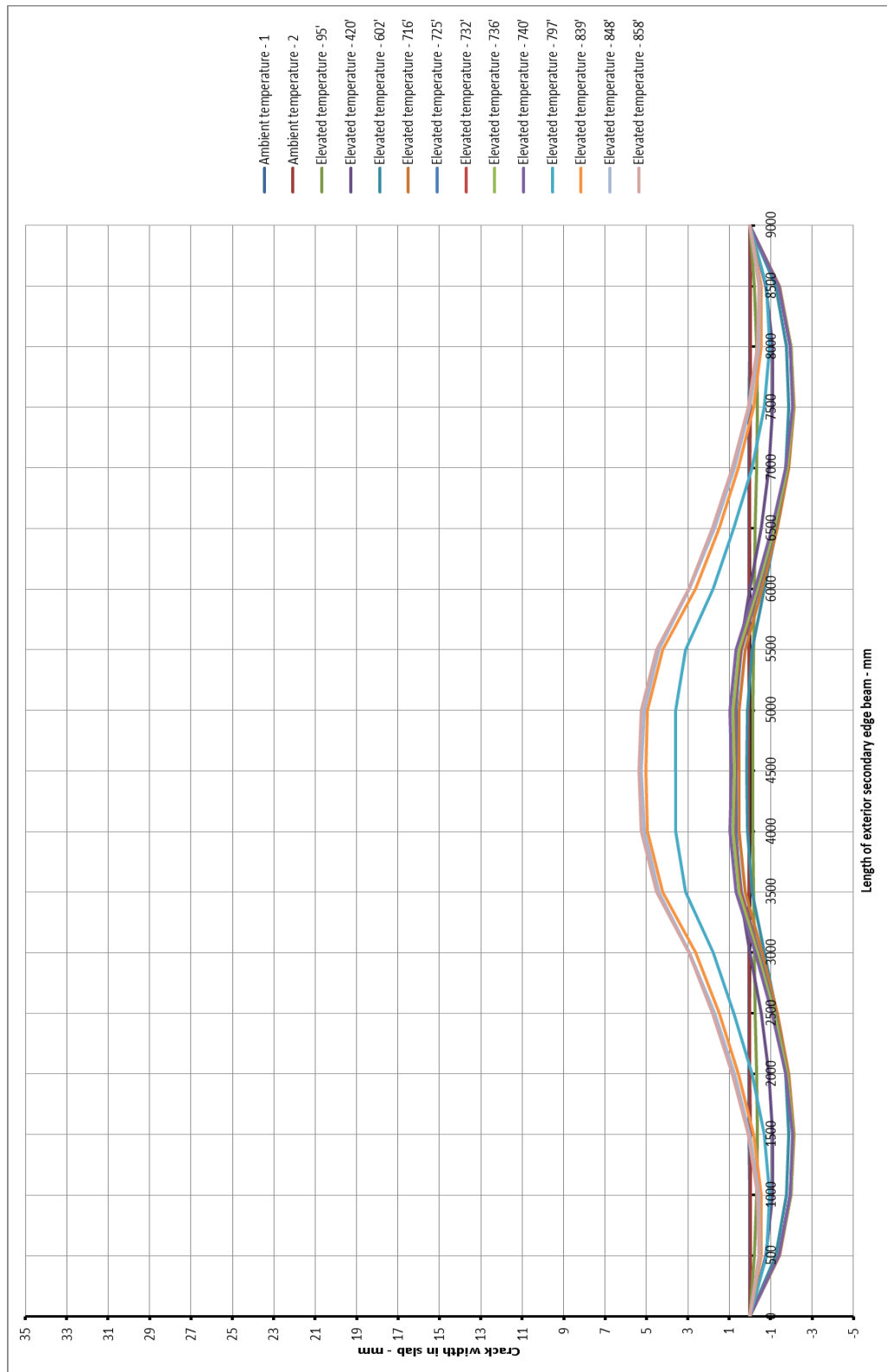


Figure 5.26: Horizontal crack development – exterior secondary edge beam- $f_y=600\text{N/mm}^2$

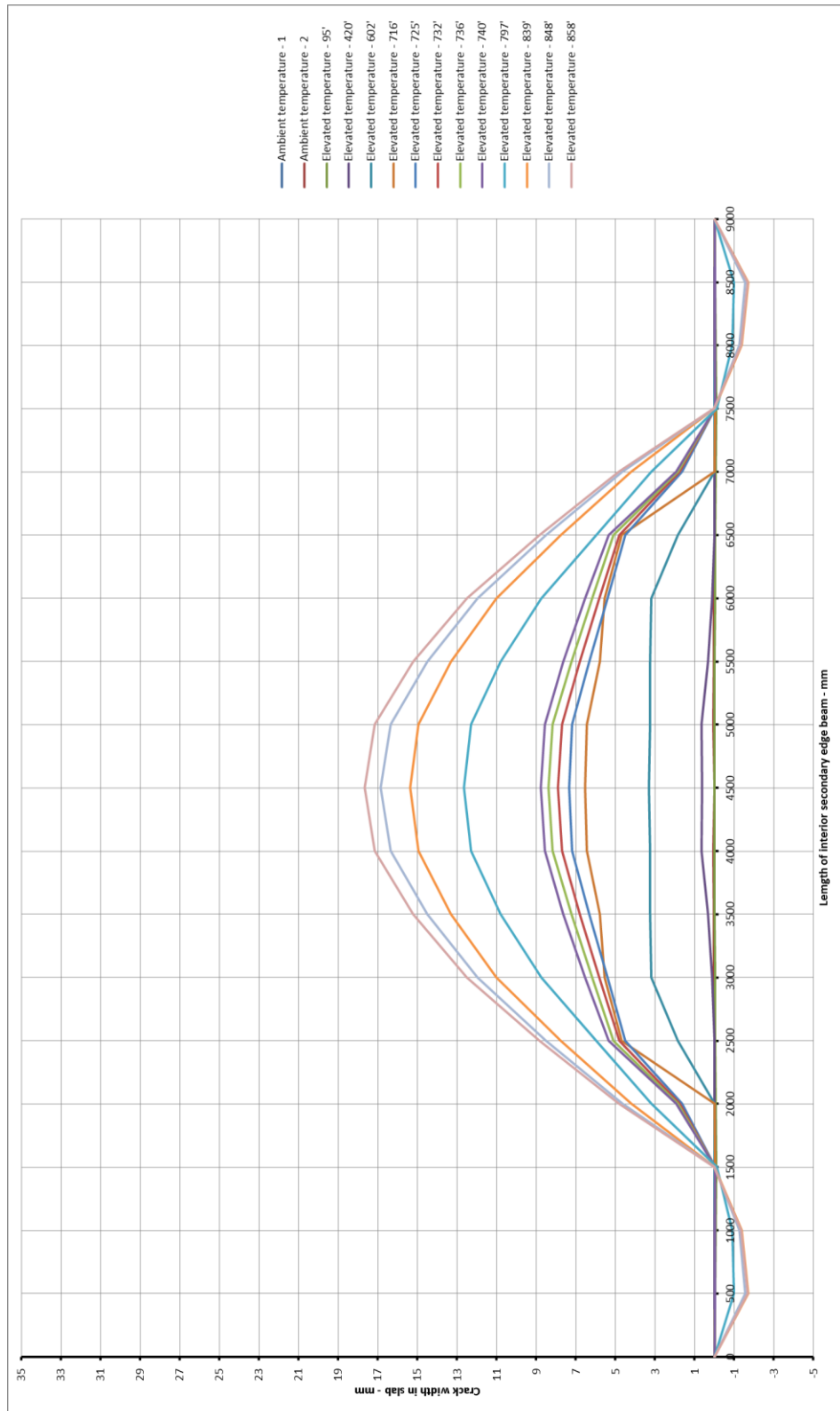


Figure 5.27: Horizontal crack development – interior secondary edge beam- $f_y=600N/mm^2$

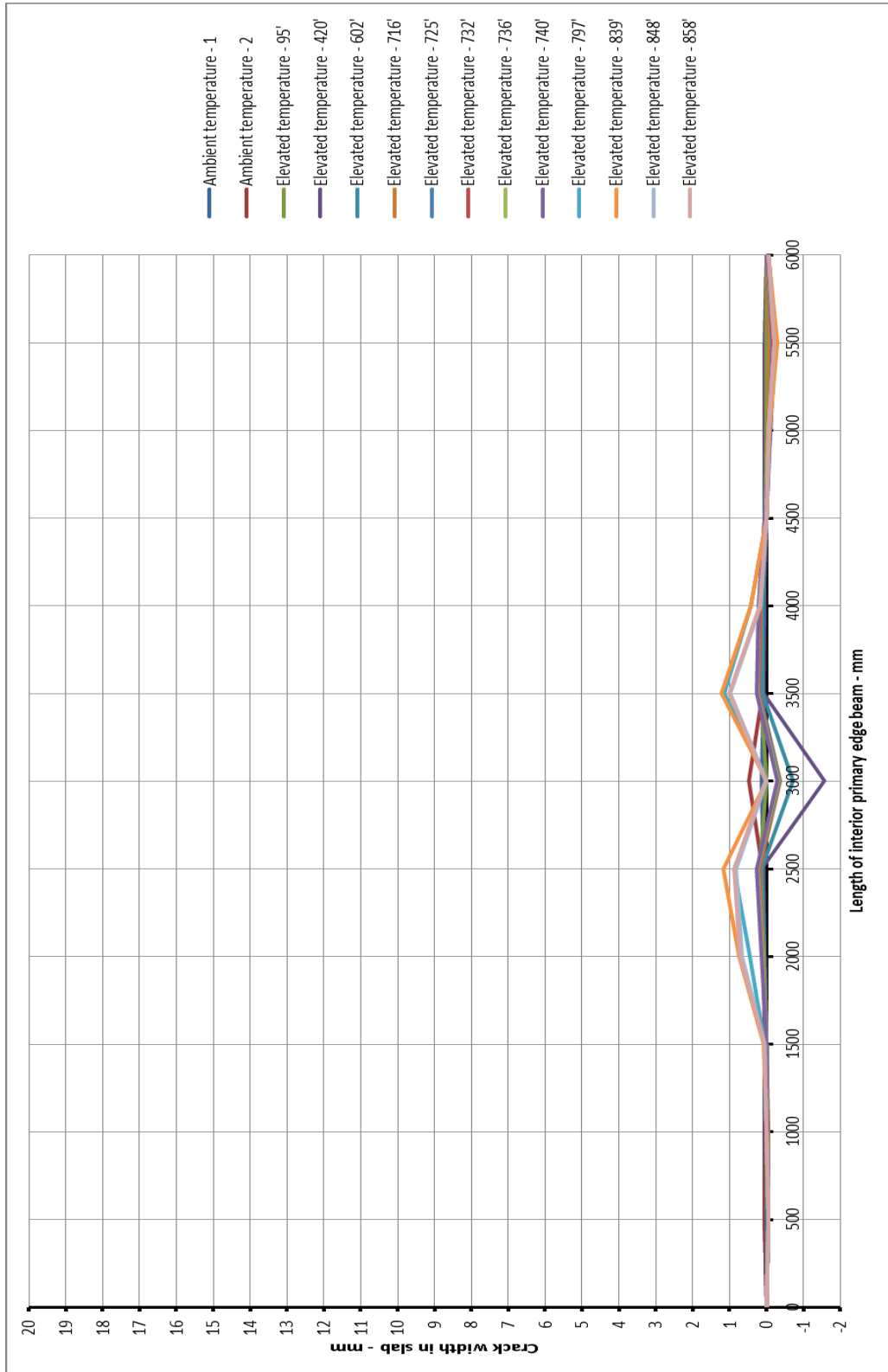


Figure 5.28: Horizontal crack development – interior primary edge beam- $f_y=600\text{N/mm}^2$

5.1.5 Influence of reinforcement material properties on connection performance of composite panel

The model-scale composite panel in section 5.1 contained a secondary unprotected beam along the longer span of the composite panel which was attached to the adjacent protected primary beams at its two ends using a simple pin connection. As the pin connections are generally assumed to have very limited rotational stiffness, therefore, it can be stated that the once the concrete is cracked in tension at its top surface the rotational response of the beam-to-beam steel joint in the proposed model is greatly depended on the amount and the material characteristics of the available reinforcement at the top of the joint. Figure 5.29 and 5.30 show the rotational displacements of the pin connection used in the numerical model with two different reinforcement characteristics of A142 at elevated temperature.

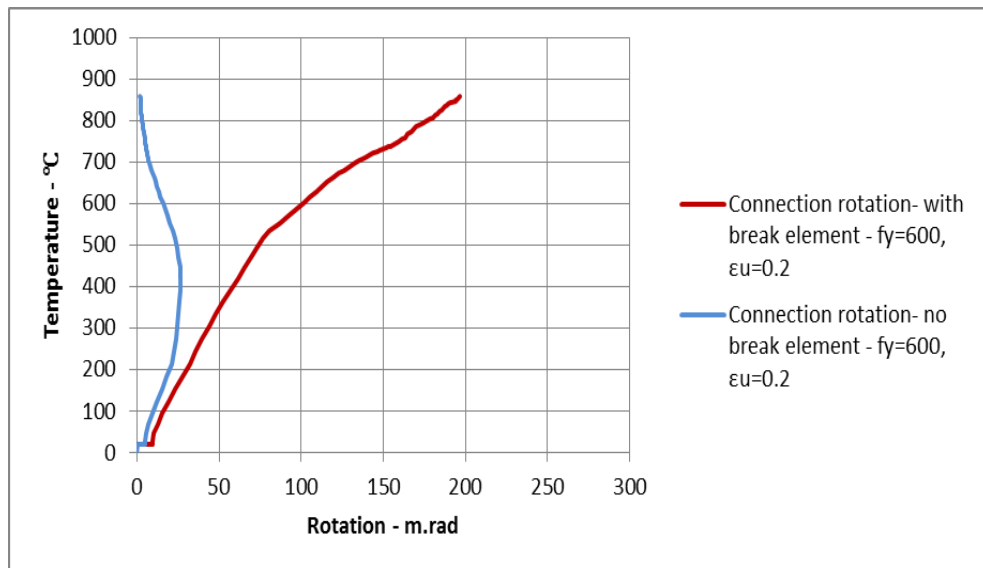


Figure 5.29: Comparison of rotational displacement at connection- A142- $f_y=600\text{N/mm}^2$

As the concrete cracks in tension, the rotational capacity of the composite pin-connection reduces to the rotational stiffness of its available reinforcement at the top of the steel joint. Figure 5.30 illustrates the rotational response of the beam-to-beam connection at the centre of the interior primary beams from *Vulcan1* and *Vulcan2*. The blue line in the figure is the rotational response of the connection from *Vulcan1* (with enhanced material characteristics); where the continuity of the slab on to top of the connection was assumed using a smeared cracking approach. The reason for the backward rotational movement of the connection from *Vulcan1* at high temperature

can be found in section 5.1.2.1. It is evident that the appropriate modelling of the slab continuity and the possible crack development in hogging moment regions can significantly influence/alter the rotational behaviour of the steel connection. This has been clearly presented by the results from *Vulcan2* (red solid lines) in the above figure. Figure 5.30 compares the rotational response of the composite pin connection from A1 (composite slab with A142, $f_y=500\text{N/mm}^2$) and A2 (composite slab with A142, $f_y=600\text{N/mm}^2$) models using both versions of the software.

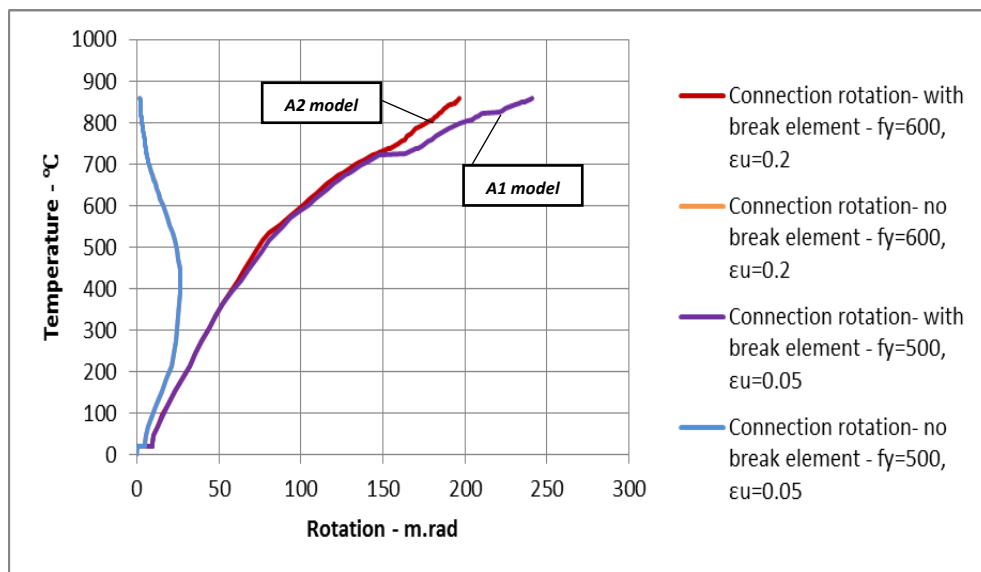


Figure 5.30: General comparison of connection rotational displacement from *Vulcan1* & *Vulcan2*

Considering the results from *Vuclan1* it can be seen that changes in the reinforcement characteristic has negligible effects on the rotational response of the connection. This is mainly due to the assumption of permanent continuity of the composite slab during the analysis, which in turn results in unrealistic rotational capacity of the connection. The results from *Vulcan2* (the red and purple lines) clearly indicates the influence of reinforcement material properties on the joint performance where a distinguishable reduction in the joint rotational displacement can be observed between A1 and A2 models. It should be noted from the graphs that the response of both models are almost identical up to the temperature level of 720°C. Referring to section 5.1.4, this is the temperature at which some reinforcement in the A1 model was fractured due to reaching the ultimate tensile capacity (a sudden change of slop in the purple line). The reinforcement in the A2 model starts to fracture at 797°C as a result of enhanced material characteristics of the reinforcement. Therefore, any changes in material

properties of the steel reinforcement within the slab would have a great influence on the rotational capacity of steel connection below the slab, which in turn results in reduced/increased rotational displacement at the connection. The A2 model results in 19% reduction of the overall rotational response of the steel joint when the yield strength characteristic of the steel reinforcement in the model was increased by 20%.

5.1.6 Influence of slab thickness on vertical deflection/ crack development of composite panel

The influence of slab thickness on the overall performance of the floor area, and in particular its effect on the overall deflection of the slab and the crack development around the edge of the slab, were studied through numerical modelling of the composite panel using different thickness for the modelled composite slab. Therefore, the same composite panel as section 5.1.2.1 (with the slab thickness of 120mm) was modelled using A142 reinforcement. However, in order to investigate the influence of slab thickness on the composite panel performance a thinner slab with the overall effective depth of 90mm was used in the model (from now on called B1 model). Similar to the A1 model the position of the reinforcing bars was assumed at half depth of the slab elements, which coincides with an assumed reference plane of the model in *Vulcan* analysis. Therefore, figures in this section are constructed based on the behaviour of different structural members at the position of the reference plane. Figure 5.31 and 5.32 illustrates the slab 3D vertical deflection and the magnified horizontal displacement of the modelled composite panel respectively.

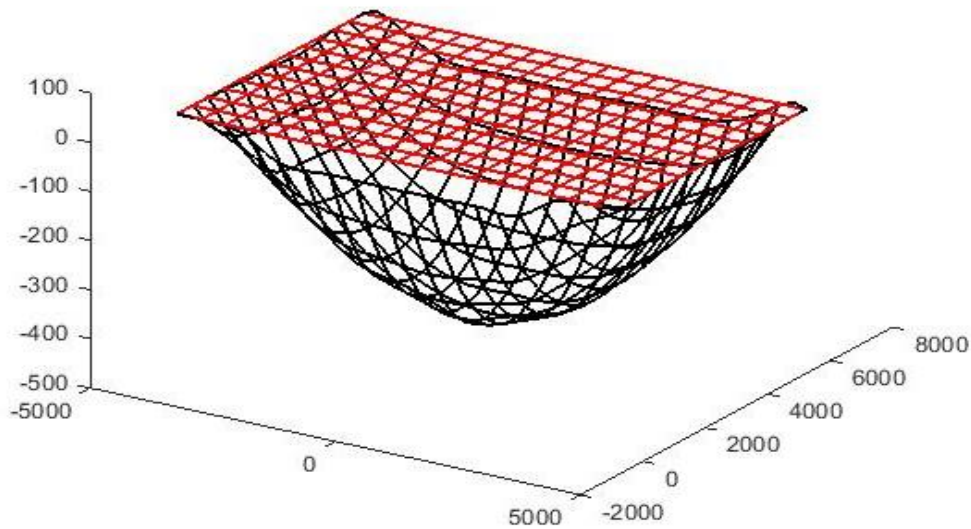


Figure 5.31: 3D view of the deformed shape of the A142 interior composite panel-90mm thickness (B1 model)

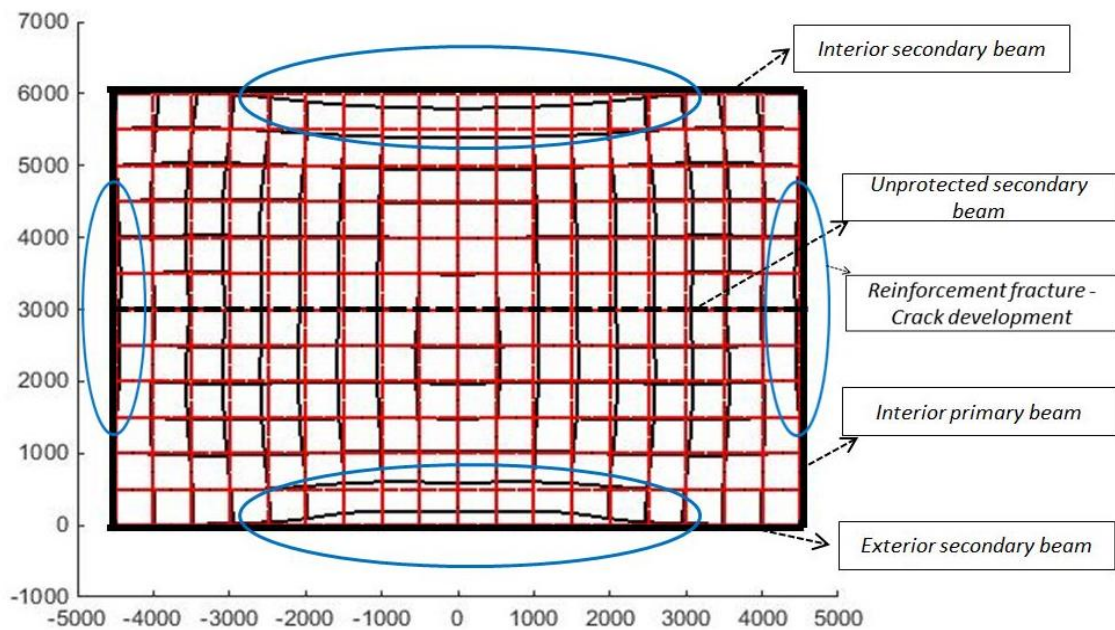


Figure 5.32: Plan view of slab horizontal movement, A142 interior composite panel- 90mm thickness (B1 model)

Large vertical deflection occurs at the centre of the slab due to the presence of full composite action between the slab and the unprotected secondary beam through shear studs. Similar to the A1 model, the B1 model also indicates large cracks along the edges of the slab over the length of the primary and secondary protected beams.

The reason for crack development along the length of the protected exterior edge beam has already been discussed in detail in section 5.1.21.

The results of the comparative analysis between *Vulcan1* and *Vulcan2* in terms of the slab vertical deflection and the horizontal crack development for the composite panel with reduced effective depth (B1 model) are shown below.

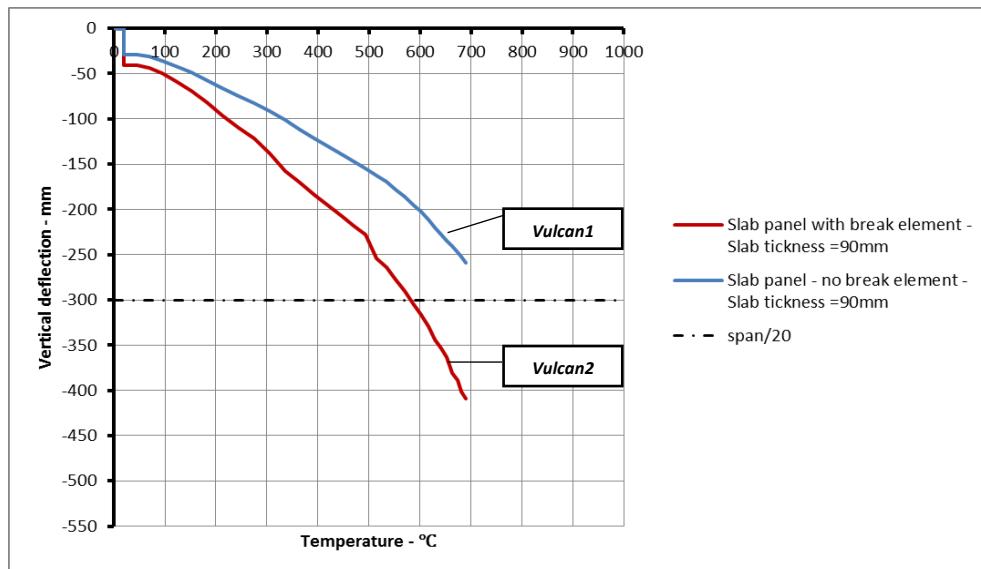


Figure 5.33: Comparison of the B1 model - slab central deflection from *Vulcan1* and *Vulcan2*

Comparison between the graphs in figure 5.33 shows the influence of discrete cracking at the edges of the slab on the central vertical deflection of the floor area for the B1 model. The presence of discrete cracking (failure of break elements) results in a larger vertical deflection in the numerical model from *Vulcan2*. The change in magnitude of vertical deflection of the slab became more obvious for the range of temperature beyond 515°C, where there is a sudden increase in the vertical deflection of the panel from the B1 model analysed in *Vulcan2*. The model indicates the maximum deflection of 418mm at the temperature of 700°C, whereas, the result obtained from *Vulcan1* shows a gradual increase in the vertical displacement till it reaches the maximum deflection of around 260mm at the same level of temperature. The vertical deflections from the software have also been compared against the well-known span/20 limit at elevated temperature. Figure 5.34 compares the vertical deflection of the modelled composite panel in section 5.1.2.1 (A1 model) with the model in section 5.1.6 (B1 model). As is evident from the graphs, the changes in the

overall depth of the composite slab can also have a great influence on the structural behaviour of the composite panel in terms of its vertical displacement. The numerical model with a lighter floor area (B1 model) indicates the maximum vertical deflection of 418mm at an elevated temperature of 700°C, whereas, the maximum vertical deflection obtained by the A1 model is just over 280mm at the same temperature. It was not possible to trace the behaviour of the structure beyond the temperature of 700°C in the B1 model as a sudden failure of the remaining break elements (available reinforcement) along the shorter edges of the slab caused significant instability within the analysis and therefore the analysis was forced to terminate. Although, it was not possible to trace the behaviour of the structure beyond 700°C, yet the comparison between the two numerical models clearly indicates the influence of slab overall thickness on the behaviour of the composite panel, where the 25% reduction in the overall depth of the concrete slab results in 33% increase of the maximum vertical deflection obtained by the numerical model.

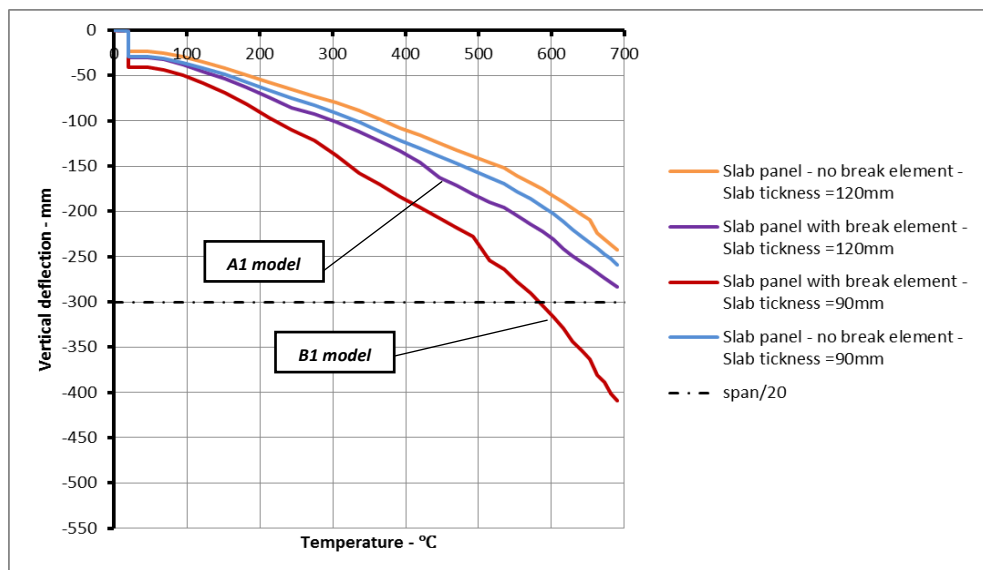


Figure 5.34: Comparison of the A142-slab central deflection from A1 and B1 models

Figure 5.35 to 5.37 illustrates the crack development along the edges of the slab in both directions. As is evident from the figures, the crack along the internal secondary beam in the B1 model starts to develop (beyond the fracture of some reinforcement) at temperatures around 420°C, where the vertical deflection of the slab is about 200mm. The edge of the slab along the internal secondary beam in the A1 model experienced the crack development (beyond the fracture of some reinforcement) at a

temperature around 400°C with the vertical displacement of 140mm. This is also reflected in figure 5.34 where the vertical displacement from the B1 model is more than the displacement from the A1 model between the temperatures of 400°C to 420°C. The B1 model also indicates the maximum crack width of about 20mm along the internal secondary beam at the maximum temperature of 700°C, whereas, the maximum crack width of only 7mm was picked up by the A1 model at the same temperature. Along the length of the exterior edge beam in the B1 model the first fracture of reinforcement occurs at temperature just less than 400°C, whereas, the A1 model shows the first fracture of reinforcement along the same edge to occur at temperature of around 725°C. The crack continued to develop beyond these temperatures in both models, where the maximum crack width of 0.5mm and 20mm were recorded by the A1 model and the B1 model at a maximum temperature of 700°C. The B1 model also indicates the first failure of reinforcement along the interior primary edge of the composite panel (figure 5.37) at a temperature of 652°C, whereas the A1 model indicates the first failure of reinforcement at around 725°C. Consequently the maximum crack width of 6.5mm along the shorter edge of the slab was obtained from the B1 model.

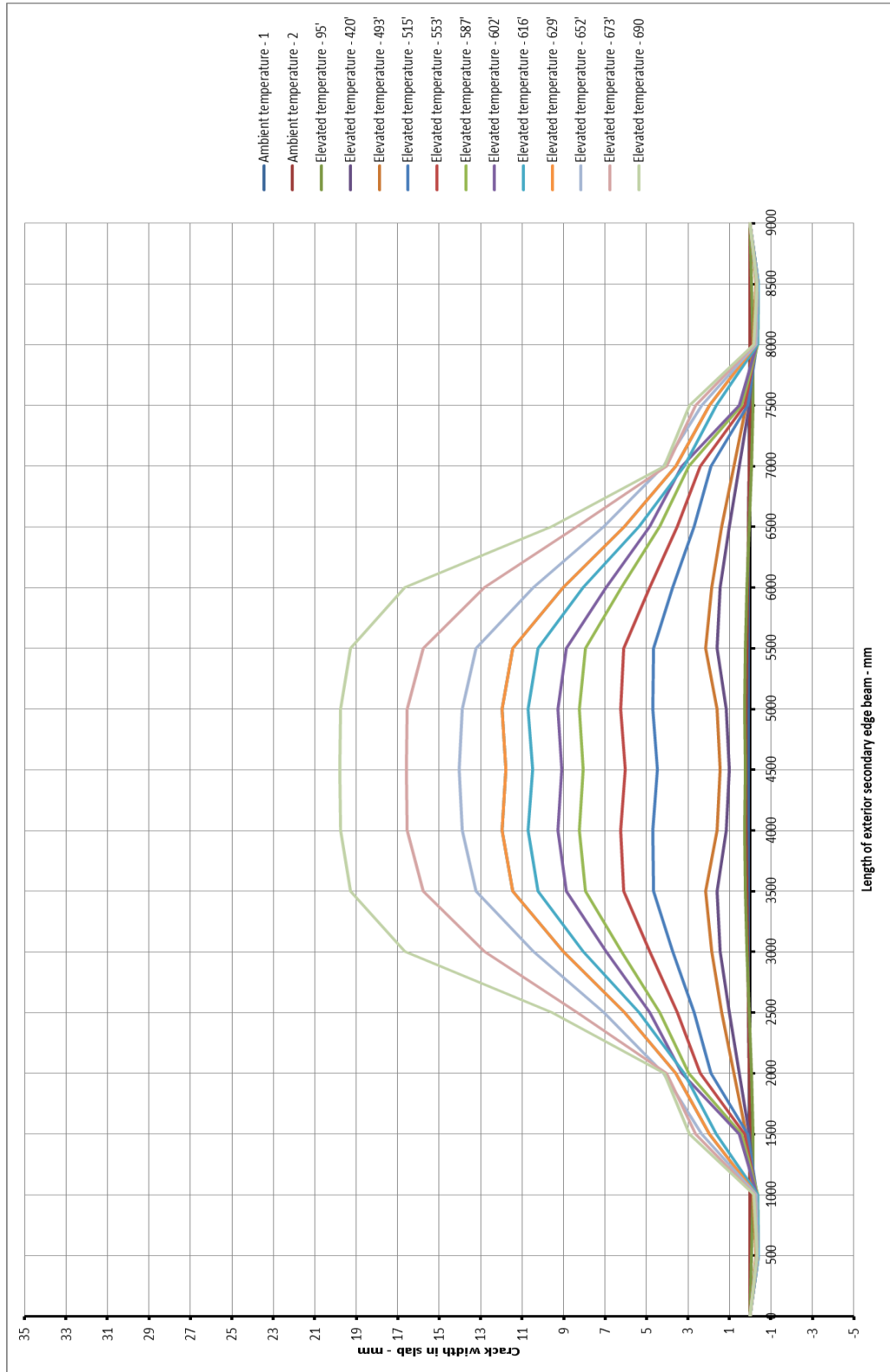


Figure 5.35: Horizontal crack development – exterior secondary edge beam – B1 model

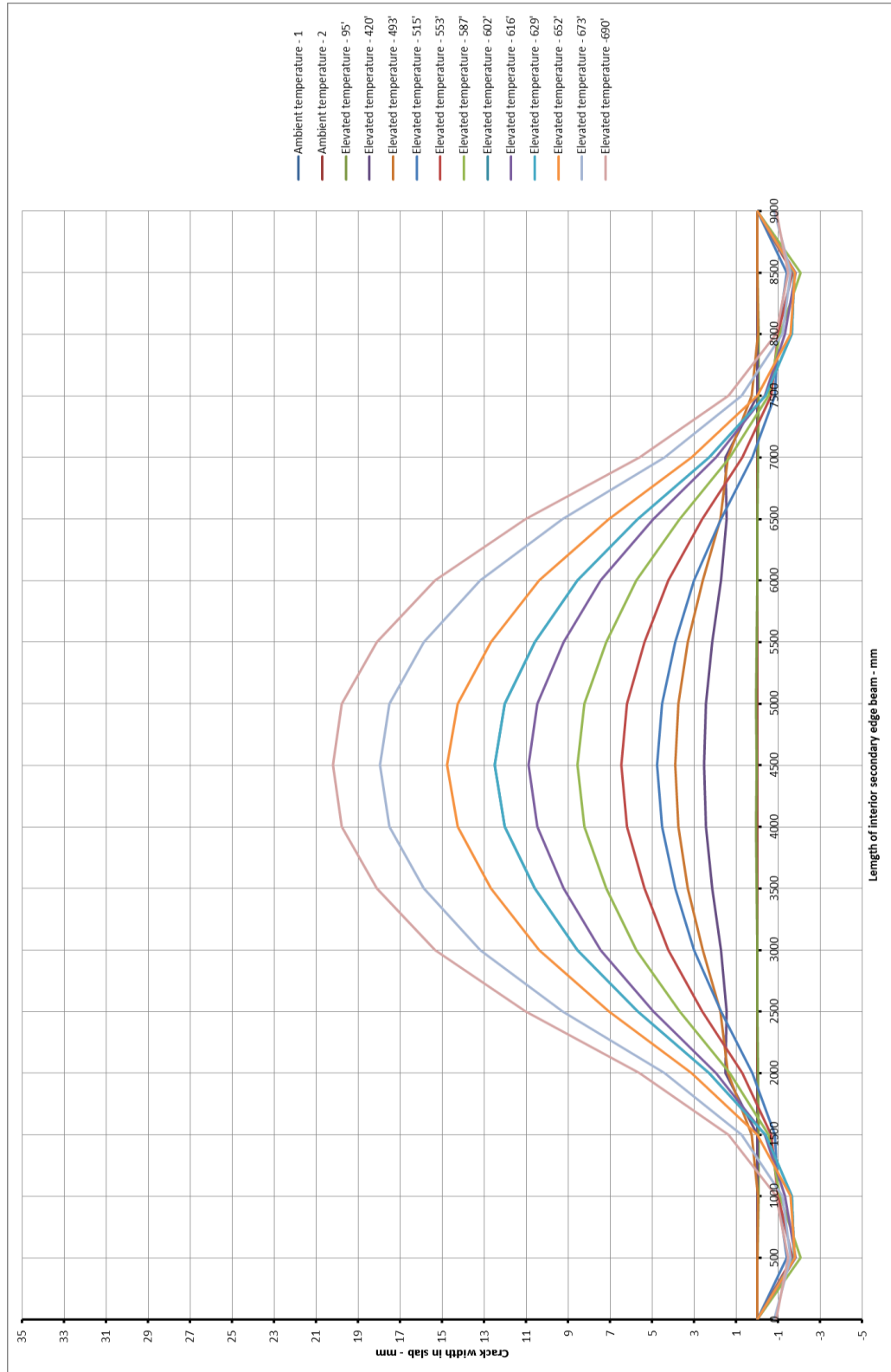


Figure 5.36: Horizontal crack development – interior secondary edge beam – B1 model

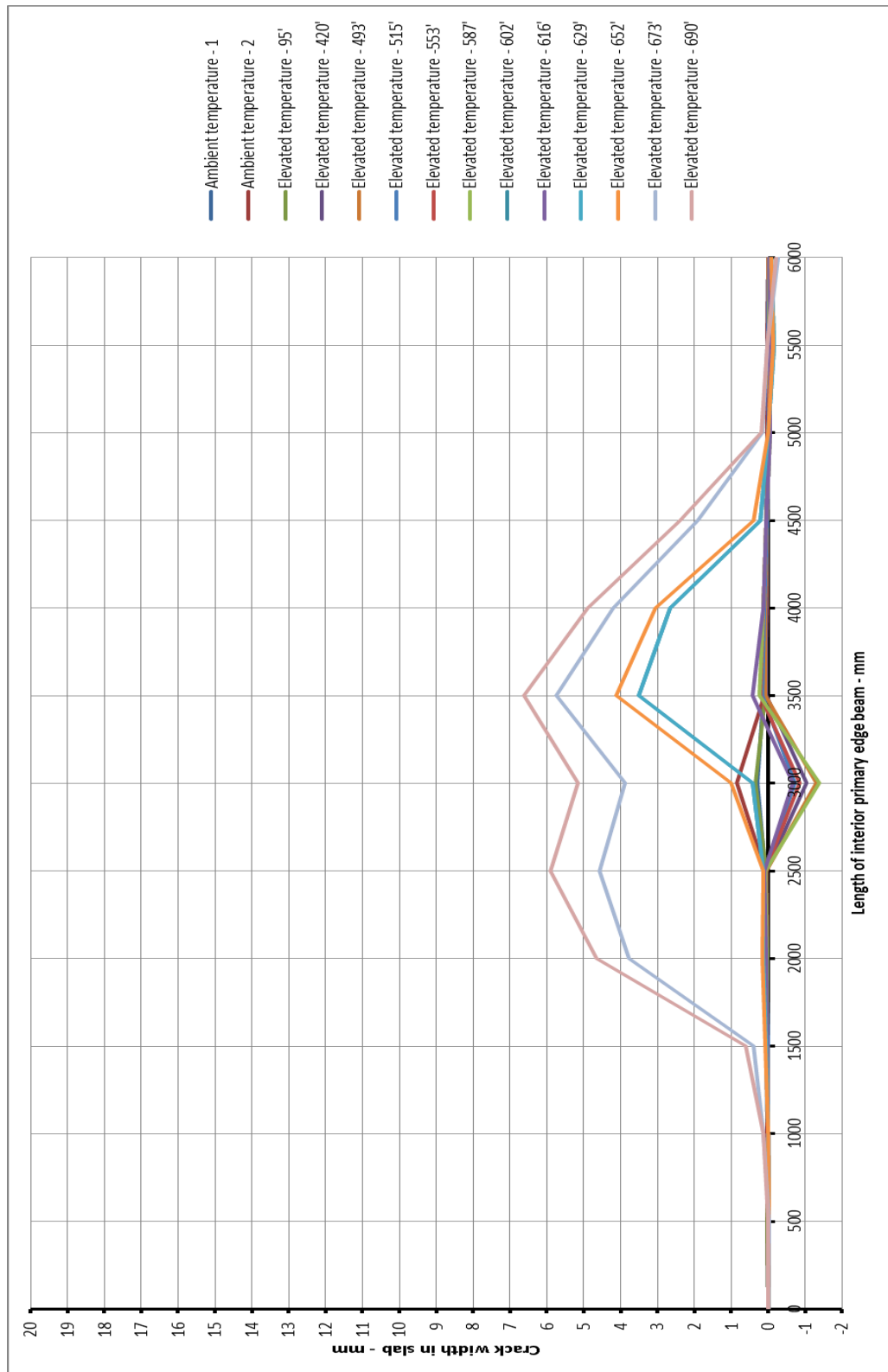


Figure 5.37: Horizontal crack development – interior primary edge beam – B1 model

5.1.7 Influence of slab thickness on connection performance of composite panel

Figure 5.38 and 5.39 show the rotational displacements of the pin connection used in the numerical model (B1 model) with a lighter concrete section at elevated temperature. Figure 5.39 illustrates the rotational response of the beam-to-beam connection at the centre of the interior primary beams from *Vulcan1* and *Vulcan2*. Similar to A1 and A2 models the blue line in the figure below also indicates the rotational displacement of the B1 model where the continuity of the slab on top of the connection was assumed using the smeared cracking approach. The reason for the backward behaviour of the connection in *Vulcan1* has been addressed previously (refer to section 5.1.2.1).

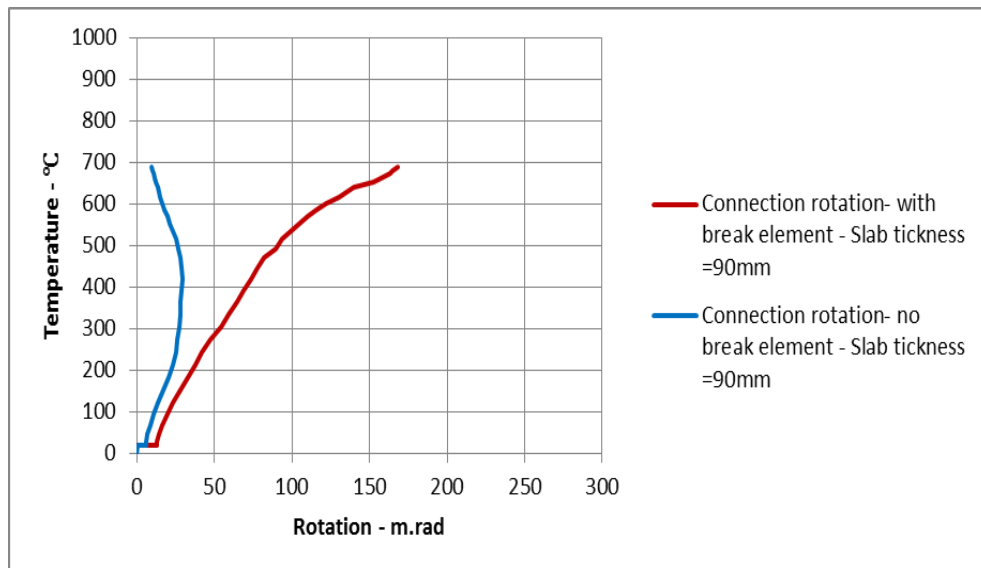


Figure 5.38: Comparison of rotational displacement at connection- B1 model

Figure 5.39 compares the rotational response of the composite pin connection from A1 (slab thickness=120mm) and B1 (slab thickness=90mm) models using both versions of the software (*Vulcan1* and *Vulcan2*). Similar to the comparisons in section 5.1.2.1 and 5.1.5, the changes in rotational response of the joint between A1 and B1 model ran in *Vulcan1* was negligible due the assumption of permanent continuity of the slab during the analysis in this particular version of the software.

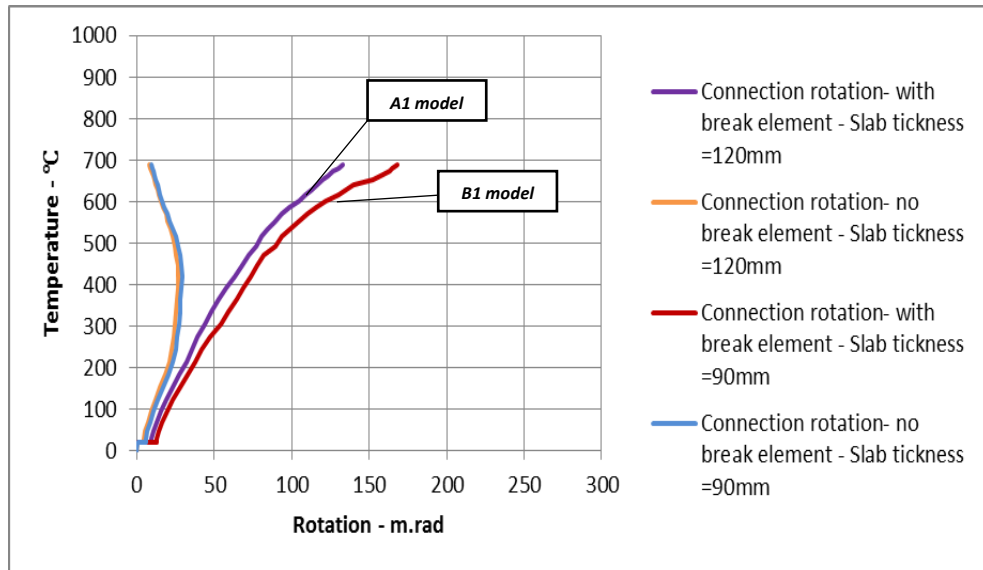


Figure 5.39: General comparison of connection rotational displacement from *Vulcan1* and *Vulcan2*

The results from *Vulcan2* (the red and purple lines) indicates the change in the magnitude of rotational displacement in the joint due to the change of slab thickness within the composite panel. The rotational response of the joint from the B1 model shows a gradual increase of rotational displacement over the time as the temperature increases up to around 652°C where a change of slope in the graph results in an increased rate of rotational displacement. This is also the temperature where the first failure of some reinforcement along the interior primary edge of the panel (figure 5.37) was indicated by the B1 model. The rotational response of the A1 model also confirms that no failure in reinforcement has occurred up to 700°C (refer to section 5.1.6). Therefore, varying the slab thickness in composite structures would have reasonable influence on the rotational capacity of the steel connection below the slab, which in turn results in either reduced or increased rotational displacement of the connection. The B1 model results in 26% increase of the overall rotational response of the steel joint when the overall depth of the slab in the model was reduced by 25%.

5.1.8 Influence of concrete compressive strength on vertical deflection/ crack development of composite panel

Characteristic compressive strength of concrete used in the composite slab is another determining factor which influences the overall behaviour of the composite floor area. Therefore, a numerical model was developed (from now on called C1 model) in order to investigate the influence of concrete material properties (characteristic compressive strength) on the overall performance of the floor area. The properties of the new model was identical to that of section 5.1.2.1 (A1 model). However, the value of characteristic compressive strength (f_{ck}) of the slab element was assumed to be equal to 50N/mm^2 , which is higher than the assumed compressive strength value of 35N/mm^2 for the A1 model. Figure 5.40 and 5.41 illustrates the slab 3D vertical deflection and the magnified horizontal displacement of the modelled composite panel respectively.

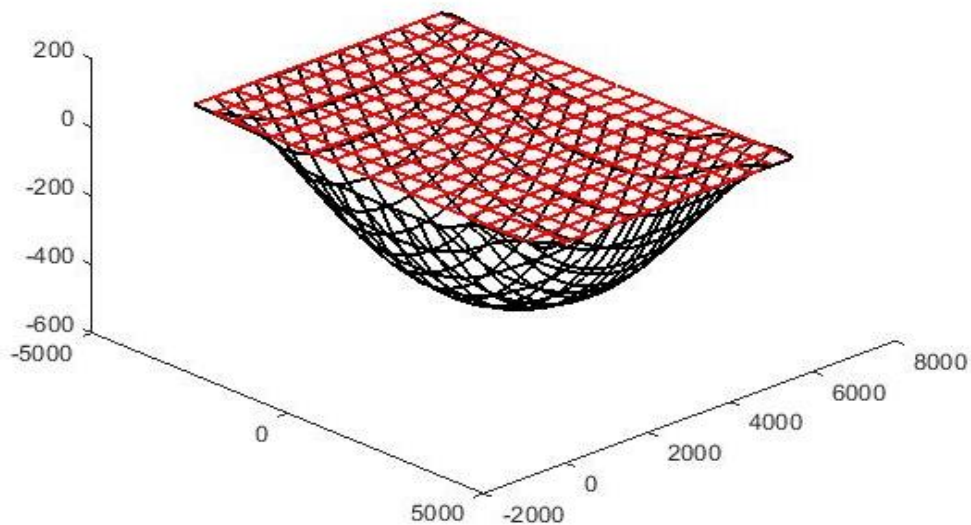


Figure 5.40: 3D view of the deformed shape of the A142 interior composite panel - C1 model

Similar to the previous models (A1, A2, and B1), the C1 model also results in large vertical deflection of the floor slab area at high temperature. The results of the comparative analysis between *Vulcan1* and *Vulcan2* in terms of slab vertical deflection and the horizontal crack development of the floor area from C1 model are shown below.

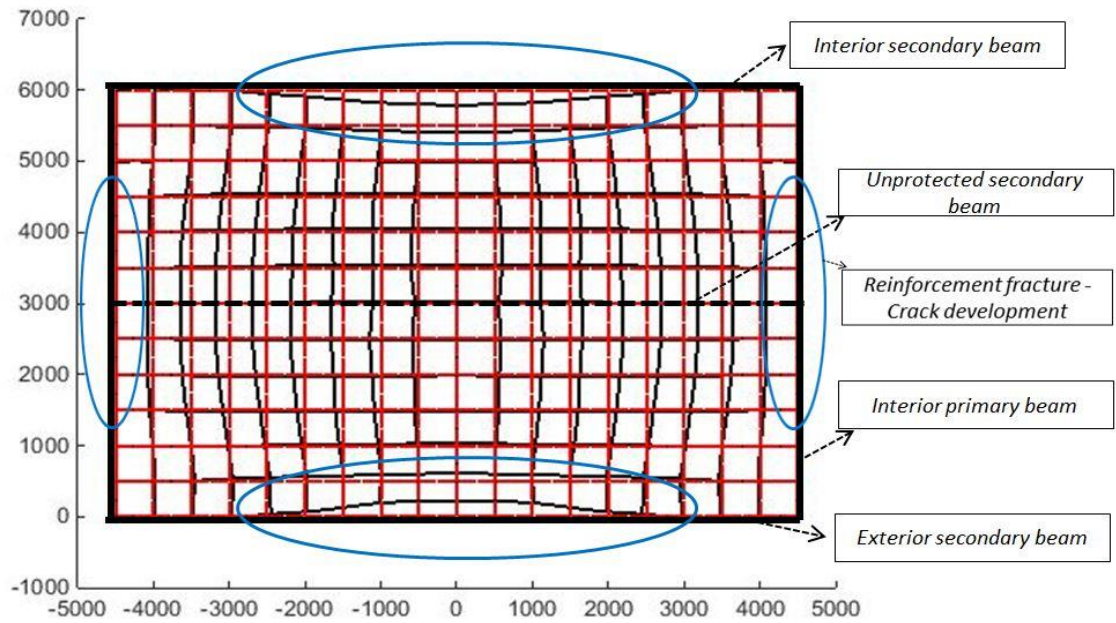


Figure 5.41: Plan view of slab horizontal movement, A142 interior composite panel - C1 model

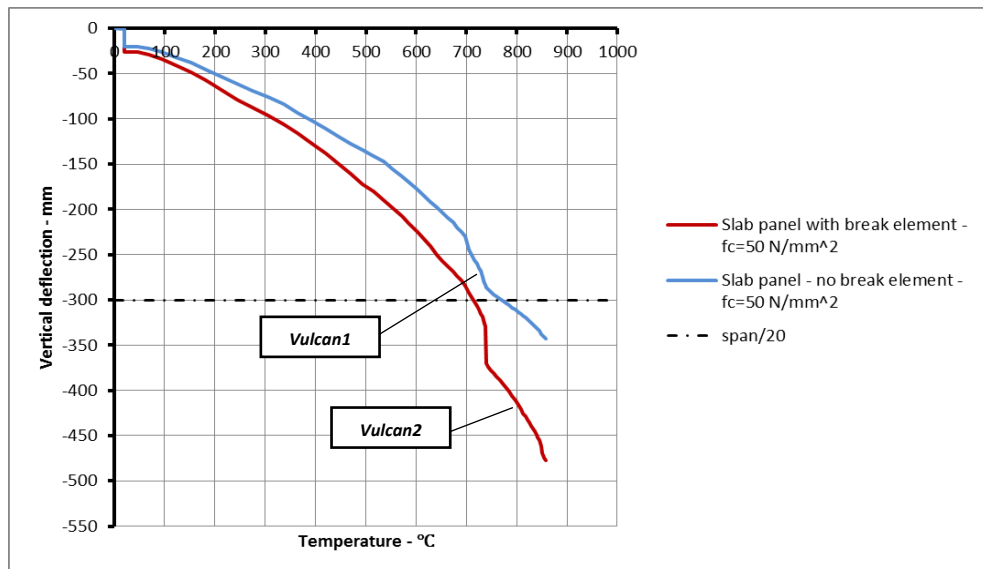


Figure 5.42: Comparison of the C1 model - slab central deflection from *Vulcan1* and *Vulcan2*

As is evident from figure 5.42, the presence of discrete cracking (failure of break elements) in the modelled structure can significantly alter the performance of the floor area at large deflection as the slab loses its horizontal restraint from the surrounding structures (continuity of the floor area) due to the fracture of the mesh reinforcement at the top surface of the slab around the edges.

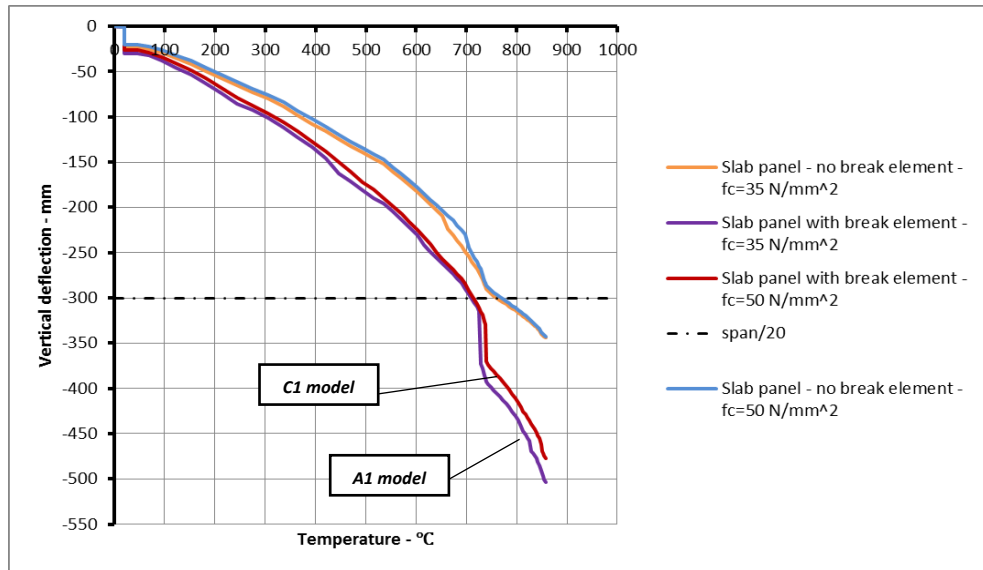


Figure 5.43: Comparison of the A142-slab central deflection from A1 and C1

Figure 5.43 compares the vertical deflection of the modelled composite panels in section 5.1.2.1 (A1) and section 5.1.8 (C1). Unlike the previous models, changing the concrete material properties did not extensively alter the performance of the composite panel. As can be seen from the figure above, the models (A1 and C1) behave in a very similar manner. The magnitudes of vertical deflection obtained by both models are very close up to the temperature of 740°C. However, the change in magnitude of the deflection became more obvious for the range of temperature beyond 740°C, when the mesh reinforcement starts to fracture due to excessive crack development within the edges of the slab. Therefore, the extra strength of the concrete material would not significantly enhance the slab performance since the slab floor area already lost its horizontal restraint from the surrounding structures (fracture of reinforcement). However, the C1 model with improved concrete characteristic still results in slightly lower central deflection within its floor area compared to the A1 model. The C1 model results in 6% reduction in the overall vertical deflection of the panel compared to that of A1 model. This is mainly due to extra stiffness of the composite slab as a result of the stronger concrete material.

Figure 5.44 to 5.46 illustrates the crack development along the edges of the slab in both directions. The C1 model has identified the crack development initially to occur (beyond the fracture of some reinforcement) along the length of secondary interior beams at the temperatures around 420°C, where the vertical deflection of the slab is

about 138mm. The edge of the slab along the internal secondary beam in the A1 model experienced the crack development (beyond the fracture of some reinforcement) at a slightly lower temperature of 400°C with a very similar vertical deflection of 140mm. This is also reflected in figure 5.43 where the vertical displacement from the C1 model is just slightly below the displacement from the A1 model between the temperatures of 400°C to 420°C. The C1 model also indicates the maximum crack width of 21mm over the length of the interior secondary beam at the ultimate temperature; this is 4mm less than the maximum crack width obtained from the A1 model along the same edge of the panel at the ultimate temperature.

Along the length of the exterior edge beam in the C1 model the first fracture of reinforcement occurs at temperature of 736°C, which is slightly higher than the temperature of 725°C at the time of the first fracture in the A1 model. The crack continued to develop beyond these temperatures in both models, where the maximum crack width of 31mm and 23mm were recorded by the A1 model and the C1 models respectively.

Justification for crack development along the exterior edge of the panel has been given in section 5.1.2.1. Comparing figure 5.46 and figure 5.9 from C1 and A1 models show that, unlike the A1 model where a series of reinforce bars were fractured simultaneously as a result of developed tensile membrane forces over the primary interior edge of the slab, the C1 model only indicates a very local failure of reinforcement along the length of the shorter edge of the panel. The A1 model shows a maximum crack width of 12mm along its shorter span, whereas the crack width along the same edge of the panel in C1 model reaches the maximum of 2mm at very local locations a short distance from the centre of the shorter span. The outward movement at the exterior edge of the panel in figure 5.46 is due to the large compressive forces applied to this edge as a result of thermal expansion of the steel beam and the concrete slab at temperatures below 736°C. Furthermore, the negligible crack width of the slab along the interior primary beams in the model account for the outward movement of the panel. The early crack development over the longer span (interior) of the slab at 420°C along with no reinforcement failure at its shorter span (presence of structural continuity) causes the slab to displace both vertically and

horizontally towards the unrestrained exterior edge of the panel, which results in large compressive forces along the length of the exterior beam and consequently the outward movement of the panel.

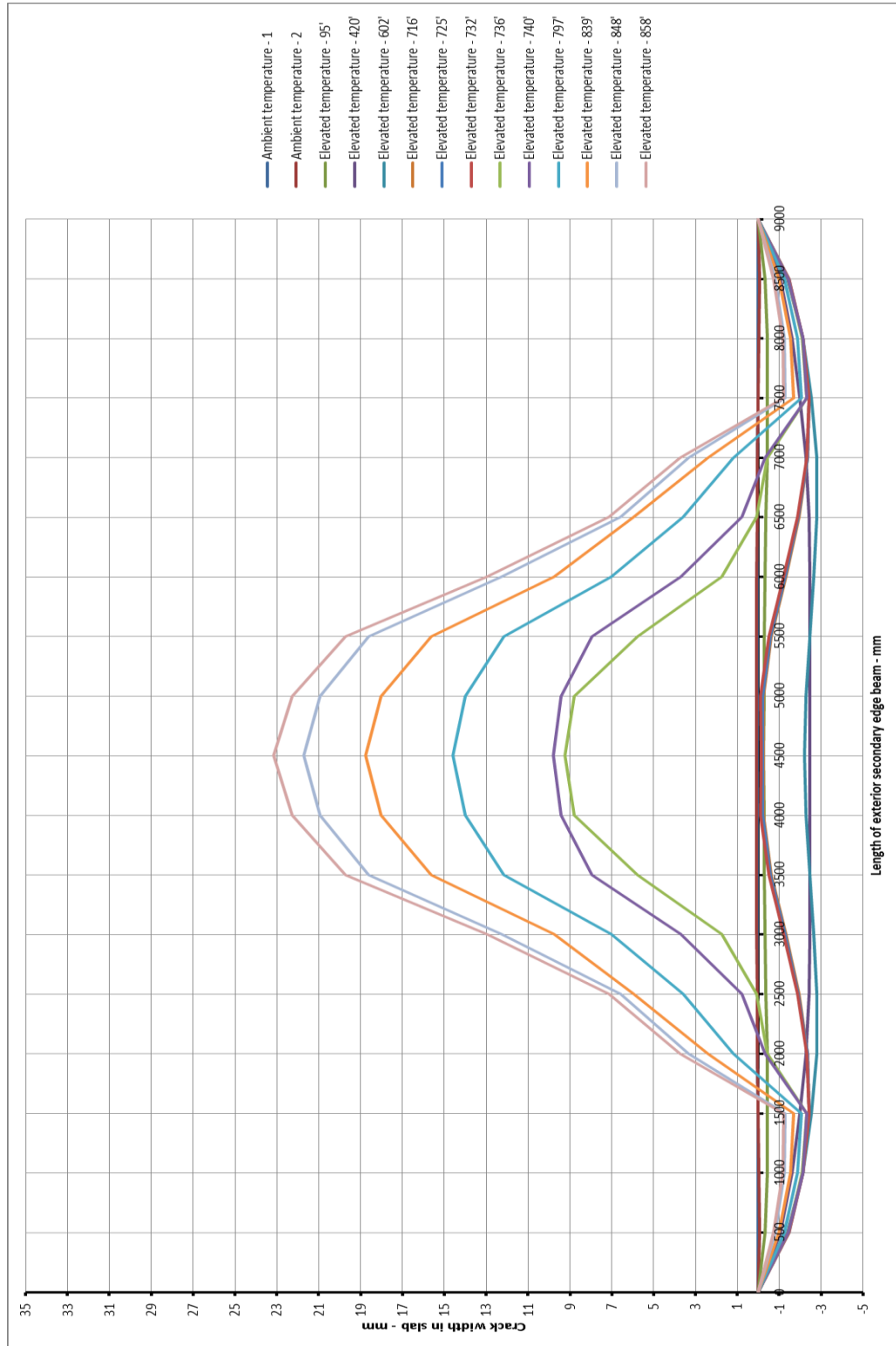


Figure 5.44: Horizontal crack development – exterior secondary edge beam – C1 model

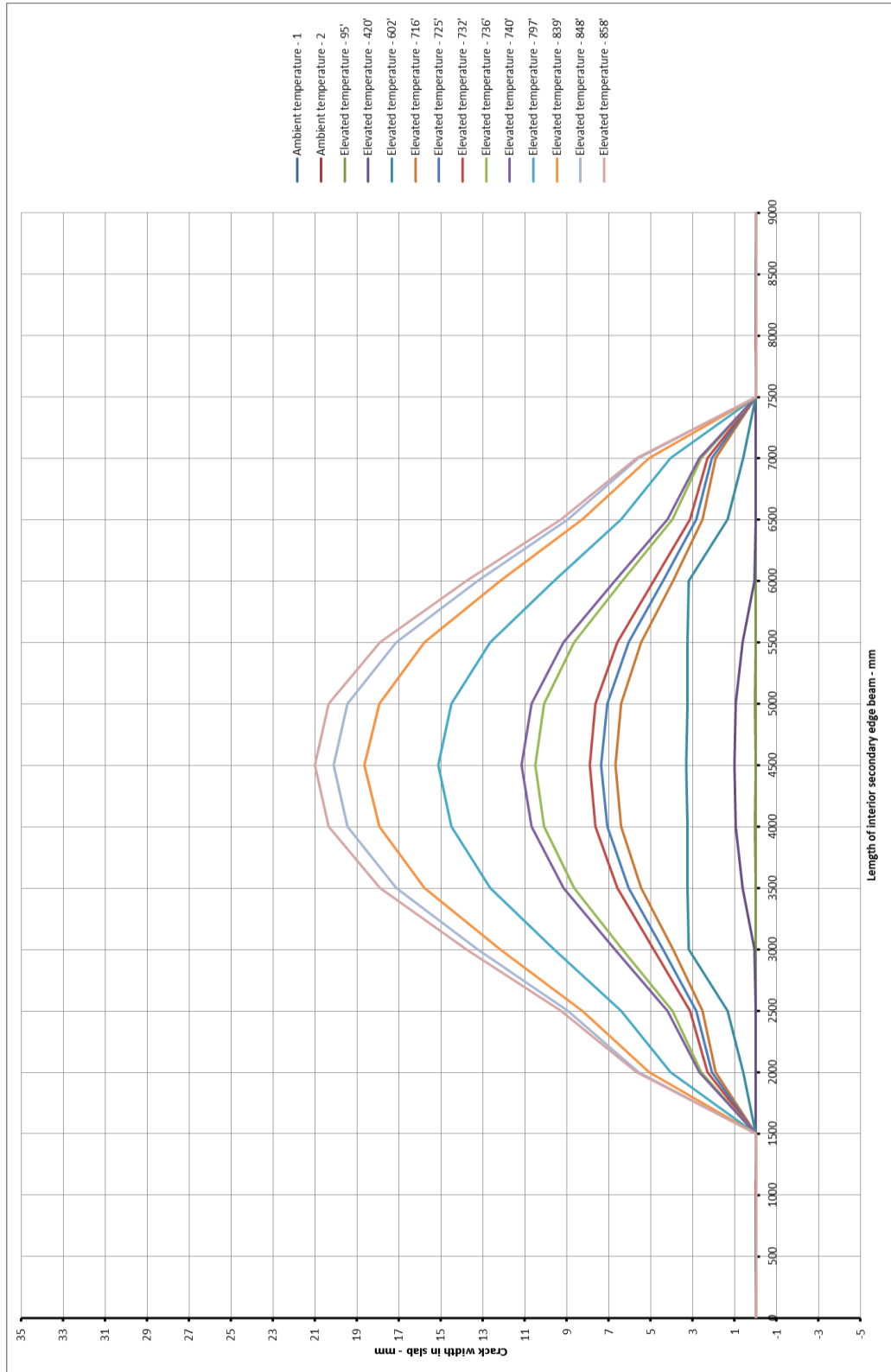


Figure 5.45: Horizontal crack development – interior secondary edge beam – C1 model

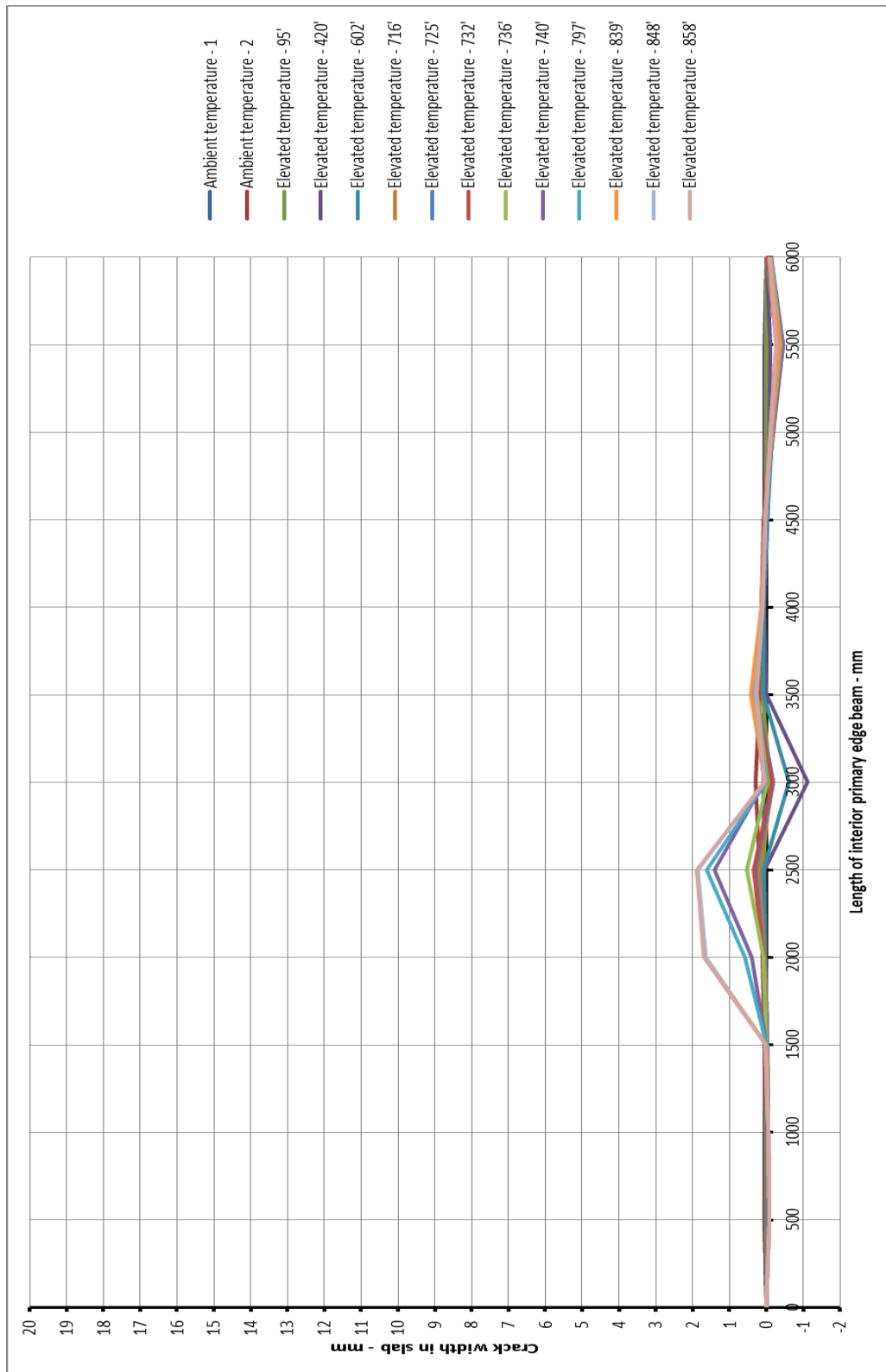


Figure 5.46: Horizontal crack development – interior primary edge beam – C1 model

5.1.9 Influence of concrete compressive strength on connection performance of composite panel

Figure 5.47 and 5.48 show the rotational displacements of the pin connection used in the C1 model (with enhanced characteristic concrete material strength) at elevated temperature. Figure 5.47 illustrates the rotational response of the beam-to-beam connection at the centre of the interior primary beams from *Vulcan1* and *Vulcan2*. Similar to the models from previous sections, the blue line indicates the rotational displacement of the C1 model where the continuity of the slab on to top of the connection was assumed using smeared cracking approach (*Vulcan1*). The reason for backward behaviour of the connection in *Vulcan1* has been addressed previously (refer to section 5.1.2.1). As is evident from the graph, proper modelling of the discrete cracks in lightly reinforced composite structures can considerably influence/alter the rotational response of the steel joint in numerical modelling. Appropriate modelling of slab continuity in any structure can result in a more realistic/reliable response of the numerical modelling.

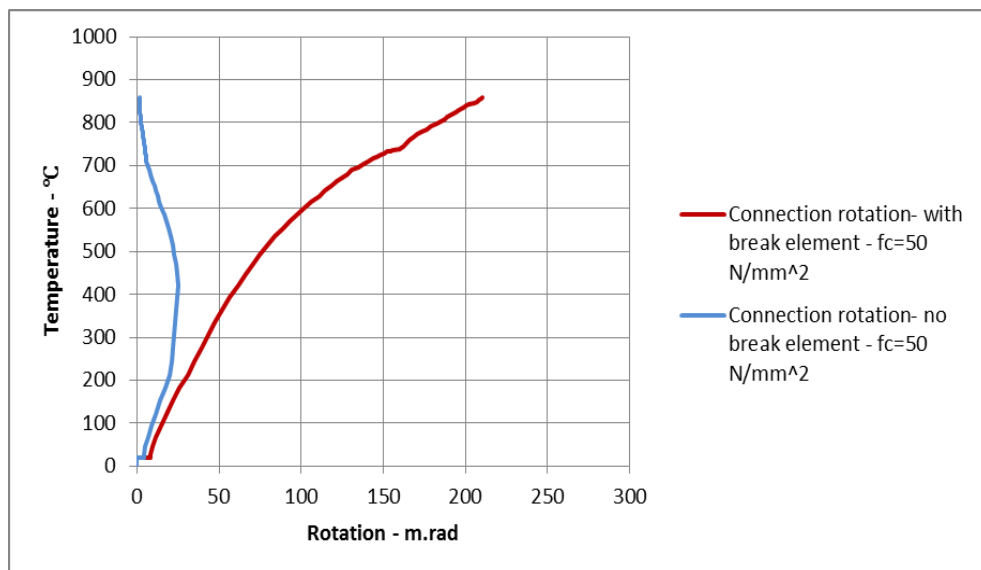


Figure 5.47: Comparison of rotational displacement at connection- C1 model

Figure 5.48 compares the rotational response of the composite pin connection from A1 ($f_{ck}=35\text{N/mm}^2$) and C1 ($f_{ck}=50\text{N/mm}^2$) models using both versions of the software (*Vulcan1* and *Vulcan2*). Similar to the previous comparisons of joint performance, the changes in rotational response of the joint between A1 and C1 model ran in

Vulcan1 was negligible due the assumption of permanent continuity of the slab during the analysis.

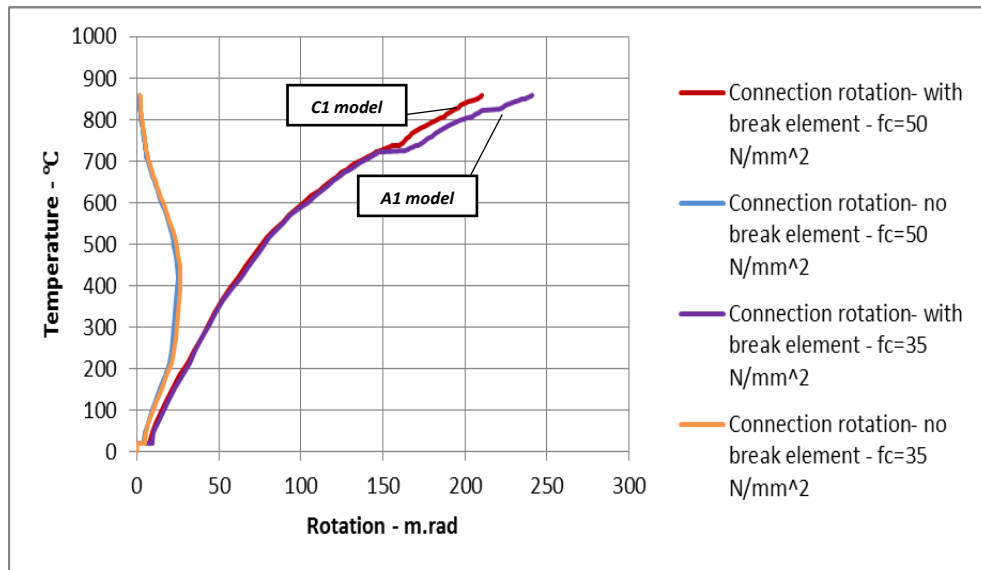


Figure 5.48: General comparison of connection rotational displacement from *Vulcan1* and *Vulcan2*

The results from *Vulcan2* (the red and purple lines) evidently shows the influence of concrete material characteristics on the joint. The responses of the both models are almost identical up to the temperature level of 725°C where a sudden increase in rotational displacement of the A1 model (purple line) occurs. Referring to section 5.1.8, this is the temperature at which some reinforcement in the A1 model was fractured due to reaching the ultimate tensile capacity. The reinforcement in the C1 model starts to fracture along the interior primary beams at slightly higher temperature of 740°C. This also can be seen by a close attention to the figure above. Beyond the fracture of the reinforcement at the top of the steel beam, the rotational response of the joint obtained from the C1 model indicates small enhancement compared to that of the A1 model. The reason for the enhanced behaviour of the C1 model can be explained by the presence of a stiffer composite slab as a result of improved strength characteristics for the concrete material. The C1 model results in 13% reduction of the overall rotational response of the steel joint when the compressive strength characteristic of the concrete material in the model increased by 42%.

5.1.10 Influence of aspect ratio on vertical deflection/ crack development of composite panel

The aspect ratio (ratio between the length and the width of the slab floor area) of composite slab is another influential factor which can affect the overall behaviour of the composite floor area where the geometrical changes of the floor slab can alter/influence the structural response of the composite panel. The new developed model (from now called D1 model) is identical to that of the A1 model in terms of the assumed material properties, loading condition and the boundary conditions. However, in order to study the effects of different aspect ratios on the overall performance of the composite panel, the width of the slab in the D1 model was increased by 1m. The aspect ratio of the slab element in D1 model assumed to be equal to 1.28 (9m x 7m), which is less than the assumed aspect ratio of 1.5 (9m x 6m) for the A1 model. Figure 5.49 and 5.50 illustrates the slab 3D vertical deflection and the magnified horizontal displacement of the modelled composite panel respectively.

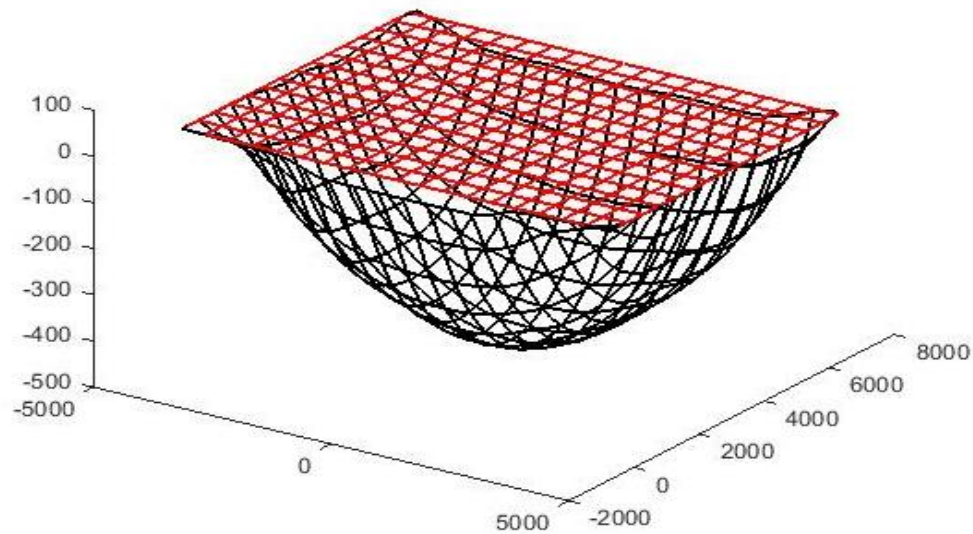


Figure 5.49: 3D view of the deformed shape of the A142 interior composite panel - D1 model

Similar to the A1 model, the results from the new model also indicate the appearance of large cracks around the edges of the composite slab as a result of large vertical deflection at the centre of the concrete floor area. The results of the comparative analysis between *Vulcan1* and *Vulcan2* in terms of slab vertical deflection and the horizontal crack development of the floor area from D1 model are shown below.

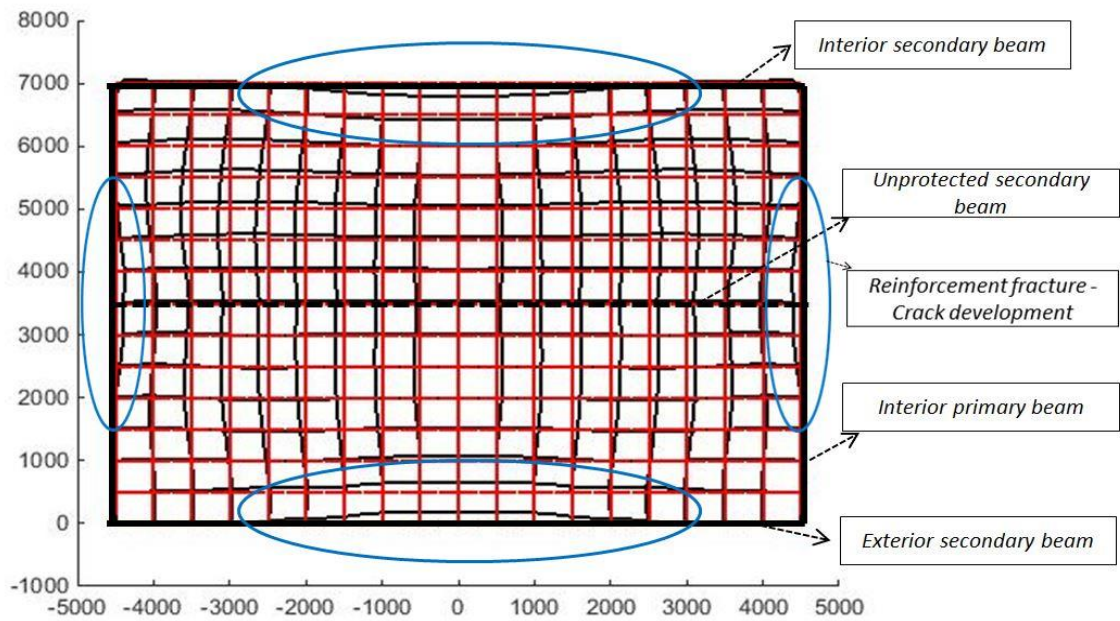


Figure 5.50: Plan view of slab horizontal movement, A142 interior composite panel - D1 model

Appropriate modelling of the slab continuity can considerably alter the performance of the floor area at high temperature. The loss of horizontal restraint in the composite structure (as a result of discrete cracking within the slab area) is properly addressed in *Vulcan2* using the new developed break element. Figure 5.51 illustrates the obtained vertical deflections of the modelled slab using both versions of the software. As is evident from the graphs, reasonable modelling of slab discontinuity results in larger overall vertical deflection of the floor area, where the ultimate vertical displacement of the panel was increased by 34% compared to the model with assumed permanent continuity. Figure 5.52 compares the vertical deflection of the modelled composite panels in section 5.1.2.1 (A1) and section 5.1.10 (D1). Both models (A1 and D1) behave in a very similar manner. The magnitudes of vertical deflection obtained by both models are very close up to the temperature of 700°C. However, the change in magnitude of the deflection became more obvious for the range of temperature beyond 700°C, where a sudden drop in the graph occurred as series of mesh reinforcement starts to fracture due to excessive crack development within the edges of the slab. The same phenomenon happened in the A1 model but at a slightly higher temperature of 720°C. However, the D1 model with a smaller aspect ratio results in slightly lower central deflection within its floor area at the ultimate temperature compared to the A1 model. The new model results in 7.5% reduction in

the overall vertical deflection of the panel compared to that of A1 model at temperature of 858°C.

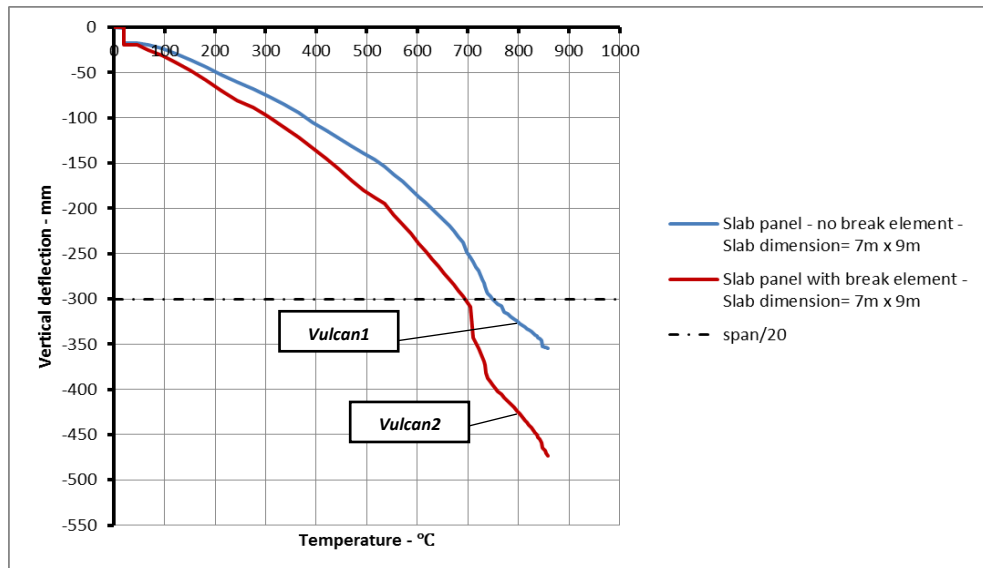


Figure 5.51: Comparison of the D1 model - slab central deflection from *Vulcan1* and *Vulcan2*

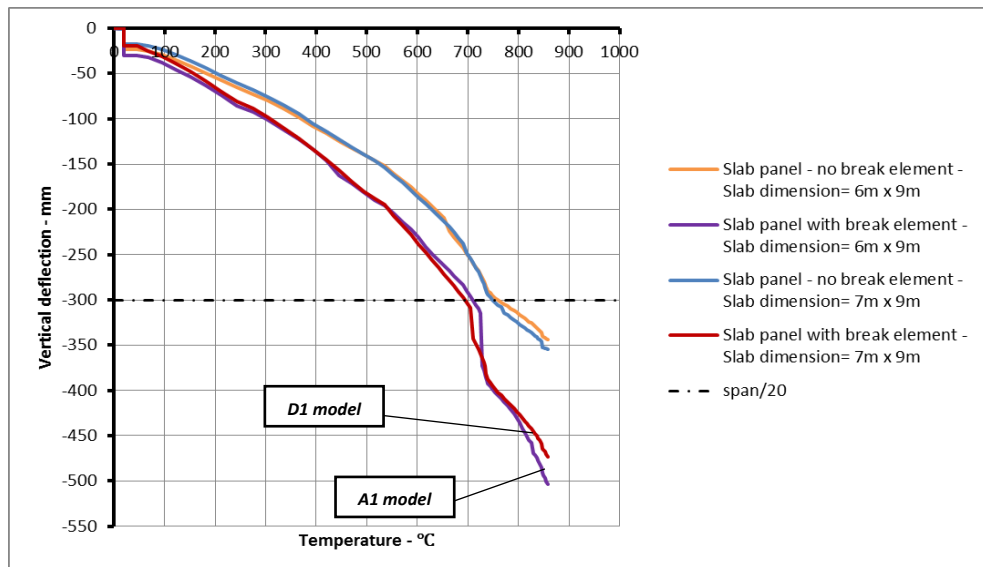


Figure 5.52: Comparison of the A142-slab central deflection from A1 and D1

Figures 5.53 to 5.55 illustrate the crack development along the edges of the slab in both directions. The D1 model has identified the crack development initially to occur (beyond the fracture of some reinforcement) along the length of secondary interior beam at the temperatures around 600°C, where the vertical deflection of the slab is about 245mm. The edge of the slab along the internal secondary beam in the A1

model experienced the crack development at lower temperature of 400°C with a vertical deflection of 140mm. The D1 model indicates the maximum crack width of 21mm over the length of the interior secondary beam at the ultimate temperature, whereas the maximum crack width of 25mm was obtained from the A1 model along the same edge of the panel at ultimate temperature. D1 model identifies the first fracture of reinforcement to occur along the exterior edge of the panel at a temperature of 705°C, which is slightly lower than the temperature of 725°C at the time of first fracture in the A1 model. This is also reflected in figure 5.53 where the vertical displacement from the D1 model is just slightly greater than the obtained displacement from the A1 model at the same temperatures. This is further indicated; when the sudden jump in the magnitude of vertical deflection in D1 model occurred at a slightly lower temperature compared to that of the A1 model as a result of the earlier fracture of reinforcement. The crack continued to develop beyond these temperatures in both models, where the maximum crack width of 31mm and 19mm were recorded by the A1 model and the D1 model respectively. Justification for crack development along the exterior edge of the panel has been given in section 5.1.2.1.

Comparing figure 5.55 and figure 5.9 from D1 and A1 models shows that the first fracture of reinforcement along the shorter span of the panel in the D1 model occurs at an early temperature of 553°C, whereas the A1 model identified the first fracture of reinforcement to occur at 725°C. As the crack in the concrete develops beyond the fracture of its reinforcement, both models reach the maximum crack width of around 12mm along the shorter edge of the panel. However, the result from the D1 model indicates an extensive irregular inward/outward movement of the slab floor area close to the interior secondary beam and along the length of the shorter span. This is due to the concrete being crushed around the interior corners of the panel as a result of excessive compression forces in that area. The outward movement along both interior and exterior edges of the panel in figures 5.53 and 5.54 is also due to the large compressive forces applied to these edge as a result thermal expansions of the steel beam and the concrete slab. The excessive outward movement of the slab at the corners of its interior secondary beam is also the direct result of concrete being crushed in that corner. Figure 5.56 is a graphical representation of the slab horizontal

displacements obtained by D1 model at the ultimate temperature of 858°C. The figure clearly indicates the development of the crack in the concrete along all edges of the slab floor area. The red dotted circle area refers to the interior corner of the panel where combined inward and outward movement of the concrete slab is visible.

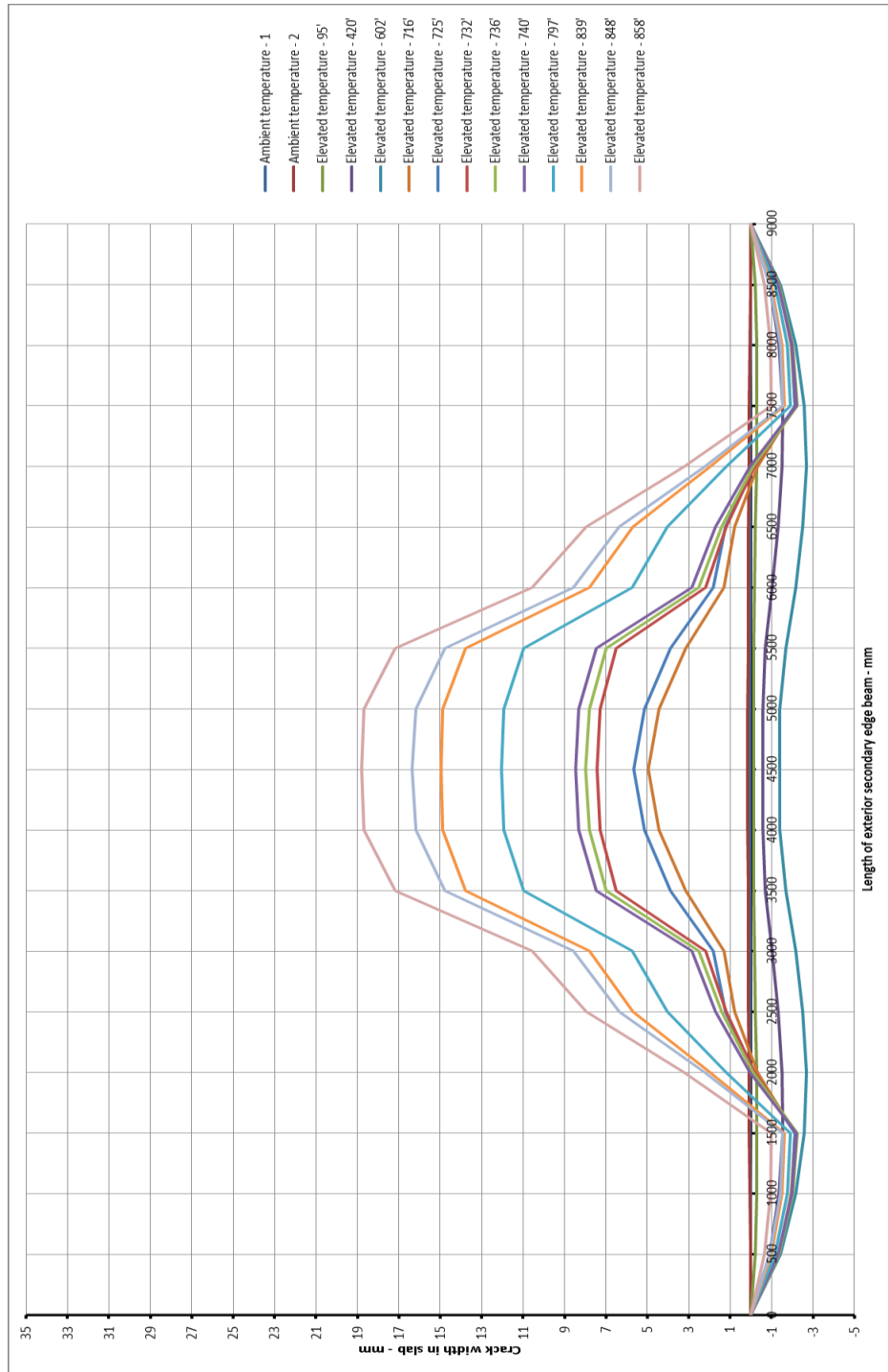


Figure 5.53: Horizontal crack development – exterior secondary edge beam – D1 model

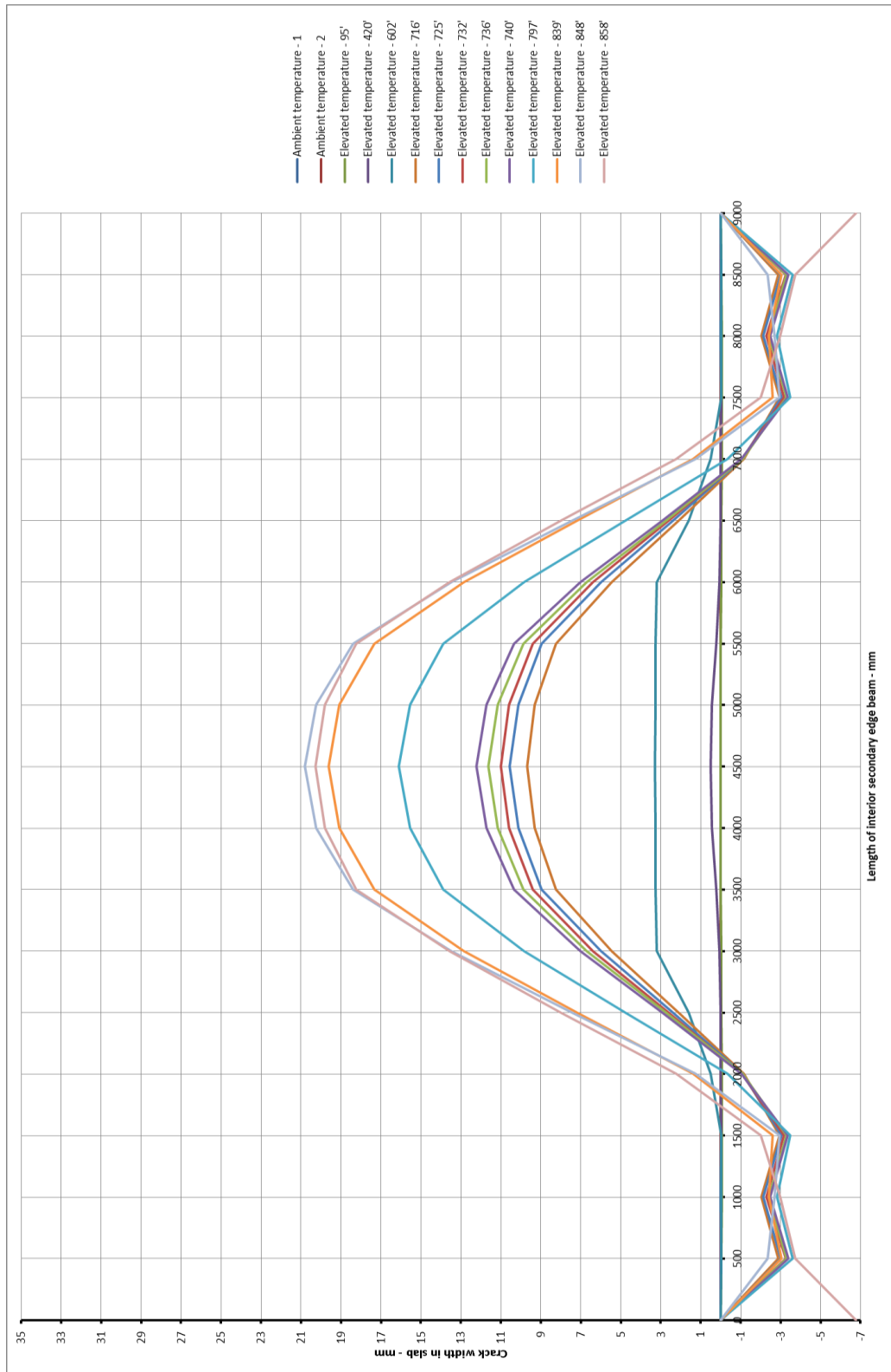


Figure 5.54: Horizontal crack development – exterior secondary edge beam – D1 model

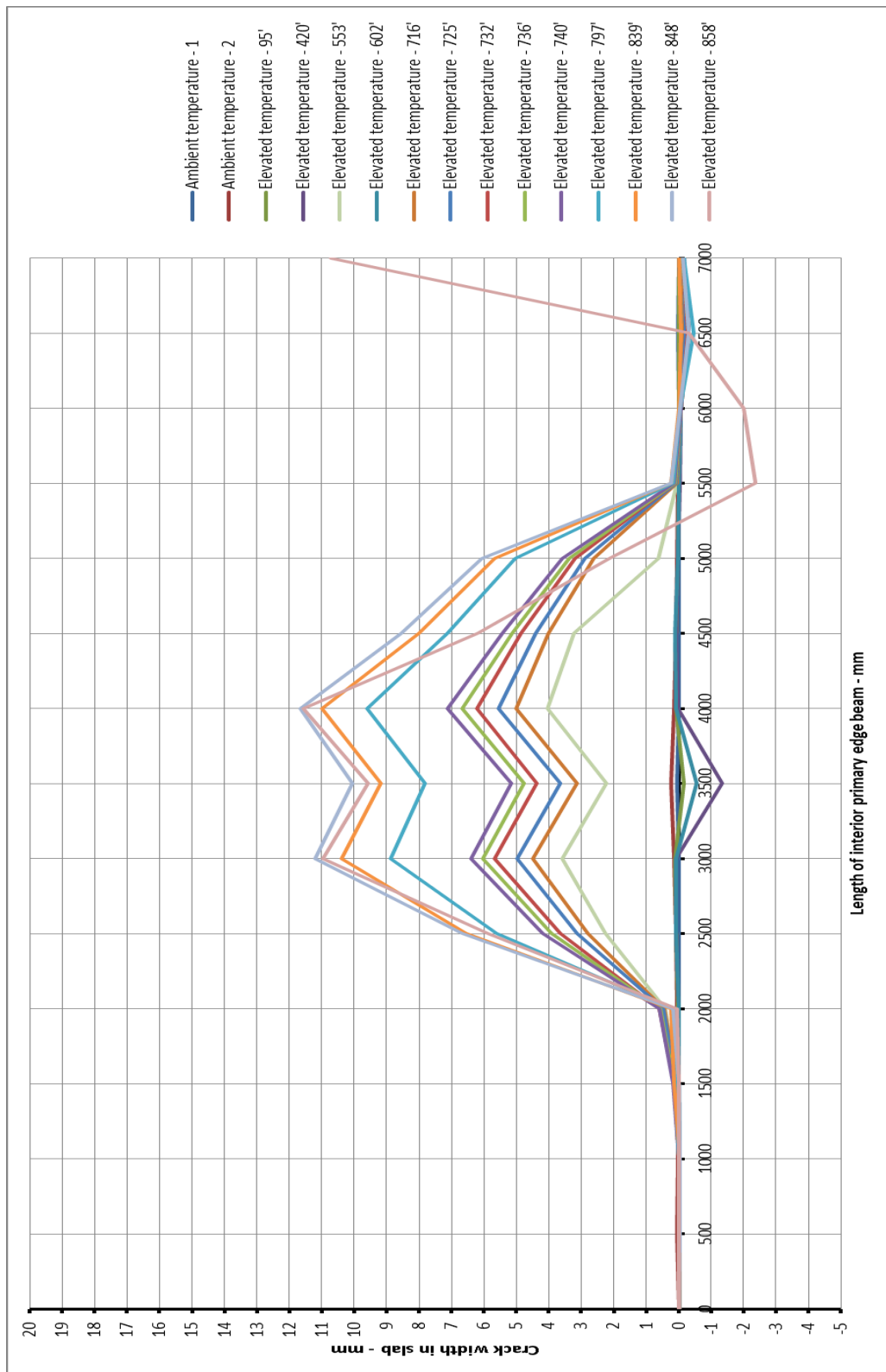


Figure 5.55: Horizontal crack development – interior primary edge beam – D1 model

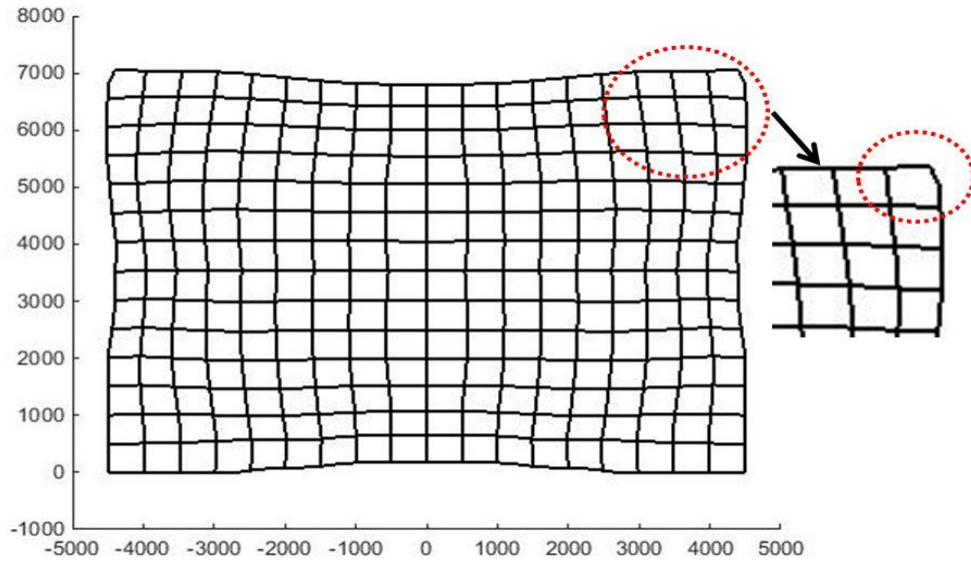


Figure 5.56: Plan view of ultimate slab horizontal movement, D1 model

5.1.11 Influence of aspect ratio on connection performance of composite panel

Figures 5.57 to 5.58 show the rotational displacements of the pin connection used in the numerical model (D1 model) with a smaller aspect ratio at elevated temperature. Figure 5.57 is the rotational response of the steel connection at the centre of the interior primary beams from *Vulcan1* and *Vulcan2*.

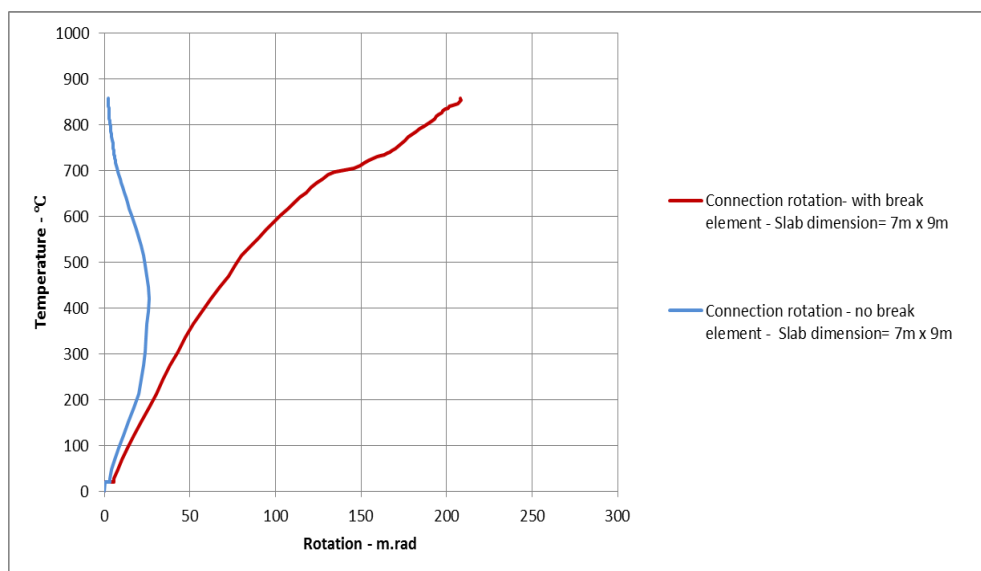


Figure 5.57: Comparison of the D1 model - slab central deflection from *Vulcan1* and *Vulcan2*

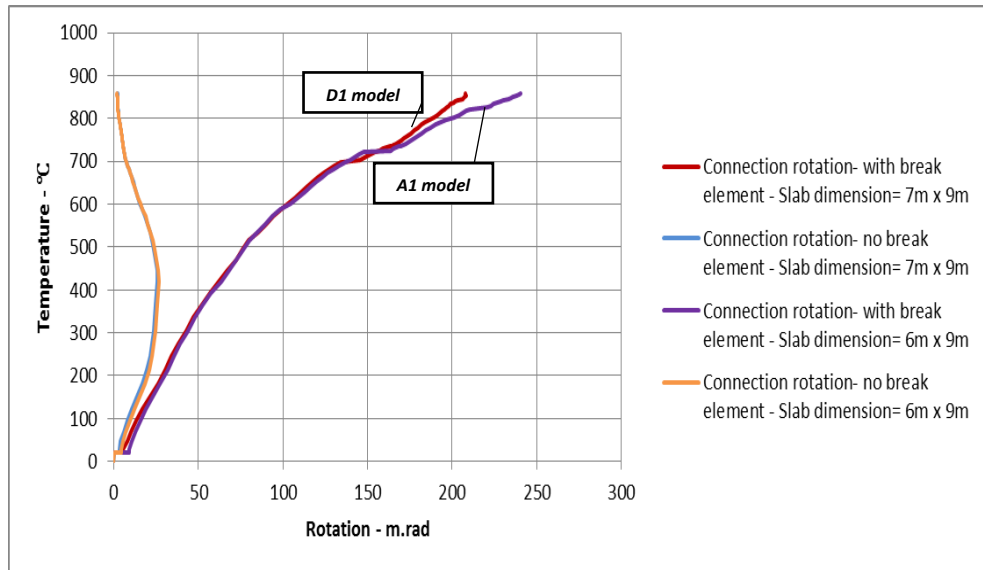


Figure 5.58: Comparison of the A142-slab central deflection from A1 and D1

Figure 5.58 compares the rotational response of the composite pin connection from A1 (aspect ratio=1.5) and D1 (aspect ratio=1.28) models using both versions of the software (*Vulcan1* and *Vulcan2*). As is evident from the figure, the geometrical changes of the panel do not reflect extensive changes in the connection performance when using *Vulcan1* with the assumption of permanent continuity of the slab during the analysis. However, the results from *Vulcan2* once again highlight the importance of proper modelling of slab continuity in the numerical analysis.

The results from *Vulcan2* (the red and purple lines) indicates the change in the magnitude of rotational displacement of the steel joint which is solely due to the changes made within the slab dimensions (aspect ratio). The rotational responses obtained from both models with different aspect ratios are almost identical up to temperature of around 700°C, where the first fracture of reinforcements occurred along the edge of the slab. This has been shown by small flat plateau in the above figure. The same phenomenon occurred in the A1 model but at slightly higher temperature of around 725°C, which is also the temperature that the first fracture of reinforcement occurred in the model. This is also correct for the slab horizontal movement beyond the fracture of reinforcements as mentioned in 5.1.10.

Beyond the fracture of the reinforcement at the top of the steel beam, the rotational response of the joint obtained from the D1 model indicates some level of enhancement compared to that of the A1 model. The reason for the enhanced

behaviour of the model can be explained by the extra stiffness of the composite slab as a result of a larger floor area (smaller aspect ratio). The D1 model results in 13% reduction of the overall rotational response of the steel joint when the aspect ratio of the floor area was reduced by 15%. Therefore, varying slab dimensions (different aspect ratios) in composite structures would reasonably influence the rotational response of the steel connection below the slab, which in turn results in either reduced or increased rotational displacement of the connection.

5.1.12 Remarks

An interior composite panel as a part of a large structural frame was modelled in software *Vulcan* in order to study the importance of appropriate modelling of the slab continuity on the overall performance of the composite frame in fire. Appropriate boundary conditions were applied and the model was analysed under combination of loading at ambient temperature followed by increasing temperature in accordance with the standard fire curve (ISO834). The model was run in two versions of the software; the original version that accounts for the slab permanent continuity during the analysis (*Vulcan1*) and the updated version of the code which contains a new developed break element to account for the slab discontinuity and the occurrence of discrete cracks during the analysis (*Vulcan2*).

Parametric studies were conducted in order to investigate the influence of reinforcement ratio, reinforcement material properties (characteristic yield strength), concrete material properties (characteristic compressive strength), composite slab thickness and the different aspect ratio on the overall performance of the composite panel using both versions of the software. The outcome of the analysis has been presented in terms of the slab vertical deflection, rotational displacement of the connection and the horizontal movement of the slab edges (crack development). The calculated result from the updated version was compared with the result from the original software. The comparison between the models clearly indicates the importance of appropriate modelling of structural continuity, where a more accurate and more realistic representation of the composite structure at rising temperature can be obtained.

5.2 Case study II: Composite frame with semi-rigid connections

In order to further investigate the influence of the recent development in modelling composite structures, a composite frame similar to that of the case study I was modelled in the software *Vulcan* but with a reduced rotational capacity of the corner connections. The corner connection elements in the model for the previous case study were assumed to be fully rigid with no horizontal or rotational relative movement, therefore, in this study the connection elements along the direction of the protected secondary beams were modelled with a reduced rotational rigidity in order to investigate influence of the joint ductility on the overall performance of the frame and in particular the relative horizontal and vertical deformation of the floor area. The behaviour of the model was studied through using a reduced ductility level for the corner connections. Isotropic reinforcing mesh of A142 was used in the numerical modelling of the slab element. All other assumptions such as: the frame dimensions, material properties, section sizes, applied loading and the boundary conditions were kept the same. Details of the tests specification, such can be found in section 5.1. Figure 5.59 shows isometric view of the panel.

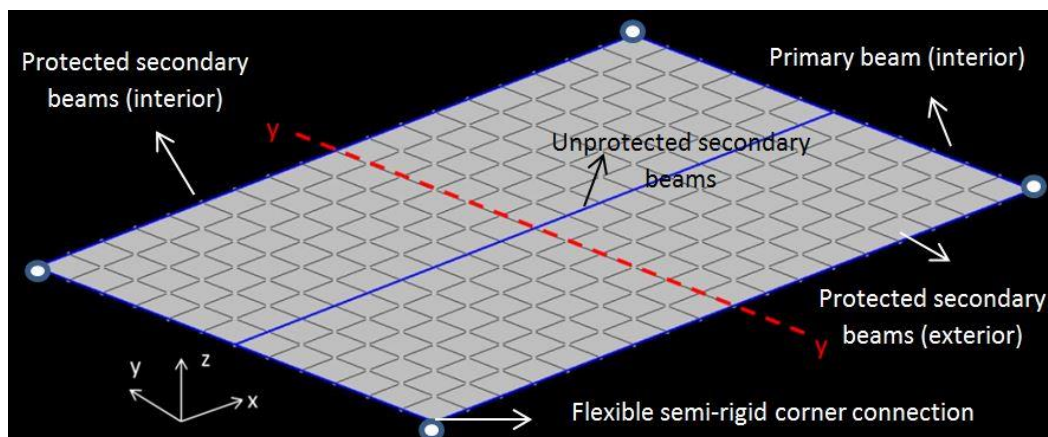


Figure 5.59: 3D isometric view of full floor slab area

In order to investigate the behaviour of the secondary edge beams in terms of their vertical deformation and its subsequent effects on the floor central deflection it was decided to reduce the rotational capacity of the corner connection elements parallel

to the x-direction. Similar to the section 5.1 the full sized model was divided into 2 equal halves using the symmetric line y-y as shown in the above figure.

5.2.1 Influence of connection ductility on vertical deflection/crack development of composite panel

The influence of the connection ductility on the overall performance of the floor area and in particular its influence on the horizontal relative movement of the slab around the edges and vertical deformation of the supporting beams were studied through numerical modelling of the composite panel. The reference plane in the model were assumed to be at half-depth through the slab, therefore all figures presented in this section are constructed based on the effects of the relative movement of the structural members at the assumed reference plane. The numerical data from this study was compared with the data obtained in section 5.1. The results of the comparative analysis between the flexible connections and the rigid connections from section 5.1 are shown in the following figures. The comparison was done in terms of the slab vertical deflection and the horizontal crack development in the slab around the edges. Figures 5.60 and 5.61 illustrate the slab three-dimensional vertical deflection and the magnified horizontal displacement of the modelled composite panel respectively.

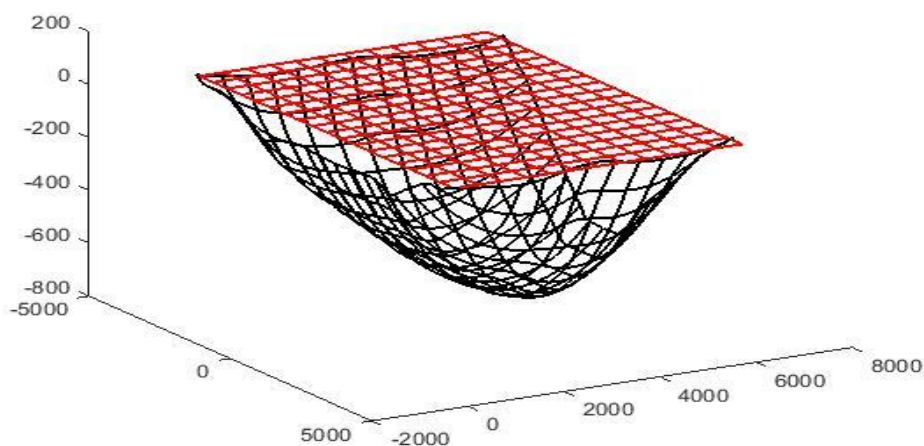


Figure 5.60: 3D view of the deformed shape of the interior composite panel

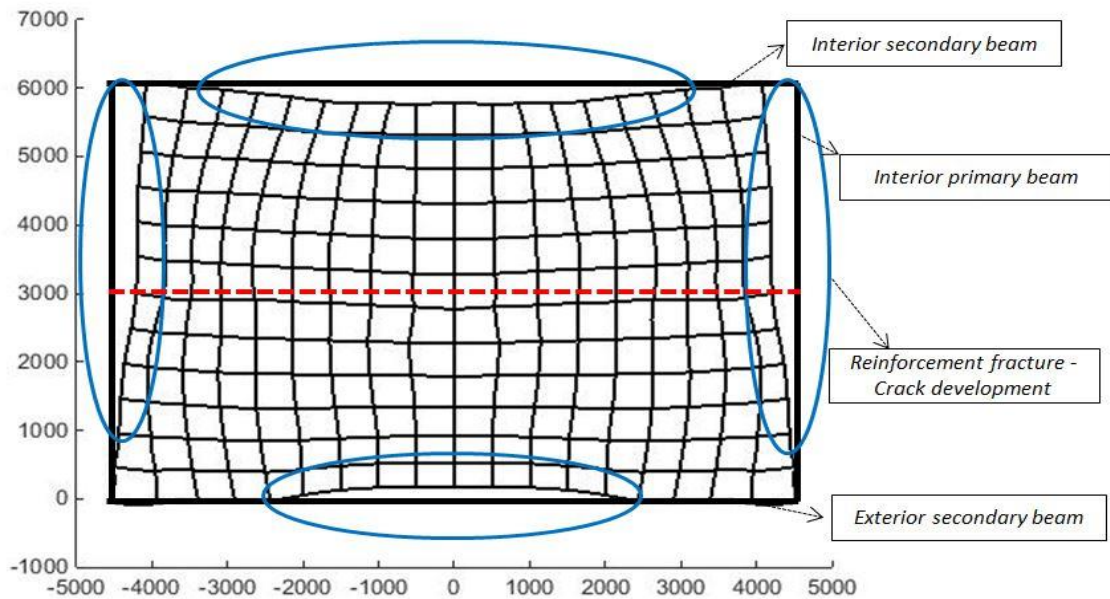


Figure 5.61: Plan view of slab horizontal movement, flexible connection

As is evident from the figure 5.61, the presence of flexible connection at the corners of the frame has significant influence of the overall frame behaviour and in particular on the integrity failure of the slab compartment. The concrete at the interior corner of the floor slab cracked along the x-direction at the early stages of the analysis, this is mainly due to the localised tensile forces in the area close to the flexible connection. More concrete failure of the slab appeared around the edges as the temperature increased. The concrete at top of the protected beams cracks as a result of combined tensile force and hogging moment induced by the vertical deformation of the slab area. Once the crack occurs tiny reinforcement ratio at the crack is unable to fully transfer the load within the section and therefore, the carrying capacity of the section reduces. Figure 5.62 illustrates the central vertical displacement of the slab under elevated temperature. Comparison of the model with the data from the composite frame in section 5.1 clearly indicates the influence of the localised failure of the slab on the overall performance of the structure. It can be seen from the figure below, that the magnitude of the overall vertical deflection from the two models are very similar up to 600°C, where a rapid increase in the vertical deflection of the flexible panel can be observed. This is due to the fact that number of break elements failed at the location closed to flexible joint at 620°C. Therefore, the rotational capacity of the composite joint reduces, which consequently results in larger vertical deformation of

the slab area above the connection. The rate of the change in the magnitude of the vertical deformation increases as more localised failure of occurs around the edges of the slab.

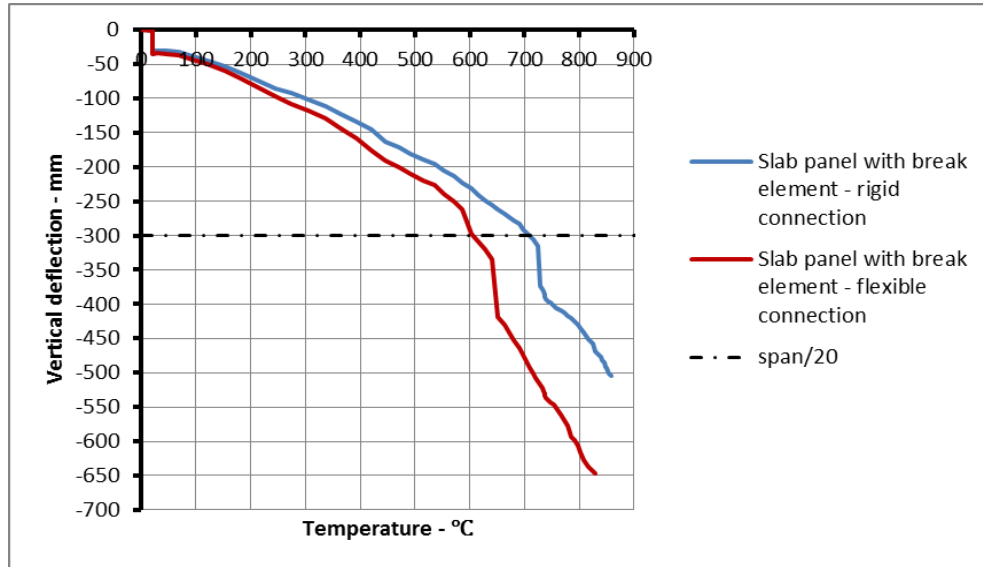


Figure 5.62: Comparison of the -slab central deflection – composite panel

Figure 5.63 shows the development of the crack pattern along the primary protected edge beam at different temperatures. Comparing this with the figure 5.61, the development of the crack along the edge can be observed. As the graph shows, the concrete at the bottom left corner of the composite panel remains uncracked since it has been subjected to a set of compressive forces during the analysis. Unlike the exterior corner connection, a wide crack was developed close to the connection along the interior secondary protected beam. The large crack development at the interior corner of the panel is a direct result of failure of series of break elements along the related edge of the slab. As is shown in the figure, the crack initially starts to develop close to the interior connection at temperature around 600°C, this is also the point where the failure of the first break element occurs. A reasonable correlation can also be observed between the development of the cracks at the interior corner and the vertical deformation of the slab in figure 5.62, where the sudden increase in the displacement can also be observed at the temperature around 600°C.

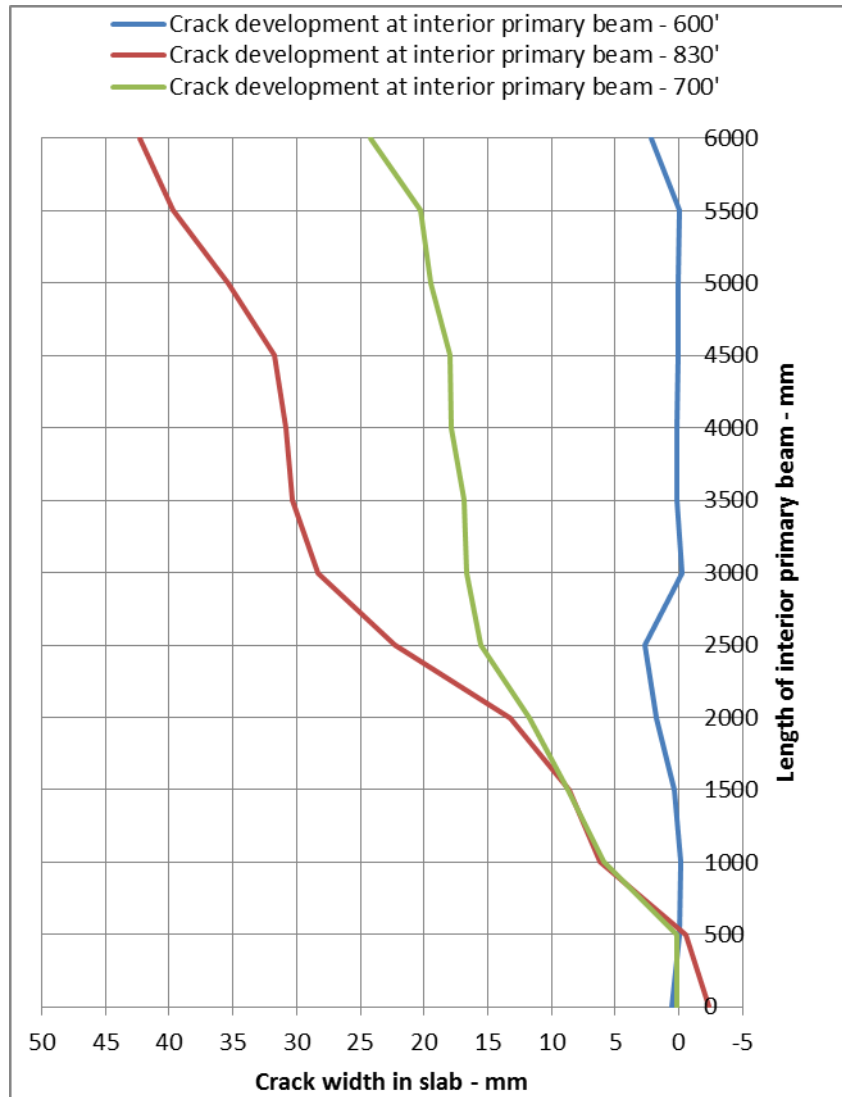


Figure 5.63: Horizontal crack development at interior primary edge beam – flexible connection

Furthermore, the behaviour of the supporting beams at edges of the slab can also be influenced by the slab discontinuity over the length of the supporting beams, since any sort failure of the slab around the edges can significantly alter the presence of composite action between the slab and the beam. Figure 5.64 illustrates the behaviour of composite beams in the two models (with rigid corner connection and flexible connection) in terms of their vertical deformation. Figure 5.65 also compares the rotational behaviour of different connections in both models.

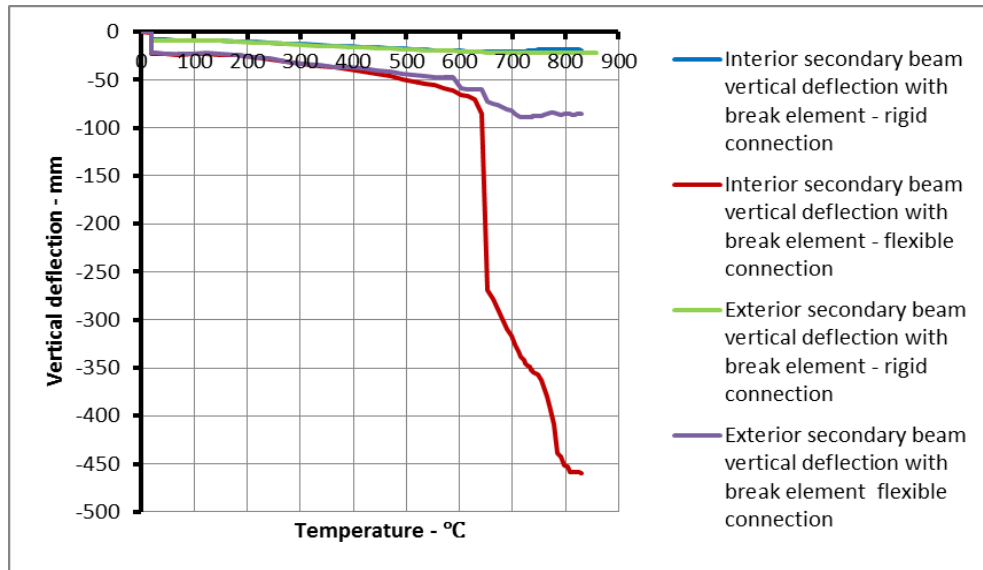


Figure 5.64: Comparison of the -beam central deflection – composite panel

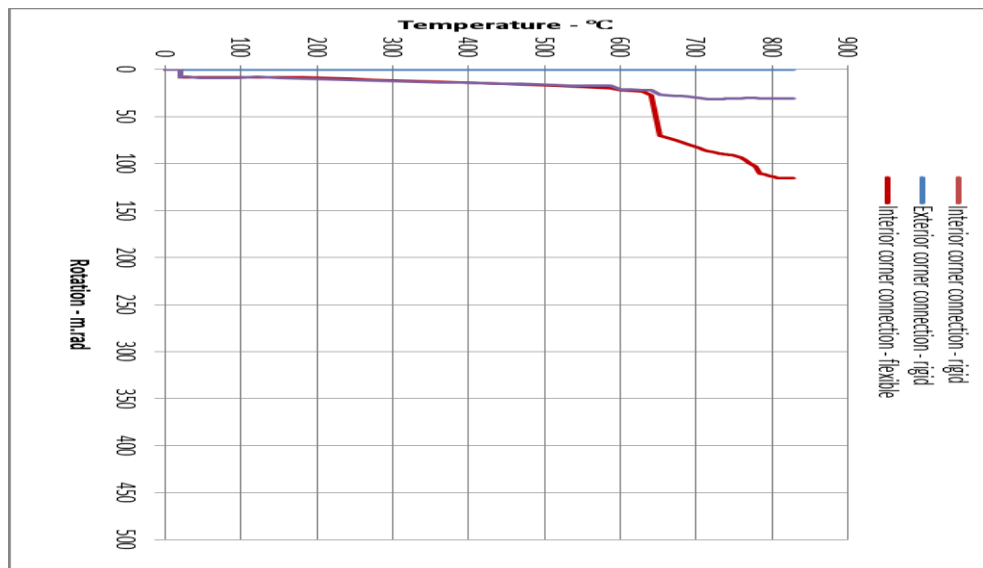


Figure 5.65: Comparison of connection rotational displacement – composite panel

Looking at the graphs it can be seen that there is a direct relation between the increase in the beam vertical deflections and the rotational displacement of the connection especially in the composite panel with flexible corner connection. Again it can be as is evident the protected secondary beams in the first model (rigid connection) experience a very low vertical deformation compare the second model. This is mainly due to the very rotationally stiff connection at the corners which does allow any form of significant rotation of the beam. On the other hand, in the model with flexible joint, once the concrete at top of the connection cracks, the rotational capacity of the connection due to its composite action with slab will be reduced,

which tend to increase the magnitude of the vertical deformation of the beam. Large vertical deformation occurs at the secondary interior beam once the reinforcement ruptures at the area close to the flexible connection. However, the vertical displacement of the exterior secondary beams stays at relative low level compared the interior edge. This is mainly due to the presence of full composite action at top of the steel connection as no fracture of the reinforcement has been observed.

5.3 Conclusion

Six sets of parametric studies were conducted in order to further investigate the influence of the slab continuity within the tension area of the largely deflected floor slab in fire. The comparisons from these studies clearly indicate the importance of the appropriate modelling of the discrete cracks in composite slabs around the slab edges. The presence of slab discontinuity results in large cracks developing followed by rupture of the mesh reinforcement. This results in reduced rotational capacity of the composite connections and consequently larger vertical deflection of the floor area

Chapter 6

6. Conclusion and Recommendations for Further Work

6.1 Conclusions

In recent years rapid progress in Structural Fire Engineering has been achieved. The development of advanced computational technology gives structural engineers good opportunities to move away from the traditional individual structural member-based fire design methods and to adopt performance based structural fire design.

Structural Fire Engineering Design focuses on building safe and economical structures. Fire safety is concerned with specific aspects of passive fire protection in terms of designing structures and adequate load bearing resistance and for limiting fire spread as relevant [5]. Therefore, structures should achieve two fundamental functions:

- Provision of adequate load bearing capacity in fire. This is achieved by ensuring that a building maintains its stability for a reasonable period of time in the event of a fire.
- Provision of sufficient fire isolation capacity. Structural members should be designed so that the safety criteria: integrity, insulation and robustness of the structure is maintained at the level required to provide fire compartmentation and thermal insulation.

Several full-scale and small-scale fire tests have been carried out during last two decades. These experiments have explored the behaviour of structural members and the interaction between these members under fire condition, to provide scientific data for the development of structural fire design. Using the advantage of gathering valuable experimental data, several numerical models such as: *VULCAN*, *SAFIR* and *ADOPTIVE*, have been developed, and validated using the test data.

The thermal and structural behaviour of composite slabs have been key research topics in the past decade, since experiments have shown that they play a very important role in maintaining structural stability, especially in situations of large deformation in the slab where the ultimate load capacity far exceeds the design load capacity based on the traditional yield-line theory.

In this research, the behaviour of composite floor slabs in fire has been studied. From experimental evidence the main failure mode of composite concrete slabs subjected to out-of-plane loading conditions and large deflections is usually an integrity failure due to the formation of large individual cracks. Smearred cracking has been assigned to the slab element in the current version of the *Vulcan* software. The slab element in *Vulcan* assumes perfect bond between the concrete and the mesh reinforcement but the bond strength between steel reinforcement and concrete in composite slab in real structures is influenced by many factors, such as the type of steel bars, the temperature, the properties of the concrete, the stress-strain state, the cracking status of concrete, etc... Many numerical models have been proposed to study the bond characteristic of steel reinforcement. Izuddin *et al.* [111] have developed an analytical model to study the failure of lightly reinforced concrete members in fire but only very simple boundary conditions were considered, and a single crack fracture was assumed at the mid-span of the bending member. A composite slab contributes to the rotational stiffness of the joint by means of its resistance to tensile force due to hogging bending moment at the top surface of the slab. The presence of composite slab increases the lever arm within the joint, which consequently results in higher rotational stiffness. However, adequate ductility in composite slabs should be retained to ensure the robustness of composite buildings in fire. Therefore, appropriate representation of the slab behaviour at cracks becomes essential in order to study to overall performance of the structural frame at rising temperature. This chapter outlines the main conclusions from the studies, and provides some recommendations for further work and applications of the developed procedure.

6.1.1 Behaviour of structural members in fire

Connections are the key component within any structure, which are responsible for transferring various types of forces (shear force, axial force) and moment (bending moment) between the adjacent structural members. The overall response of a structure can be greatly influenced by the rotational behaviour of the beam-to-column connections. The composite slab and the steel connection are working together to withstand the gravity load and the generated horizontal load from axial restraint. Predicting the behaviour of a structure in the connection zone is complex since there are wide ranges of parameters involved in order to establish the behaviour of a connection.

- Connections are the primary elements that make the whole assembly of structural members work with each other. Therefore, the performance of different structural elements can be significantly influenced by ductility and strength of the connections. Connections in a structural frame need to be ductile enough to allow a reliable deformation of each floor beam prior to their failure under fire condition. Despite the risk of progressive collapse of the structure, joint failure can also lead to structural failure in terms of integrity “E” by passing the fire to the upper floor through the gaps in the cracked zone.
- Extensive previous fire tests on composite floor slabs have revealed that the escalation in load carrying capacity of the slab is the direct result of tensile membrane action being developed in the central area of the slab, assuming that sufficient vertical support is provided. The composite slab contributes to the rotational stiffness of a joint by means of its resistance to tensile force due to hogging bending moment at the top surface of the joint. The presence of the composite slab increases the lever arm within the joint, which consequently results in higher rotational stiffness. The development of cracking at the corners of a composite slab panel during fire can result in reduced rotational capacity of the steel beam-column connection below the composite slab, which consequently causes the joint to be overloaded, and therefore joint failure is possible. In all currently available simple calculation

models for slab capacity the contribution of the mesh reinforcement has been ignored, and the slab floor area is considered as an isolated slab panel, since in these methods it is assumed that the reinforcement at the slab edges is indeed ruptured. However, it is important for the slab to meet the safety criterion “E” to ensure that no smoke or flames can penetrate to the floor above.

Therefore, appropriate modelling of the crack development at the slab perimeter especially at locations close to the connections, is essential in order to consider the effect of horizontal restraint from the mesh reinforcement and the possible effects of reinforcement failure on the overall stability of the structure.

6.1.2 Numerical modelling and validation

6.1.2.1 *Component-based model*

A component model is generally a 2D model, but the slab is a member which is three-dimensional in nature. Therefore, the additional spring element on a 2D joint model should accurately represent the lumped properties of the slab. The width of the slab on top of the joint plays an important role in the joint rotational stiffness since it determines the amount of reinforcement and number of shear studs within the section. The simple formula recommended by EC4: part 5.4.1 to determine the effective width of the slab is based on the sagging bending moment distribution within the composite beam, of which the slab is the compressive flange, whereas the effective width of slab over a joint should be determined with respect to applied tension and hogging bending moment. Therefore, the recommended design method for the calculation of the effective width is certainly not appropriate for the purpose of fire engineering design of connections. Furthermore, the composite slab in *Vulcan* is currently assumed to be continuous over the lengths of internal beams using a smeared cracking assumption. Therefore, even if the effective width of the slab over the joint can be determined, the problem arises as to whether the slab’s presence has been accounted for twice in the analysis; once as part of the joint and once as a three dimensional layered shell element, which accounts for continuity by using the smeared cracking technique.

6.1.2.2 Bare steel connection with 3D slab shell element

In order to avoid the limitations set out in section 6.1.2.1 a simplified model of the behaviour of the composite slab within the tension area has been produced. The new method uses the advantage of the existing two-dimensional component-based model for the bare steel connection, along with the 3D slab shell element resting on top of it, and connected to the beam with link elements representing shear studs. With this method the limitations from using the 2D component model can be overcome, since the effect of the concrete slab is applied to the joint directly, not as a single spring element with certain mechanical characteristics but as a three-dimensional layered shell element. The new element represents the behaviour of the composite slab beyond the failure of concrete at the crack faces. The element is modelled as a 2-noded line element connecting the slab nodes to the adjacent beam nodes. Furthermore, the influence of high temperature on material properties and the appropriate bond-slip model have been considered in the model. The developed model has been successfully implemented in the software *Vulcan*. The element is capable of tracing discontinuity of the composite slab over the crack face in tension areas; the compatibility of the use of the new model with the recently developed static/dynamic solver is ensured. The new model represents the continuing concrete slab and its reinforcement in modelling beam-column and beam-beam connections, and is capable of modelling localised crack initiation and the development of the cracks in a composite slab subjected to large deflections under fire condition. The new element can be placed between all individual slab elements, along the edges between slab and beam elements, or within the floor area in both locations where cracks are most likely to occur.

6.1.2.3 Validation of the model

Three series of previous experimental tests on composite joints with different steel-to-steel connections and varied member sizes have been modelled in the updated version of the *Vulcan* software incorporating the newly developed break element. The numerical models were validated against the recorded experimental data. The data from the models have been presented in terms of the moment-rotation behaviour of the steel connection and the crack development along the edges of the floor slab in

its vicinity. Furthermore, the force-displacement behaviour of a number of individual break elements was also studied for the two of the models. The results from the models were in the accordance with the experimental data. Modelling the detailed steel-to-steel connections from these tests was not possible due to some technical limitations in using the software; therefore, a nominal pin-connection element with a limited level of rotation has been used for the purpose of the analysis. Flexible end plate connections are generally assumed to act as a pin connection with only a limited level of rotational rigidity; therefore, a semi-rigid connection element with bilinear rotational stiffness property was used to represent the equivalent rotational stiffness of the tested joints in the experiments in both the elastic and the plastic zones up to the failure of the mesh reinforcement in tension. The rotational stiffness for the connection element in all numerical models was calculated from the moment-rotation curve of the tested steel connection. The performance of the newly developed break element was further investigated through a qualitative comparison between the *FRACOF* floor test [49] and the numerical model in *Vulcan*.

6.1.3 Parametric studies

Six parametric studies were conducted in order to investigate the influence of the slab continuity in tension areas on the overall and local performance of the structural frame in fire, in terms of slab vertical deflection and the crack propagation around the edges. The calculated result from the updated version was compared with the result from the original software.

Parametric study 1: a rectangular composite panel was modelled as a part of a larger structure. Rigid and nominal pin connections were respectively assumed to connect corners and middle beam-to-beam connections. The model was studied with three different reinforcement ratios of A142, A252 and A393, and the continuity of slab elements over the length of the edge beam was taken into account using the break elements. The moment-rotation behaviour at the middle beam-to-beam connection and the slab central deflection of the model were compared with the same model from the original version of software *Vulcan*, assuming full composite action between the slabs and the beams. The comparison between the models with three

reinforcement ratios using *Vulcan2* shows a reduction in magnitude of both slab vertical deflection and connection rotation as the reinforcement ratio increases. The model in *Vulcan2* with A142 mesh reinforcement indicates a maximum slab central deflection of 503mm and the maximum connection rotational displacement of 240m.rad at the ultimate temperature of 858°C. The use of A252 mesh reinforcement in *Vulcan2* results in 23% and 17% reduction of the overall slab deflection and connection's rotation respectively. Comparison between the model with A142 and A393 as a mesh reinforcement also shows a 41% and 38% reduction in magnitude of vertical and rotational displacement for slab area and the steel connection respectively. Comparing the results from *Vulcan1* and *Vulcan2* on the study of reinforcement ratio shows that the presence of break element in the modelled structure generally results in larger vertical deflection and rotational displacement of floor area and the steel joint respectively. Therefore, assuming the permanent continuity (smeared cracking approach) of the slab area in the finite element analysis may underestimate the real slab capacity in terms of its maximum vertical deflection.

Parametric study 2: the influence of reinforcement material properties on the overall performance of the floor area was investigated through numerical modelling of the similar composite panel as that in the first parametric study (A1model). However, in order to study the influence of different material properties of steel reinforcement on the composite panel performance a higher yield strength of 600 N/mm² along with an ultimate strain rate of 20% was assigned to the reinforcement of the modelled composite panel (A2 model). The comparison between the two numerical models clearly indicates the importance of material properties of steel reinforcement on the overall behaviour of the slab panel, where the 20% increase in the yield strength of the reinforcement results in 25% reduction in the maximum vertical deflection obtained by the numerical model. The A2 model also indicates the maximum crack width of 18mm along the internal secondary beam at the maximum temperature of 858°C, whereas, the maximum crack width of 25mm was picked up by the A1 model at the same temperature. The maximum crack width of 29mm and 5mm along the length of exterior secondary beam were recorded by A1 model and A2 model respectively. The model also indicates no failure of reinforcement along the interior primary edge of the composite panel. Additionally, the A2 model results

in a 19% reduction of the overall rotational response of the steel joint when the yield strength characteristic of the steel reinforcement in the model was increased by 20%. As is evident from the result of this study, the performance of composite structure can be significantly altered due to the changes in steel material properties. The effects of these changes are more pronounced in the numerical models from *Vulcan2*. The appropriate modelling of discrete cracks using break elements provides a more realistic reflection of the altered structural behaviour due to the changes in material properties. Whereas, the changes in material properties of *Vulcan1* model results in almost identical response of the structural frame in terms of both slab vertical deflection and connection rotation. Furthermore, the assumption of continuity in structure (*Vulcan1*) may overestimate the fire safety criteria “R” and “I” for the composite slab within the structure. Appropriate modelling of the slab continuity (using break element) provides a more realistic representation of the floor area at the cracked region; therefore, a more accurate estimation of the fire safety criteria can be obtained.

Parametric study 3: The influence of slab thickness on the overall performance of the floor area was investigated. In order to study the influence of different slab thicknesses on the composite panel performance a thinner slab with an overall effective depth of 90mm was used in the model (B1 model) and the results were compared with the A1 model (with slab thickness of 120mm) from the first parametric study. Although, it was not possible to trace the behaviour of the structure beyond 700°C, the comparison between the two numerical models clearly indicates the influence of slab overall thickness on the behaviour of the composite panel, where the 25% reduction in the overall depth of the concrete slab results in a 33% increase of the maximum vertical deflection obtained by the numerical model. The B1 model also indicates the maximum crack width of about 20mm along the internal secondary beam at the maximum temperature of 700°C, whereas, the maximum crack width of 7mm was picked up by the A1 model at the same temperature. The maximum crack widths of 0.5mm and 20mm were recorded along the length of exterior secondary beam by the A1 model and the B1 model respectively at a maximum temperature 700°C. Furthermore, the B1 model results in 26% increase of the overall rotational response of the steel joint when the overall depth of the slab

in the model was reduced by 25%. It is also evident from the obtained data that changing the slab thickness or increase/decrease slab stiffness has a noticeable influence on the overall performance of the structure. Comparing the results of the models with different slab overall depth (A1 and B1) ran in both *Vulcan1* and *Vulcan2* clearly indicates the importance of composite slab break element and its influence on the global and local behaviour of the composite floor area. The results obtained from *Vulcan1* did not identify a significant difference of slab load capacity in term of vertical deflection at high temperature. Both A1 and B1 models from *Vulcan1* performed very similar in terms of magnitude and the general behaviour, whereas, the results from *Vulcan2* (with reasonable modelling of crack propagation) show a clear distinction in the performance of these models. Therefore, the true effects of varying slab thickness on the overall performance of composite structure can be properly appreciated using the break element, which accurately represents the initiation/development of the through depth discrete cracks along the edges of the composite slab panel.

Parametric study 4: a numerical model was developed (C1 model) in order to investigate the influence of concrete material properties (characteristic compressive strength) on the overall performance of the floor area. The value of characteristic compressive strength (f_{ck}) of the slab element was assumed to be equal to 50N/mm^2 , which is higher than the assumed compressive strength value of 35N/mm^2 for the A1 model. The C1 model with improved concrete characteristic strength results in slightly lower central deflection within its floor area compared to the A1 model. The model shows a 6% reduction in the overall vertical deflection of the panel compared to that of A1 model. This is mainly due to extra stiffness of the composite slab as a result of stronger concrete material. The model also indicates the maximum crack width of 21mm over the length of the interior secondary beam at ultimate temperature; this is 4mm less than the maximum crack width obtained from the A1 model along the same edge of the panel at ultimate temperature. The maximum crack width of 31mm and 23mm along the exterior edge of the slab panel were recorded by A1 model and C1 model respectively. Unlike the A1 model, the C1 model only indicates a very local failure of reinforcement along the length of the shorter edge of the panel. The A1 model shows a maximum crack width of 12mm

along its shorter span, whereas the crack width along the same edge of the panel in C1 model reaches the maximum of 2mm at very local locations a short distance from the centre of the shorter span. Also, the C1 model results in 13% reduction of the overall rotational response of the steel joint when the compressive strength characteristic of concrete material in the model increased by 42%. Changing of concrete material properties does not make a significant influence on the general behaviour of the composite floor structure subject to high temperature, especially at large deflection. Therefore, as is evident from the runs in *Vulcan2* for A1 and C1 models, the corresponding vertical deflection for C1 model with an enhanced concrete strength is very similar to that of the A1 model in terms of magnitude. Higher compressive strength will provide a higher tensile capacity for concrete within the tension zones; however, it does not significantly influence the occurrence of discrete cracks along the perimeter of the floor area.

Parametric study 5: In order to study the effects of different aspect ratios on the overall performance of the composite panel, the width of the slab in the model was increased by 1m. The new model (D1 model) is identical to that of the A1 model in term of the assumed material properties, loading condition and the boundary conditions. The aspect ratio of the slab element in D1 model assumed to be equal to 1.28 (9m x7m), which is less than the assumed aspect ratio of 1.5 (9m x 6m) for the A1 model. The new model with smaller aspect ratio results in a slightly lower central deflection within its floor area at ultimate temperature compared to the A1 model. The model results in 7.5% reduction in the overall vertical deflection of the panel compared to that of A1 model at temperature of 858°C. This is mainly due to extra stiffness of the composite slab as a result of larger concrete floor area due to reduced aspect ratio of the slab. The D1 model indicates the maximum crack width of 21mm over the length of the interior secondary beam at ultimate temperature, whereas the maximum crack width of 25mm was obtained from the A1 model along the same edge of the panel at ultimate temperature. The maximum crack width of 31mm and 19mm over the exterior edge of the panel were recorded by A1 model and D1 model respectively. The D1 model also results in 13% reduction of the overall rotational response of the steel joint when the aspect ratio of the floor area was reduced by 15%.

Parametric study 6: In the last study the rigid corner connections were replaced by nominal pin-connections with a limited level of rotational capacity. The model was studied in terms of moment-rotation behaviour of the connections, slab central deflection and beam vertical deflection, and the results were compared with the data from the same model assuming permanent continuity of the slab over the edge beams. The comparisons from both case studies clearly indicate the importance of the appropriate modelling of the discrete cracks in composite slabs around the slab edges. The presence of slab discontinuity results in large cracks developing followed by rupture of the mesh reinforcement. This results in reduced rotational capacity of the composite connections and consequently larger vertical deflection of the floor area.

Remarks

The results of the parametric studies indicate the effects of the reinforcement material properties and the reinforcement ratio of the slab as the main significant factors influencing the overall performance of any composite structure in terms of its total vertical deflection of the floor area, connection rotation and the crack propagation at rising temperature. Variation in slab thickness and the aspect ratio was also found to be an important factor determining the ultimate deflection of the slab floor area and the rotational displacement of the connection. The change in magnitude of concrete compressive strength was found to be the least important factor influencing the overall performance of the modelled composite structure.

6.2 Recommendations for further work

- To carry out a series of experiments to obtain reliable test data on the bond characteristics between steel reinforcement and the concrete slab under fire conditions. In these tests, the reinforcement details (i.e. surface condition, material properties), and concrete details, position of the reinforcement, load and support conditions should be taken into account. Furthermore, the change in temperature, deformation and the fracture status of concrete and reinforcement should be recorded.

- To perform detailed studies on the influence of support conditions, bond characteristics and reinforcement details, such as the requirements for anchorage and continuity of bars across supporting beams, on localised failure of reinforcement in composite slabs under large deflection.
- The collapse mechanisms of frames initiated by column failure may be changed if composite floor slabs are taken into consideration, because their non-linear stiffness and strength provide much higher restraint to the columns and more effective load-sharing paths after column buckling has commenced. The failure or buckling of a supporting column also affects the behaviour of the slab since it then loses a vertical support. Therefore; applying the newly break element to represent the continuity of the slabs, the effects of column failure on the slab performance can be investigated further.
- A beam-to-column connection has no shear capacity after its complete fracture. This can cause large through-depth cracks within the composite floor above this connection, but collapse may not occur if the beam shear is subsequently carried by the floor slab. These effects need further detailed studies using three-dimensional structural analysis.
- To employ a more recent version of the program compiler for the software *Vulcan*, so the use of the newly developed break element can be better exploited by investigating the influencing of slab discontinuity on the behaviour of previously developed/validated component-based connection models [110] through both static and dynamic states.

Based on the presented numerical analysis in this work, the newly developed model is shown to be capable of representing the discontinuity of the floor area in composite structures at both ambient and elevated temperature. The structural numerical model incorporating the break elements can identify the initiation of the cracks in concrete followed by tracing the relative movements of the slab between the cracks. Despite the fact the new model has a reasonable influence on the local and global performance of the structural frame, the accuracy of the pre-made assumptions within the new element should be further investigated.

The characteristics of the break element can be generally divided in two phases; before the occurrence of tensile cracking in concrete, and the failure of the reinforcing mesh beyond the through-depth cracking of concrete. As has been mentioned in previous chapters, the Vulcan software uses a smeared cracking method in modelling the failure of concrete within its slab element. Identification of the through-depth cracking of concrete in the new break element is based on the existing smeared property of the slab element, where the concrete slab is assumed to be fully cracked through its depth when the concrete layers above and below the reinforcing layers are flagged as cracked (due to exceeding the tensile capacity of the concrete material) within the analysis of the slab shell element. However, predicting the cracks in a concrete slab based on the smeared property may not be a reasonable approach as the cracking of the floor slab in a structural frame is a very local effect, which can be influenced by series of different factors such as; the quality of the particles, the curing condition and the quality of a batch.

Furthermore, once the concrete cracks, the shear bond interaction between the steel and concrete becomes the key factor in determining the failure criterion of an individual break element. Once concrete fails in tension the reinforcement area crossing the crack face will continue to strain by developing a shear (bond) interaction between the concrete and the embedded part of the steel rebar. The break element fails when the allocated reinforcement area within an element reaches its tensile strength. The empirical bond-slip relationship adopted in modelling the break element has been derived on the basis of extensive experimental data on pull-out failure from reinforced concrete sections. Although, the applied bond-slip model has proved to be reasonably accurate it should be remembered that bond-slip models are generally based on the limited embedded length of the rebar inside the concrete (the development length), whereas, the principle differs when considering a discrete cracks in composite slabs where the mesh is embedded all the way through the both lengths of the slab and is anchored at intervals by the welding of the orthogonal mesh reinforcement. In addition, the slip model is based on tests done at ambient temperature. Degradation of material properties is a direct result of increasing temperature. The rates of this degradation for steel reinforcement and concrete have been explained in section 2.1. Lightweight concrete experiences a rate of reduction

of its compressive strength capacity for temperatures beyond 300°C; this is even more obvious for normal-weight concrete for which the strength reduces continuously as the temperature increases. In the current model for crack development, the effect of increasing temperature on the bond quality has been taken into account by applying the appropriate retention factor to the characteristic compressive strength variable in the slip equation. The validity of this assumption needs to be further investigated by conducting a series of experiments to study the effects of rising temperature on the bond-slip performance.

Despite the fact that the newly developed model has certain limitations, it has still proved to be a strong foundation model to use in medium-scale software such as *Vulcan* to represent slab continuity, discrete local failures of the slab, and their consequent effects on the overall behaviour of the structural frame.

7. References

- [1] Yu, X. *Modelling Reinforced Concrete Slabs in Fire*. Ph.D. thesis, University of Sheffield, 2008.
- [2] Gillie, M. *The behaviour of steel-framed composite structures in fire conditions*. Ph.D. thesis, University of Edinburgh, 2000.
- [3] Yu, C. *Three-dimensional analysis of composite structural elements at elevated temperatures*. Ph.D. thesis, University of Sheffield, 2007.
- [4] Andrew, H.B., *Structural Design for Fire Safety*, England, 2001.
- [5] BSI. *BS EN 1994-1-2: Eurocode 4: Design of composite steel and concrete structures, Part 1-2: General rules – Structural fire design*, London, UK: BSI, 2005b.
- [6] BSI. *BE EN 1991-1-1: Eurocode 1: Design of concrete structures – Part 1-1: General rules and rules for buildings*, London, UK: BSI, 2004a.
- [7] Bailey, C.G. and Moore, D.B. The structural behaviour of steel frames with composite floorslabs subject to fire: Part 1: Theory. *The Structural Engineer*. 2006, **78**(11), pp. 19–27.
- [8] Newman, G.M., Robinson, J.T. and Bailey, C.G. *Fire Safe Design: A New Approach to Multi-Storey Steel-Framed Buildings*, SCI Publication P288, The Steel Construction Institute, UK, 2000.
- [9] Newman, G.M., Robinson, J.T. and Bailey, C.G. *Fire Safe Design: A New Approach to Multi-Storey Steel-Framed Buildings*, Second Edition, SCI Publication P288, The Steel Construction Institute, UK, 2006.
- [10] BSI. *BS 5950 Structural Use of Steelwork in Building: Part 1: Code of Practice for Design in Simple and Continuous Construction*. London, UK: BSI, 1985.
- [11] CEN. *Eurocode 3: Design of Steel Structures – Part 1.2: General Rules – Structural Fire Design*, (Draft), European Committee for Standardization, 1995.
- [12] Foster, S., Chladna, M., Hsieh, C., Burgess, I.W. and Plank, R.J. Thermal and structural behaviour of a full-scale composite building subject to a severe compartment fire. *Fire Safety Journal*. 2007, **42**, pp. 183–199.
- [13] Confidential Report, *Fire damage structural survey report to Churchill Plaza, Churchill Way, Basingstoke*, Amos Broome Associates plc, UK, 1991.
- [14] Bailey, C.G. and Moore D.B. The structural behaviour of steel frames with composite floorslabs subject to fire: Part 2: Design. *The Structural Engineer*. 2000c, **78**(11), pp. 28–33.
- [15] ASFP. *Fire protection for structural steel in buildings* (2nd ed., revised), The Association for Specialist Fire Protection, Ascot, The Steel Construction Institute, 1992.

References

- [16] Narayanan, R. ed. *Structural connections: stability and strength*, London: Elsevier Applied Science, 1989.
- [17] Wang, Y.C., Dai, X.H. and Bailey, C.G. An experimental study of relative structural fire behaviour and robustness of different types of steel joint in restrained steel frames. *Journal of Constructional Steel Research*. 2011, **67**(7), pp. 1149–1163.
- [18] NIST. *Federal building and fire safety investigation of the world trade center disaster: final report on the collapse of world trade centre building 7. Report NCSTAR 1-1A*, 2008.
- [19] FEMA. *Federal Emergency Management Agency. Overview of Fire Protection in Buildings*, 2002.
- [20] Wang, Y.C. *Steel and composite structures: behaviour and design for fire safety*. London: Spon, 2002.
- [21] OPDM. *The Building Regulations 2000, Approved Document B, Fire Safety*, TSO. 2000.
- [22] Huang, Z., Burgess, I.W. and Plank, R.J. Modelling Membrane Action of Concrete Slabs in Composite Buildings in Fire. I: Theoretical Development. *Journal of Structural Engineering*. 2003, **129**(8), pp. 1093–1102.
- [23] ECS. *EC3: Design of Steel Structures, Part 1.1: Revised Annex J Joints and building Frames*. (Draft), Document CEN/TC250/SC3 N419E, European Committee for Standardization, 1994.
- [24] Badoo, N. Stainless Steel in Fire. *The Structural Engineer*, 1999, **77**(19), pp. 16–17.
- [25] Cooke, G.M.E. An Introduction to the Mechanical Properties of Steel at Elevated Temperatures. *Fire Safety Journal*. 1988, **13**(1), pp. 45–54.
- [26] Kirby, B.R. and Preston, R.R. High Temperature Properties of Hot Rolled Structural Steels for Use in Fire Engineering Design Studies. *Fire Safety Journal*. 1988, **13**, pp. 27–37.
- [27] Purkiss, J.A. *Fire safety engineering, Design of structures*. Butterworth-Heinemann, Linacre House, Jordon Hill, Oxford, UK, 1966.
- [28] SSEDTA. Lecture 11a: Introduction to Structural Fire Engineering, 2001.
- [29] Idorn, G.M. Expansive Mechanisms in Concrete. *Cement Concrete Research*. 1992, **22**, pp. 1039–1046.
- [30] Schneider, U. Concrete at High Temperatures- a general review. *Fire Safety Journal*. 1988, **13**, pp. 55–68.
- [31] Bazant, Z.P. and Kaplan, F.M. *Concrete at High Temperature: Material Properties and Mechanical Models*, Longman Group Limited, 1996.
- [32] CEN. *Eurocode 2: Design of Concrete Structures – Part 1.2: General Rules – Structural Fire Design*, European Committee for Standardization, 2004.

References

- [33] Twilt, L. and Kruppa, J. European Research into the Fire Behaviour of Composite Floors and Beams. *3rd International Conference on Steel-Concrete Composite Structures*, Fukuoka, Japan, September 1991.
- [34] Twilt, L. and Kruppa, J. Current Research on Fire Resistance of Composite Floors and Beams. *International Conference on Materials and Design Against Fire*, London, United Kingdom, October 1992.
- [35] Al-Jabri K.S. *The behaviour of steel and composite beam-to-column connections in Fire*. Ph.D. thesis, University of Sheffield, 1999.
- [36] Davison, J.B. and Nethercot D.A. Overview of Connection Behaviour. In the *Structural Connection-Stability and Strength*. Ed. Narayanan, R., Elsevier Applied Science, 1989, pp. 1–22.
- [37] Wainman, D.E. and Kirby, B.R. *Compendium of UK Standard Fire Test Data, Unprotected Structural Steel – 2*, Ref. No. RS/RSC/S1199/8/88/B, British Steel Corporation (now Corus), Swinden Laboratories, Rotherham, 1988.
- [38] Elghazouli, A.Y., Izzuddin, B.A. and Richardson, A. J. Numerical modelling of the structural fire behaviour of composite buildings. *Fire Safety Journal*. 2000, **35**, pp. 279–297.
- [39] Usmani, A.S., Rotter, J.M., Lamont, S., Sanad, A.M. and Gillie, M. Fundamental principles of structural behaviour under thermal effects. *Fire Safety Journal*. 2001, **36**, pp. 721–744.
- [40] Sanad, A.M., Lamont, S., Usmani, A.S. and Rotter, J.M. Structural behaviour in fire compartment under different heating regimes – Part 1: Slab thermal gradients. *Fire Safety Journal*. 2000a, **35**, pp. 99–116.
- [41] Allam, A.M., Burgess, I.W. and Plank, R.J. Performance-Based Simplified Model for a Steel Beam at Large Deflection in Fire. *Proc. 4th International Conference on Performance-Based Codes and Fire Safety Design Methods*, Melbourne, Australia, 2002.
- [42] Hayes, B. Allowing for membrane action in the plastic analysis of rectangular reinforced concrete slabs. *Magazine of Concrete Research*. 1968a, **20**(65), pp. 205–212.
- [43] Kemp, K.O. Yield of a square reinforced concrete slab on simple supports, allowing for membrane forces. *The Structural Engineer*. 1967, **45**(7), pp. 235–240.
- [44] Wood, R.H. *Plastic and Elastic Design of Slabs and Plates*, London: Thames and Hudson, 1961.
- [45] Cameron, N. J. K. and Usmani, A.S. New design method to determine the membrane capacity of laterally restrained composite floor slabs in fire. Part 1: Theory and method. *The Structural Engineering*. 2005, **83**(19), pp. 28–33.
- [46] Bailey, C.G. Membrane action of slab/beam composite floor systems in fire. *Engineering Structures*. 2004, **26**, pp. 1691–1703.
- [47] Bailey, C.G., Lennon, T. and Moore, D.B. The behaviour of full-scale steel-framed buildings subjected to compartment fires. *The Structural Engineering*. 1999, **77**(8), pp. 15–21.

References

- [48] Bailey, C.G. and Toh, W.S. Behaviour of concrete floor slabs at ambient and elevated temperatures. *Fire Safety Journal*. 2007a, **42**, pp. 425–436.
- [49] Simms, W. and Zhao, B. *Fire Resistance Assessment of Partially Protected Composite Floors (FRACOF): Engineering Background*, 2009.
- [50] Abu, A.K. *Behaviour of Composite Floor Systems in Fire*. Ph.D. thesis, University of Sheffield, 2009.
- [51] Xiao, Y., Choo, B.S. and Nethercot, D.A. Composite Connections in Steel and Concrete. I. Experimental Behaviour of Composite Beam-Column Connections. *Journal of Constructional Steel Research*. 1994, **31**, pp. 3–30.
- [52] Xiao, Y., Choo, B.S. and Nethercot, D.A. Composite Connections in Steel and Concrete: Part 2 – Moment Capacity of End Plate Beam to Column Connections. *Journal of Constructional Steel Research*. 1996, **37**(1), pp. 63–90.
- [53] Lam, D. *Influence of composite flooring on steel beam-to-column connections*. M.Phil. thesis, University of Sheffield, 1989.
- [54] Tschemmerneegg, F. A New Spring Model for Composite Joints. *Proc. COST C1 Workshop, Strasbourg*, 1992, pp. 356–368
- [55] BSI. *BS EN 1993-1-8: Eurocode 3: Design of steel structures – Part 1-8: Design of joints*, London, UK: BSI, 2005a.
- [56] Spyrou, S., Davison, J.B., Burgess, I.W. and Plank, R.J. Experimental and analytical investigation of the “compression zone” component within a steel joint at elevated temperatures. *Journal of Constructional Steel Research*. 2004, **60**, pp. 841–865.
- [57] Spyrou, S., Davison, J.B., Burgess, I.W. and Plank, R.J. Experimental and analytical investigation of the “tension zone” component within a steel joint at elevated temperatures. *Journal of Constructional Steel Research*. 2004, **60**, pp. 867–896
- [58] Leston-Jones, L.C. *The influence of semi-rigid connections on the performance of steel framed structures in fire*. Ph.D. thesis, University of Sheffield, 1997.
- [59] da Silva, L.S., Santiago, A. and Real, V.P. Component model for the behaviour of steel Joints at elevated temperature. *Journal of Constructional Steel Research*. 2001, **57**(11), pp. 1169–1195.
- [60] Al-Jabri, K.S., Burgess, I.W. and Plank, R.J. Prediction of the degradation of connection characteristics at elevated temperature. *Journal of Constructional Steel Research*. 2004, **60**, pp. 771–781.
- [61] Block, F.M., Burgess, I.W., Davison, J.B. and Plank, R.J. The development of a component-based connection element for endplate connections in fire. *Fire Safety Journal*. 2007, **42**, pp. 437–451.
- [62] Sarraj, M. *The behaviour of steel fin plate connections in fire*. Ph.D. thesis, University of Sheffield, 2007.

References

- [63] Al-Jabri, K.S. Modelling and simulation of beam-to-column joints at elevated temperature: A review. *Journal of the Franklin Institute*. 2011, **348**, pp. 1695–1716.
- [64] Huang, Z., Burgess, I.W. and Plank, R.J. Modelling of six full-scale fire tests on a composite building. *The Structural Engineering*. 2002, **80**(19), pp. 30–37.
- [65] Huang, Z., Burgess, I.W. and Plank, R.J. Modelling Membrane Action of Concrete Slabs in Composite Buildings in Fire. I: Theoretical Development. *Journal of Structural Engineering*, 2003a, **129**(8), pp. 1093–1102.
- [66] Huang, Z., Burgess, I.W. and Plank, R.J. Modelling Membrane Action of Concrete Slabs in Composite Buildings in Fire. II: Validations. *Journal of Structural Engineering*. 2003b, **129**(8), pp. 1103–1112.
- [67] Huang, Z., Burgess, I.W. and Plank, R.J. Fire resistance of composite floors subject to compartment fires. *Journal of Constructional Steel Research*. 2004b, **60**(2), pp. 339–360.
- [68] Bailey, C.G. and Toh, W.S. Small-scale concrete slab tests at ambient and elevated temperatures. *Engineering Structures*. 2001, **29**, pp. 2275–2791.
- [69] Jirasek, M. and Zimmermann, T. Embedded crack model: I. Basic formulation. *International Journal of Numerical Methods in Engineering*. 2001, **50**, pp. 1269–1290.
- [70] Chen, W.F. and Saleeb, A.F. *Constitutive equations for engineering materials, Volume 1: Elasticity and modelling*, 2nd edition, New York, USA: Elsevier Sciences B.V., 1994.
- [71] Ohtani, Y. and Chen, W.F. A plastic-softening model for concrete materials. *Computers & Structure*. 1988, **33**(4), pp. 1047–1055.
- [72] Foster, S.J. *Tensile Membrane Action of Reinforced Concrete Slabs at Ambient and Elevated Temperatures*. Ph.D. thesis, University of Sheffield, 2006.
- [73] Sun, R.R. *Numerical Modelling for Progressive Collapse of Steel Framed Structures in Fire*, Ph.D. thesis, University of Sheffield, 2012.
- [74] Sun, R., Huang, Z. and Burgess, I.W. Progressive collapse analysis of steel structures under fire conditions. *Engineering Structures*. 2012, **34**, pp. 400–413
- [75] Brown, N. and Anderson, D. Structural properties of composite major axis end plate connections. *Journal of Constructional Steel Research*. 2001, **57**(3), pp. 327–349.
- [76] Abu, A.K., Burgess, I.W. and Plank, R.J. Slab panel vertical support and tensile membrane action in fire. *Steel and Composite Structures*. 2008, **8**(3), pp. 217–230.
- [77] Stadler, M. *Design of Composite Slab Systems in Case of Fire Using Simplified Finite Element Analysis*. Technische Universität München, 2012.
- [78] Mensinger, M., Schaumann, P. and Stadler, M. *Nutzung der Membranwirkung von Verbundträger-Decken-Systemen im Brandfall*, DASt-Forschungsbericht. 2012.

References

- [79] DIN EN 1994-1-2: *Eurocode 4: Bemessung und Konstruktion von Verbundtragwerken aus Stahl und Beton – Teil 1-2: Allgemeine Regeln – Tragwerksbemessung für den Brandfall*. December 2010.
- [80] Zandonini, R., Puhali, R. and Smotlak, I. Semi-Rigid Composite Action: Experimental Analysis and a Suitable Model. *Steel Research*. 1990, **15**, pp. 121–151.
- [81] Collins, D. *Steel Concrete Composite Bridge*, London: Thomas Telford Ltd, 2005.
- [82] Oehlers, D.J. and Bradford, M.A. *Elementary Behaviour of Composite Steel and Concrete Structural Member*, Oxford: Elsevier Science, 1999.
- [83] BSI. *BS EN 1994-1-1: Eurocode 4: Design of composite steel and concrete structures – Part 1-1: General rules and rules for buildings*. London, UK: BSI, 2004c.
- [84] Chen, S. and Zhang, Z. Effective width of a concrete slab in steel–concrete composite beams prestressed with external tendons. *Journal of Constructional Steel Research*. 2006, **62**(5), pp. 493–500.
- [85] Spyrou, S. *Development of a component-based model of steel beam-to-column joints at elevated temperatures*. Ph.D. thesis, University of Sheffield, 2002.
- [86] Al-Jabri, K.S., Davison, J.B. and Burgess, I.W. Performance of beam-to-column joints in fire – A review. *Fire Safety Journal*. 2008, **43**, pp. 50–62.
- [87] Huang, Z., Burgess, I.W. and Plank, R.J. The Influence of Tensile Membrane Action on the Behaviour of Composite Steel-Framed Buildings in Fire. *Proc. ASCE Structures Congress 2001*, Washington DC, May 2001, pp. 1–14.
- [88] BSI. *BE EN 1992-1-1: Eurocode 2: Design of concrete structures – Part 1-1: General rules and rules for buildings*, London, UK: BSI, 2004a.
- [89] Díaz, C., Martí, P., Victoria, M. and Querin, O.M. Review on the modelling of joint behaviour in steel frames. *Journal of Constructional Steel Research*. 2011, **67**(5), pp. 741–758.
- [90] BSI. *BS EN 1992-1-2: Eurocode 2: Design of concrete structures – Part 1-2: General rules – Structural fire design*, London, UK: BSI, 2004b.
- [91] Topçu, İ.B. and Karakurt, C. Properties of Reinforced Concrete Steel Rebars Exposed High Temperatures, *Research Letters in Materials Science*. 2008, Vol. 2008, Article ID 814137, 4 pages.
- [92] Vassart, O. and Zhao, B. *Fire resistance assessment of partially protected composite floors (FRACOF): Design Guide*, 2011.
- [93] Shima, H., Choo, L. and Okamura, H. Bond Characteristics in post-yield of deformed bars. *Concrete Library of JSCE*. 1987, **10**, pp. 113–124.
- [94] Eligehausen, R., Popov, E. and Bertero, V. *Local bond stress-slip relationships of deformed bars under generalized excitations*. Report No. UCB/EERC-83/23, Earthquake Engineering Research Center, University of California, Berkeley, CA, 1983.

References

- [95] CEB-FIP (MC90). *CEB-FIP Model Code 1990: Design Code*. Comite Euro-International Du Beton (CEB), 1993.
- [96] Lehman, D. and Moehle, J. *Seismic Performance of Well-confined Concrete Bridge Column*. Pacific Earthquake Engineering Research Center, University of California, Berkeley, 2000.
- [97] Sezen, H. *Seismic Behaviour and Modeling of Reinforced Concrete Building Columns*. Ph.D. thesis, University of California, Berkeley, 20002002.
- [98] Sezen, H. and Setzler, E. Reinforcement Slip in Reinforced Concrete Columns. *ACI Structural Journal*. 2008, **105**(3), pp. 280–289.
- [99] Otani, S. and Sozen, M.A. Behaviour of multi-storey reinforced concrete frames during earthquakes. *Structural Research Series No. 392*, University of Illinois, Urbana, IL, 1972.
- [100] Alswiwat, J.M. and Saatcioglu, M. Reinforcement Anchorage Slip under Monotonic. *Journal of Structural Engineering*. 1992, **118**(9), pp. 2421–2438.
- [101] Pochanart, S. and Harmon, T. Bond-slip model for generalized excitation including fatigue. *ACI Materials Journal*, 1989, **86**(5), pp. 465–474.
- [102] Soroushian, P. and Choi, K. Local Bond Deformed Bars with Different Diameters in Confined Concrete. *ACI Structural Journal*. 1989, **86**(2), pp. 217–222.
- [103] Huang, Z. Modelling the bond between concrete and reinforcing steel in a fire. *Engineering Structures*. 2010, **32**(11), pp. 3660–3669.
- [104] Bazant, Z.P and Kaplan, M.F. *Concrete at high temperatures*. Longman Group Limited, 1996.
- [105] Huang, Z., Burgess, I.W. and Plank, R.J. Nonlinear Analysis of Reinforced Concrete Slabs Subjected to Fire. *ACI Structures Journal*. 1999, **96**(1), pp. 127–135.
- [106] Huang, Z., Burgess, I.W. and Plank, R.J. The Influence of Shear Connectors on the Behaviour of Composite Steel-Framed Buildings in Fire. *Journal of Constructional Steel Research*. 1999, **51**(3), pp. 219–237.
- [107] Davison, J.B., Lam, D. and Nethercot, D.A. Semi-rigid action of composite joints. *The Structural Engineer*. 1990, **68**(24), pp. 489–499.
- [108] Huang, Z., Burgess, I.W. and Plank, R.J. Effective Stiffness Modelling of Composite Concrete Slabs in Fire. *Engineering Structures*. 2000, **22**(9), pp. 1133–1144
- [109] Boreman, J., Kirby, P.A. and Davison, J.B. *Cardington Steel Frame Building: Tests on Nine Additional Isolated Bare Steel Connections*. Preliminary Report to BRE, University of Sheffield, October 1995.
- [110] Dong, G., Burgess, I.W., Davison, J.B. and Sun, R.R. Development of a General Component-Based Connection Element for Structure Fire Engineering Analysis. *Application of Structure Fire Engineering conference*, Prague, Czech Republic, April 2013, pp. 207–213.

References

[111] Izzuddin, B.A. and Elghazouli, A.Y. Failure of Lightly Reinforced Concrete Members under Fire – Part I: Analytical Modelling. *Journal of Structural Engineering*. 2004, **130**(1), pp. 3–17.

8. APPENDIX I

```

SUBROUTINE BREAK_ELM (M,X,Y,SS2,RR2,INCON,SD,LI,YPOINT,
*   NODPB,NOD,NODP,INCE,NFJ)
C*****
C...THIS SUBROUTINE FORMS ELEMENT STIFFNESS MATRIX AND INTERNAL FORCE
C...VECTOR IN GLOBAL COORDINATE FOR SHEAR CONNECTOR ELEMENTS
C
C*****
  IMPLICIT REAL*8(A-H,O-Z)
  IMPLICIT INTEGER*4(I-N)
  PARAMETER (NUMNOD=2000,NUMMEM=1000,NUMTEM=30,NZ=30,NCE=500,
*   MCON=1000)
  PARAMETER (NSEGME=500,NIINB=50)
    PARAMETER (MIGC=9)

  COMMON /PROBCV/ UNIT,FL1,FL2,TOL,F1INC,TOLINC,SEMIRIGD,AXISRIGD,
*   SLACK,EXPAND,NJ,NE,NEQ,NEBEL,NDXST,NDMT,NDRT,IN,IO,ITLIM,
*   IREF,IRCO,IC,NFE,NMT,NDTEMP,NTINC,NTEMP,IEQ,NS,NEWFILE,KKK
  COMMON /SLABNL1/ FAI(20,NZ),DLOAD(NUMMEM),YL(20,NZ),FCP20(20),
*   FAYP20(20),EAP20(20),BATAP(20),VCP(20),NSLAYER(20,NZ),
*   NRCL(NCE,NZ),INMREIN(20,NZ),MTEMSL(NUMMEM),MOUTSL(NUMMEM),
*   IHOTROL(20),NLAYER(20),MCROSS(NUMMEM),NDTEMSL,NTEMSL,
*   N THERMAL,MLINCR,NBOUNRD,LCONCRE,NCROSS,NSHEAR,NMREIN,NDIAG

  COMMON /SLABNL2/ TL(NCE,NZ),TL1(NCE,NZ),TLM(NCE,NZ)
  COMMON /CONNECT1/ IBEAMS(2,NUMMEM),MSHEAR(NUMMEM),

```

```

*   NBAR(20),DBRK(20),SLDEPTH(20),BFDP20(20),
*   BFYP20(20),BFUP20(20),BEAP20(20),BSUP20(20),BSYP20(20),
*   BSSHP20(20),NBRK,IDAN,NJLAY1,NJLAY2 COMMON /SEMIJO1/
TDMRD(NUMMEM*12),TDMRDO(NUMMEM*12)
COMMON /BEAMNL4/ TLB(NUMMEM,NSEGME),TLB1(NUMMEM,NSEGME),
*   TLBM(NUMMEM,NSEGME),TEMPNB(NIINB,NSEGME+1),
*   TEMPNB2(NIINB,NSEGME+1),TEMPNB3(NIINB,NSEGME+1),
*   MTEMNB(NUMMEM)
COMMON /HAMINJURI/ DKSH25(5,NUMMEM),ISADEGH(2,NUMMEM),
*   LLCRACK(2,NUMMEM),LLPHASE(2,NUMMEM),ITENS(2,NUMMEM)
COMMON /SLABNL6/ NDEGRA(MIGC,NZ,NCE),NDEGRA2(MIGC,NZ,NCE),
*   SITA1(MIGC,NZ,NCE),SITA2(MIGC,NZ,NCE),
*   EPERTSLO(MIGC,NZ,NCE),EPERTSL(MIGC,NZ,NCE)

DIMENSION SCON(10,10),SS2(12,12),RR2(12),RRBREAK(10),
*YPOINT(NUMMEM),NODP(9,NUMMEM),NODP0(9,NUMMEM),
*X(NUMNOD),Y(NUMNOD),MTEMP(NUMMEM),KTP1(MCON),KTP2(MCON),
*DICON(12),DDCON(10),DKSH(5),DSHF(10),NODPB(3,NUMMEM),
*NOD(2,NUMMEM),IFIND(2,4),SD(NUMNOD*6),NODPB0(3,NUMMEM),B(2000),
*IFINDBEAM(2,1),FORCE(10),SLIPMAX(NUMMEM),SLIPMAXX1(NUMMEM),
*SLIPMAXX2(NUMMEM),SLIPMAXX3(NUMMEM),SLIP(2000,NUMMEM),
*DK(2000,NUMMEM),DSHF1(2000,NUMMEM),DSHF11(2000,NUMMEM),
*DSHF111(2000,NUMMEM)

```

```

C*****IMPORTANTNOTE*****
*

```

```

C***** REMEMBER TO CHECK THE XLX,YLY,AREBARX,AREBARY, FOR THE CASE
WHEN ISS=1,

```

```

C***** MAKE SUR THAT THE CODE PICKS THE CURRENT AREBARX AND AREBARY
FOR ALL CONDITIONS

```

```
*****  
*****
```

```
PI=3.1415927
```

```
NODP0=NODP
```

```
    NODPB0=NODPB
```

```
IMSHEAR=MSHEAR(M)
```

```
DO I=1,10
```

```
    RRBREAK(I)=0.0D0
```

```
    DO J=1,10
```

```
        SCON(I,J)=0.0D0
```

```
    ENDDO
```

```
ENDDO
```

```
    DVLPL=((1000/(NBAR(IMSHEAR)))/2)
```

```
! CALCULATION OF EMBEDDED LENGTH OF REBAR INSIDE CONCRETE
```

```
DVLPL=100
```

```
! CALCULATION OF CONCRETE TENSILE STRENGTH
```

```
! CHECK THE POSITION OF NOD(1,M) IN THE SLAB ELEMENT
```

```
#####
```

```
    DO IPP=1,2
```

```
    DO IPP1=1,2
```

```
    IFIND(IPP,IPP1)=0
```

```
    ENDDO
```

```
    ENDDO
```

```
    DO JJJ0=1,NE
```

```
    DO III2=1,8
```

```
    IF (NODP0(III2,JJJ0).EQ.NOD(1,M))THEN
```

```
        IF(ICOUNT.EQ.0)THEN
```

```
            IFIND(1,1)=III2
```

```
IFIND(2,1)=JJ0
  JJJ10=JJ0
  ENDIF
  ICOUNT=ICOUNT+1
  IF(ICOUNT.EQ.2)THEN
    IFIND(1,2)=III2
    IFIND(2,2)=JJ0
  ENDIF
  ENDIF
ENDDO
  ENDDO

ILP=IFIND(1,1)
ILO=IFIND(2,1)
  IAB=ILO-NFE+3
  IF(ICOUNT.EQ.2)THEN
    ILP3=IFIND(1,2)
    ILO3=IFIND(2,2)
    IAB3=ILO3-NFE+3
  ENDIF
  J=NOD(1,M)
  IX=(2*ILP)-1
  IY=(2*ILP)
  DO JJJ1=1,NE
DO III3=1,8
IF(NODP0(III3,JJJ1).EQ.NOD(2,M))THEN
  ISS=1
  IF(ICOUNTT.EQ.0)THEN
    IFIND(1,3)=III3
    IFIND(2,3)=JJJ1
```

```

        ENDIF
        ICOUNTT=ICOUNTT+1
        IF(ICOUNTT.EQ.2)THEN
            IFIND(1,4)=III3
            IFIND(2,4)=JJJ1
        ENDIF
    ENDIF
END DO
END DO

        ILP5=IFIND(1,3)
        ILO5=IFIND(2,3)
        IAB5=ILO5-NFE+3
        IF(ICOUNTT.EQ.2)THEN
            ILP6=IFIND(1,4)
            ILO6=IFIND(2,4)
            IAB6=ILO6-NFE+3
        ENDIF
C     IF(ICOUNT.EQ.1)THEN
        IF ((ILP.LE.4))THEN          ! ILP<4 MEANS THAT NOD (1,M) IS IN THE CORNER
            IF ((ILP.EQ.1))THEN
                I1=NODP0(ILP+1,ILO)
                I2=NODP0(ILP+3,ILO)
            ELSE IF ((ILP.EQ.2))THEN
                I1=NODP0(ILP+1,ILO)
            ! NOD(1,M) OF BREAK ELEMENT IS ALWAYS IN THE SLAB ELEMENT
                I2=NODP0(ILP-1,ILO)

            !NOD(1,M) OF BREAK ELEMENT IS ALWAYS IN THE SLAB ELEMENT

```

! CALCULATED LENGTH OF SLAB IS USED TO DETERMINE NUMBER OF REBAR IN ORDER TO CHARACTERISE THE BREAK ELEMENT

ELSE IF ((ILP.EQ.3))THEN !

XLX=LENGTH OF SLAB FOR BREAK ELEMENT WORKING IN X-DIRECTION

I1=NODP0(ILP+1,ILO)

! YLY=LENGTH OF SLAB FOR BREAK ELEMENT WORKING IN Y-DIRECTION

I2=NODP0(ILP-1,ILO)

ELSE IF ((ILP.EQ.4))THEN

I1=NODP0(ILP-3,ILO)

I2=NODP0(ILP-1,ILO)

END IF

DX1=X(J)-X(I1)

DY1=Y(J)-Y(I1)

DX2=X(J)-X(I2)

DY2=Y(J)-Y(I2)

IF ((X(NOD(1,M)).EQ.X(I1)).AND.(Y(NOD(1,M)).EQ.Y(I2)))THEN

XLX=DSQRT(DX1**2+DY1**2)

YLY=DSQRT(DX2**2+DY2**2)

ELSEIF ((X(NOD(1,M)).EQ.X(I2)).AND.(Y(NOD(1,M)).EQ.Y(I1)))THEN

XLX=DSQRT(DX2**2+DY2**2)

YLY=DSQRT(DX1**2+DY1**2)

END IF

XLEQ=XLX/4

YLEQ=YLY/4

IF(ISS.EQ.0.AND.NDIAG.EQ.0)THEN

!NDIAG= A FLAG TO IDENTIFY IF THERE IS DIAGONAL BREAK ELEMENT AT CORNERS

IYES=0

```
DO JJJ6=1,NE

!NDIAG=0 MEANS NO DIAGONAL ELEMENT, NDIAG=1, MEANS DIAGONAL BREAK
ELEMENT AT CORNERS.

DO III6=1,3
  IF (NODPB0(III6,JJJ6).EQ.NOD(2,M))THEN
    IF(IYES.EQ.0)THEN
      IFINDBEAM(1,1)=III6
      IFINDBEAM(2,1)=JJJ6
    ENDIF
    IYES=IYES+1
  END IF
ENDDO

ENDDO

ILP1=IFINDBEAM(1,1)
ILO1=IFINDBEAM(2,1)
IF(Y(NODPB0(ILP1,ILO1)).EQ.Y(NODPB0(3,ILO1)))THEN
  XLEQ=0
  YLEQ=YLY/4
ELSEIF(X(NODPB0(ILP1,ILO1)).EQ.X(NODPB0(3,ILO1)))THEN
  XLEQ=XLX/4
  YLEQ=0
ENDIF

ELSEIF(ISS.EQ.1.AND.NDIAG.EQ.0)THEN
  IYES=0
ILP=IFIND(1,1)
ILO=IFIND(2,1)
  ILP5=IFIND(1,3)
  ILO5=IFIND(2,3)
```

```
IF(Y(NODP0(ILP,ILO)).EQ.Y(NODP0(ILP5,ILO5)))THEN
XLEQ=XLX/4
YLEQ=0
ELSEIF(X(NODP0(ILP,ILO)).EQ.X(NODP0(ILP5,ILO5)))THEN
XLEQ=0
YLEQ=YLY/4
ENDIF
ENDIF

ELSE IF ((ILP.GT.4))THEN
! ILP>4 MEANS THAT NOD(1,M) IS IN THE MID LENGHT OF SLAB
IF ((ILP.LE.7))THEN
I1=NODP0(ILP-4,ILO)
I2=NODP0(ILP-3,ILO)
ELSE IF ((ILP.EQ.8))THEN
I1=NODP0(ILP-4,ILO)
I2=NODP0(ILP-7,ILO)
END IF
DX=X(I2)-X(I1)
DY=Y(I2)-Y(I1)

IF(X(NOD(1,M)).EQ.X(NODP0(9,ILO)))THEN
XLX=0
YLY=DSQRT(DX**2+DY**2)
ELSE IF (Y(NOD(1,M)).EQ.Y(NODP0(9,ILO)))THEN
YLY=0
XLX=DSQRT(DX**2+DY**2)
END IF
XLEQ=XLX/2
YLEQ=YLY/2
```

```
END IF

      IF(ICOUNT.EQ.2)THEN
      IF(ISS.EQ.0)THEN
      IYES=0
      DO JJJ6=1,NE
      DO III6=1,3
      IF (NODPB0(III6,JJJ6).EQ.NOD(2,M))THEN
      IF(IYES.EQ.0)THEN
      IFINDBEAM(1,1)=III6
      IFINDBEAM(2,1)=JJJ6
      ENDIF
      IYES=IYES+1
      END IF
      ENDDO
      ENDDO
      ILP1=IFINDBEAM(1,1)
      ILO1=IFINDBEAM(2,1)

      IF(Y(NODPB0(ILP1,ILO1)).EQ.Y(NODPB0(3,ILO1)))THEN
      INY=1
      XLEQ=0
      YLEQ=YLY/2
      ELSEIF(X(NODPB0(ILP1,ILO1)).EQ.X(NODPB0(3,ILO1)))THEN
      INX=1
      XLEQ=XLX/2
      YLEQ=0
      ENDIF

      ELSEIF(ISS.EQ.1)THEN
```

```

      IF(Y(NOD(2,M)).EQ.Y(NOD(1,M)))THEN
      XLEQ=XLX/2

      YLEQ=0

      ELSEIF(X(NOD(1,M)).EQ.X(NOD(2,M)))THEN
      XLEQ=0

      YLEQ=YLY/2

      ENDIF

      ENDIF

      ENDIF

      XLEQ1=(XLEQ)/1000

      YLEQ1=(YLEQ)/1000

      EBRKX=XLEQ1*NBAR(IMSHEAR)

      EBRKY=YLEQ1*NBAR(IMSHEAR)

      AREBARX=EBRKX*PI*(DBRK(IMSHEAR)/2)**2

      AREBARY=EBRKY*PI*(DBRK(IMSHEAR)/2)**2

C
C.....TRANSFER GLOBAL NODAL DISPLACEMENT VECTOR, SD(), TO LOCAL
C.....ELEMENT NODAL DISPLACEMENT,[Du], DICON(12)

C

      I1=NOD(1,M)

      I2=NOD(2,M)

      I11=(I1-1)*6

      I12=(I2-1)*6

      DO KJ=1,6

      DICON(KJ)=SD(I11+KJ)

      DICON(KJ+6)=SD(I12+KJ)

      ENDDO

C.....CALCULATE LOCAL ELEMENT NODAL DISPLACEMENT [uc], DDCON(10)

C

```

```
DDCON(1)=DICON(1)
DDCON(2)=DICON(2)
DDCON(3)=DICON(3)
DDCON(4)=DICON(4)
DDCON(5)=DICON(5)
DDCON(6)=DICON(7)
DDCON(7)=DICON(8)
DDCON(8)=DICON(9)
DDCON(9)=DICON(10)
DDCON(10)=DICON(11)
```

```
    RDISPX=DDCON(1)-DDCON(6)
    RDISPY=DDCON(2)-DDCON(7)
    ROTX=DDCON(4)-DDCON(9)
    ROTY=DDCON(5)-DDCON(10)
```

```
AX1=X(NOD(1,M))
    AY1=Y(NOD(1,M))
    AX2=X(NOD(2,M))
    AY2=Y(NOD(2,M))

AX=AX1-AX2
    AY=AY1-AY2
    AXX=ABS(AX)
    AYY=ABS(AY)
```

c

! INITIAL STIFFNESS OF BREAK ELEMENT BEFORE CRACK OF THE CONCRETE

```
    IF(ISADEGH(1,M).NE.1)THEN
        ISADEGH(1,M)=0
    ENDIF
    IF(ISADEGH(2,M).NE.1)THEN
        ISADEGH(2,M)=0
```

```
ENDIF
```

```
IF(ISADEGH(1,M).EQ.0.AND.ISADEGH(2,M).EQ.0)THEN
```

```
IV=ILP*6
```

```
DKSH(1)=1.0D8
```

```
DKSH(2)=1.0D8
```

```
DKSH(3)=1.0D8
```

```
DKSH(4)=1.0D12
```

```
DKSH(5)=1.0D12
```

```
ENDIF
```

```
UB=(BFCP20(IMSHEAR))**(0.5)
```

```
UBP=(0.5*(BFCP20(IMSHEAR))**(0.5))
```

```
IF(ISS.EQ.0)THEN
```

```
IF((TL(IAB,NJLAY2).GT.100.AND.TL(IAB,NJLAY2).LE.200).OR.
```

```
*(TL(IAB3,NJLAY2).GT.100.AND.TL(IAB3,NJLAY2).LE.200))THEN
```

```
UB=0.95*UB
```

```
UBP=0.95*UBP
```

```
OPEN (UNIT=5002, FILE='TEMP1.DAT')
```

```
WRITE(5002, '(2X,I3,2X,I3,2X,I3,2X,I2,2X,F10.5,2X,F10.5)') LI,M,
```

```
*IAB,NJLAY2,TL(IAB3,NJLAY2),TL(IAB,NJLAY2)
```

```
ELSEIF((TL(IAB,NJLAY2).GT.200.AND.TL(IAB,NJLAY2).LE.300).OR.
```

```
*(TL(IAB3,NJLAY2).GT.200.AND.TL(IAB3,NJLAY2).LE.300))THEN
```

```
UB=0.9*UB
```

```
UBP=0.9*UBP
```

```
ELSEIF((TL(IAB,NJLAY2).GT.300.AND.TL(IAB,NJLAY2).LE.400).OR.
```

```
*(TL(IAB3,NJLAY2).GT.300.AND.TL(IAB3,NJLAY2).LE.400))THEN
```

```
UB=0.85*UB
```

```
UBP=0.85*UBP
```

```
ELSEIF((TL(IAB,NJLAY2).GT.400.AND.TL(IAB,NJLAY2).LE.450).OR.  
*(TL(IAB3,NJLAY2).GT.400.AND.TL(IAB3,NJLAY2).LE.450))THEN  
UB=0.8*UB  
UBP=0.8*UBP  
ELSEIF((TL(IAB,NJLAY2).GT.450.AND.TL(IAB,NJLAY2).LE.500).OR.  
*(TL(IAB3,NJLAY2).GT.450.AND.TL(IAB3,NJLAY2).LE.500))THEN  
UB=0.75*UB  
UBP=0.75*UBP  
ENDIF
```

```
ELSEIF(ISS.EQ.1)THEN  
IF((TL(IAB5,NJLAY2).GT.100.AND.TL(IAB5,NJLAY2).LE.200).OR.  
*(TL(IAB6,NJLAY2).GT.100.AND.TL(IAB6,NJLAY2).LE.200))THEN  
UB=0.95*UB  
UBP=0.95*UBP  
OPEN (UNIT=5003, FILE='TEMP2.DAT')  
WRITE(5003, '(2X,I3,2X,I3,2X,I3,2X,I2,2X,F10.5,2X,F10.5)') LI,M,  
*IAB5,NJLAY2,TL(IAB5,NJLAY2),TL(IAB6,NJLAY2)
```

```
ELSEIF((TL(IAB5,NJLAY2).GT.200.AND.TL(IAB5,NJLAY2).LE.300).OR.  
*(TL(IAB6,NJLAY2).GT.200.AND.TL(IAB6,NJLAY2).LE.300))THEN  
UB=0.9*UB  
UBP=0.9*UBP  
ELSEIF((TL(IAB5,NJLAY2).GT.300.AND.TL(IAB5,NJLAY2).LE.400).OR.  
*(TL(IAB6,NJLAY2).GT.300.AND.TL(IAB6,NJLAY2).LE.400))THEN  
UB=0.85*UB  
UBP=0.85*UBP  
ELSEIF((TL(IAB5,NJLAY2).GT.400.AND.TL(IAB5,NJLAY2).LE.450).OR.  
*(TL(IAB6,NJLAY2).GT.400.AND.TL(IAB6,NJLAY2).LE.450))THEN  
UB=0.8*UB
```

```

UBP=0.8*UBP
ELSEIF((TL(IAB5,NJLAY2).GT.450.AND.TL(IAB5,NJLAY2).LE.500).OR.
*(TL(IAB6,NJLAY2).GT.450.AND.TL(IAB6,NJLAY2).LE.500))THEN
UB=0.75*UB
UBP=0.75*UBP
ENDIF
ENDIF

```

```

DIAX=2*((AREBARX/PI)**(0.5))
DIAY=2*((AREBARY/PI)**(0.5))
RCX=AREBARX/PI
RCIRCLEX=SQRT(ABS(RCX))
RCY=AREBARY/PI
RCIRCLEY=SQRT(ABS(RCY))
BLD=1
BLDP=1
EAPP20=((BFUP20(IMSHEAR)-BFYP20(IMSHEAR))/(BSUP20(IMSHEAR)-
*BSYP20(IMSHEAR)))
DKSHHX=(BEAP20(IMSHEAR)*PI*((DIAX/2)**4))/(4*10*(1.3))
DKSHHPX=(EAPP20*PI*((DIAX/2)**4))/(4*10*(1.3))
DKSHHY=(BEAP20(IMSHEAR)*PI*((DIAY/2)**4))/(4*10*(1.3))
DKSHHPY=(EAPP20*PI*((DIAY/2)**4))/(4*10*(1.3))

```

```

C%%%%%%%%%%%%%%%%%%%%%%%%%%%%%%%%%%%%%%%%%%%%%%%%%%%%%%%%%%%%%%%%%%%%%%%% BREAK ELEMENT WORKING INDIRECTION
%%%%%%%%%%%%%%%%%%%%%%%%%%%%%%%%%%%%%%%%%%%%%%%%%%%%%%%%%%%%%%%%%%%%%%%%
%%%%%%%%%%%%%%%%%%%%%%%%%%%%%%%%%%%%%%%%%%%%%%%%%%%%%%%%%%%%%%%%%%%%%%%%

```

```

IF (AREBARY.EQ.0)THEN

```

```

IF(LLCRACK(1,M).EQ.0)THEN
DO I=1, (BFUP20(IMSHEAR))
B(I)=I
ENDDO
DO I=1, (BFUP20(IMSHEAR))
IF(I.LE.BFYP20(IMSHEAR))THEN
SLIP(I,M)=(((B(I)**2)*DIAX)/(8*UB*BEAP20(IMSHEAR)))
ELSE
KK=I-BFYP20(IMSHEAR)
SLIP(I,M)=(((BFYP20(IMSHEAR)**2)*DIAX)/(8*BEAP20(IMSHEAR)*UB))
*+(((KK)*BFYP20(IMSHEAR)*DIAX)/(4*UBP*BEAP20(IMSHEAR)))+
*(((KK)**2)*DIAX)/(8*UBP*EAPP20))
ENDIF
ENDDO
SLIPMAX(M)=SLIP(BFUP20(IMSHEAR),M)
IF(ISS.EQ.1)THEN
DO II2=1, (BFUP20(IMSHEAR))
SLIP(II2,M)=2*SLIP(II2,M)
ENDDO
ENDIF

ISTEEL1=NJLAY1-1
ISTEEL2=NJLAY2+1
IF(ICOUNT.EQ.1)THEN
IF(ISADEGH(1,M).EQ.0)THEN
IF(ISS.EQ.0)THEN
IF(NDEGRA(ILP,ISTEEL2,IAB).GT.0)THEN
ISADEGH(1,M)=1
ENDIF
ELSEIF(ISS.EQ.1)THEN

```

```
IF(NDEGRA(ILP,ISTEEL1,IAB).GT.0.OR.NDEGRA(ILP5,ISTEEL1,IAB5).GT.0.
*OR.NDEGRA(ILP,ISTEEL2,IAB).GT.0.OR.NDEGRA(ILP5,ISTEEL2,IAB5).
*GT.0)THEN
  ISADEGH(1,M)=1
ENDIF
ENDIF
ENDIF
ELSEIF(ICOUNT.EQ.2)THEN
  IF(ISADEGH(1,M).EQ.0)THEN
    IF(ISS.EQ.0)THEN
      IF(NDEGRA(ILP,ISTEEL2,IAB).GT.0.OR.NDEGRA(ILP3,ISTEEL2,IAB3).
*GT.0)THEN
        ISADEGH(1,M)=1
      ENDIF
    ELSEIF(ISS.EQ.1)THEN
      IF(NDEGRA(ILP,ISTEEL1,IAB).GT.0.OR.NDEGRA(ILP5,ISTEEL1,IAB5).
*GT.0.OR.NDEGRA(ILP3,ISTEEL1,IAB3).GT.0.OR.
*NDEGRA(ILP6,ISTEEL1,IAB6).GT.0)THEN
        ISADEGH(1,M)=1
      ENDIF
    IF(NDEGRA(ILP,ISTEEL2,IAB).GT.0.OR.NDEGRA(ILP5,ISTEEL2,IAB5).
*GT.0.OR.NDEGRA(ILP3,ISTEEL2,IAB3).GT.0.OR.
*NDEGRA(ILP6,ISTEEL2,IAB6).GT.0)THEN
      ISADEGH(1,M)=1
    ENDIF
  ENDIF
ENDIF
ENDIF
ENDIF
ENDIF
IF(ISADEGH(1,M).EQ.1)THEN
```

```

C*****
*****

      IF(ITENS(1,M).EQ.0)THEN

      DKSH(1)=(B(1)*AREBARX)/(SLIP(1,M))

      DKSH(2)=((12*BEAP20(IMSHEAR)*(PI/4)*((RCIRCLEX)**4))/((BLD)**3))

      DKSH(3)=((12*BEAP20(IMSHEAR)*(PI/2)*((RCIRCLEX)**4))/((BLD)**3))

      DKSH(4)=1.0D8

      DKSH(5)=1.0D8

      ENDIF

C*****
*****

      IF(RDISPX*SIGN(1.0,AX).GT.0)THEN

      ITENS(1,M)=1

      FX1=ABS(RR2(1))/AREBARX

      UX1=FX1/BEAP20(IMSHEAR)

      IF(FX1.GT.BFYP20(IMSHEAR))THEN

      UX1=((FX1-BFYP20(IMSHEAR))/EAPP20)+BSYP20(IMSHEAR)

      ENDIF

      RDISPX=ABS(RDISPX)

      IF(RDISPX.LE.SLIP(BFYP20(IMSHEAR),M))THEN

      IF(RDISPX.LE.SLIP(100,M))THEN

      DKSH(1)=(B(10)*AREBARX)/(SLIP(10,M))

      DKSH(2)=((12*BEAP20(IMSHEAR)*(PI/4)*((RCIRCLEX)**4))/((BLD)**3))

      DKSH(3)=((12*BEAP20(IMSHEAR)*(PI/2)*((RCIRCLEX)**4))/((BLD)**3))

      DKSH(4)=1.0D8

      DKSH(5)=1.0D7

      ENDIF

      DO I=10, (BFYP20(IMSHEAR)-1)

      IF(RDISPX.GT.SLIP(I,M).AND.RDISPX.LE.SLIP(I+1,M))THEN

      DKSH(1)=(B(I+1)*AREBARX)/(SLIP(I+1,M))

```

```

      DKSH(2)=((12*BEAP20(IMSHEAR)*(PI/4)*((RCIRCLEX)**4))/((BLD)**3))
DKSH(3)=((12*BEAP20(IMSHEAR)*(PI/2)*((RCIRCLEX)**4))/((BLD)**3))
DKSH(4)=1.0D8
DKSH(5)=1.0D7

      DK(I,M)=(B(I+1)*AREBARX)/(SLIP(I+1,M))
      DSHF1(I,M)=DK(I,M)*RDISPX
      DSHF11(I,M)=(0.5*(B(I)+B(I+1)))*AREBARX
      DSHF111(I,M)=DSHF11(I,M)/DSHF1(I,M)
      DKSH(1)=DSHF111(I,M)*DK(I,M)
      OPEN (UNIT=501, FILE='X-ELASTIC.DAT')
      WRITE(501,'(2X,I3,2X,I3,2X,3F10.5,2X,2F10.3)') LI,M,AREBARX,RDISPX
      *,SLIP(BFYP20(1),M),DK(I,M),DKSH(1)
ENDIF
      ENDDO

ELSEIF(RDISPX.GT.SLIP(BFYP20(IMSHEAR),M).AND.RDISPX.LE.
      *SLIP(BFUP20(IMSHEAR),M))THEN
      DO I=BFYP20(IMSHEAR), (BFUP20(IMSHEAR)-1)
      IF(RDISPX.GT.SLIP(I,M).AND.RDISPX.LE.SLIP(I+1,M))THEN
      DKSH(1)=(B(I+1)*AREBARX)/(SLIP(I+1,M))
      DKSH(2)=((12*EAPP20*(PI/4)*((RCIRCLEX)**4))/((BLDP)**3))
DKSH(3)=((12*EAPP20*(PI/2)*((RCIRCLEX)**4))/((BLDP)**3))
DKSH(4)=1.0D8

      DK(I,M)=(B(I+1)*AREBARX)/(SLIP(I+1,M))
      DSHF1(I,M)=DK(I,M)*RDISPX
      DSHF11(I,M)=(0.5*(B(I)+B(I+1)))*AREBARX
      DSHF111(I,M)=DSHF11(I,M)/DSHF1(I,M)
      DKSH(1)=DSHF111(I,M)*DK(I,M)
DKSH(5)=DKSH(1)*YPOINT(M)

```

```
IF(((ABS(RDISPX))-((ABS(ROTY))*(SLDEPTH(IMSHEAR)/2))).GT.0)THEN
DKSH(5)=DKSH(1)*YPOINT(M)
    ENDIF

    OPEN (UNIT=503, FILE='X-PLASTIC.DAT')
    WRITE(503,'(2X,I3,2X,I3,2X,3F10.5)') LI,M,AREBARX,RDISPX,
    *SLIP(BFUP20(1),M)
    ENDIF
    ENDDO

    ELSEIF(RDISPX.GT.SLIP(BFUP20(IMSHEAR),M))THEN
DKSH(1)=1.0D3
    DKSH(2)=1.0D3
DKSH(3)=1.0D3
DKSH(4)=1.0D3
DKSH(5)=1.0D3
    SLIPMAXX3(M)=4*SLIPMAX(M)
    B1=BFYP20(IMSHEAR)-100
DKSH(1)=(B1*AREBARX)/(SLIPMAXX3(M))
    LLCRACK(1,M)=1
    ENDIF

    ENDIF
    ENDIF
ELSEIF(LLCRACK(1,M).EQ.1)THEN
    OPEN (UNIT=504, FILE='X-FRACTURE.DAT')
    WRITE(504,'(2X,I3,2X,I3,2X,3F10.5)') LI,M,AREBARX,RDISPX,
    *SLIP(BFUP20(1),M)

DKSH(1)=1.0D2
```

```

      DKSH(2)=1.0D2
DKSH(3)=1.0D2
DKSH(4)=1.0D2
DKSH(5)=1.0D2
      SLIPMAXX1(M)=10*SLIPMAX(M)
      SLIPMAXX2(M)=20*SLIPMAX(M)
      SLIPMAXX3(M)=30*SLIPMAX(M)

      ELSEIF(RDISPX.GT.SLIPMAXX3(M))THEN
DKSH(1)=1.0D2
      DKSH(2)=1.0D2
DKSH(3)=1.0D2
DKSH(4)=1.0D2
DKSH(5)=1.0D2
      OPEN (UNIT=508, FILE='X-FRACTURE-4.DAT')
      WRITE(508,'(2X,I3,2X,I3,2X,3F10.5)') LI,M,AREBARX,RDISPX,
      *SLIP(BFUP20(1),M)
      ENDIF
      ENDIF
      ENDIF

C%%%%%%%%%%%%%%%%%%%%%%%%%%%%%%%%%%%%%%%%%%%%%%%%%%%%%%%%%%%%%%%%%%%%%%%%
%%%%%%%%%%%%%%%%%%%%%%%%%%%%%%%%%%%%%%%%%%%%%%%%%%%%%%%%%%%%%%%%%%%%%%%%

C%%%%%%%%%%%%%%%%%%%%%%%%%%%%%%%%%%%%%%%%%%%%%%%%%%%%%%%%%%%%%%%%%%%%%%%% BREAK ELEMENT WORKING IN    DIRECTION
%%%%%%%%%%%%%%%%%%%%%%%%%%%%%%%%%%%%%%%%%%%%%%%%%%%%%%%%%%%%%%%%%%%%%%%%
%%%%%%%%%%%%%%%%%%%%%%%%%%%%%%%%%%%%%%%%%%%%%%%%%%%%%%%%%%%%%%%%%%%%%%%%

      IF (AREBARX.EQ.0)THEN
          IF(LLCRACK(1,M).EQ.0)THEN
              DO I=1, (BFUP20(IMSHEAR))
                  B(I)=I
              ENDDO
          
```

```
DO I=1, (BFUP20(IMSHEAR))
  IF(I.LE.BFYP20(IMSHEAR))THEN
    SLIP(I,M)=((((B(I)**2)*DIAY)/(8*UB*BEAP20(IMSHEAR)))
  ELSE
    KK=I-BFYP20(IMSHEAR)
    SLIP(I,M)=(((BFYP20(IMSHEAR)**2)*DIAY)/(8*BEAP20(IMSHEAR)*UB))
      *+((((KK)*BFYP20(IMSHEAR)*DIAY)/(4*UBP*BEAP20(IMSHEAR)))+
      *((((KK)**2)*DIAY)/(8*UBP*EAPP20))
  ENDIF
ENDDO

SLIPMAX(M)=SLIP(BFUP20(IMSHEAR),M)
OPEN (UNIT=600, FILE='CHECK.DAT')
WRITE(600,'(2X,I3,2X,I3,2X,4F10.5)') LI,M,AREBARY,RDISPY,
*SLIP(BFUP20(1),M),SLIPMAX(M)
IF(ISS.EQ.1)THEN
  DO II2=1, (BFUP20(IMSHEAR))
    SLIP(II2,M)=2*SLIP(II2,M)
  ENDDO
ENDIF

ISTEEL1=NJLAY1-1
ISTEEL2=NJLAY2+1
IF(ICOUNT.EQ.1)THEN

IF(ISADEGH(1,M).EQ.0)THEN
IF(ISS.EQ.0)THEN
IF(NDEGRA(ILP,ISTEEL2,IAB).GT.0)THEN
  ISADEGH(1,M)=1
ENDIF
```

```
ELSEIF(ISS.EQ.1)THEN
  IF(NDEGRA(ILP,ISTEEL1,IAB).GT.0.OR.NDEGRA(ILP5,ISTEEL1,IAB5).GT.0.
    *OR.NDEGRA(ILP,ISTEEL2,IAB).GT.0.OR.NDEGRA(ILP5,ISTEEL2,IAB5).
    *GT.0)THEN
    ISADEGH(1,M)=1
  ENDIF
ENDIF
ENDIF
ENDIF
ELSEIF(ICOUNT.EQ.2)THEN
  IF(ISADEGH(1,M).EQ.0)THEN
    IF(ISS.EQ.0)THEN
      IF(NDEGRA(ILP,ISTEEL2,IAB).GT.0.OR.NDEGRA(ILP3,ISTEEL2,IAB3).
        *GT.0)THEN
        ISADEGH(1,M)=1
      ENDIF
    ELSEIF(ISS.EQ.1)THEN
      IF(NDEGRA(ILP,ISTEEL1,IAB).GT.0.OR.NDEGRA(ILP5,ISTEEL1,IAB5).
        *GT.0.OR.NDEGRA(ILP3,ISTEEL1,IAB3).GT.0.OR.
        *NDEGRA(ILP6,ISTEEL1,IAB6).GT.0)THEN
        ISADEGH(1,M)=1
      ENDIF
    IF(NDEGRA(ILP,ISTEEL2,IAB).GT.0.OR.NDEGRA(ILP5,ISTEEL2,IAB5).
      *GT.0.OR.NDEGRA(ILP3,ISTEEL2,IAB3).GT.0.OR.
      *NDEGRA(ILP6,ISTEEL2,IAB6).GT.0)THEN
        ISADEGH(1,M)=1
      ENDIF
    ENDIF
    ENDIF
    ENDIF
  ENDIF
ENDIF
ENDIF
IF(ISADEGH(1,M).EQ.1)THEN
```

```
C*****
*****
```

```
IF(ITENS(1,M).EQ.0)THEN
```

```
DKSH(2)=(B(10)*AREBARY)/(SLIP(10,M))
```

```
DKSH(1)=((12*BEAP20(IMSHEAR)*(PI/4)*((RCIRCLEY)**4))/((BLD)**3))
```

```
DKSH(3)=((12*BEAP20(IMSHEAR)*(PI/2)*((RCIRCLEY)**4))/((BLD)**3))
```

```
DKSH(5)=1.0D8
```

```
DKSH(4)=1.0D8
```

```
ENDIF
```

```
C*****
*****
```

```
IF(RDISPY*SIGN(1.0,AY).GT.0)THEN
```

```
ITENS(1,M)=1
```

```
FX1=ABS(RR2(1))/AREBARY
```

```
UX1=FX1/BEAP20(IMSHEAR)
```

```
IF(FX1.GT.BFYP20(IMSHEAR))THEN
```

```
UX1=((FX1-BFYP20(IMSHEAR))/EAPP20)+BSYP20(IMSHEAR)
```

```
ENDIF
```

```
RDISPY=ABS(RDISPY)
```

```
IF(RDISPY.LE.SLIP(BFYP20(IMSHEAR),M))THEN
```

```
IF(RDISPY.LE.SLIP(10,M))THEN
```

```
DKSH(2)=(B(10)*AREBARY)/(SLIP(10,M))
```

```
DKSH(1)=((12*BEAP20(IMSHEAR)*(PI/4)*((RCIRCLEY)**4))/((BLD)**3))
```

```
DKSH(3)=((12*BEAP20(IMSHEAR)*(PI/2)*((RCIRCLEY)**4))/((BLD)**3))
```

```
DKSH(5)=1.0D8
```

```
DKSH(4)=1.0D7
```

```
ENDIF
```

```
DO I=10, (BFYP20(IMSHEAR)-1)
```

```

IF(RDISPY.GT.SLIP(I,M).AND.RDISPY.LE.SLIP(I+1,M))THEN
DKSH(2)=(B(I+1)*AREBARY)/(SLIP(I+1,M))
DKSH(1)=((12*BEAP20(IMSHEAR)*(PI/4)*((RCIRCLEY)**4))/((BLD)**3))
DKSH(3)=((12*BEAP20(IMSHEAR)*(PI/2)*((RCIRCLEY)**4))/((BLD)**3))
DKSH(5)=1.0D8
DKSH(4)=1.0D7
DK(I,M)=(B(I+1)*AREBARY)/(SLIP(I+1,M))
DSHF1(I,M)=DK(I,M)*RDISPY
DSHF11(I,M)=(0.5*(B(I)+B(I+1)))*AREBARY
DSHF111(I,M)=DSHF11(I,M)/DSHF1(I,M)
DKSH(2)=DSHF111(I,M)*DK(I,M)
OPEN (UNIT=509, FILE='Y-ELASTIC.DAT')
WRITE(509,'(2X,I3,2X,I3,2X,3F10.5,2X,2F10.3)') LI,M,AREBARY,RDISPY
*,SLIP(BFYP20(1),M),DK(I,M),DKSH(2)
ENDIF
ENDDO
ELSEIF(RDISPY.GT.SLIP(BFUP20(IMSHEAR),M).AND.RDISPY.LE.
*SLIP(BFUP20(IMSHEAR),M))THEN
DO I=BFUP20(IMSHEAR), (BFUP20(IMSHEAR)-1)
IF(RDISPY.GT.SLIP(I,M).AND.RDISPY.LE.SLIP(I+1,M))THEN
DKSH(2)=(B(I+1)*AREBARY)/(SLIP(I+1,M))
DKSH(1)=((12*EAPP20*(PI/4)*((RCIRCLEY)**4))/((BLDP)**3))
DKSH(3)=((12*EAPP20*(PI/2)*((RCIRCLEY)**4))/((BLDP)**3))
DKSH(5)=1.0D8
DK(I,M)=(B(I+1)*AREBARY)/(SLIP(I+1,M))
DSHF1(I,M)=DK(I,M)*RDISPY
DSHF11(I,M)=(0.5*(B(I)+B(I+1)))*AREBARY
DSHF111(I,M)=DSHF11(I,M)/DSHF1(I,M)
DKSH(2)=DSHF111(I,M)*DK(I,M)
DKSH(4)=1.0D7

```

```
IF(((ABS(RDISPY))-((ABS(ROTX))*(SLDEPTH(IMSHEAR)/2))).GT.0)THEN
DKSH(4)=DKSH(2)*YPOINT(M)
    OPEN (UNIT=510, FILE='Y-PLASTIC-ROT.DAT')
    WRITE(510,'(2X,I3,2X,I3,2X,A3)') LI,M,'YES'
    ENDIF
    ENDIF
    ENDDO

    ELSEIF(RDISPY.GT.SLIP(BFUP20(IMSHEAR),M))THEN
DKSH(1)=1.0D2
    DKSH(2)=1.0D2
DKSH(3)=1.0D2
DKSH(4)=1.0D2
DKSH(5)=1.0D2
    SLIPMAXX3(M)=4*SLIPMAX(M)
    B1=BFYP20(IMSHEAR)-100
DKSH(2)=(B1*AREBARY)/(SLIPMAXX3(M))
    LLCRACK(1,M)=1
ELSEIF(LLCRACK(1,M).EQ.1)THEN
DKSH(1)=1.0D2
    DKSH(2)=1.0D2
DKSH(3)=1.0D2
DKSH(4)=1.0D2
DKSH(5)=1.0D2
    ELSEIF(RDISPY.GT.SLIPMAXX3(M))THEN
DKSH(1)=1.0D2
    DKSH(2)=1.0D2
DKSH(3)=1.0D2
DKSH(4)=1.0D2
DKSH(5)=1.0D2
```

```

        ENDIF
        ENDIF
        ENDIF

C%%%%%%%%%%%%%%%%%%%%%%%%%%%%%%%%%%%%%%%%%%%%%%%%%%%%%%%%%%%%%%%%%%%%%%%%
%%%%%%%%%%%%%%%%%%%%%%%%%%%%%%%%%%%%%%%%%%%%%%%%%%%%%%%%%%%%%%%%%%%%%%%%

        DO I=1,5
        DSHF(I)=DKSH(I)*(DDCON(I)-DDCON(5+I))
        DSHF(I+5)=-DSHF(I)
        END DO
        DO I=1,10
        RRBREAK(I)=DSHF(I)
        END DO
C  FORM ELEMENT STIFFNESS MATRIX,SCON(10,10)
        DO I=1, 5
        SCON(I,I)=DKSH(I)
        SCON(I,I+5)=-DKSH(I)
        SCON(I+5,I)=-DKSH(I)
        SCON(I+5,I+5)=DKSH(I)
        END DO
C
C.....FOLLOWING CALCULATION CORESPONDENT TO EACH ELEMENT
C.....FORM STIFFNESS MATRIX INTO GLOBAL
        IF(LLCRACK(1,M).EQ.0.OR.LLCRACK(2,M).EQ.0)THEN
                DO I=1,12
                DO J=1,12
                SS2(I,J)=0.0D0
                ENDDO
                ENDDO
                ENDIF
        DO I=1,12

```

```
RR2(I)=0.0D0
```

```
ENDDO
```

```
IF(LLCRACK(1,M).EQ.0.OR.LLCRACK(2,M).EQ.0)THEN
```

```
SS2(1,1)=SCON(1,1)
```

```
SS2(1,2)=SCON(1,2)
```

```
SS2(1,3)=SCON(1,3)
```

```
SS2(1,4)=SCON(1,4)
```

```
SS2(1,5)=SCON(1,5)
```

```
SS2(1,7)=SCON(1,6)
```

```
SS2(1,8)=SCON(1,7)
```

```
SS2(1,9)=SCON(1,8)
```

```
SS2(1,10)=SCON(1,9)
```

```
SS2(1,11)=SCON(1,10)
```

```
C
```

```
SS2(2,1)=SCON(2,1)
```

```
SS2(2,2)=SCON(2,2)
```

```
SS2(2,3)=SCON(2,3)
```

```
SS2(2,4)=SCON(2,4)
```

```
SS2(2,5)=SCON(2,5)
```

```
SS2(2,7)=SCON(2,6)
```

```
SS2(2,8)=SCON(2,7)
```

```
SS2(2,9)=SCON(2,8)
```

```
SS2(2,10)=SCON(2,9)
```

```
SS2(2,11)=SCON(2,10)
```

```
C
```

```
SS2(3,1)=SCON(3,1)
```

```
SS2(3,2)=SCON(3,2)
```

```
SS2(3,3)=SCON(3,3)
```

```
SS2(3,4)=SCON(3,4)
```

```
SS2(3,5)=SCON(3,5)
```

SS2(3,7)=SCON(3,6)

SS2(3,8)=SCON(3,7)

SS2(3,9)=SCON(3,8)

SS2(3,10)=SCON(3,9)

SS2(3,11)=SCON(3,10)

C

SS2(4,1)=SCON(4,1)

SS2(4,2)=SCON(4,2)

SS2(4,3)=SCON(4,3)

SS2(4,4)=SCON(4,4)

SS2(4,5)=SCON(4,5)

SS2(4,7)=SCON(4,6)

SS2(4,8)=SCON(4,7)

SS2(4,9)=SCON(4,8)

SS2(4,10)=SCON(4,9)

SS2(4,11)=SCON(4,10)

C

SS2(5,1)=SCON(5,1)

SS2(5,2)=SCON(5,2)

SS2(5,3)=SCON(5,3)

SS2(5,4)=SCON(5,4)

SS2(5,5)=SCON(5,5)

SS2(5,7)=SCON(5,6)

SS2(5,8)=SCON(5,7)

SS2(5,9)=SCON(5,8)

SS2(5,10)=SCON(5,9)

SS2(5,11)=SCON(5,10)

C

SS2(7,1)=SCON(6,1)

SS2(7,2)=SCON(6,2)

SS2(7,3)=SCON(6,3)
SS2(7,4)=SCON(6,4)
SS2(7,5)=SCON(6,5)
SS2(7,7)=SCON(6,6)
SS2(7,8)=SCON(6,7)
SS2(7,9)=SCON(6,8)
SS2(7,10)=SCON(6,9)
SS2(7,11)=SCON(6,10)

C

SS2(8,1)=SCON(7,1)
SS2(8,2)=SCON(7,2)
SS2(8,3)=SCON(7,3)
SS2(8,4)=SCON(7,4)
SS2(8,5)=SCON(7,5)
SS2(8,7)=SCON(7,6)
SS2(8,8)=SCON(7,7)
SS2(8,9)=SCON(7,8)
SS2(8,10)=SCON(7,9)
SS2(8,11)=SCON(7,10)

C

SS2(9,1)=SCON(8,1)
SS2(9,2)=SCON(8,2)
SS2(9,3)=SCON(8,3)
SS2(9,4)=SCON(8,4)
SS2(9,5)=SCON(8,5)
SS2(9,7)=SCON(8,6)
SS2(9,8)=SCON(8,7)
SS2(9,9)=SCON(8,8)
SS2(9,10)=SCON(8,9)
SS2(9,11)=SCON(8,10)

C

```
SS2(10,1)=SCON(9,1)
SS2(10,2)=SCON(9,2)
SS2(10,3)=SCON(9,3)
SS2(10,4)=SCON(9,4)
SS2(10,5)=SCON(9,5)
SS2(10,7)=SCON(9,6)
SS2(10,8)=SCON(9,7)
SS2(10,9)=SCON(9,8)
SS2(10,10)=SCON(9,9)
SS2(10,11)=SCON(9,10)
```

C

```
SS2(11,1)=SCON(10,1)
SS2(11,2)=SCON(10,2)
SS2(11,3)=SCON(10,3)
SS2(11,4)=SCON(10,4)
SS2(11,5)=SCON(10,5)
SS2(11,7)=SCON(10,6)
SS2(11,8)=SCON(10,7)
SS2(11,9)=SCON(10,8)
SS2(11,10)=SCON(10,9)
SS2(11,11)=SCON(10,10)
```

ENDIF

C.....FORM INTERNAL NODAL FORCE VECTOR INTO GLOBAL

```
RR2(1)=RRBREAK(1)
RR2(2)=RRBREAK(2)
RR2(3)=RRBREAK(3)
RR2(4)=RRBREAK(4)
RR2(5)=RRBREAK(5)
```

RR2(7)=RRBREAK(6)

RR2(8)=RRBREAK(7)

RR2(9)=RRBREAK(8)

RR2(10)=RRBREAK(9)

RR2(11)=RRBREAK(10)

RETURN

END

